Solder Joint Reliability Based Prognostic Health Management (PHM) Models for Life Prediction of Electronics Subjected to Harsh Thermo-mechanical Environments

by

Mahendra Harsha

A dissertation submitted to the Graduate Faculty of
Auburn University
in partial fulfillment of the
requirements for the Degree of
Doctor of Philosophy

Auburn, Alabama
December 14, 2013

Keywords: PHM, Solder Joint Reliability, Life Prediction
Prognostics, Electronic Packaging

Copyright 2013 by Mahendra Harsha

Approved by

Pradeep Lall, Chair, Thomas Walter Professor of Mechanical Engineering
Jeffrey C Suhling, Quina Distinguished Professor of Mechanical Engineering
Roy W Knight, Assistant Professor of Mechanical Engineering
Michael J. Bozack, Professor of Physics Department

Abstract

Field deployed electronics may accrue damage due to environmental exposure and usage after finite period of service but may not often have any macro-indicators of failure such as cracks or delamination. In real world setting it is often required to know during the service life of the system what is the amount of life consumed well before the actual failure occurs to schedule maintenance well in advance. The thermal conditions can change according to the change in the usage profile or also during redeployment from one field environment to another. For example in case of defense applications, military equipments come back from a particular field environment and are redeployed in different field environments after certain time intervals. Or in case of space missions the electronic systems embedded in the space equipments have to undergo different operational temperatures depending on the field conditions. It is important to note that different field environments have different magnitudes of damage incursions on electronic systems. Also electronic systems are often stored for a very long time before they are deployed in the intended environment. It is extremely important to quantify the expended life during storage especially for electronic systems used in mission critical applications. Although ambient temperature storage does not lead to any macro indicators of failure like cracks or de-lamination but it is well known that aging has an adverse effect on the life of electronics. Modern day electronic systems perform well when exposed to such multiple harsh environments and often times may not fail before their designed service life however the latent damage incurred at each stage cannot be neglected

and has to be taken in to account to avoid catastrophic failures and system down time in the field. Quantification of thermal environments during use-life is often not feasible because of the data-capture and storage requirements, and the overhead on core-system functionality. Thus there is a growing need to develop and demonstrate technologies that can monitor and predict the remaining useful life (RUL) of electronics in single thermal environments and also assess operational readiness of the electronic system during redeployment.

Proposed prognostic models are based on physics-of-failure based damage-proxies of second level solder interconnects found in today's commercially available high I/O packaging architectures. Test vehicles have been carefully selected for the development and implementation of the models so that they are relevant to the current packaging trends. Prognostic framework involves the use of condition monitoring devices for gathering data on damage pre-cursors at periodic intervals. The presented Prognostic Health Management (PHM) framework lies in the pre-failure space without any knowledge of prior stress histories i.e. in the absence of macro-indicators like cracks or de-lamination. In this thesis, test cases have been presented to demonstrate the viability of the approach for assessment of prior damage, operational readiness, cyclic life reduction due to long-term storage and residual life for electronic assemblies exposed to single and multiple thermo-mechanical environments.

Acknowledgments

To describe this as a journey is an understatement. It has been hard work, difficult at times, but extremely rewarding, and I am surprised and amazed to have made it to this point. I have a number of people to thank for their support in getting this far on this doctoral journey.

First, I would like to express my deep gratitude to my research advisor Dr. Pradeep Lall for giving me the opportunity to work under his guidance and mentorship at NSF Center for Advanced Vehicle and Extreme Environment Electronics ($CAVE^3$) as a Graduate Research Assistant at Auburn University.

Special thanks go to Dr. Jeff C. Suhling, under whom I took several courses and learned a lot. Thanks to all the other committee members Dr. Roy Knight and Dr. Michael J. Bozack for serving on this committee and helping me finish this degree. Thanks to Dr. Adit Singh for serving as external reader for this dissertation. Thanks to all the sponsors at CAVE3 for providing financial support for my graduate studies.

To my Mom and Dad, Vimala and Jyoti Prakash Harsha, I owe them more thanks than I can ever put into words, as I do the rest of my family – S.P Harsha, Dr. R. K Purohit, M.L Purohit, Sangeeta Harsha, Kirti, Aditya, Pragya & Neha for their limitless care, support, sacrifice and confidence.

The biggest of all the giants is my elder brother Dr. Suraj Prakash Harsha, who I cannot thank enough for the opportunities he has given me, the constant encouragement he provides and for always being there for me. Thank you for your love, support, and unwavering belief in me. Without you, I would not be the person I am today.

To my friends Sonali, Arjun, Rahul, Khushboo and Rucha – thank you for your continued friendship, support, laughs and lending money along the way.

Other colleagues at Auburn, past and present, both staff and students, whose help I have appreciated over the course of this PhD include:

John Marcell, Liz Hartwick, Cortney Daniels, Bob Hinshaw, Geeta, Vikalp, Kazi, Peter, Mandar, Prashant and many others whose names are not mentioned here.

Table of Contents

Abstract……………………………………………………………………………..…….ii

Acknowledgments……………………………………………………………...………...iv

List of Figures………………………………………………………………………….xi

List of Tables……………………………………………………………………...xxii

CHAPTER 1 Introduction

1.1 Electronic Packaging Overview...1

1.2 Reliability Concerns...3

1.3 Prognostic Health Management Systems...7

1.4 Thesis Layout……………………..……………………………………………8

CHAPTER 2 Literature Review

2.1 Solder Joint Reliability……………..……………..……………....……..…………14

2.1.1 Reliability of BGA Packages……………………………………………15

2.1.2 Lead free (Pb-free) Solders……………………………………………...16

2.2 Life Prediction Models…………………..………………………………...…..……18

2.2.1 Physics of Failure (POF) Models……………………………………..19

2.2.2 Finite Element Analysis (FEA) Models…………………………………20

2.3 Diagnostic Models…………..……………………..……………………..…….22

2.4 Applications of Prognostic Health Management (PHM) Systems……………..……...25

2.4.1 General PHM Applications……………….……..……………….……..……….26

2.4.2 PHM of Electronics…………………………...……….…………...……...28

CHAPTER 3 Interrogation of Accrued Damage and Remaining Life in Field-Deployed Electronics Subjected to Multiple Thermal Environments

3.1 Overview……………………………………………………......……..……………32

3.2 Test Vehicle ……………………………………………………………...……...33

3.3 Approach for Prognosticating Damage………..………………………….………..35

3.3.1 Micro-structural Evolution of Damage under Single Stresses……………..………37

3.3.2 Damage Equivalency Relationships for Thermal Aging and Thermal Cycling…...42

3.3.3 Validation of Damage Equivalency and Prognostication under Overlapping Stresses………………………………………………………………………..….45

3.4 Levenberg-Marquardt Algorithm………………………………..…………………...47

3.5 Prognostication of Damage in Leadfree Area- Array Interconnects under Sequential Stresses…………..………………………………………………………………49

3.5.1 Micro-structural Evolution Under Thermal Cycling ………………….………..……53

3.6 Damage Equivalency Relationships between Thermal Aging and Thermal-Cycling…..…...57

3.7 Prognostication of Damage Under Multiple Stresses ……………………………………61

3.8 Prognostics Performance Metrics…………………………………………………………66

3.9 Residual Life in Multiple Environments…………………………………...…...…………73

3.10 Summary and Conclusions…………………………...……………………..……..76

CHAPTER 4 Determination of Accrued Damage and Remaining Life during Field-Usage in Lead-Free Electronics Subjected to Multiple Thermo-mechanical Environments

4.1 Overview………………………...………………………………………………………78

4.2 Test Vehicle………………………...……………………………………………………79

4.3 Approach for Prognostication of Damage from Sequential Exposure to Thermo-mechanical Stresses……………………………………………………………………...82

4.3.1 Measurment of Leading Indicators…………………………………………………...85

4.4 Levenberg-Marquardt Algorithm……………………………………………………………….88

4.5 Damage Accrual Relationships……………………………………………………………90

4.5.1 Thermal Aging at 125°C (TA)…………………………………………………..90

4.5.2 Thermal Cycling -40 to 125C (TC1)……………………………………………94

4.5.3 Thermal Cycling 0 to 100C (TC2)………………………………………………98

4.6 Damage Equivalency Relationships between Thermal Aging @ 125°C and Thermal-Cycling @ -40°C to 125°C………………………………………………………………102

4.7 Damage Equivalency Relationships for Thermal-Cycling: TC1 (-40°C to 125°C) and TC2 (0°C to 100°C)……………………………………………………………………………...107

4.8 Assessment of Differential damage and Residual Life after withdrawn from TA1 + TC1 and Redeployment in TC2…………………………………………………………….111

4.9 Residual Life in Multiple Environments…………………………………………………116

4.10 PROGNOSTICS PERFORMANCE METRICS……………………………………..123

4.11 Summary and Conclusions…………………………………………………………...129

CHAPTER 5 Damage Pre-cursor Based Assessment of Impact of High Temperature Storage on Reliability of Lead-free Electronics

5.1 Overview………………………………………………………………………………...131

5.2 Test Vehicle……………………………………………………………………………..133

5.3 Approach for Interrogation of Damage in Thermal Aging…………………………...135

5.3.1 Micro-structural Evolution of Damage……………………………………...135

5.3.2 Damage Mapping Relationships for Phase Growth………………………………138

5.3.3 Damage Mapping Relationships for IMC Growth………………………………..139

5.4 Leading Indicators for Thermal Aging…………………………...……………...140

5.4.1 Phase-Growth Damage Proxy…………………………………………………141

5.4.2 Intermetallic Thickness Damage Proxy………………………………………..146

5.5 Damage Mapping……………………..…………………………………………………...151

5.5.1 Using Damage Mapping for Overlapping Thermal Environments……………….153

5.6 Summary and Conclusion…………………………………………………………...156

CHAPTER 6 Damage Pre-cursors Based Prognostication of Accrued Damage and Assessment of Operational Readiness of Leadfree Electronics

6.1 Overview…………………………………………………………..………………...158

6.2 Test Vehicle……………………………………………………………………….159

6.3 Approach for Prognostication of Damage from Sequential Exposure to Thermo-mechanical Stresses…………………………………………………………………….……162

6.3.1 Micro-structural Evolution of Damage……………………………………...163

6.4 Damage Accrual Relationships……………………………………………………..166

6.4.1 Thermal Aging at 60°C, 85°C and 125°C……………………..………………….166

6.4.2 Thermal Cycling at -55°C to 125°C, -40°C to 95°C and 3°C to 100°C……………..176

6.5 Damage Equivalency Relationships between Thermal Aging and Thermal-Cycling……...187

6.6 Prognostication of Damage under Overlapping Stresses…………………………...191

6.7 Summary and Conclusions………………………………………………………208

CHAPTER 7 Summary and Future Work…………………………………………...209

7.1 PHM Model for Field –deployed Electronics subjected to Overlapping Thermo-Mechanical Environments………………………………………………………………………210

7.2 PHM Model for Sequential Thermal Environments of Thermal Aging and Thermal Cycling ……………………………………………………………………………………...211

7.3 PHM Model for Overlapping Sequential Thermal Environments of Thermal Aging and Thermal Cycling…………………………………………………………………...212

7.4 Scope for Future Work……………………………………………………………...212

Bibliography………………………………………………………………………214

Appendix…………………………………………………………………………..246

List of Figures

Figure 1 Electronic Packaging Trends [Evans 2008, ELEC 6740]……………………………..……2

Figure 2 Typical Ball Grid Array (BGA) Electronic Package Architecture……..……………..……3

Figure 3 BGA with Heat Sink……………………………………………………………………34

Figure 4 X-ray images showing 26 X 26 Perimeter Array………………………………………35

Figure 5 Stepwise Approach……………………………………………………………………..36

Figure 6 Life vs Damage Curve for Thermal Environments……………………………………37

Figure 7 Phases in Traditional Eutectic Solder…………………………………………………..38

Figure 8 Microanalysis Spectrum of Phase Growth using Energy Dispersion Spectroscopy (EDS)……………………………………………………………………………………..39

Figure 9 Microanalysis Spectrum of IMC using Energy Dispersion Spectroscopy (EDS)……...39

Figure 10 Micrograph and Gray scale mapping of image using Image analysis software………39

Figure 11 IMC measurements at board side copper pad………………………………………42

Figure 12: Concept of Damage Equivalency and Mapping of Life Consumed Due to Storage…44

Figure 13: Prognostication of AGED+THERMAL CYCLED Sample at the same thermal cycle count N1……..………………………………………………………………………45

Figure 14: Microscope images of Phase growth versus different aging time intervals (Thermal aging at 60°C, 456 I/O PBGA, magnification 1000x)……………………..……...50

Figure 15: Plot of Normalized Phase growth versus Thermal Aging Time 456 PBGA, subjected to thermal aging at 60°C……………………..……………………………………50

Figure 16 Microscope images of Intermetallic Thickness versus different aging time intervals (Thermal aging at 60°C, 456 I/O PBGA, magnification 1000x)……… …………...51

Figure 17 Plot of Normalized IMC thickness versus Aging Time for 456 PBGA, subjected to thermal aging at 60°C………………..…………………………………………52

Figure 18: Microscope image of Phase growth versus different aging time intervals (Thermal cycling -40°C to 125°C, 456 I/O PBGA, magnification 1000x)…… ………..……54

Figure 19 Plot of Normalized Phase growth versus Aging Time for 456 PBGA, subjected to thermal cycling from -40°C to 125°C…………………………………………..55

Figure 20 Microscope image of Intermetallic Thickness versus different aging time intervals (Thermal Cycling at -40 to 125°C, 456 I/O PBGA, magnification 1000x)…… ……56

Figure 21: Plot of Normalized IMC thickness versus No of Cycles for 456 PBGA, subjected to thermal Cycles from - 40°C to 125°C………………..…………………………56

Figure 22 Combined plot Normalized Phase growth versus thermal aging time/thermal cycling..……………………………………………………………………59

Figure 23 Combined plot of Normalized IMC thickness versus thermal aging time/thermal cycling………..……………………………………………………………59

Figure 24: Combine plot of No of Cycles (N) versus Time in hrs, due to damage mapping from Phase growth and IMC thickness……………………………………………..…...61

Figure 25: 3D plot of error versus Number of Cycles, damage incurred due to storage in Thermal Cycling Environment (N)………………………………. ……………………..62

Figure 26: 3D plot of error versus Number of Cycles, damage incurred due to storage in Thermal Cycling Environment (N+ΔN)…………… ………………………………………....63

Figure 27: 3D plot of error versus Aging time damage incurred due to storage in Isothermal Aging Environment (t)………………… …………………………………………...64

Figure 28: 3D plot of error versus Aging time damage incurred due to storage in Isothermal Aging Environment (t+144) hours…………..……………………………………65

Figure 29: α-λ curve for Prognostication Using Phase Growth as the Damage Proxy…………..70

Figure 30: α-λ curve for Prognostication Using IMC as the Damage Proxy……………………70

Figure 31: Combined α-λ curve for Prognostication …………………………………………71

Figure 32: Weibull plot for pristine 456 BGA packages subjected to thermal cycle -40ºC to 125ºC……………………..……………………………………………………..74

Figure 33: Cross-section of identical field extracted part subjected to thermal cycle -40ºC to 125ºC for additional………………..……………………………………………...74

Figure 34: Top and Bottom part of PBGA 676 and PBGA 256 Packages………………………80

Figure 35: Test Assembly Design……………………………………………………………..81

Figure 36: Reflow Profile for SAC Alloy…………………………………………………………..82

Figure 37: Exposure of Electronics Sequential Stresses of Thermal Aging and Cycling……….84

Figure 38: Life Vs Damage Curve for Multiple Thermal Environments………………………..84

Figure 39: Micrograph and Gray scale mapping of image using image analysis software……...86

Figure 40: Back-scattered images of IMC growth (Magnification 1000x)……………………...87

Figure 41: Backscattered image of Phase Growth versus different aging time intervals of thermal aging at 125°C (a) 676 I/O PBGA, magnification 1000x (b) 256 I/O PBGA, magnification 1000x…………………………..……………………………….91

Figure 42: Phase growth parameter under thermal aging at125°C (a) 676 I/O BGA (b) 256 I/O BGA…………………………..………………………………………………...92

Figure 43: Normalized IMC growth under thermal aging at 125°C (a) 676 I/O BGA (b) 256 I/O BGA……………………………………………………………………………….92

Figure 44: Backscattered image of Phase Growth versus different cycling time intervals after thermal cycling at -40°C to 125°C (a) 676 I/O PBGA, magnification 1000x (b) 256 I/O CABGA, magnification 1000x………………..………………………………..93

Figure 45: Phase growth parameter under thermal cycling at - 40°C to 125°C (a) 676 I/O BGA (b) 256 I/O BGA………………………………………..………………………95

Figure 46: Backscattered image of Intermetallic thickness versus different cycling time intervals after thermal cycling at -40°C to 125°C (a) 676 I/O PBGA, magnification 1000x (b) 256 I/O CABGA, magnification 1000x…………………………….……………..96

Figure 47: IMC growth under thermal cycling at -40°C to 125°C (a) 676 I/O BGA (b) 256 I/O BGA……………………..…………………………………………………………...96

Figure 48: Backscattered image of Phase Growth versus different cycling time intervals of thermal cycling at 0°C to 100°C (a) 676 I/O PBGA, magnification 1000x (b) 256 I/O PBGA, magnification 1000x……………………………………………………..97

Figure 49: Phase growth parameter under thermal cycling from 0°C to 100°C (a) 676 I/O BGA (b) 256 I/O BGA……………………..……………………………………………99

Figure 50: Backscattered image of Intermetallic thickness versus different cycling time intervals of thermal cycling at - 0°C to 100°C (a) 676 I/O PBGA, magnification 1000x (b) 256 I/O PBGA, magnification 1000x…………………………………………………...100

Figure 51: IMC growth under thermal cycling from 0°C to 100°C (a) 676 I/O BGA (b) 256 I/O BGA…………………………………………………………..…………….100

Figure 52: Combined plot Normalized Phase growth versus thermal aging time/thermal cycling for 676 PBGA………………………..……………………………………..101

Figure 53: Combined plot for 676 PBGA of Normalized IMC thickness versus thermal aging time/thermal cycling………………………..………………………………102

Figure 54: Combined plot Normalized Phase growth versus thermal aging time/thermal cycling for 256 CABGA…………………………………………..………………...103

Figure 55: Combined plot for 256 CABGA of Normalized IMC thickness versus thermal aging time/thermal cycling………………………..………………………………104

Figure 56: Combined plot Normalized Phase growth versus - 40°C to 125°C and thermal cycles in 0°C to 100°C for 676 PBGA………………………………….……………....107

Figure 57: Combined plot for 676 PBGA of Normalized IMC thickness versus TC-1 and TC-2 ..…………………………..…………………………………………………109

Figure 58: Combined plot Normalized Phase growth versus - 40°C to 125°C and thermal cycles in 0°C to 100°C for 256 CABGA………………………….…………………....110

Figure 59: Combined plot for 256 CABGA of Normalized IMC thickness -40°C to 125°C and thermal cycles in 0°C to 100°C…………….……………………………………110

Figure 60: Back-scattered Images for samples exposed to Multiple Environments of 168 hours @ 125OC + 250 Cycles TC-1 + x-Cycles TC-2, 676 I/O PBGA, magnification 1000x (a) Phase Growth (b) IMC growth…………………..………………………………...112

Figure 61: 3D plot of error versus Number of Cycles, Life computed from LM-algorithm for 168hrs TA + 250 cycles TC1 + 250 cycles TC2 and 168hrs TA + 250 cycles in TC1 + 500 cycles in TC2 for 676 PBGA………………………………………………..113

Figure 62: Back-scattered Images for samples exposed to Multiple Environments of 168 hours @ 125OC + 250 Cycles TC-1 + x-Cycles TC-2, 256 I/O PBGA, magnification 1000x (a) Phase Growth (b) IMC growth……………………...…………………………...114

Figure 63: 3D plot of error versus Number of Cycles, Life computed from LM-algorithm for 168hrs TA + 250 cycles TC1 + 250 cycles TC2 and 168hrs TA + 250 cycles in TC1 + 500 cycles in TC2 for 256 PBGA………………………………………………..115

Figure 64: Weibull plot for 676-PBGA packages subjected to thermal cycle 0ºC to 100ºC…...117

Figure 65: Weibull plot for 256-CABGA packages subjected to thermal cycle 0ºC to 100ºC...118

Figure 66: α-λ curve for Prognostication using phase-growth as the damage proxy…………..124

Figure 67: α-λ curve for Prognostication using IMC as the damage proxy……………………125

Figure 68: α-λ curve for Prognostication using phase-growth as the damage proxy…………..127

Figure 69: α-λ curve for Prognostication using IMC as the damage proxy……………………127

Figure 70: CABGA 256 Package……………………………………………………………133

Figure 71: Micrograph and Gray scale mapping of image using image analysis software…….135

Figure 72: Image of IMC growth……………………………………………………………136

Figure 73: Optical Microscopic images of Phase Growth in CABGA256 at different time intervals at 60°C (Magnification 1000X)………………… ………………………141

Figure 74: Optical Microscopic images of Phase Growth in CABGA256 at different time intervals at 75°C (Magnification 1000X)……………………… …………………141

Figure 75: Optical Microscopic images of Phase Growth in CABGA256 at different time intervals at 125°C (Magnification 1000X)…………… …………………………..142

Figure 76: Relation between Normalized Phase Growth (Sn) and Aging Time (t) for CABGA 256………………………………………………………………………………142

Figure 77: Plot of ln(a′) and Aging temperature for CABGA256…………………………...143

Figure 78: Plot of ln(b_0) and Aging temperature for CABGA256…………………………...144

Figure 79: Optical Microscopic images of IMC Growth in CABGA256 at different time intervals at 60°C (Magnification 1000X)……………………. …………………………...146

Figure 80: Optical Microscopic images of IMC Growth in CABGA256 at different time intervals at 75°C (Magnification 1000X) …………………..…………………………..146

Figure 81: Optical Microscopic images of IMC Growth in CABGA256 at different time intervals at 125°C (Magnification 1000X)……………………. …………………………147

Figure 82: Relation between Normalized IMC Growth (Yn) and Aging Time (t) for CABGA 256 …………………………………………………………………………………....148

Figure 83: Plot of ln(a′) and Aging temperature for CABGA256 Activation Energy for IMC Growth Coefficient…………………………………………………………..149

Figure 84: Iso-phase growth plots of Aging temperature (T) vs Aging time(t) for Phase Growth (CABGA 36)…………… ………………………………………………………151

Figure 85: Iso-IMC growth plots of Aging Time, ln(T) vs Aging Temperature for CABGA 36. ……………………………………………………………………………..151

Figure 86: Back-scattered Images for samples exposed to Multiple Environments of 168 hours @ 125OC + 250 Cycles TC-1 + x-Cycles TC-2, 256 I/O PBGA, magnification 1000x (a) Phase Growth (b) IMC growth…...…………………………………………………...153

Figure 87: 3D plot of error versus Number of Cycles, Life computed from LM-algorithm for 168hrs TA + 250 cycles TC1 + 250 cycles TC2 and 168hrs TA + 250 cycles in TC1 + 500 cycles in TC2 for 256 PBGA. ………………………………………………154

Figure 88: 324 I/O Package & Assembly…………………………………………………159

Figure 89: Reflow Profile for SAC Alloy…………………………………………………160

Figure 90: Exposure of Electronics Sequential Stresses of Thermal Aging and Cycling……...161

Figure 91: Micrograph and Gray scale mapping of image using image analysis software…….163

Figure 92**:** Back-scattered images of IMC growth (Magnification 1000x) ……………………165

Figure 93: Backscattered image of Phase Growth versus different aging time intervals of thermal aging at (a) 60°C, (b) 85°C and (c) 125°C for 324 I/O PBGA, magnification 1000x……………………………………………………………………….….167

Figure 94**:** Phase growth parameter under thermal aging at 60°C, 85°C and 125°C…………..168

Figure 95: Plot between ln a_1 and Cycling temperature……………………………………..169

Figure 96: Backscattered image of IMC Growth versus different aging time intervals of thermal aging at (a) 60°C, (b) 85°C and (c) 125°C for 324 I/O PBGA, magnification 1000x…………………………………………………………………………..170

Figure 97: Relation between Normalized IMC Growth (Y_n) and Aging Time (t) for PBGA 324……………………………………………………………………………172

Figure 98: Plot of ln k_0 and Aging temperature Activation energy, coefficients & exponent for all the aging temperatures……………………..…………………………………173

Figure 99: Backscattered image of Phase Growth versus different aging time intervals of thermal cycling at (a) -55 to 125°C, (b) -40 to 95°C and (c) 3 to 100°C for 324 I/O PBGA, magnification 1000x……………………..…………………………………174

Figure 100: Plot of Phase growth parameter vs No. of cycles under thermal cycling at -55 to 125°C, -40 to 95°C and 3 to 100°C for 324 I/O PBGA ……………..…………177

Figure 101: Plot between ln a_0 and cycling temperature ……………………………………....178

Figure 102: Plot between ln b_0 and cycling temperature………………………………………179

Figure 103: Backscattered image of IMC Growth versus different aging time intervals of thermal cycling at (a) -55 to 125°C, (b) -40 to 95°C and (c) 3 to 100°C for 324 I/O PBGA, magnification 1000x…………………………………………..…………………180

Figure 104: IMC growth parameter under thermal cycling at -55 to 125°C, -40 to 95°C and 3 to 100°C for 324 I/O PBGA…………………………………………………………183

Figure 105: Plot between $\ln k_0$ and Cycling Temperature………………………………………183

Figure 106: Plot between $\ln b_0$ and Cycling Temperature………………………………………184

Figure 107: Combined plot Normalized Phase growth and Normalized IMC growth versus thermal aging time/thermal cycling…………………….……………………….185

Figure 108: Combined plot Normalized Phase growth and Normalized IMC growth versus thermal aging time/thermal cycling……………………………………..……….187

Figure 109: Combined plot Normalized Phase growth and Normalized IMC growth versus thermal aging time/thermal cycling……………………………………..……….188

Figure 110: Back-scattered Images for samples exposed to Environments of x hours @ 125°C + y CyclesTC-1 magnification 1000x (a) Phase Growth (b) IMC, 324 I/O PBGA…189

Figure 111: 3D plot of error versus Number of Cycles, Life computed from LM-algorithm for x-hrs TA3 + 250 cycles TC1 using Phase Growth as damage Proxy……...……...191

Figure 112: 3D plot of error versus Number of Cycles, Life computed from LM-algorithm for x-hrs TA3 + 250 cycles TC1 using IMC as damage Proxy………………………..193

Figure 113: Back-scattered Images for samples exposed to Environments of x hours @ 85°C + y CyclesTC-2 magnification 1000x (a) Phase Growth (b) IMC, 324 I/O PBGA…194

Figure 114: 3D plot of error versus Number of Cycles, Life computed from LM-algorithm for x-hrs TA2 + 250 cycles TC2 using Phase Growth as damage Proxy……………..197

Figure 115: 3D plot of error versus Number of Cycles, Life computed from LM-algorithm for x-hrs TA2 + 250 cycles TC2 using IMC Growth as damage Proxy……………………………………………………………..……...199

Figure 116: Back-scattered Images for samples exposed to Environments of x hours @ $60^{O}C$ + y CyclesTC-3 magnification 1000x (a) Phase Growth (b) IMC, 324 I/O PBGA….200

Figure 117: 3D plot of error versus Number of Cycles, Life computed from LM-algorithm for x-hrs TA1 + 250 cycles TC3 using Phase Growth as damage Proxy…………….....203

Figure 118: 3D plot of error versus Number of Cycles, Life computed from LM-algorithm for x-hrs TA1 + 250 cycles TC3 using IMC as damage Proxy………………………...204

Figure 119: 3D plot of error versus Number of Cycles, Life computed from LM-algorithm for x-hrs TA1 + 250 cycles TC3 using IMC as damage Proxy………………………….205

List of Tables

Table 1: Thermal and Mechanical Attributes of Various Materials in BGA Package……………3

Table 2: Package Architecture………………………………………………………………...34

Table 3 Damage mapping from leading indicators of failure………………………………..….60

Table 4: Comparison of the prognosticated and experimental incremental damage…………….64

Table 5: Comparison of the prognosticated and experimental incremental damage…………….65

Table 6 Comparison of for both the algorithm………………………………………………..72

Table 7: Attributes of Test Vehicles…………………………………………………………..80

Table 8: Damage accrual relationships using Phase Growth and IMC Growth as leading indicators for 676 BGA and 256 BGA……………………………………………………..94

Table 9: Damage Equivalency Relationships using Phase Growth and IMC Growth as Leading Indicators for the 676 BGA and the 256 BGA…………………………………………..97

Table 10: Damage equivalency between TA @ 125C and TC1 @ -40C to 125C for the 676 I/O BGA…………………………………………………………………………………101

Table 11: Damage equivalency between TA @ 125C and TC1 @ -40C to 125C for the 676 I/O BGA…………………………………………………………………………………104

Table 12: Effect of exposure to 168 hours of thermal aging at 125C on the thermal cycling life under -40 to 125C……………………………………………………………………106

Table 13: Damage equivalency between TC1 @ -40C to 125C and TC2 @ 0C to 100C for the 676 I/O BGA…………………………………………………………………………….109

Table 14: Damage equivalency between TC1 @ -40C to 125C and TC2 @ 0C to 100C for the 256 I/O BGA……………………………………………………………………….…111

Table 15: RUL for 676 BGA after 168 hours TA + 250 Cycles TC1 + 250 Cycles TC2 using phase-growth and IMC growth as damage proxies…………………………….……..119

Table 16: RUL for the 256 BGA after 168 hours TA + 250 Cycles TC1 + 250 Cycles TC2 using Phase-Growth as Damage Proxy…………………………….……………………121

Table 17: Comparison of Prognostics Metrics for the Two Leading Indicators………………126

Table 18: Comparison of Prognostics Metrics for the Two Leading Indicators………………..128

Table 19: Package Attributes……………………………………………………………...132

Table 20: Normalized Phase Growth Coefficients and Exponents for the CABGA256 Package……………………………………………………………….…………143

Table 21: Activation Energy for Phase Growth Coefficient……………………………144

Table 22: Activation Energy for Phase Growth Exponent…………………………...144

Table 23: Normalized Phase Growth Coefficients and Exponents for the CABGA 256 Package ……………………………………………………………………………………..148

Table 24: Activation Energy for CABGA 256…..……………………………………..149

Table 25: Attributes of Test Vehicles…………………………………………………..159

Table 26: Damage accrual relationships using phase growth as leading indicator for the 324 BGA ……………………………………………………………………………………..168

Table 27: Activation energy, coefficients & exponent for all the aging temperatures…………169

Table 28: Activation energy of Phase Growth………………………………………….170

Table 29: Values for the IMC growth coefficient………………………………………174

Table 30: Activation Energy for IMC…………………………………………………..175

Table 31: Damage accrual relationships using phase growth as leading indicators for the 324 BGA………………………..……………………………………………………….176

Table 32: Activation energy, coefficients & exponent for all the cyclic temperatures………...180

Table 33: Activation Energy for exponent……………………………………………...181

Table 34: Damage accrual relationships using IMC growth as leading indicators for the 324 BGA…….………………………………………………………………………….184

Table 35: Activation energy, coefficients & exponent for all the cyclic temperatures………...185

Table 36: Value of Activation Energy………………………………………………….186

Table 37: Damage equivalency between TA3 @ 125C and TC1 @ -55C to 125C for the 324 PBGA…….…………………………………………………………………………...187

Table 38: Damage equivalency between TA2 @ 85C and TC2 @ -45C to 95C for the 324 PBGA ……………………………………………………………………………………..188

Table 39: Damage equivalency between TA1 @ 60C and TC3 @ 0 to 100C for the 324 PBGA……………………………………………………………………………189

Table 40: Effect of exposure to x-hours of thermal aging at 125C on the thermal cycling life under -55 to 125C……………………………………………………………….191

Table 41: Prognostication of Overlapping Damage…………………………………………….195

Table 42: Effect of exposure to x-hours of thermal aging at 85C on the thermal cycling life under -45 to 95C……………………………………………………………………………192

Table 43: Prognostication of Overlapping Damage…………………………………………….201

Table 44: Effect of exposure to x-hours of thermal aging at 60C on the thermal cycling life under 3 to 100C...…………………………………………………………………………203

Table 45: Prognostication of Overlapping Damage ……………………………………………206

Chapter-1

Introduction

1.1 Electronic Packaging Overview

Electronic packaging is an inter-disciplinary field of study which deals with methods of construction and integration of diverse electronic circuits on a chip broadly referred to as IC's (Integrated Circuits) or Packages. A single IC Package can fit multiple electronic circuits or devices thereby drastically reducing the size of a system as a whole. Nanotechnology has brought the microelectronic revolution over the last couple of decades. Wide scale research and development is carried out in this area in employing advanced techniques to further shrink the size of the individual packages to achieve higher component density per area. However it is extremely important to take into account the design considerations while scaling down the size like the mechanical or structural damage caused due to shock and exposure to extreme environments or the electrical constraints like electromagnetic interference, undesirable shorting of tracks and heat dissipation requirements.

The Packaging techniques can broadly be classified into two main types' viz. Through-hole technology and Surface Mount technology. Through hole technology of mounting electronic components was in use from 1950's – 1970's and is no longer employed for the manufacturing of commercial electronic products because although the through-hole mounting provides strong mechanical bonds and are more reliable and robust, the shrinkage of the component size is restricted which makes the overall

electronic assembly bulky. In order to find the solution to the size constraints in through hole technology industry came up with the new mounting technology called surface mount technology which was invented in 1970's and still finds its application in today's electronic manufacturing. Components became much smaller and component placement on both sides of a board became far more common with surface-mounting than through-hole mounting, allowing much higher circuit densities. It has evolved greatly in all these years with the current version requiring complete rethinking of design and production, along with new infrastructure to develop and sustain it. Figure 1 shows the schematic depicting evolution of electronic packaging over the years.

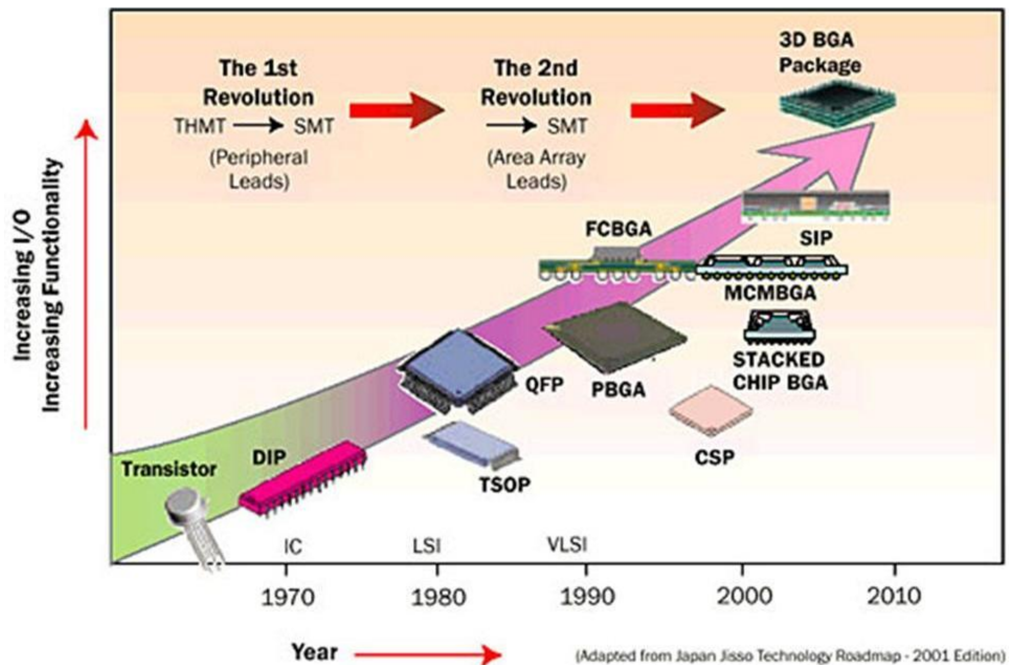

Figure 1: Electronic Packaging Trends [Evans 2008, ELEC 6740]

1.2 Reliability Concerns

Microelectronic device integration has progressed to the point where complete systems-on-a-chip (SoC), Multi-chip Module (MCM) and 3D Stacking are being realized these days. It is inevitable to ensure product reliability to fully exploit the device shrinkage accomplished with the advent of Very Large Scale Integration (VLSI) and nanotechnology. Typically an electronic package consists of various materials (Figure 2) having different mechanical and thermal properties as shown in Table 5. The individual behavior and the interaction with other materials at different operating or field conditions raise mechanical, structural and electrical reliability issues in a package.

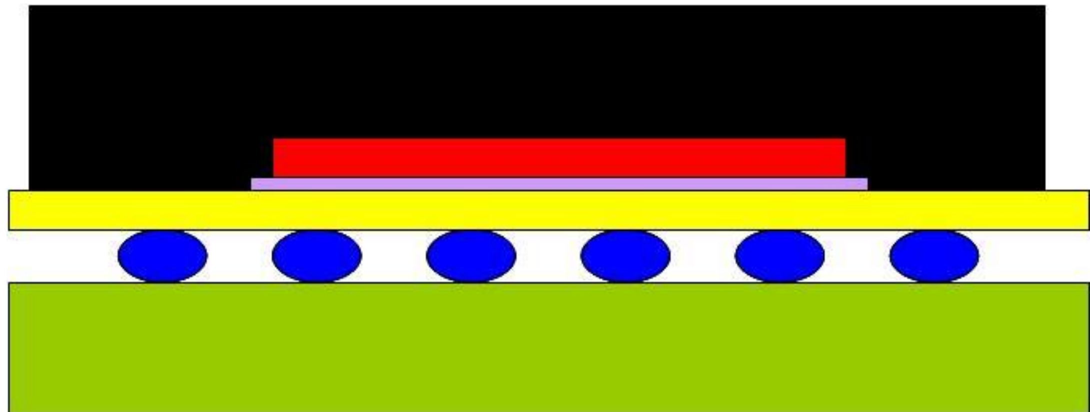

Figure 2: Typical Ball Grid Array (BGA) Electronic Package Architecture

Table 5: Thermal and Mechanical Attributes of Various Materials in BGA Package

Color	**Material**	**Elastic Modulus (E) (GPA)**	**Coefficient of Thermal Expansion (CTE) (10^{-6} 1/K)**
Black	Mold Compound	23.5	15
Red	Silicon Die	162.7	2.5

Lavender	Adhesive	6.8	52
Yellow	BT Substrate	18	12.4
Blue	Solder Balls	30.5	24.5
Green	Printed Circuit Board	17	14.5

Electronic assemblies undergo numerous unavoidable stresses and strains during their service life. The stresses are induced due to the different operational conditions. For example the electronic circuitry inside a commercial laptop undergoes power and or thermal cycling even during normal usage which induces thermal-structural stresses on electronic packages embedded inside. It is not unlikely that a portable electronic product like a cellular phone is accidently drop from a certain height. This typically is a high strain rate phenomenon which stresses various materials at different rates in a package and eventually after repeated drops the cellular phone stops working due to mechanical or electrical failures. Electronics used in automobiles have to undergo harsh thermal cycling environments (-55C to 125C) and demands high reliability for ideal functioning.

Stresses are induced on an electronic system when it is exposed to one or more combinations of operating conditions like thermal cycling, isothermal aging, thermal shock, drop, shock, vibration, hazardous chemical exposure etc. It is important to identify the failure modes associated with different field conditions for ensuring long term reliability of the products. Some of the commonly encountered failures are solder joint fatigue, die fracture, chip delamination, silicon cratering, underfill cracking, pop-corn effect, corrosion etc. Some of these failures are attributed to as material and or processing defects like pop-corn failure which occurs during high temperature reflow due to the

moisture absorbed by the package during storage. The presented work lies in the area of solder joint reliability under low cycle thermal fatigue and hence this has been discussed in great detail in the subsequent section.

Electronic package design and development is a concurrent approach which takes into account many material and process variables. Solder is one of the crucial variables which have to be taken into account for reliable electronic performance. Solders used in surface mount technology not only have to serve the purpose of electrical connection but also has to ensure robust mechanical connection. Solder joint cracking is the most dominant failure mode in microelectronics. The coefficient of thermal expansion (CTE) of electronic package and the printed circuit board (PCB) are different as a result of which they expand and contract at different rates during power and thermal cycling. This CTE mismatch induced disparity in rates of expansion causes shear stress in the solder joints which leads to fracture in extreme cases and has been a major reliability concern. [Ye 2006, Abdulhamid 2008] have also reported on electro-migration and thermo-migration in high temperature power electronic modules and its detrimental effect on solder joint reliability. Various techniques are used to reduce stress on the solder joints to improve solder joint reliability. Some of the techniques include developing substrates with matching CTEs thereby minimizing CTE differences in the substrate and package being mounted, developing substrates with compliant top layers that can absorb some stress and using underfill that provide stability to the solder joints during shearing thereby maintaining integrity of the joints.

With the advent of Restriction of Hazardous Substances (RoHS) compliance and lead-free restrictions, electronics industry is looking into lead-free solders that can replace the universally accepted and widely used tin-lead solder. Research and development efforts are focused on the study of potential alloys that provide physical, mechanical, thermal and electrical properties similar to those of eutectic tin-lead solder. It has not been a smooth transition to switch from leaded to lead-free solders as the conventional eutectic Sn/Pb solder has been in use for almost half a century and all its properties pertaining to electronics assemblies is readily available. The biggest obstacle in switching to lead-free solders is the lack of material characterization data available for these solders for varied applications. Also the mechanical behavior of lead-free solder alloys is radically different from eutectic tin-lead which only compounds the sustainability and reliability issues of lead-free electronics. As a result electronic systems are not used to the desired degree in terms of life, especially in mission critical applications, in order to reduce the probability of failure in the field. Current tools and techniques cannot perform reliability assessment of the system due to lack of sufficient information about the ongoing damage and its progression. The major problem in the industry today is the need to extend the useful life of such critical systems. Also the electronic components used in commercial applications like automotive safety systems are used to a lesser degree than desirable to avoid prospective malfunction in the long run. This is because the reliability associated with such safety equipments cannot be compromised at any given point which forces the use of dependable components in such

critical applications. Health monitoring of electronics is very relevant to such high reliability applications and there is a growing need to develop techniques that can evaluate the reliability of the system and provide information about the health of the system. The work presented in this thesis is based on health management of electronics using solder joint reliability and its associated damage proxies under thermo-mechanical loading.

1.3 Prognostic Health Management Systems

Health Management (HM) refers to the broad concept of assessing the on-going, in-service performance of a system using variety of measurement techniques. Prognostics can be thought of as a predictive diagnostics which includes determining the remaining life of the operational component. Prognostic Health Management (PHM) is the methodology of interrogation of state of a system based on computation of certain damage proxies to predict the Remaining Useful Life (RUL) of the system. The core function of any PHM model is to detect fault in the system and compute residual life at any given time. Typically fault detection involves interrogation of system state for physics-of-failure (POF) based damage proxies that provide information about the ongoing damage and impending failure. These damage proxies are classified as the leading indicators of failure and are used in PHM model development which directly or indirectly relates to the overall life of the system.

Health monitoring of electronics has always gained utmost importance from the research community as it provides information about the current state of health of a

system, identify faults and their behavior and assess accumulated damage thereby providing estimates of remaining life of the product [Lopez 2007]. Application of prognostic and health management (PHM) in electronics is still relatively at a nascent stage compared to its applications in other domains like aerospace, medicine, finance and weather [Saxena 2008].

There is a growing need to develop techniques for reliability prediction of electronics that are exposed to sequential or overlapping multiple thermal environments. State-of-Art prognostic health management models are proposed in this thesis which helps in reliability assessment of electronics deployed in single and complex multiple thermal environments. The strength of the techniques lies in its ability to predict reliability of the electronic system without worrying about the previous usage profiles or materials used in the electronic component except for the solder joint. The models provide the decision framework for operational readiness of systems during redeployment and also account for reduction in cyclic life due to long-term dormant storage. The prognostic models have been developed based on micro-structural evolution of second level solder interconnects.

1.4 Thesis Layout

Chapter 2 encompasses literature survey on solder joint reliability and various life prediction models used in electronics. Since the presented work is for high I/O electronic packages, significant amount of literature has been reviewed pertaining to Ball Grid Array (BGA) packages. Reliability enhancement techniques for BGAs have also been

discussed in detail. Transition from eutectic tin-lead solders to lead-free solders and its effect on solder joint reliability and overall package reliability has also been discussed in great detail. Life prediction models have been systematically classified into physics-of-failure (POF) based models and finite element analysis (FEA) models for lucid understanding of the reader. To set the stage for Prognostic Health Management (PHM) systems, an overview of diagnostic models has also been presented in this chapter. Lastly vast literature on PHM systems and its application in various engineering domains has been discussed followed by its motivation and scope in electronics.

Chapter 3 presents the prognostic model has been developed for the interrogation of system state and the estimation of remaining useful life of systems subjected to sequential stresses which will enable the spot-assessment of the system's health and provide method for estimation of remaining useful life. Prognostication of field-deployed parts after sequential thermo-mechanical damage under thermal aging and thermal cycling based on damage pre-cursors is currently beyond the state of art. Data on damage pre-cursors has been collected and analyzed for both aging and cycling to develop a technique that can map aging time into number of cycles and thus account for reduction in life due to dormant storage. The methodology involves the use of condition monitoring devices which have been interrogated for aging, cycling and different combinations of aging and cycling for residual life predictions. Developed PHM technique is based on non-linear least-squares method called Levenberg-Marquardt (LM) algorithm which has been developed for two different damage proxies. Prognostic model

performance based on standard prognostic metrics has also been evaluated for both the damage proxies to determine which leading indicator of failure can be employed for accurate life prediction. Results of interrogation of system state have been compared with a second set of experimental-matrix to validate the proposed methodology.

Chapter 4 expands the realm of application of PHM systems for electronics from single environment to multiple thermo-mechanical environments. The presented PHM framework is targeted towards high reliability applications such as avionic and space systems. In this part, Sn3.0Ag0.5Cu alloy packages have been subjected to multiple thermal cycling environments in combination with isothermal aging environments. Assemblies investigated include area-array packages soldered on FR4 printed circuit cards. The methodology involves the measurement of damage pre-cursors at periodic intervals. Damage-state interrogation technique has been developed based on the Levenberg- Marquardt Algorithm in conjunction with the microstructural damage evolution proxies. Test cases have been presented to demonstrate the viability of the technique for assessment of prior damage, operational readiness and residual life for assemblies exposed to multiple thermo-mechanical environments. Damage equivalency methodologies have been developed to map damage accrued in thermal aging to the reduction in thermo-mechanical cyclic life based on damage proxies. Assemblies have been prognosticated to assess the error with interrogation of system state and assessment of residual life.

Chapter 5 includes the effect of storage at different temperature conditions can be mapped using the presented approach. A framework has been developed to investigate the system state and estimate the remaining useful life of solder ball subjected to a variety of isothermal aging conditions including 60°C, 75°C and 125°C for periods of time between 1-week and 4-week. Data on damage precursors has been collected and analyzed to derive physics based damage mapping relationships for aging. Mathematical relationships have been derived for the damage mapping to various thermal storage environments to facilitate determining appropriate time-temperature combination to reach a particular level of damage state. Activation energy for the leading indicators of failure is also computed. Specific damage proxies examined include the phase-growth indicator and the intermetallic thickness. The viability of the approach has been demonstrated for leadfree test assemblies subjected to multiple thermal aging at 60° C, 75°C and 125°C. Damage mapping relationships are derived from data based on the two separate leading indicators.

Chapter 6 presents an approach in which leadfree assemblies with Sn3Ag0.5Cu solder have been subjected to variety of thermal aging conditions including 60°C, 85°C and 125°C for periods of time between 1-week and 2-months, thermal cycling from -55°C to 125°C, -40°C to 95°C and 3°C to 100°C .The presented methodology uses leading indicators of failure based on microstructural evolution of damage to identify accrued damage in electronic systems subjected to sequential stresses of thermal aging and thermal cycling. Damage equivalency relationships have been developed to map

damage accrued in thermal aging to the reduction in thermo-mechanical cyclic life based on damage proxies. Accrued damage between different thermal cyclic magnitudes has also been mapped for from -55°C to 125°C, -40°C to 95°C and 3°C to 100°C thermal cycles. The presented method for interrogation of the accrued damage for the field deployed electronics, significantly prior to failure, may allow insight into the damage initiation and progression of the deployed system. The expected error with interrogation of system state and assessment of residual life has been quantified.

Chapter 7 presents an approach in which leadfree assemblies with Sn3Ag0.5Cu solder have been subjected to variety of thermal aging conditions including 60°C, 85°C and 125°C for periods of time between 1-week and 2-months, thermal cycling from 50°C to 150°C, -25°C to 75°C and -50°C to 50°C. The presented methodology uses leading indicators of failure based on microstructural evolution of damage to identify accrued damage in electronic systems subjected to sequential stresses of thermal aging and thermal cycling. Damage equivalency relationships have been developed to map damage accrued in thermal aging to the reduction in thermo-mechanical cyclic life based on damage proxies. Accrued damage between different thermal cyclic magnitudes has also been mapped for from 50°C to 150°C, -25°C to 75°C and -50°C to 50°C thermal cycles. The presented method for interrogation of the accrued damage for the field deployed electronics, significantly prior to failure, may allow insight into the damage initiation and progression of the deployed system. The expected error with interrogation of system state and assessment of residual life has been quantified.

Chapter 8 presents an approach in which leadfree assemblies with Sn3Ag0.5Cu solder have been subjected to variety of thermal aging conditions including 60°C, 85°C and 125°C for periods of time between 1-week and 2-months, thermal cycling from 50°C to 100°C , -25°C to 100°c and -25°C to 50°C. The presented methodology uses leading indicators of failure based on microstructural evolution of damage to identify accrued damage in electronic systems subjected to sequential stresses of thermal aging and thermal cycling. Damage equivalency relationships have been developed to map damage accrued in thermal aging to the reduction in thermo-mechanical cyclic life based on damage proxies. Accrued damage between different thermal cyclic magnitudes has also been mapped for from 50°C to 100°C, -25°C to 100°C and -25°C to 100°C thermal cycles. The presented method for interrogation of the accrued damage for the field deployed electronics, significantly prior to failure, may allow insight into the damage initiation and progression of the deployed system. The expected error with interrogation of system state and assessment of residual life has been quantified.

Chapter 9 includes the conclusion of the presented prognostic health management models and briefly discusses the scope for future work.

Chapter 2

Literature Review

2.1 Solder Joint Reliability

In electronics the integrity of solder joints remains the backbone for ensuring quality of the product. A perfect joint is a joint showing complete wetting of solder to pad and this is a universal requirement that applies to surface mount as well as through-hole components. As suggested by [Woodgate 1987] the only acceptable joint is the perfect joint. In the pursuit of device shrinkage and circuit miniaturization, surface mount technology in itself has vastly evolved over the last couple of decades. With the potent need for small form factor packaging architectures, fine pitch packaging in the range of 0.8mm-1.27mm became a reality which gave rise to the conception of ball grid array (BGA) packages. Manufacturing of fine pitch leaded chip carriers was a major issue which was one of the instrumental factors in pushing BGA packaging in the mainstream electronic manufacturing. BGAs appear to be the answer to the high pin count packaging trend since they can accommodate high I/O in a very small form. Fine pitch packages with their fragile leads pose serious handling problems and are difficult to place and solder. BGAs became popular because during placement and reflow, robust balls outperform fragile leads as they self-align and provide better control during reflow at ultra-fine pitches.

In surface mount devices (SMDs) like BGA packages, solder joints not only provide electrical connectivity but also ensure mechanical integrity between the package and the printed circuit board (PCB). The major reliability issue with BGA package is the thermal mismatch between the BT substrate and the printed circuit board (PCB). The difference in the coefficient of thermal expansion (CTE) of the BT substrate and the PCB induces shear stress in the second level solder interconnects due to disparity in the rate of expansion and contraction of the two materials when exposed to thermal loads. Repeated shearing of solder joints lead to cyclic stress or fatigue build-up in the solder joints causing them to fail eventually. Different techniques are employed to reduce cyclic thermal fatigue of solder joints as the solder joint reliability is directly proportional to the overall package reliability.

2.1.1 Reliability of BGA Packages

[Chiang 2000] proposed that a better reliability characteristic of BGA type packages can be achieved by using the 2nd reflow process. He showed 2X increase in the characteristic life of BGAs under thermal cycling due to significant reduction in equivalent plastic strain, the energy density and the Von-Mises stress of the solder joint. [Syed 1996] reported on package architecture variables affecting the solder joint reliability of BGA packages. He showed that perimeter array packages had a better solder joint reliability than full array packages. He also showed that the BT thickness had a direct impact on solder joint reliability with thicker BT substrate enhancing the solder join reliability.

[Charles 1990] reported that increase in fatigue life under power cycling can be attained by fabricating solder joints with large fillets and low standoff heights. The large fillet geometry

significantly reduces harmful stress concentrations while increasing the net cross-sectional area within the joint. Both factors tend to improve the fracture toughness of the joint. Temperature cycling studies indicate joints with slightly higher standoffs and low fillet angles are more resistant to cyclic fatigue than pillar type joints which tend to focus shear strains at the interfaces.

Generally, for enhanced solder joint reliability of stacked die BGA, it is recommended to have smaller top and bottom dice sizes, thicker top or bottom die, thinner PCB, thicker substrate, higher solder ball standoff, larger solder mask opening size, smaller maximum ball diameter, smaller PCB pad size, smaller thermal cycling temperature range, longer ramp time, and shorter dwell time. It is possible to greatly enhance the solder joint performance through simple optimization in mold compound material and package thickness. The layout of solder balls is important as it affects the load distribution on critical solder ball [Tee 2004].

[Zhong 1999] presented the effects of solder ball pad metallurgy, intermetallic compound (IMC) thickness and thermal cycling on the shear strengths of PBGA package solder balls. The study of the microstructures of solder balls revealed that only a very thin layer of intermetallic compound existed between solder balls and Ni or Ni alloy barrier layers immediately after ball placement and reflow. [Bradley 1996 and Suhling 2002] showed superior HASL pad finish thermal reliability performance over immersion nickel and palladium based pad finishes for BGA packages.

2.1.2 Lead-Free (Pb-Free) Solders

Recent global environmental projects like Restriction of Hazardous Substances (RoHS) and Waste from Electrical and Electronic Equipment (WEEE) has put a full stop on further use

of tin-lead components in electronic manufacturing industry which gives a call for all the possible Pb-free alloys. There are hundreds of lead-free alloy compositions that are been studied for their applicability in electronics. The tin-silver-copper (Sn/Ag/Cu or "SAC") family of alloys is one of the leading contenders which have been accepted by electronics industry as a substitute for tin-lead solders.

[Syed 2001, Zhang 2003 and Vandevelde 2004] have shown that the SAC alloy performance varies with different packaging architectures and has strong temperature dependence. The experimental studies have confirmed that the use of lead free solders with low Ag content significantly improves board level reliability during drop test when compared with high Ag content SAC alloys. On the contrary it has been reported by [Zhang 2008 and 2009] that higher Ag content SAC alloys enhance thermal reliability.

[Schubert 2003 and Clech 2005] reported on the relative SAC solder alloy performance over conventional tin-lead solders. Their experimental studies have shown that there is significant enhancement in solder-joint reliability of second level interconnects with SAC alloys than tin-lead when used with compliant plastic substrates.

As the SAC alloys are ternary system alloys the microstructure is pretty complex compared to binary system solder alloys. In case of eutectic tin-lead solders the intermetallic compound formation is so fast that the solder attains equilibrium condition quickly. The biggest problem with SAC alloys is that the intermetallic formation is very slow compared to eutectic tin-lead due to high percentage of tin [Henderson 2004]. [Zhang 2003] reported that the fine microstructure of SAC alloys right after reflow help prevent grain boundary sliding and hence SAC alloys perform better than tin-lead in low stress

regimes. [Dutta 2004] emphasized on the need for incorporating coarsening kinetics in the existing solder creep models as the microstructure of SAC alloys evolves rapidly during thermal cycling and creep behavior is related with microstrucure. [Liu 2004 and Tsai 2005] have reported on the difference in the mechanical behavior and characterization of intermetallic compounds found in SAC and Sn-Pb alloys and its effect on solder joint reliability.

Apart from SAC alloys other potential metals that can be used as lead-free alloys are Indium, Zinc, Bismuth etc. [Seelig 2003] reported that Bismuth poses a potential supply problem since it is a by-product of lead mining, and also has embrittlement problems. Bismuth is also a poor conductor, both thermally and electrically. [Lung 2004] reported on potential Pb-free Sn-Zn and its relative performance with SAC alloys. [Shimizu 1995] showed that Indium-alloy solders have better mechanical properties for solder joints, and their flip-chip interconnection models showed a longer fatigue life than that of Pb-Sn solder in thermal shock tests between liquid nitrogen and room temperatures. He proposed lead-free solders such as indium (In)-alloy solders are a possible alternative to conventional lead-tin (Pb-Sn) solders and are suitable for fabricating reliable interconnections.

2.2 Life Prediction Models

Electronics is a fast paced industry and because the market life of individual commercial electronic product is typically 6-12 months it is impractical for any electronic manufacturing company to test every new product in the real field environment and evaluate mechanical reliability or life of the product. Instead, accelerated tests such as Highly Accelerated Life Tests (HALT) or Highly Accelerated Stress Tests (HAST) are used which impose harsher conditions

on the electronic product causing them to fail in a shorter time to make reliability predictions in the actual field applications. There are number of life prediction techniques for electronics ranging from simple analytical methods to complex damage mechanics based finite elements models that are available in literature especially based on solder joint reliability mechanics.

2.2.1 Physics of Failure (POF) Models

Classical [Coffin 1954, Manson 1964 and Goldmann 1969] models have proposed physics of failure based life prediction equations that relate the plastic strain in the solder joints with failure life of the package. [Norris 1969, Lau 1995] studied the effect of cycling frequency and maximum temperature of cycling on fatigue failure of solder joints.

[Wong 1990] proposed a mechanistic model for eutectic Pb/Sn solder life predictions wherein he studied crack initiation, crack propagation, microstructure coarsening and deformation kinetics models of the solder during thermal cycling. By merging these models together he predicted the time to crack initiation and the time to failure of the solder joints. Low cycle fatigue testing of a eutectic alloy 63Sn/37Pb was carried out by [Shi 1999] to study Morrow energy-based model, the frequency-modified Coffin-Manson model, and the frequency-modified energy-based model by [Solomon 1986] for life prediction.

[Engelmaier 1982 and 1984] developed a surface mount solder joint reliability prediction model containing all the parameters influencing the shear fatigue life of a solder joint due to shear displacement caused by thermal expansion mismatch between component and substrate. [Wong 1988 and Yamada 1989] implemented fracture mechanics concept to study solder joint cracking and compute time to failure.

[Choi 2003, Ye 2003 and Chiu 2006] studied the effect of joule heating, electro-migration and thermo-migration on flip-chip solder joints. They proposed damage mechanics of flip-chip joints under high current densities and have related mean time to failure using Black's equation. Overwhelming mechanical property degradation of solder joints was observed due to current stressing. Mass accumulation was reported to be primary reason for void formation and subsequent crack propagation in such high current density applications.

[Lau 2002 and 2003] developed empirical equation for predicting the thermal-fatigue life of wafer level chip scale package (WLCSP) solder joints. It is derived by combining the measured thermal-fatigue crack growth rate of the corner solder joint and the simulated nonlinear fracture characteristics i.e. average strain energy density per cycle around the crack tip of the corner solder joint with various crack lengths.

2.2.2 Finite Element Analysis (FEA) Models

Numerous researchers in the field of electronic packaging have used the power of finite element methods to make solder joint life predictions under different operating conditions like thermal and power cycling, drop and shock, vibration and bending. Majority of finite element life prediction models are based on accumulated field quantities and derivatives of field quantities like creep strain, inelastic strain energy density and nonlinear plastic work etc.

[Amagai 1998 and Popelar 1997] proposed a viscoplastic constitutive model to analyze thermally induced plastic and creep deformation and low cycle fatigue behavior of the solder joints in Chip Scale Packages (CSP).

[Frear 1997 and Vianco 1999] developed a finite element simulation methodology to predict solder joint mechanical behavior that includes micro-structural evolution. The micro-structural evolution was incorporated through a series of mathematical relations that describe mass flow in a temperature/strain environment.

[Wang 2001] applied [Anand 1985] unified creep model to represent viscoplastic deformation behavior of solders. He concluded that inelastic deformation behavior calculated by the model can be applied for solder joint reliability predictions. [Zhang 2000] proposed a novel life prediction model that takes into account the damage evolution to accurately predict solder joint reliability.

[Darveaux 2000] established 63Sn37Pb eutectic alloy damage relationships correlating crack growth rate with inelastic strain energy density per cycle. This relationship is widely incorporated by other researchers in their life prediction frameworks to compute the characteristic life of ceramic BGAs on solder masked defined pads using finite element simulations. Later [Lall 2004] widened the scope of Darveaux's work by updating damage relationship constants and applied that for life prediction of plastic BGAs with non-solder masked defined pads. [Syed 2004] proposed accumulated creep strain and energy density based thermal fatigue life prediction models for lead-free SAC solder alloys using advanced finite element modeling and analysis. He used different constitutive equations proposed by [Wiese 2003, Schubert 2003, Zhang 2003 and Morris 2003] to model solder creep and studied its effect on life prediction accuracy.

[Zahn 2003] presented a three-dimensional finite element analysis methodology which explored global, sub-structure, and sub-modeling solution options using both slice and symmetry models for the purpose of deriving life prediction equations that determine the fatigue response of microelectronic package structures using both eutectic (63Sn37Pb) and lead-free (95.5Sn4Ag0.5Cu) solder materials.

[Tee 2004] presented a life prediction model to estimate number of drops to failure for a package subjected to board level drop test. The maximum normal peel stress of the critical solder joint extracted from finite element simulation was used as the failure criteria to predict mean number of drops to failure.

One of the potential causes for mechanical failure of component interconnects is the bending of the PCB. [Shetty 2003] demonstrated the application of three-point and four-point bending tests for evaluating the reliability of chip scale packages under curvature loads. He proposed deformation energy based empirical reliability model to calculate mean life time to failure of solder joints under mechanical bending. The relationship between average cycles to failure and average strain energy density is established in this reliability model by volume averaging the strain energy density over the top layer of the solder joint, volume average technique proposed by [Zhan 20003, Darveaux 1992 and 2000].

2.3 Diagnostic Models

Life prediction models discussed in previous section are based on fear of failure, i.e. they provide estimate on failure life, which are only useful in making reliability predictions upfront i.e. before deployment in the intended field. Although these models help in benchmarking the

overall life of electronics, they are of no use in the need of in-field fault detection during the service life. This is especially important for hi-reliability, mission critical applications wherein the characteristic life of the component is important before deployment but also continuous monitoring of system is equally important. Thus condition monitoring leading to fault diagnosis has attracted researchers in the past few years because of its considerable influence on the operational continuation of many industrial processes. Correct diagnosis and early detection of incipient faults result in fast unscheduled maintenance and short downtime for the process under consideration. They also avoid harmful, sometimes devastating, consequences and reduce financial loss. An ideal diagnostic procedure should take the minimum measurements necessary from a machine and by analysis extract a diagnosis, so that its condition can be inferred to give a clear indication of incipient failure modes in a minimum time [Bellini 2008].

The diagnostic methods can generally be classified into the three basic categories. The model-based diagnostics checks how the system responds to inputs. It relies on some model of correct behavior of the diagnosed system. Using the inputs the model makes predictions of correct outputs; the differences between the actual outputs and the predictions are diagnostic variables called residuals. The latter are usually compared with certain threshold values and the results of the comparisons are the basis for the ultimate diagnostic decisions. The reference-band diagnostics is only applicable to closed-loop control systems. As the closed-loop system outputs should follow the commanded values, excessive discrepancies between the outputs and commanded values can be indicative of faults. In other words, the reference-band diagnostics checks how the system tracks the reference values. The signal-based diagnostics disregards any

input–output relationships and exploits the fact that the output signals themselves can convey information about the health of a system [Sleszynski 2009].

The very first efforts in this area is the usage of Built- In-Self Test (BIST) circuit, which is an onboard hardware and software diagnostic means to identify and locate faults and includes error detection and correction circuits [Drees 2004]. BIST is a methodology that embeds additional functionality in the product to give it the ability to test and diagnose itself with minimal interaction from external test equipment [Chandramouli 1996, Hassan 1992, Williams 1983, Zorian 1994]. BIST, when effectively designed in a chip / board / system, can yield an enormous amount of diagnostic information. BIST controllers can also output failure data that can be correlated to show exactly when the failure occurred. This data can then be interpreted by diagnostic software to analyze the cause of failure. For example, Pseudo-Random Binary-Sequence (PRBS) test pattern generators, apply input vectors to digital or analog [Al-Qutayri 1992] modules. Self-Checking circuit designs provide on-line test for digital [Lala 1985] as well as for analog circuits [Kolarik 1993]. The obtained output is then compared with a golden response. The results obtained from BIST functions can generate diagnostic information which in turn provides additional confidence in the measurement result and confirm the device availability.

Though BIST helps in minimizing the interaction with external automated test equipment (ATE) as well as provides the advantage of a more robust "at-speed" test of the circuitry, the current form gives little insight about the system level reliability or the remaining useful life of the system. Also, several studies conducted [Allen 2003, Drees 2004, Gao 2002, Rosenthal 1990]

have shown that BIST can be prone to false alarms and can result in unnecessary costly replacement, re-qualification, delayed shipping, and loss of system availability.

Also, Fuses and Canaries are mounted on the part to provide advance warning of failure due to specific wear out failure mechanism. The basic procedure here is to take some form of action, after an initial failure or malfunction, to prevent additional or secondary failures. By reducing the number of failures, techniques such as enhancing product reliability can be considered, although they also affect availability and product effectiveness. However, replacement of fuses and canaries does impact the maintenance, repair and part replacement making it difficult to integrate these systems with host system.

Although diagnostic models are able to detect faults in the system but they are unable to provide any information about the ongoing damage such as damage initiation and damage progression. In other words a fault is detected or diagnosed only when failure occurs. It also lacks insight about the remaining useful life of the systems. There is a growing need to develop techniques that can provide information about the impending failure way before the system is about to fail and use this information to predict remaining useful life. Prognostic Health Management (PHM) systems have the ability to perform fault diagnosis before the actual failure occurs and compute remaining useful life, and hence its application is relevant especially in hi-reliability applications.

2.4 Applications of Prognostic Health Management (PHM) Systems

Maintenance has evolved over the years from corrective maintenance to performing time-based preventive maintenance. Future improvements in reduction of system downtime require

emphasis on early detection of degradation mechanisms. Incentive for development of prognostics and health management methodologies has been provided by need for reduction in operation and maintenance process costs [Jarell 2002]. New advances in sensor technology and failure analysis have catalyzed a broadening of application scope for prognostication systems to include large electromechanical systems such as aircraft, helicopters, ships, power plants, and many industrial operations. Current PHM application areas include, fatigue crack damage in mechanical structures such as those in aircraft [Munns 2000], surface ships [Baldwin 2002], civil infrastructure [Chang 2003], railway structures [Barke 2005] and power plants [Jarrell 2002].

2.4.1 General PHM Applications

Previously PHM of mechanical structures has been done by dynamic analysis based on natural frequencies, mode shapes, damping factors, and static analysis based on deformation or changes in structure orientation due to load or unexpected damage using innovative signal processing, new sensors, and control theory [Kok 2005].

PHM systems for fault detection and characterization such as BEAM have also been proposed for spacecrafts which involves system characterization using all available observation followed by training of the characterization with respect to normal phase operation [Park 2002]. The use of multiple sources of information for the interrogation of system state and fault detection in aircrafts has been proposed in which predictions from various subsystems is used for fault diagnosis [Oza 2003]. Wayside detection involving fault identification using interrogating sensors placed along the sides of railway tracks has been used in the railway industry for gathering information about the vehicle performance. Information on the vehicle condition and

performance over an extended period of time is recorded in an online database, which is interrogated for critical performance parameters to provide information on condition of in-service railway vehicles [Barke 2005].

A model-based method has been used for the on-line identification of cracks in a rotor of aircraft engines which start and stop quite frequently and run at high speeds [Sekhar, 2003]. Detection of surface corrosion has been used to reduce the maintenance required, and trigger preventive repair for increased aircraft availability and significantly reduced cost of ownership. Fluorescent fiber optic sensors that detect aluminum coating from the early stages of the corrosion process have been used for providing early warning of corrosion in susceptible areas of an aging aircraft [Maalej 2004]. Crack modeling approach in beam has been used to demonstrate the structural HM using low frequency vibration; simple models of crack flexibility based on beam elements are adequate [Friswell 2002]. Optical fiber based sensor system has been used on concrete structure to evaluate its performance for health monitoring [Fernando 2003]. Monitoring bridge performance has been done to answer questions on the performance of existing bridges, refine techniques needed to evaluate different bridge components, and develop approaches that can be used to provide a continuous picture of a bridge's structural integrity using structural health monitoring [DeWolf 2002]. These techniques help in detection of damage of bridges or building to avoid the economic and social effect of aging and deterioration [Chang 2003]. In other applications, signal feature analysis is used to detect abnormalities related to impending failure indication by an inference system using an historical database [Hess 2001].

2.4.2 PHM for Electronics

Implementation of PHM algorithms in electronics for the interrogation of system state and residual life calculations is still relatively at a latent stage compared to its application in other domains. Prognostics based health monitoring of electronics require leading indicators in the system for fault detection and decision support. A prognostic feature provides an advanced warning of impending failure to predict remaining useful life (RUL). Prognostic features may be extracted from a combination of device, circuit, or system parameters sensitive to damage accumulation [Brown 2007].

Modern aircrafts are increasingly dependent on avionic systems for a variety of roles ranging from effective communication and navigation to flight control, engine control and fuel management. Most of the avionics are intended for flight safety and thus the reliability associated with it cannot be compromised at any point of time. Routine maintenance of such high reliability equipments requires advance planning and high expertise. On board diagnostic systems are intended to identify and localize component failures but it is well known that electronic parts can fail in number of different modes at different times resulting in ambiguous diagnosis. There is a growing need to develop prognostic techniques for such high reliability applications which can provide early device degradation warning for maintenance with considerable reduction in variability. Some of the damage indicators that have been incorporated in the development of the prognostic techniques for avionics include power dissipation, output degradation and aging of semiconductors [Hecht 2006].

In case of mission critical applications like space explorations the reliability of the spacecraft is extremely important as they are away from the earth for considerably long periods of time. Effective on-board prognostic systems not only increase safety by detecting problems before they become serious and prevent major failures but also help schedule efficient maintenance [Schwabacher 2005]. Switch mode power supplies (SMPS) commonly used aboard aircraft for various electrical power requirements are susceptible to malfunction due to component failures. Previously prognostic approach dealing with SMPS health management has been developed in which components like switching transistors, filtering capacitors and rectifying diodes inside SMPS have been indentified as critical components for prognosis [Orsagh 2005].

Reliability of the electronic power modules used in vehicles has always been a concern as it consists of numerous electronic components which undergo thermal stresses and fatigue due to power dissipation during usage. The nature of the gradual degradation of these power modules has enabled the development of prognostic systems for the same. Some of the signatures of impending failures including increase in forward on-voltage, leakage current and thermal impedance have been used as the damage proxies for the on-board prognostic system [Xiong 2008].

Field data from aircraft has been evaluated for the continuous health assessment of avionics and a prognostic software has been developed that involves mining of data from multiple sources, trending and ranking of anomalous indicators, development of on-board built-in-test (BIT) data and automated advanced reasoning for reduced ambiguity [Dussault 2006].

For many years, commercial telecom systems have adopted many forms of reliability enhancements all intended to improve system up-time. While these changes have been effective, the surprise factor is still prevalent in systems carrying vitally important traffic over the network. Providers and technicians alike often wish there was some signal or other indicator of an upcoming problem in order to take some action in advance of a system shutdown [Wood 2006].

Electronics systems may be subjected to prolonged periods of thermal exposure over wide temperature extremes and long periods of thermal aging at often high ambient temperatures. High-rel systems may have very long operating life times with low downtime during operation. Historical environmental conditions to which the systems may have been subjected may be often unavailable. PHM for electronics has wide applicability spanning a number of different areas. Electronics used in critical applications like space, military and avionics require multiple deployments with sequential thermal stresses. Systems may also be subjected to long term dormant storage in uncontrolled thermal environments. Ultra high reliability is needed to ensure predictable operation when needed and avoid any catastrophic damage during the service life.

There is need for tools and techniques which will enable the spot-assessment of the system's health and provide method for estimation of remaining useful life. Prognostication of sequential thermo-mechanical damage under thermal aging and thermal cycling based on damage pre-cursors is currently beyond the state of art.

Previously [Lall 2005, 2006[a,b], 2007[a,b] and 2008] has developed leading indicators based prognostic and health management methodologies for residual life computation of electronics

subjected to single thermal environments comprising of isothermal aging and thermal cycling. Examples of damage pre-cursors include micro-structural evolution of second level solder interconnects, inter-metallic compound growth, stress and stress gradients. Pre-cursors have been developed for both eutectic 63Sn37Pb and various lead-free alloy compositions like Sn4Ag0.5Cu, Sn3Ag0.5Cu, Sn1Ag0.5Cu, Sn0.3Ag0.7Cu, Sn3Ag0.5Cu-Bi, Sn3Ag0.5Cu-Bi-Ni, 96.5Sn3.5Ag alloy systems on a variety of area-array architectures.

In this thesis, PHM models have been developed and implemented for the interrogation of system state and the estimation of remaining useful life of electronic systems subjected to single steady-state environment and multiple thermal environments of isothermal aging and thermal cycling. Data on damage pre-cursors has been collected and analyzed for both aging and cycling to develop a technique that can map aging time into number of cycles and thus account for reduction in life due to dormant storage. The methodology involves the use of condition monitoring devices which have been interrogated for aging, cycling and different combinations of aging + cycling for residual life predictions. Developed PHM technique is based on non-linear least-squares method called Levenberg-Marquardt (LM) algorithm which has been developed for two different damage proxies. Prognostic model performance based on standard prognostic metrics has also been evaluated for both the damage proxies to determine which leading indicator of failure can be employed for accurate life prediction. Results of interrogation of system state have been compared with a second set of experimental-matrix to validate the proposed methodology.

Chapter 3
Interrogation of Accrued Damage and Remaining Life in Field-Deployed Electronics Subjected to Multiple Thermal Environments

3.1 Overview

Field deployed electronics may accrue damage due to environmental exposure and usage after finite period of service but may not often have any macro-indicators of failure such as cracks or delamination. A method to interrogate the damage state of field deployed electronics in the pre-failure space may allow insight into the damage initiation, progression, and remaining useful life of the deployed system. Aging has been previously shown to affect the reliability and constitutive behaviour of second-level lead-free interconnects. Prognostication of accrued damage and assessment of residual life can provide valuable insight into impending failure. In this proposal, field deployed parts have been extracted and prognosticated for accrued damage and remaining useful life in an anticipated future deployment environment. A subset of the field deployed parts has been tested to failure in the anticipated field deployed environment to validate the assessment of remaining useful life. In addition, some parts have been subjected to additional know thermo-mechanical stresses and the incremental damage accrued validated with respect to the amount of additional damage imposed on the assemblies. The presented methodology uses leading indicators of failure based on micro-structural evolution of damage to identify accrued damage in electronic systems subjected to sequential stresses of thermal aging and thermal cycling. Damage equivalency methodologies have been developed to map damage accrued in thermal aging to the reduction in thermo-mechanical cyclic life based on damage proxies.

The expected error with interrogation of system state and assessment of residual life has been quantified. Prognostic metrics including alpha-lambda metric, sample standard deviation, mean square error, mean absolute percentage error, average bias, relative accuracy, and cumulative relative accuracy have been used to compare the performance of the damage proxies.

3.2 Test Vehicle

In the present study, the perimeter type ball-grid arrays with traditional eutectic tin-lead solder have been studied under thermo-mechanical loads. Figure 3 shows the PBGA with heat-sink mounted over it and X-ray image showing the array of solder balls in Figure 4. The table below shows I/O counts and other package variables for the test vehicles used in this study. Phase growth and IMC data has been gathered and analyzed using image processing. Components analyzed are perimeter type ball-grid arrays with I/O counts of 456 (Table 2). The boards contain six trace layers to simulate the thermal mass of a true production board, though all functional traces were run on the topmost layer. All pads on the board were non-solder mask defined (NSMD) and had an immersion silver finish. The package attributes of this board are shown in Table 2.

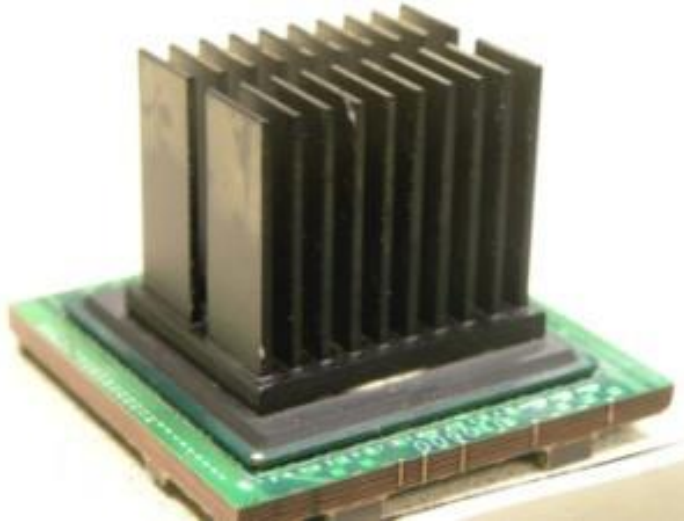

Figure 3 BGA with Heat Sink

Table 2: Package Architecture

Ball Count	456
Package type	26 X 26 Perimeter array
Alloy System	Sn63Pb37
Ball Pitch (mm)	1.27
Pad Type	NSMD
Ball Diameter (mm)	0.80
No of parts	11

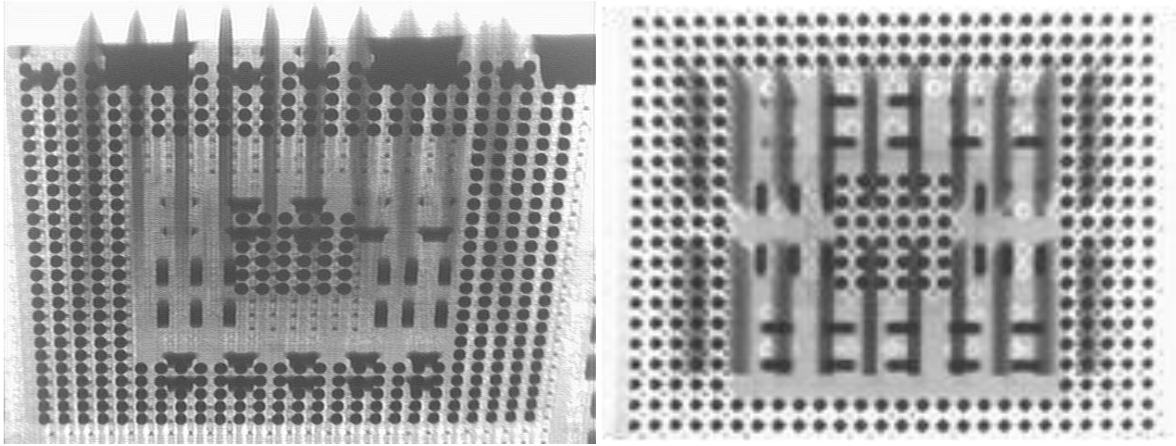

Figure 4 X-ray images showing 26 X 26 Perimeter Array

3.3 Approach for Prognosticating Damage

Field deployed electronic systems may be subjected to different environment profiles and usage profiles during service life. Assemblies may accrue damage at different rates in different field environments. Insight into the pre-failure space is necessary to understand damage initiation and the rate of damage progression. Samples have been withdrawn from the field deployed population to determine the prior accrued damage and assess the remaining useful life. The samples were then subjected to combinations of thermal aging and thermal cycling in the intended application environment and the accrued damage studied using damage precursors. Information is intended to aid decision making regarding assembly preparedness for future deployment. The withdrawn samples have been subjected to two different thermal environments including thermal aging and thermal cycling. Thermal aging is performed at 60ºC for varying lengths of time. Assemblies were subjected to thermal

cycling between - 40ºC and 125ºC at 2.5 hours per cycle. A combined plot for both the environments in terms of damage accrual and remaining-life in terms of number of cycles is shown in Figure 5. Information on progression of damage proxies has been used to estimate prior damage and remaining useful life. Commonality of the damage proxies between thermal aging and thermal cycling has been used to superimpose damage in the two environments. The difference in the slopes between thermal aging and thermal cycling indicates the differing rates of damage accrual in the two environments.

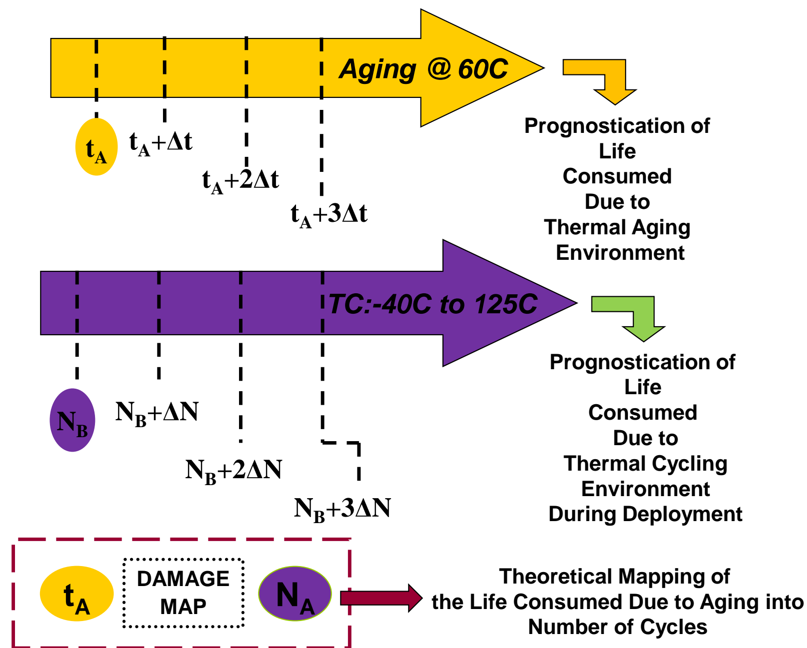

Figure 5 Stepwise Approach

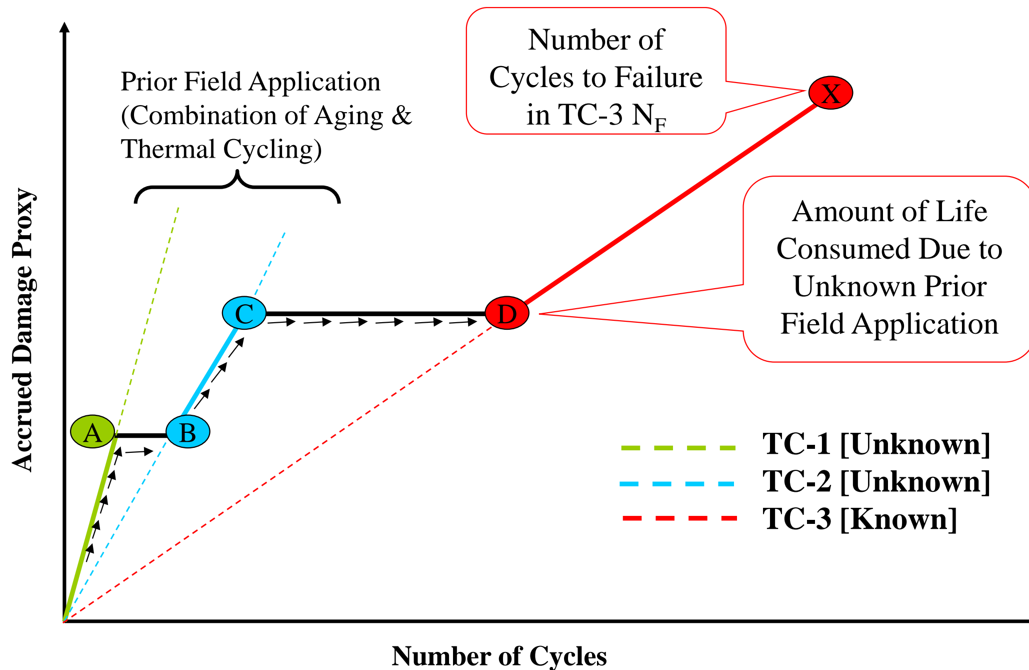

Figure 6 Life vs Damage Curve for Thermal Environments

3.3.1 Micro-structural Evolution of Damage under Single Stresses

In this step, board assemblies have been subjected to single stresses of thermal aging and thermal cycling. Samples have been withdrawn periodically and cross-sectioned. Damage proxies studied include the phase-growth parameter and the intermetallic thickness. Previously, it has been shown that the rate of change in phase growth parameter [d(lnS)/d(lnN)] is valid damage proxy for prognostication of thermo-mechanical damage in solder interconnects and assessment of residual life under thermal aging and thermal cycling type of thermo-mechanical stresses [Lall 2004[a-d], 2005[a-b], 2006[a-f], 2007[a-e], 2008[a-f], 2009[a-d]]. The damage proxy [d(lnS)/d(lnN)] is related to the microstructural evolution of damage by the following equation:

$$S = g^4 - g_0^4 = a(N)^b \qquad (1)$$

$$\ln S = \ln\left(g^4 - g_0^4\right) = \ln a + b \ln N$$
$$\frac{d(\ln S)}{d(\ln N)} = b \qquad (2)$$

Where, g is the average grain size at time of prognostication, g_0 is the average grain size of solder after reflow, N is the number of thermal cycles, S is the phase growth parameter, parameters a and b are the coefficient and exponent respectively. The log-plot of the equation provides a straight line relationship between the phase growth parameter and the number of cycles.

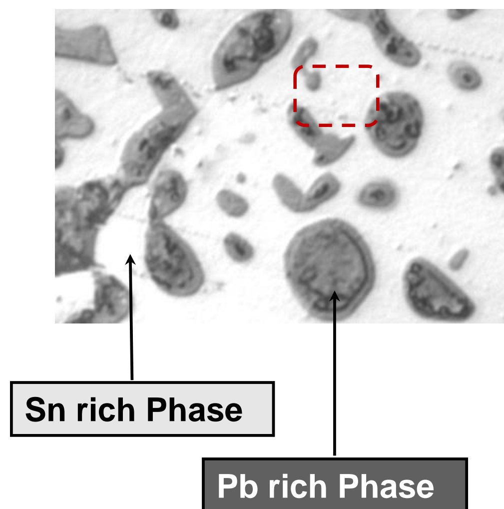

Figure 7 Phases in Traditional Eutectic Solder

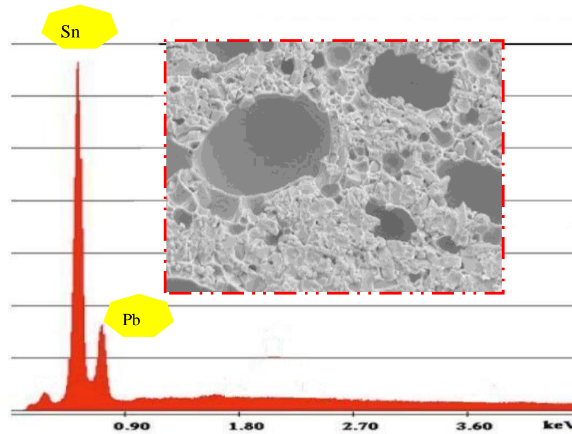

Figure 8 Microanalysis Spectrum of Phase Growth using Energy Dispersion Spectroscopy (EDS)

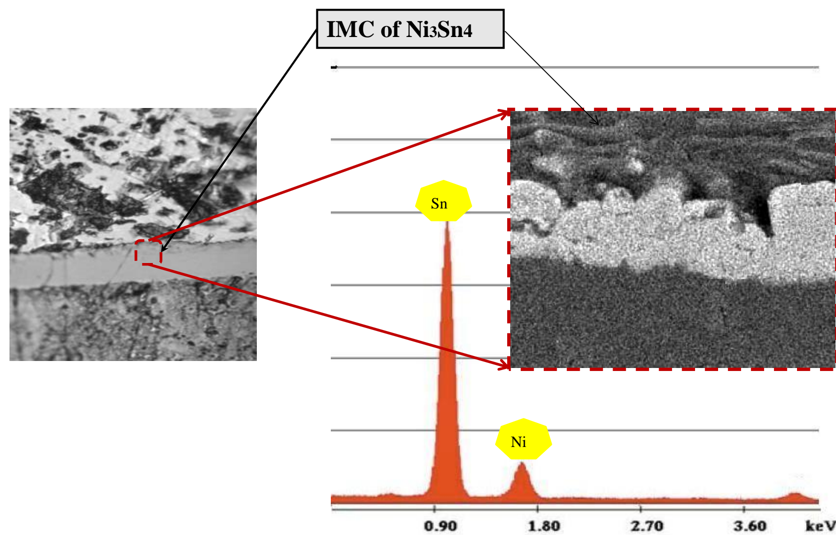

Figure 9 Microanalysis Spectrum of IMC using Energy Dispersion Spectroscopy (EDS)

It is anticipated that the higher temperature cycle magnitude will result in more accrued thermo-mechanical damage and a higher slope of the phase growth parameter versus number of thermal cycle curve. Cross-sectioned/polished samples were then gold sputter coated so as to take SEM images at 750x magnification. Energy Dispersion Spectroscopy (EDS) @ *5000X* to

analyze the composition of the solder. Figure 7 shows the Sn-rich and Pb-rich phases in interconnect and Figure 8 shows the Microanalysis Spectrum. Figure 9 shows the composition and spectrum for Intermetallic Compound (IMC). To measure the phase size, first the images were cropped to a size of 60μm x 45μm and then mapped to gray scale image to calculate the average phase size for selected region using imaging software. Figure 10 shows the mapping of actual image to gray scale using imaging software.

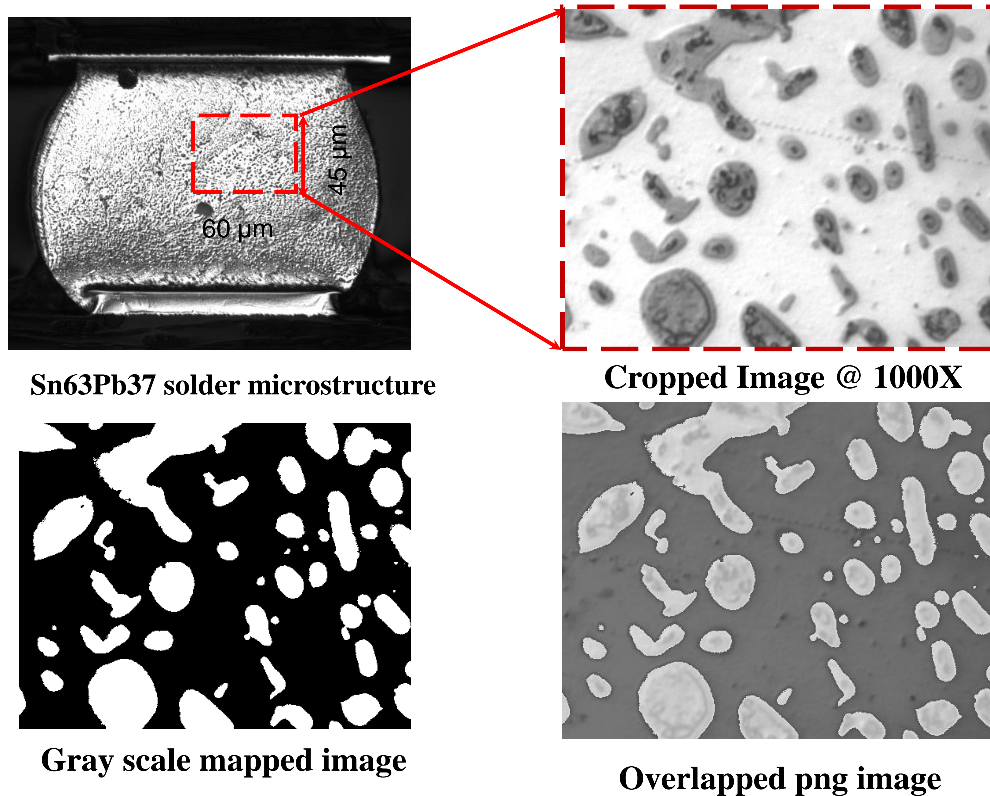

Figure 10 Micrograph and Gray scale mapping of image using Image analysis software

Growth of Inter-Metallic thickness during thermal aging has been studied as another leading indicator of failure in bulk solder. From past studies it has been established that growth of

Intermetallic thickness is used as a damage precursor for computation of remaining useful life [Lall 2005[a], 2006[c, d], 2007[c, e], 2008[c, d] and 2009c[, d]]. The interfacial intermetallic layers are formed between solder and copper, and some precipitates appear near the interface of the IMCs/solder. These intermetallic layers have been identified in SEM micrographs to consist of Cu_3Sn and Cu_6Sn_5 phases [Lall 2005[a]]. In order to investigate the correlation of interfacial intermetallic thickness growth versus thermal aging and thermal cycling, components have been withdrawn and cross sectioned at various intervals of thermal aging. The aged components were cross-sectioned periodically to measure the intermetallic thickness in SEM using 1000x magnification. The mean thickness of intermetallic layers was measured using commercial image processing software on SEM images, as a shown in Figure 6. Trend analysis of intermetallic thickness growth on SEM using image processing software, indicates a square root dependence of IMC thickness versus aging time,

$$y(t) = y_0 + Kt^{1/2} \qquad (5)$$

Where y(t) is IMC growth thickness during aging, y_0 is the initial thickness of intermetallic compounds, k is the coefficient standing for the square root of the diffusivity at aging temperature, and t is test time. The exponent value, n = ½ has been used in the above equation, which reveals a diffusion-controlled mechanism during aging. The aged components were sliced periodically to measure the Intermetallic thickness in SEM using 1000x magnification. The mean thickness of Intermetallic layers were measured using commercial image processing software on SEM images, as a shown in Figure 11.

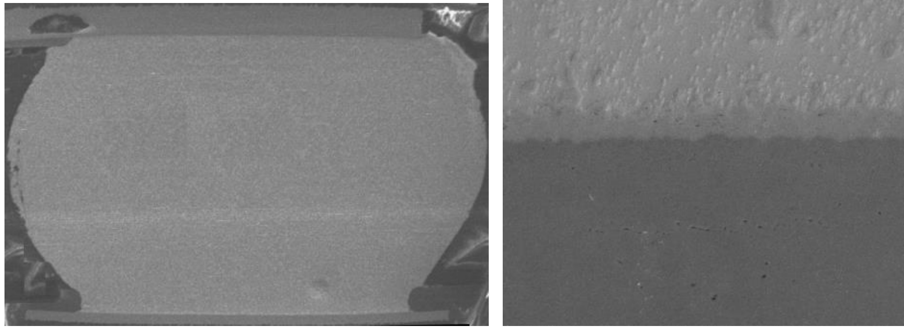

Figure 11 IMC measurements at board side copper pad

3.3.2 Damage Equivalency Relationships for Thermal Aging and Thermal Cycling

A combined plot for thermal-aging and thermal-cycling in terms of damage accrual proxy and life in terms of number of cycles is shown in Figure 11. For overlapping stresses of thermal aging and thermal cycling, the phase-growth damage proxy has been normalized as follows:

$$S_{N\Delta T} = \left[\left(\frac{g_p}{g_0} \right)^4 - 1 \right] = a_{N\Delta T} (N)^{b_{N\Delta T}} \quad (4)$$

Where g is the phase-growth, subscripts p and 0 indicate point “p” and initial time respectively, $S_{N\Delta T}$ is the normalized phase-growth parameter during thermal cycling, $a_{N\Delta T}$ and $b_{N\Delta T}$ are the normalized phase-growth coefficient and phase growth exponent during thermal cycling. The normalized equation has been used for developing damage equivalency relations between damage accrued in thermal aging and thermal cycling. Phase-coarsening will also occur during thermal aging also. Micro-structural evolution in thermal aging can be represented as follows:

$$S_{nt} = \left[\left(\frac{g_p}{g_0} \right)^4 - 1 \right] = a_{nt} (t)^{b_{nt}} \quad (5)$$

Where, g is the phase-growth, subscripts p and 0 indicate point “p” and initial time respectively, SNt is the normalized phase-growth parameter during thermal aging, ant and bnt are the normalized phase-growth coefficient and phase growth exponent for thermal aging. Since the same value of normalized phase coarsening can be achieved on in either thermal aging or thermal cycling, damage equivalency relationship has been derived by equating the normalized phase-growth parameter:

$$a_{N\Delta T}(N)^{b_{N\Delta T}} = a_{nt}(t)^{b_{nt}} \quad (6)$$

$$N = \left[\left(\frac{a_{nt}}{a_{N\Delta T}}\right)(t)^{b_{nt}}\right]^{\frac{1}{b_{N\Delta T}}} \quad (7)$$

Figure 12 illustrates the solution for damage equivalency at point A and B in thermal cycling and thermal aging respectively. In an operational component, the accrued damage in thermal aging will result in reduction in the thermo-mechanical fatigue life of the component. The normalized phase growth parameter S_A has been measured at point A or at the end of storage and prior to deployment. This damage parameter S_A was then mapped back on the thermal cycling curve (marked by point B) that corresponds to S_B to find the equivalent number of cycles N_B. Point A and point B are points on the thermal aging and thermal cycling curves respectively, corresponding to identical values of the normalized phase-growth parameter, i.e. $S_A = S_B$. Mapped cyclic life, N_B, corresponding to t_A hours of thermal aging represents the reduction in thermal cycle reliability because of pre-conditioning at a high temperature.

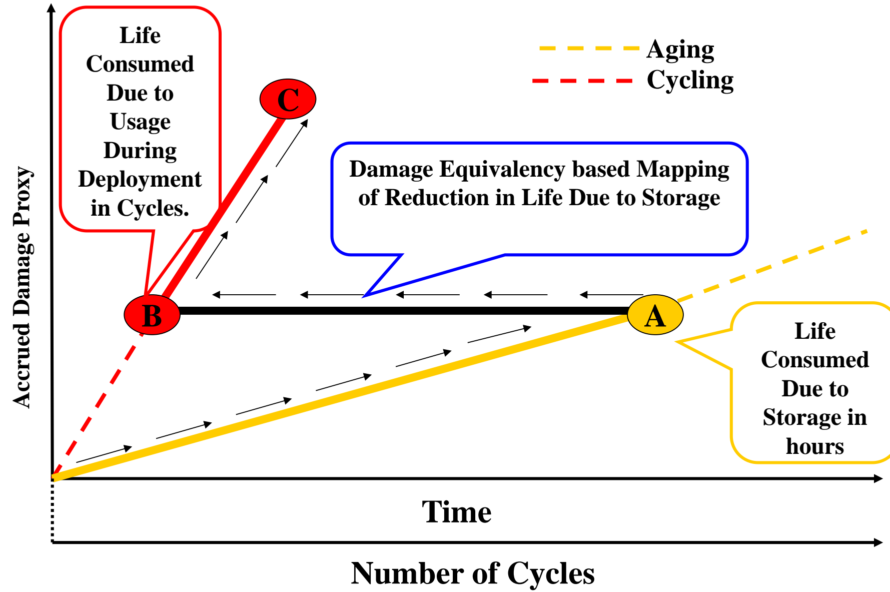

Figure 12: Concept of Damage Equivalency and Mapping of Life Consumed Due to Storage.

Similar damage equivalency relationships have been derived from the intermetallic growth measurements under thermal cycling and thermal aging. A normalized measure of microstructural evolution has been used in this case.

$$\left[\frac{y_p}{y_0}-1\right]=k_{N\Delta T}(N)^{N\Delta T} \qquad (8)$$

$$\left[\frac{y_p}{y_0}-1\right]=k_{nt}(t)^{nt} \qquad (9)$$

Where y is the intermetallic thickness, subscripts p and 0 indicate point "p" and initial time respectively, $k_{n\Delta T}$ and $n_{n\Delta T}$ are the normalized intermetallic growth coefficient and intermetallic growth exponent during thermal cycling, and k_{nt} and n_{nt} are the normalized intermetallic growth

coefficient and intermetallic growth exponent during thermal aging. Convergence between the relationships has been used to validate that damage equivalency from thermal aging to thermal cycling reflects the underlying failure physics.

3.3.3 Validation of Damage Equivalency and Prognostication under Overlapping Stresses

Test assemblies have been subjected to varying periods of thermal aging and separate test assemblies have been subjected to varying periods of thermal cycling. In each case the assemblies were previously field deployed and thus subjected to unknown combinations of thermal aging and thermal cycling. Prior damage in each case has been prognosticated based on the micro-structural evolution of damage. Prognostication involves withdrawal of four samples from the deployed population of devices at four periodic intervals. The samples were then cross-sectioned and the damage proxies including phase-growth parameter and the intermetallic thickness were measured.

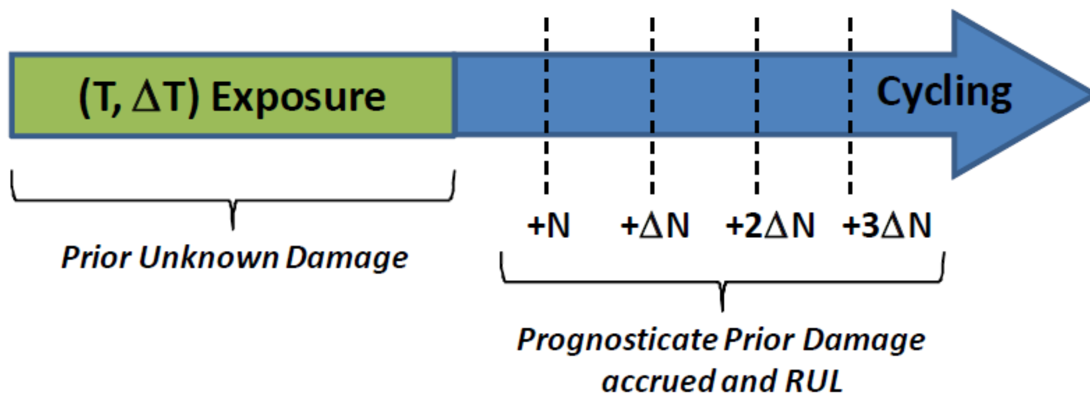

Figure 13: Prognostication of AGED+THERMAL CYCLED Sample at the same thermal cycle count N1.

Prior damage accrued was prognosticated. Normalized phase growth parameter was used to compute life consumed due to cycling alone

$$\left[\left(\frac{g_N}{g_0}\right)^4 - 1\right] = a_{N\Delta T}(N)^{b_{N\Delta T}} \qquad (10)$$

$$\left[\left(\frac{g_{N+\Delta N}}{g_0}\right)^4 - 1\right] = a_{N\Delta T}(N+\Delta N)^{b_{N\Delta T}} \qquad (11)$$

$$\left[\left(\frac{g_{N+2\Delta N}}{g_0}\right)^4 - 1\right] = a_{N\Delta T}(N+2\Delta N)^{b_{N\Delta T}} \qquad (12)$$

$$\left[\left(\frac{g_{N+3\Delta N}}{g_0}\right)^4 - 1\right] = a_{N\Delta T}(N+3\Delta N)^{b_{N\Delta T}} \qquad (13)$$

The prognosticated damage was mapped using the damage equivalency relationships. Identical damage can be obtained by several combinations of thermal aging and thermal cycling. However, the user may be interested in particular solution relevant to the system of interest. The solution of the system of equations is thus bounded using trust regions for range of acceptable values. Most operational systems have date-codes indicating the vintage of manufacture and deployment logs. This enables bounding of the analysis. The prognosticated value of accrued damage is represented by N_C. Reduction in cyclic life due to thermal aging is then be mapped to account for the storage time t_A prior to exposure to cycling. The mapped reduction in cyclic life is represented by N_B. The remaining life is then:

$$N_{CYCLIC} = N_F - N_C \qquad (14)$$

where N_{CYCLIC} is the life of the electronic system in thermal cycling. Field-deployed parts were then subjected to thermal cycling to determine the time-to-failure (N_F) and experimentally measure the remaining useful life. The remaining useful life can then be calculated from the prognostic horizon.

3.4 Levenberg-Marquardt Algorithm

The relationship between Phase growth parameter vs time relationship is highly non-linear due to the presence of terms with fourth power and also due to the fact that experimental data has been fitted using power fit. Levenberg-Marquardt (LM) algorithm is an iterative technique that computes the minimum of a non-linear function in multi-dimensional variable space [Madsen 2004, Lourakis, 2005, Nielsen 1999]. The Levenberg-Marquardt method is combination of steepest descent and the Gauss-Newton method. It is comparatively more robust because it converges to the solution even if it starts very far off the final minimum. [Mittelmann 2004].

Let *f* be a assumed functional relation between a measurement vector referred to as prior damage and the damage parameter vector, p, referred to as predictor variables. The measurement vector is the current values of the leading-indicator of failure and the parameter vector includes the prior system state, and accumulated damage and the damage evolution parameters. An initial parameter estimate p0 and a measured vector x are provided and it is desired to find the parameter vector p, that best satisfies the functional relation *f* i.e. minimizes the squared distance or squared-error, $\varepsilon^T\varepsilon$ with $\varepsilon = x - f(p)$. Assume that g(p) = ε in the squared error. The minimizer parameter vector, p, for the error function has been represented as,

$$F(p) = \frac{1}{2}\sum_{i=1}^{m}(g_i(p))^2 = \frac{1}{2}g(p)^t g(p) \qquad (15)$$

$$F'(p) = J(p)^T g(p) \qquad (16)$$

$$F''(p) = J(p)^T g(p) + \sum_{i=1}^{m} g_i(x) g_i''(x) \qquad (17)$$

where F(p) represents the objective function for the squared error term $\varepsilon T \varepsilon$, J(p) is the Jacobian, and F'(p) is the gradient, and F"(p) is the Hessian. The variation of an F-value starting at "p" and with direction "h" is expressed as a Taylor expansion, as follows:

$$F(p + \alpha h) = F(p) + \alpha h^T F'(p) + O(\alpha^2) \qquad (18)$$

where α is the step-length from point "p" in the descent direction, "h". Mathematically, "h" is the descent direction of F(p) if $h^T F'(p) < 0$. If no such "h" exists, then F'(p)=0, showing that in this case the function is stationary. Since the condition for the stationary value of the objective function is that the gradient is zero, i.e. f '(p + h) = L'(h) = 0. The descent direction can be computed from the equation,

$$(J^T J)h_{gn} = -J^T g \qquad (19)$$

In each step, Newton method uses α = 1 and $p = p + \alpha h_{gn}$, where subscript 'g_n' indicates gauss-newton. The value of α is found by line search principle described above. Levenberg-Marquardt algorithm is a hybrid method which utilizes both steepest descent principle as well as the Gauss-Newton method. When the current solution is far from the correct one, the algorithm behaves like a steepest descent method: slow, but guaranteed to converge. When the current solution is

close to the correct solution, it becomes a Gauss-Newton method. The LM method actually solves a slight variation of Equation (20), known as the augmented normal equations

$$(J^TJ+\mu I)\ h = -J^Tg \qquad (20)$$

The term μ is called as the damping parameter, $\mu>0$ ensures that coefficient matrix is positive definite, and this ensures that h is a descent direction. When the value of μ is very small, then the step size for LM and Gauss-Newton are identical. Algorithm has been modified to take the equations of phase growth and inter-metallic growth under both isothermal aging and cycling loads to calculate the unknowns.

3.5 Prognostication of Damage in Leadfree Area- Array Interconnects under Sequential Stresses

Samples subjected to single and sequential stresses have been prognosticated for damage equivalency and assessment of cumulative accrued damage resulting from a combination of thermal aging and thermal cycling. Prognosticated life has been correlated with experimental values. In addition, prognostic metrics have been computed to compare the robustness of the leading indicators and their accuracy in reference to the prognostic horizon.

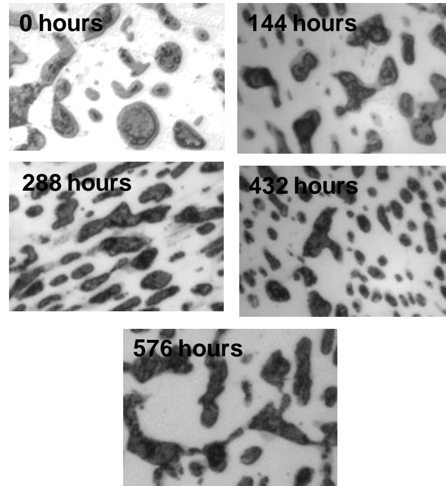

Figure 14: Microscope images of Phase growth versus different aging time intervals (Thermal aging at 60°C, 456 I/O PBGA, magnification 1000x)

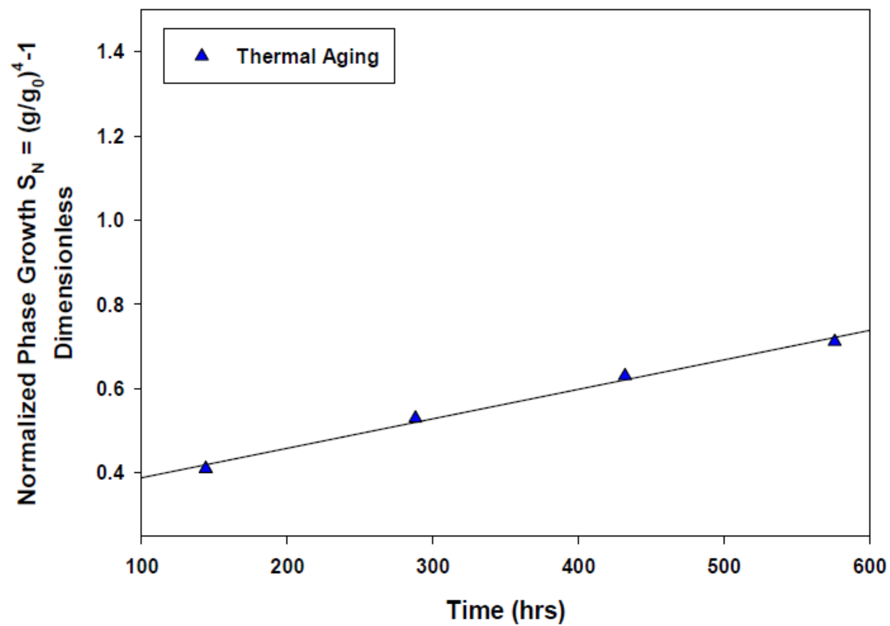

Figure 15: Plot of Normalized Phase growth versus Thermal Aging Time 456 PBGA, subjected to thermal aging at 60°C

The image analysis software has been used to measure the average phase size. Figure 14 shows phase size at different aging time intervals and Figure 16 shows the plot of normalized phase growth at various time intervals. The test data has been represented by the following equation:

$$S_{nt} = \left[\left(\frac{g_p}{g_0} \right)^4 - 1 \right] = a_{nt} (t)^{b_{nt}} \qquad 21$$

Where, g is the phase-growth, subscripts p and 0 indicate point “p” and initial time respectively, S_{Nt} is the normalized phase-growth parameter during thermal aging, a_{nt} and b_{nt} are the normalized phase-growth coefficient and phase growth exponent for thermal aging.

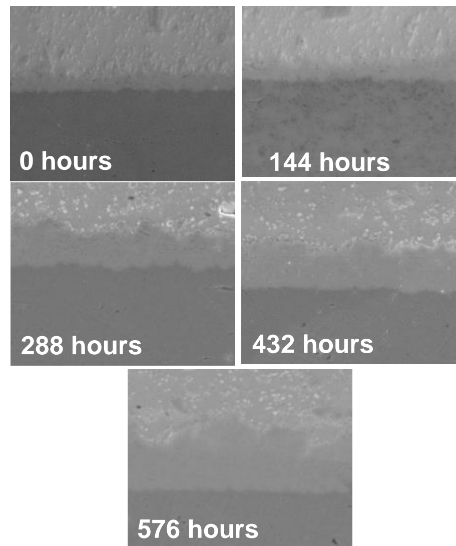

Figure 16 Microscope images of Intermetallic Thickness versus different aging time intervals

(Thermal aging at 60°C, 456 I/O PBGA, magnification 1000x)

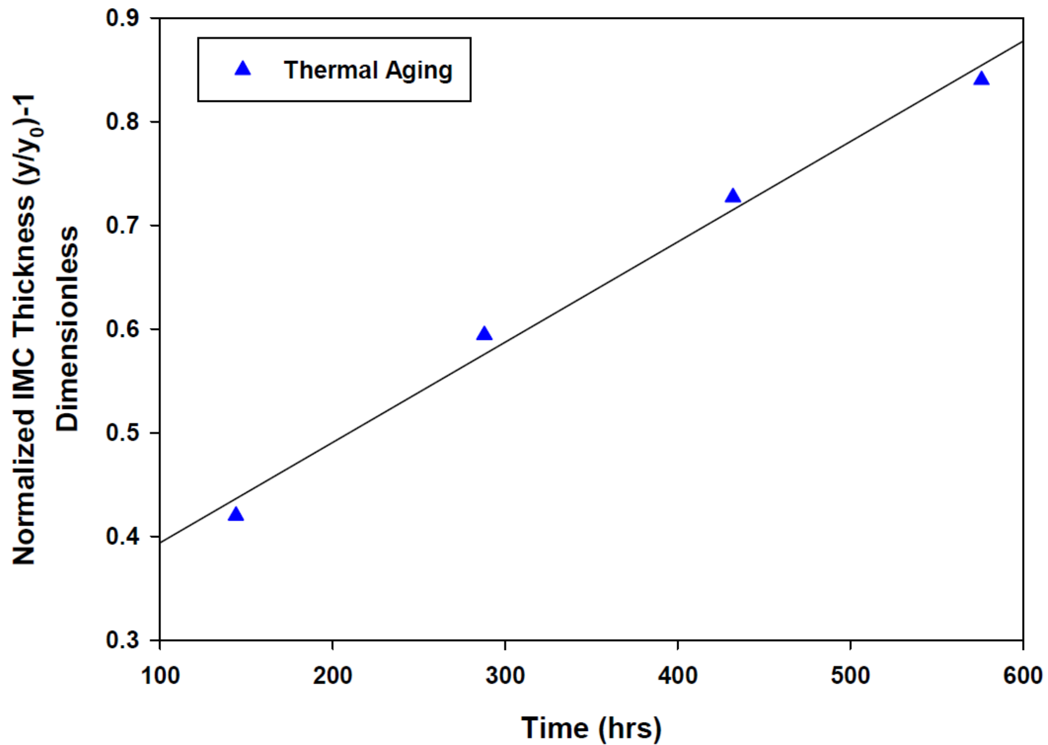

Figure 17 Plot of Normalized IMC thickness versus Aging Time for 456 PBGA, subjected to thermal aging at 60°C

The following relationship represents the evolution of phase growth parameter in thermal aging based on experimental data. The equation parameters have been derived based on experimental measurements of the phase-growth parameters from cross-sections.

$S_N = 0.056(t)^{0.4}$ (22)

Figure 15 shows the growth of intermetallic thickness at various interval of time when subjected to thermal aging at 60°C. Figure 17 shows a plot of normalized intermetallic growth versus thermal aging time. The data has been fit to an equation for the following form:

$$\left[\frac{y_p}{y_0}-1\right]=k_{nt}(t)^{nt} \qquad (23)$$

Where y is the intermetallic thickness, subscripts p and 0 indicate point "p" and initial time respectively, knt and nnt are the normalized intermetallic growth coefficient and intermetallic growth exponent during thermal aging. The following relationship represents the evolution of intermetallic growth in thermal aging based on experimental data. The equation parameters have been derived based on experimental measurements of the intermetallic growth from cross-sections.

$$\left[\frac{y_p}{y_0}-1\right]=0.035(t)^{0.5} \qquad (24)$$

3.5.1 Micro-structural Evolution Under Thermal Cycling

A different set of assembly was subjected to thermal cycling from -40°C to 125°C and were withdrawn after each 100 cycle increments. The samples were cross-sectioned, polished. Phase growth and intermetallic growth was studied using SEM images at each cyclic intervals

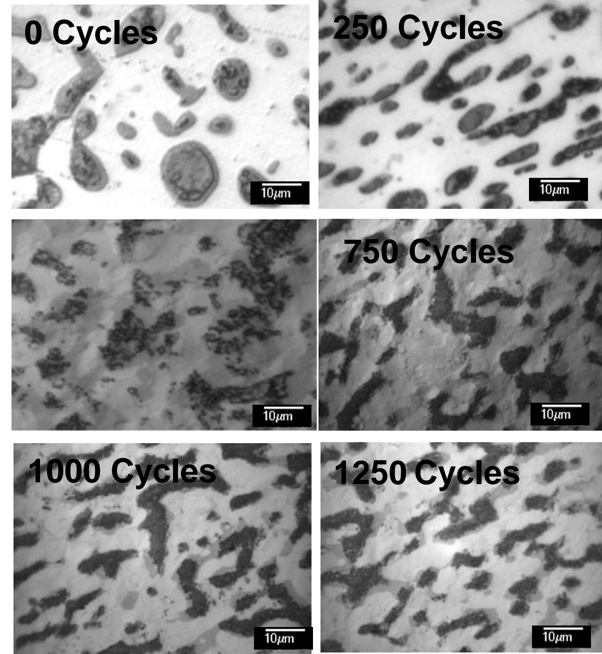

Figure 18: Microscope image of Phase growth versus different aging time intervals (Thermal cycling -40°C to 125°C, 456 I/O PBGA, magnification 1000x)

The image analysis software has been used to measure the average phase size. Figure 18 shows phase size at different intervals of cycles and Figure 19 shows the plot of normalized phase growth at various intervals of cycles. The test data has been fit to the following equation:

$$S_{N\Delta T} = \left[\left(\frac{g_p}{g_0} \right)^4 - 1 \right] = a_{N\Delta T} (N)^{b_{N\Delta T}} \qquad (26)$$

Where g is the phase-growth, subscripts p and 0 indicate point "p" and initial time respectively, $S_{N\Delta T}$ is the normalized phase-growth parameter during thermal cycling, $a_{N\Delta T}$ and $b_{N\Delta T}$ are the normalized phase-growth coefficient and phase growth exponent during thermal cycling. The following relationship represents the evolution of phase-growth parameter in thermal cycling

based on experimental data. The equation parameters have been derived based on experimental measurements of the phase-growth parameters from cross-sections.

$S_N = 0.0128(N)^{0.645}$ (26)

Where S_N is the normalized phase-growth parameter and N is the number of cycles. Figure 20 shows the growth of intermetallic thickness at various interval of time when subjected to thermal cycling from -40 to 125°C. Figure 21 shows a plot of normalized intermetallic growth versus thermal cycles.

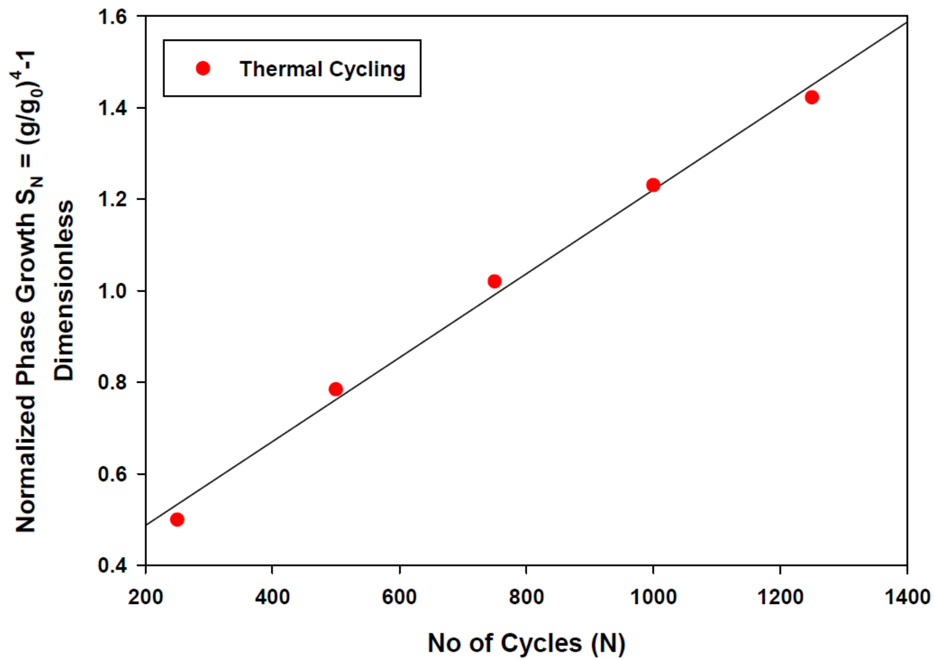

Figure 19 Plot of Normalized Phase growth versus Aging Time for 456 PBGA, subjected to thermal cycling from -40°C to 125°C

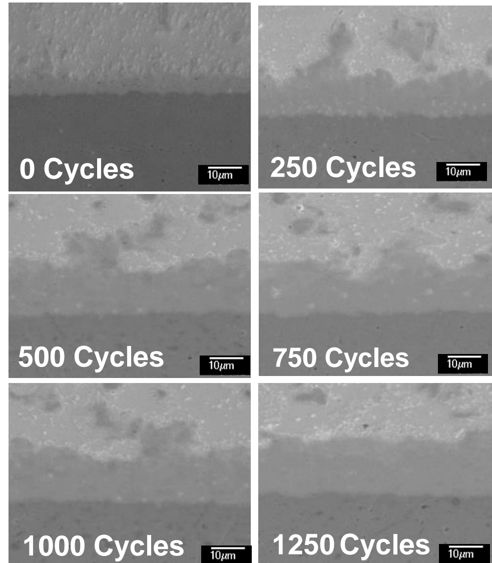

Figure 20 Microscope image of Intermetallic Thickness versus different aging time intervals

(Thermal Cycling at -40 to 125°C, 456 I/O PBGA, magnification 1000x)

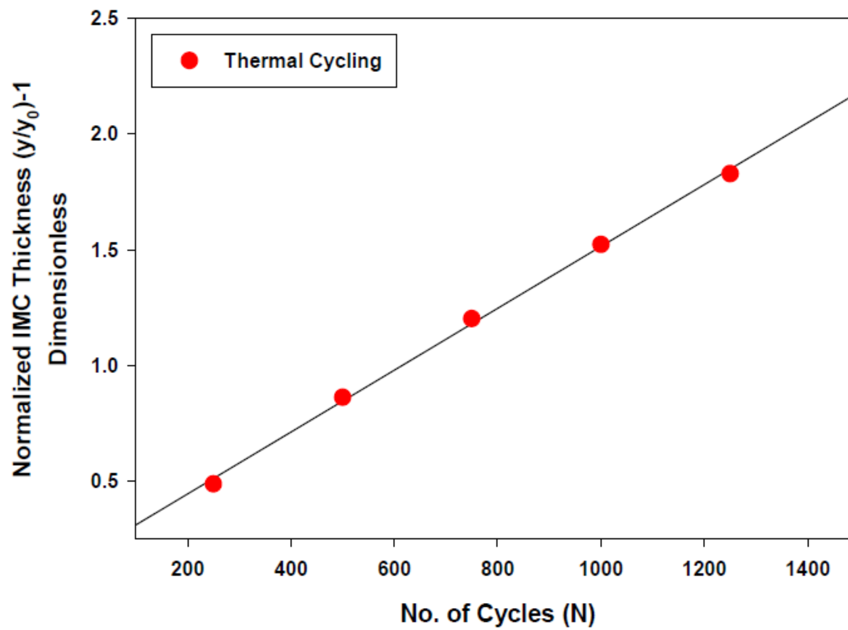

Figure 21: Plot of Normalized IMC thickness versus No of Cycles for 456 PBGA, subjected to thermal Cycles from - 40°C to 125°C

The data has been fit to an equation for the following form:

$$\left[\frac{y_p}{y_0}-1\right]=k_{N\Delta T}(N)^{N\Delta T} \qquad (27)$$

Where y is the intermetallic thickness, subscripts p and 0 indicate point "p" and initial time respectively, $k_{n\Delta T}$ and $n_{n\Delta T}$ are the normalized intermetallic growth coefficient and intermetallic growth exponent during thermal cycling. The following relationship represents the evolution of intermetallic growth in thermal cycling based on experimental data. The equation parameters have been derived based on experimental measurements of the intermetllic growth from cross-sections.

$$\left[\frac{y_p}{y_0}-1\right]=0.0053(N)^{0.82} \qquad (28)$$

3.6 Damage Equivalency Relationships between Thermal Aging and Thermal-Cycling

Figure 22 shows the combined plot normalized Phase growth versus time and cycles on x-axis. Damage accrued from aging and cycling environments has been equivalenced based on two damage proxies including normalized intermetallic thickness and normalized phase growth. The evolution of normalized phase growth has been plotted versus thermal cycles in -40 to 125°C and thermal aging time at 60°C (Figure 21). A similar value of damage proxy can be obtained by exposure to single stresses of thermal aging and thermal cycling. The exposure length to the environmental stresses however, will be different in each case. This combined plot is helpful for mapping of damage from thermal aging onto thermal cycling. Phase-growth

parameter has been used for damage equivalency using previously derived equations for evolution of S_N versus thermal aging time and thermal cycles. Equations (22) and (26) have been equated to derive the damage equivalence relationships based on phase-growth parameter:

$$0.0128(N)^{0.645} = 0.056(t)^{0.4} \quad (29)$$

$$N = 9.93(t)^{0.62} \quad (30)$$

Where N is the number of thermal cycles at -40 to 125°C and t is the time in hours at 125°C. Damage equivalency has also been studied using the intermetallic growth in second-level interconnects. The evolution of normalized intermetallic growth has been plotted versus thermal cycles in -40 to 125°C and thermal aging time at 60°C (Figure 23). A similar value of intermetallic thickness can be obtained by exposure to single stresses of thermal aging and thermal cycling. The exposure length to the environmental stresses however, will be different in each case.

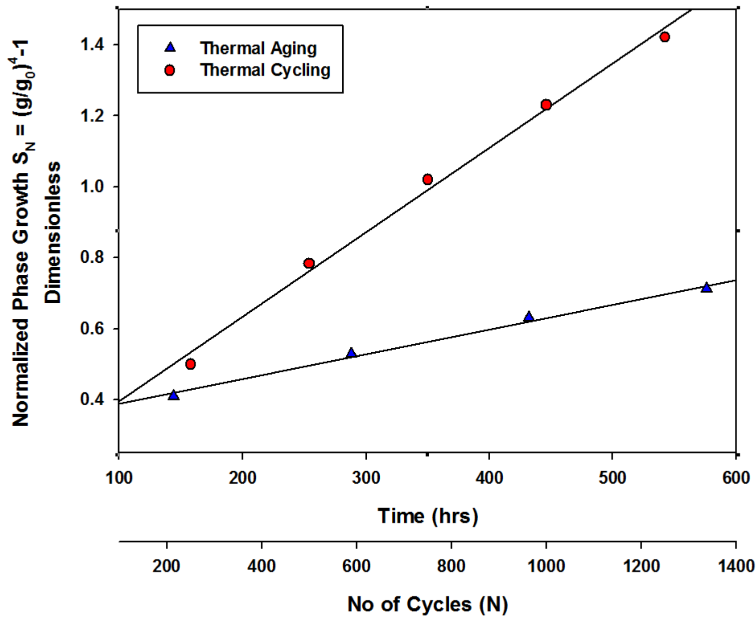

Figure 22 Combined plot Normalized Phase growth versus thermal aging time/thermal cycling.

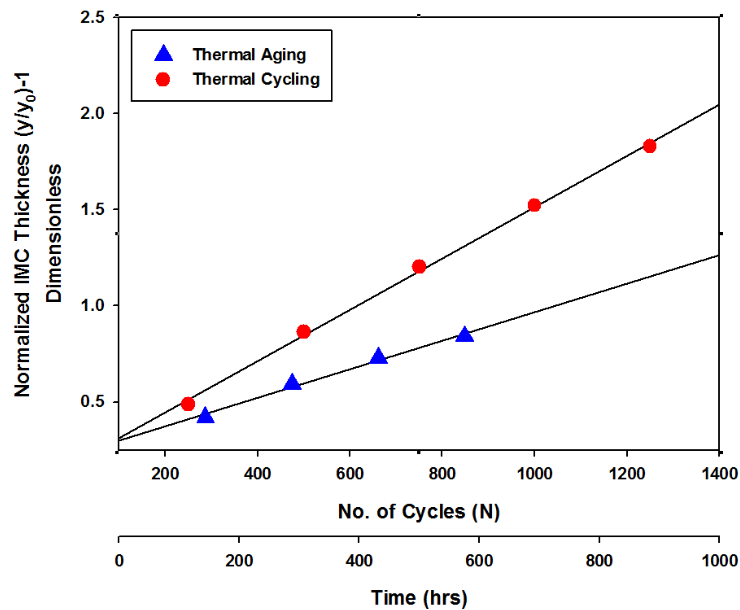

Figure 23 Combined plot of Normalized IMC thickness versus thermal aging time/thermal cycling.

This combined plot is helpful for mapping of damage from thermal aging onto thermal cycling. Equations (24) and (28) have been equated to develop the damage equivalence relationships based on intermetallic growth:

$0.0053(N)^{0.82} = 0.035(t)^{0.5}$ (31)

$N = 9.99(t)^{0.61}$ (32)

Comparison of the damage equivalency relationships between thermal aging at 125°C and thermal cycling from -40 to 125°C developed based on the phase-growth parameter shows that both equations have similar coefficients and exponents (Equations (30), (32)). The values on the graph and the table have been plotted and shown respectively. The convergence of the damage equivalency parameters from two separate damage proxies bolsters the validity of the correlation. Figure 24 and Table 3 show the reduction in thermo-mechanical fatigue life derived based on the two damage proxies.

Table 3 Damage mapping from leading indicators of failure

Time in Hrs	Reduction in life from Normalized Phase Parameter	Reduction in life from Normalized IMC Parameter
144	207	217
288	316	333
432	404	428
576	481	511

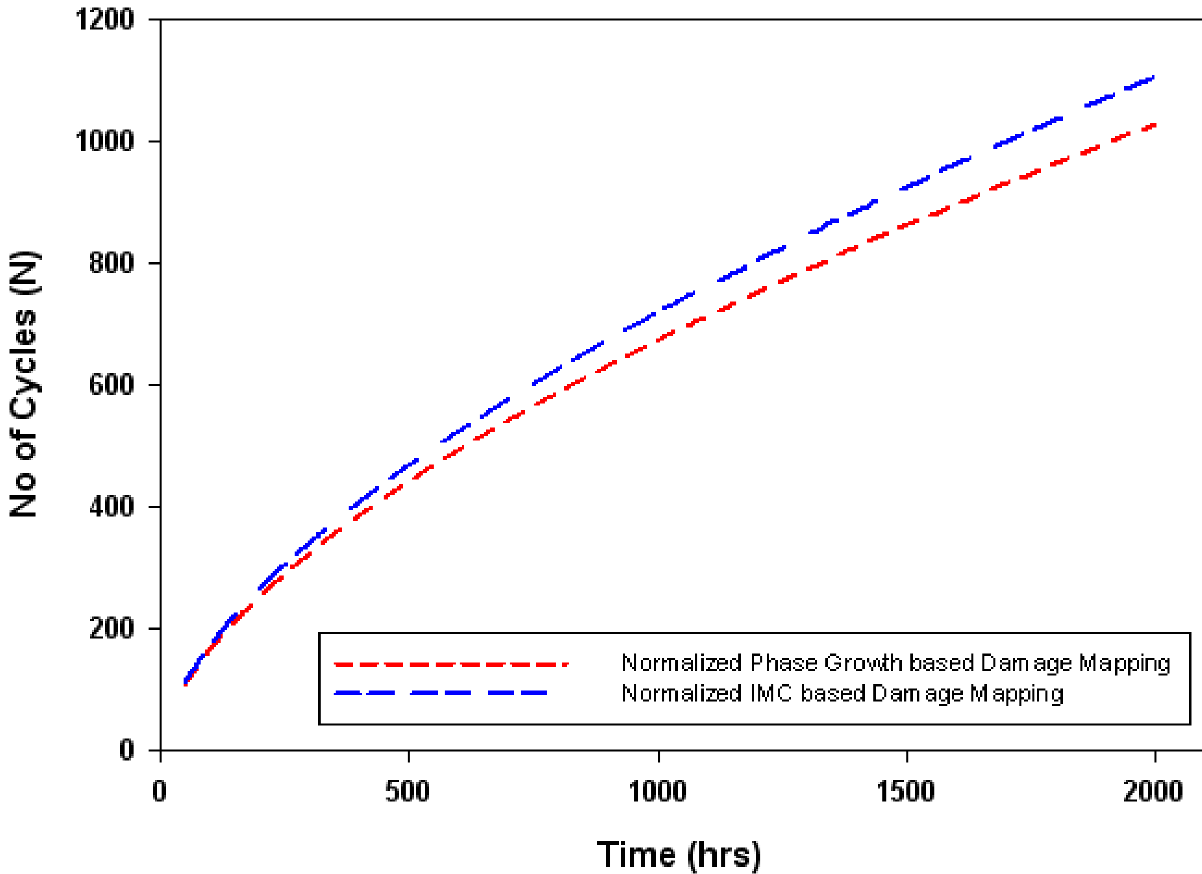

Figure 24: Combine plot of No of Cycles (N) versus Time in hrs, due to damage mapping from Phase growth and IMC thickness.

3.7 Prognostication of Damage Under Multiple Stresses

The system state has been interrogated in test assemblies that have been exposed to different stresses of thermal aging at 60C and thermal cycling from -40 to 125C using both the damage proxies discussed in this proposal. Samples have been withdrawn at periodic intervals and cross-sectioned for measurement of the damage proxies. The LM-Algorithm has been used for

interrogation of system-state for accrued damage. Figure 24 shows the prognosticated value of prior accrued thermo-mechanical damage in field withdrawn parts without any additional imposed exposure to thermo-mechanical stresses. The prognosticated life has been computed in terms of the number of cycles of accrued damage from -40 to 125C. The environmental conditions used were identified based on anticipated future deployment environment. Figure 25 shows the prognosticated value of prior accrued damage for field withdrawn parts after they had been subjected to 250 cycles of -40 to 125C.

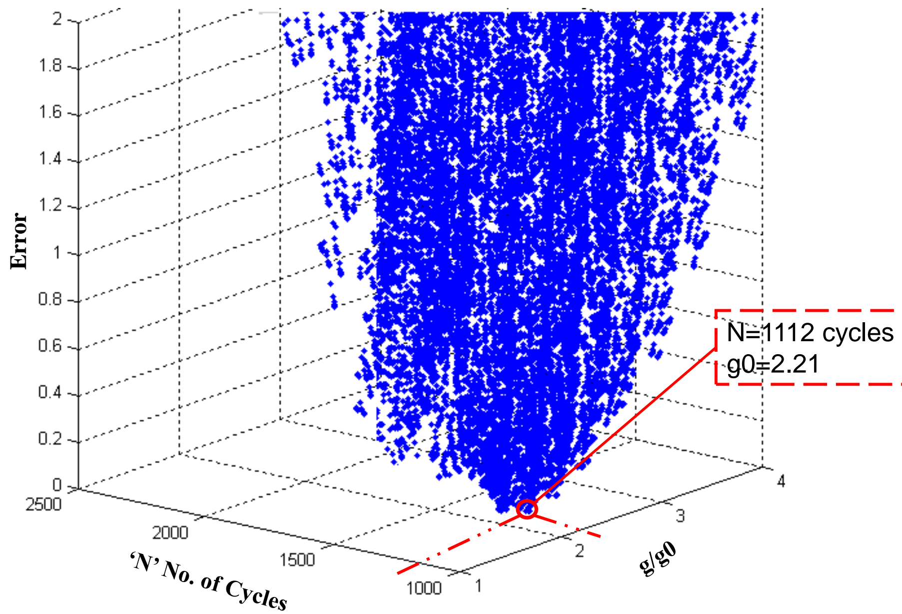

Figure 25: 3D plot of error versus Number of Cycles, damage incurred due to storage in Thermal Cycling Environment (N)

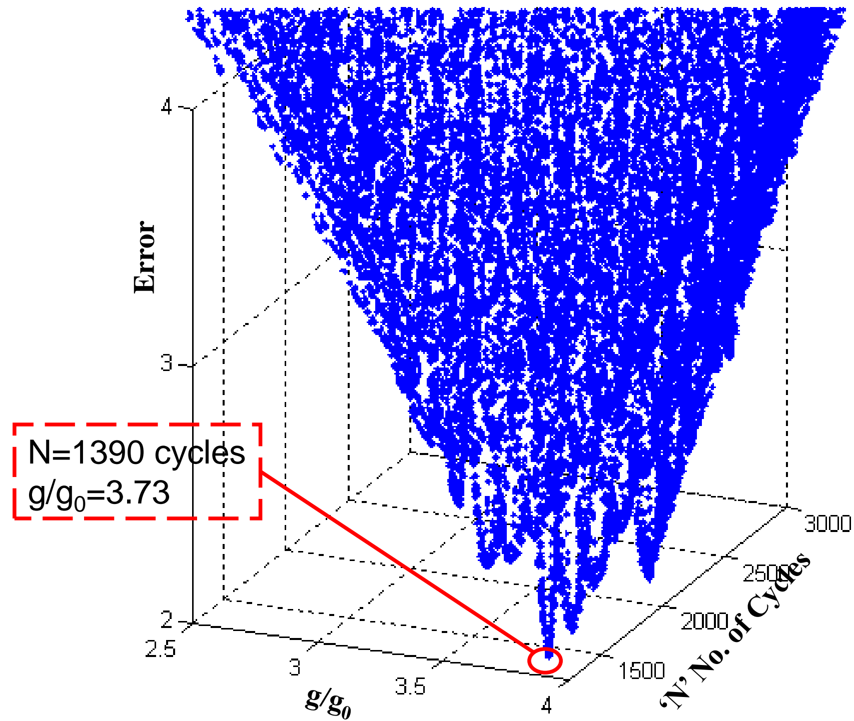

Figure 26: 3D plot of error versus Number of Cycles, damage incurred due to storage in Thermal Cycling Environment (N+ΔN)

Validation of the prognosticated damage can be assessed by the difference between the field withdrawn parts and the field withdrawn parts with additional 250 cycles of thermo-mechanical damage. Comparison of the prognosticated incremental damage between the two thermal-event waypoints has been compared with experimental incremental damage in Table 4. The prognosticated value of 278 cycles correlates well with the experimental value of 250 cycles.

Table 4: Comparison of the prognosticated and experimental incremental damage

	Field Withdrawn parts	Field Withdrawn parts + 250 cycles	ΔN Incremental Accrued Damage
Prognosticated ΔN	**1112**	**1390**	**278 Cycles**
Actual ΔN			**250 Cycles**

The prior accrued damage under steady-state thermal exposure has also been studied in the field withdrawn parts. A separate batch of field withdrawn parts has also been subjected to additional thermal exposure of 144 hours. Figure 27 shows the prior accrued damage in field withdrawn parts. Figure 28 shows the prior accrued damage in field withdrawn parts with increment thermal exposure.

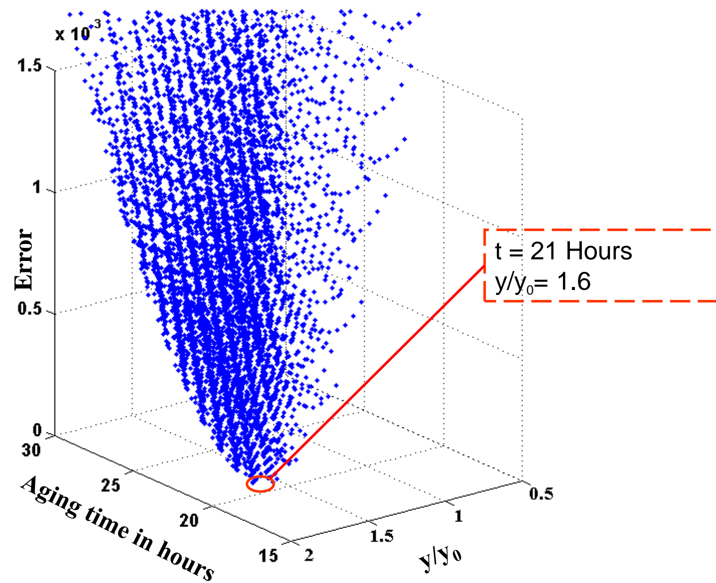

Figure 27: 3D plot of error versus Aging time damage incurred due to storage in Isothermal Aging Environment (t)

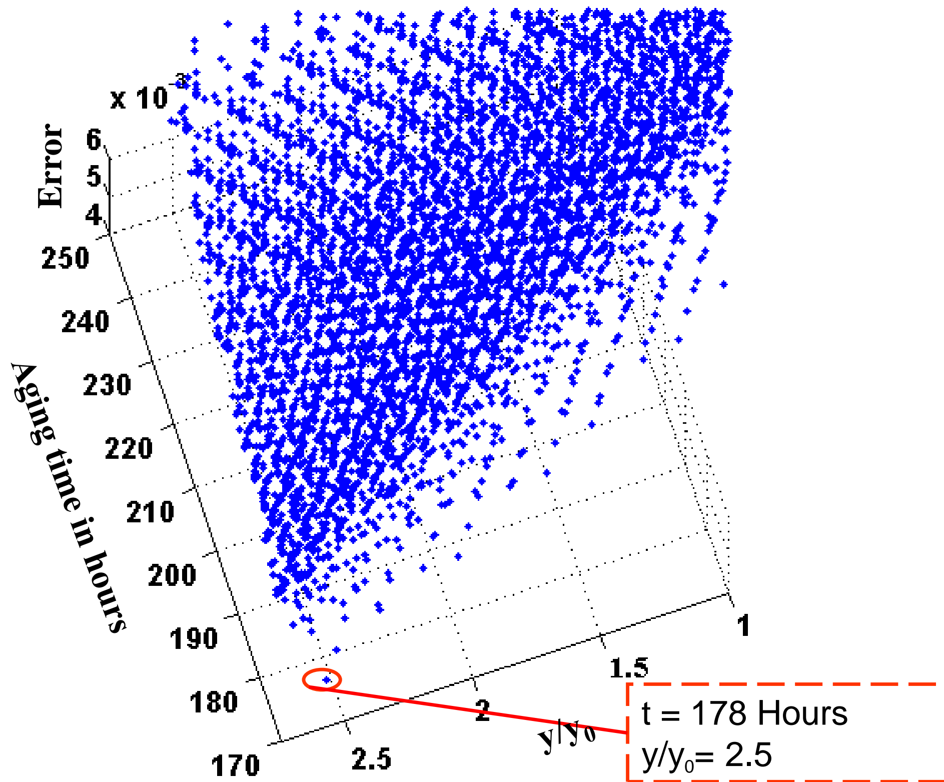

Figure 28: 3D plot of error versus Aging time damage incurred due to storage in Isothermal Aging Environment (t+144) hours

Table 5: Comparison of the prognosticated and experimental incremental damage

	Field Withdrawn parts	**Field Withdrawn parts + 144 hours**	**Δt Incremental Accrued Damage**
Prognosticated Δt	**21**	**178**	**157 hours**
Actual Δt			**144 hours**

The prognosticated value of incremental damage has been compared with the experimental value of incremental damage (Table 5). The prognosticated thermal exposure time-frame has been computed in terms of exposure time at 60C. The temperature level for prognostication has been identified based on the anticipated temperature of future deployment.

3.8 Prognostics Performance Metrics

Prognostics is an emerging concept in condition based maintenance (CBM) of critical systems, where it is desired to predict residual life left in the system before any catastrophic failure takes place and so it is extremely important to check the validation of such prediction algorithms. Since these prognostics concepts are relatively new they lack standard definitions and there is an inconsistency in their interpretations. The lack of standards is in part due to the wide variety of end user requirements for different application, wide range of time scales involved, available domain information, domain dynamics etc. So there is actually very little means of comparing different prognostics approaches based on a common ground. Further in order to evaluate prognostics approach in real world condition a rigorous testing of variety of parameters is required before they can be used in any critical system. So to serve this purpose performance metrics were established. Performances metrics help establish design requirements that must be met for comparison. In the absence of standardized metrics it has been difficult to quantify acceptable performance limits and specify crisp and unambiguous requirements to the designers. These metrics allows comparing different algorithms and also yields constructive feedback to further improve these algorithms. There are various performance metrics which have been used

in domains like Aerospace, Electronics, medicine, Finance, Weather prediction, Nuclear and Automotive.

In this proposal two separate prognostication models based on two leading indicators of failure viz. phase-growth and inter-metallic compound growth of second level solder interconnects have been proposed and implemented for the life prediction of electronics. The sole purpose of evaluating various performance metrics was to relatively compare the two models and see which leading indicator of failure accurately predicts life. For this seven different performance metrics viz. accuracy, precision, Mean Squared Error (MSE), and Mean Absolute Percentage Error (MAPE), α-λ accuracy, relative accuracy (RA) and cumulative relative accuracy (CRA) have been computed to compare the two models.

Terms and Notations:

- UUT is unit under test
- $\Delta^l(i)$ is the error between the predicted and the true RUL at time index i for UUT l.
- EOP (End-of-Prediction) is the earliest time index, i, after prediction crosses the failure threshold.
- EOL represents End-of-Life, the time index for actual end of life defined by the failure threshold.
- P is the time index at which the first prediction is made by the prognostic system.
- $r^l(i)$ is the RUL estimate for the lth UUT at time t_i as determined from measurement and analysis.

- $r_*^l(i)$ is the true RUL at time t_i given that data is available up to time t_i for the lth UUT.
- ℓ is the cardinality of the set of all time indices at which the predictions are made, i.e. $\ell = (i \mid P \leq i \leq EOP)$.
- Error $\Delta^l(i) = r_*^l(i) - r^l(i)$

Average Bias:

Average bias method averages the error in predictions made at all subsequent times after prediction starts for the lth UUT. The metric can be extended to average bias over all UUTs to establish overall bias [1].

$$B_l = \frac{\sum_{i=P}^{EOP} \left\{ \Delta^l(i) \right\}}{\left(EOP - P + 1 \right)}$$

Sample Standard Deviation (S):

Sample standard deviation measures the dispersion/speed of the error with respect to the sample mean of the error. This metric is restricted to the assumption of normal distribution of the error. It is, therefore, recommended to carry out a visual inspection of error plots.

SSD $$S(i) = \sqrt{\frac{\sum_{l=1}^{n} \left(\Delta^l(i) - M \right)^2}{n-1}}$$

Where M is sample mean of the error

Mean squared error (MSE):

Mean squared error averages the square prediction error for multiple UUTs at the same prediction horizon. A derivative of MSE is root mean square error (RMSE).

$$MSE(i) = \frac{1}{L}\sum_{i=1}^{L}\Delta^{l}(i)^{2}$$

Mean absolute percentage error (MAPE):

MAPE averages the absolute error in the predictions of multiple UUTs at the same prediction horizon. Instead of the mean, median can be used to compute Median absolute percentage error (MdAPE) in similar fashion.

$$MAPE(i) = \frac{1}{L}\sum_{l=1}^{L}\left|\frac{100\Delta^{l}(i)}{r_{*}^{l}(i)}\right|$$

α-λ accuracy:

Conventionally the primary purpose of plotting α-λ curve for any prognostication model is to find the prognostic horizon point. The detailed technical definitions and discussion can be found in [Saxena 2008]. However it also helps visually understand the model performance at different intervals of time. In this proposal the α-λ curve has been plotted for both the models as shown in Figures 29 and 30. It is a normalized plot of Remaining Useful Life (RUL) Vs Life which is compared against the ground truth and the error bounds. In this case the ground truth is the experimental data obtained from accelerated testing shown by blue line in the plots and ± 10% error bounds are imposed shown by dotted lines. It should be noted that the selection of error

bounds is application specific and typically tighter bounds are imposed as the criticality of the system increases.

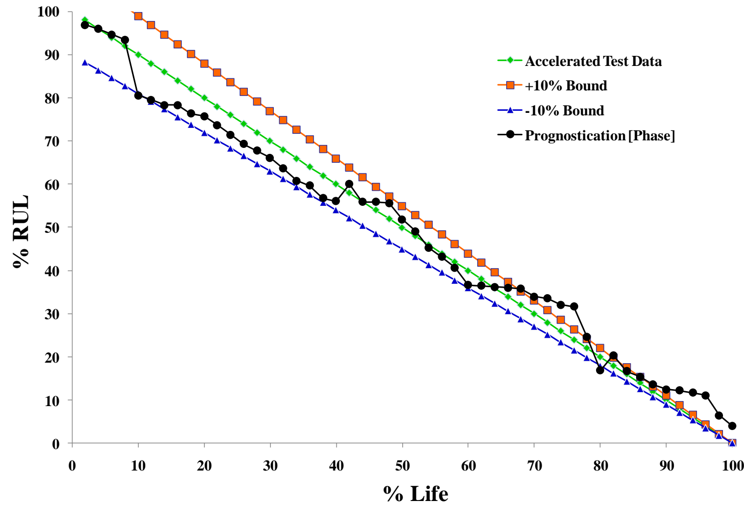

Figure 29: α-λ curve for Prognostication Using Phase Growth as the Damage Proxy

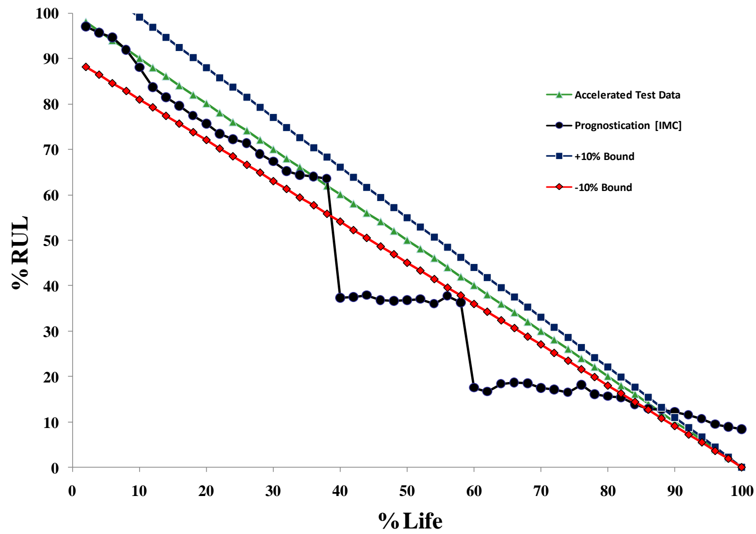

Figure 30: α-λ curve for Prognostication Using IMC as the Damage Proxy

In this proposal the main idea to plot α-λ curves for the two models was not to find the prognostic horizon point but to compare the relative performance of the models visually.

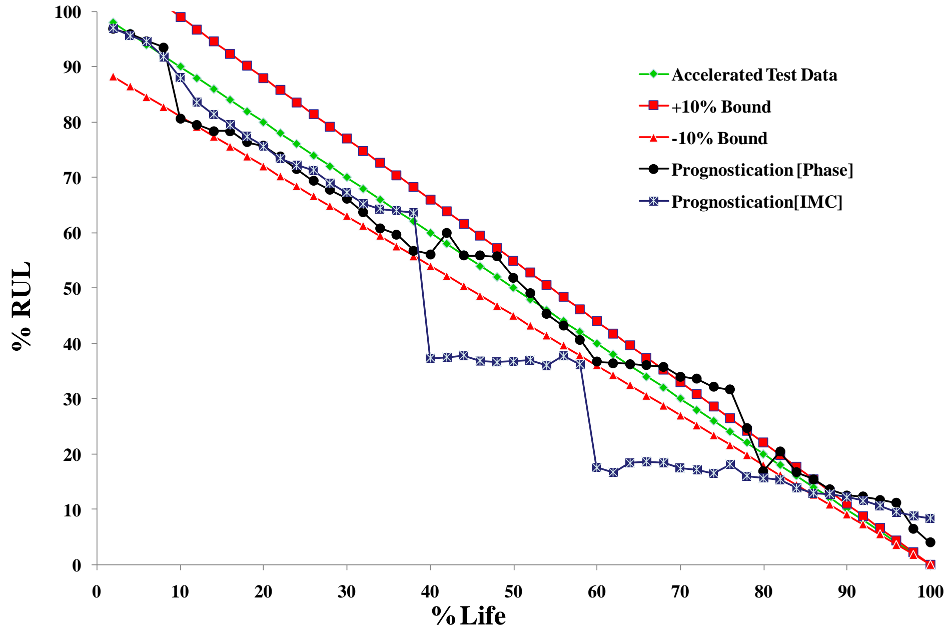

Figure 31: Combined α-λ curve for Prognostication

A compared Figure 31 helps to conclude that the prognostication model developed using phase-growth parameter as the leading indicator of failure performs better than the prognostication model developed using IMC for the current field conditions.

Also α-λ curve does not provide absolute value based comparison but it provides useful information about the model at different intervals. For example visually it is evident from both the plot that the IMC model works better than the phase growth model until 40% of the life and then the IMC model diverges more than the Phase-growth model. Thus this information can be used to modify the model by tweaking certain critical parameters and also check the factors affecting the variability.

Relative accuracy (RA):

Relative prediction accuracy is a notion similar to α-λ *accuracy* where, instead of finding out whether the predictions fall within a given accuracy levels at a given time instant, we measure the accuracy level. The time instant is again described as a fraction of actual remaining useful life from the point when the first prediction is made. An algorithm with higher relative accuracy is desirable

$$RA = 1 - \frac{\left| r_*(t_\lambda) - r^l(t_\lambda) \right|}{r_*(t_\lambda)}$$

Where $t_\lambda = P + \lambda\,(EOP - P)$

CRA:

Relative accuracy can be evaluated at multiple time instances. To aggregate these accuracy levels, we define Cumulative Relative Accuracy as a normalized weighted sum of relative prediction accuracies at specific time instances

$$CRA = \frac{1}{EOP - P + 1} \sum_{l=P}^{EOL} RA$$

Where *w* is a weight factor as a function of RUL at all time indices. In most cases it is desirable to weigh the relative accuracies higher closer to the EOL.

Table 6 Comparison of for both the algorithm

Prognostic Metrics	LM prognostication (Phase)	LM prognostication (IMC)

Sample Standard Deviation (S)	61.79280896	195.85
MSE	11225.04082	61228.84
MAPE	0.0157601	0.25
RA (λ=0.5)	0.9624	0.734
CRA	0.016282	0.0141

Table 6 shows Relative accuracy for a point where 50% of the life of system is consumed. Based on all performance metrics from table, we can say that LM prognostication algorithm based on Phase growth as leading indicator of failure work better than LM prognostication algorithm based on growth of Inter-metallic thickness as leading indicator of failure.

3.9 Residual Life in Multiple Environments

The residual life of the assemblies subjected to multiple thermal environments has been be computed based on the following equation,

$RUL = 1 - (N / N_{1\%})$

Where, $N_{1\%}$ is the time to one-percent failure of the population, $N_{1\%}$ is the prognosticated prior damage in the test assemblies. The $N_{1\%}$ may be procured by accelerated testing of the part and correlation with the field conditions. Weibull chart will provide the value of $N_{1\%}$ for test part shown in Figure 32.

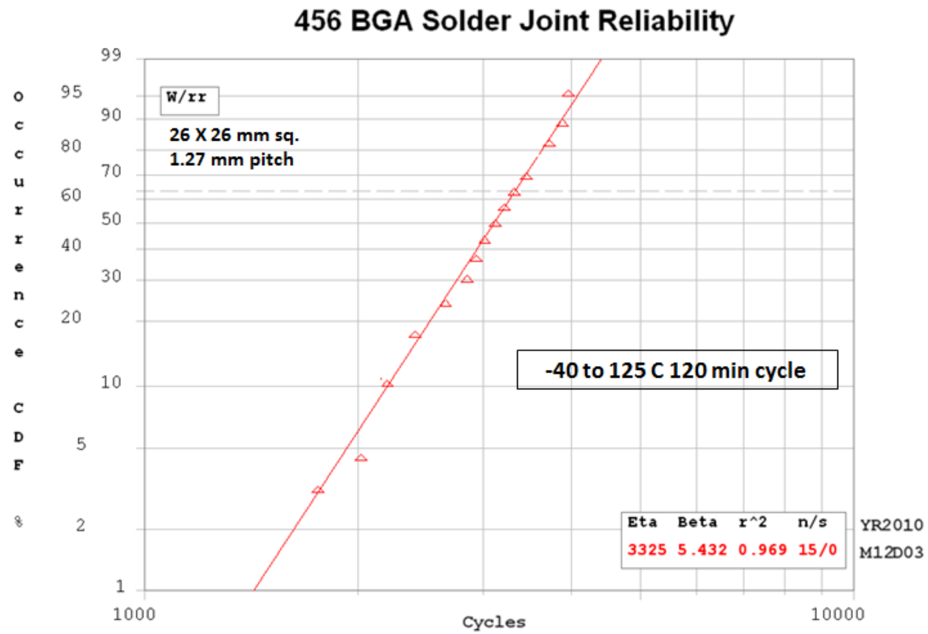

Figure 32: Weibull plot for pristine 456 BGA packages subjected to thermal cycle -40ºC to 125ºC.

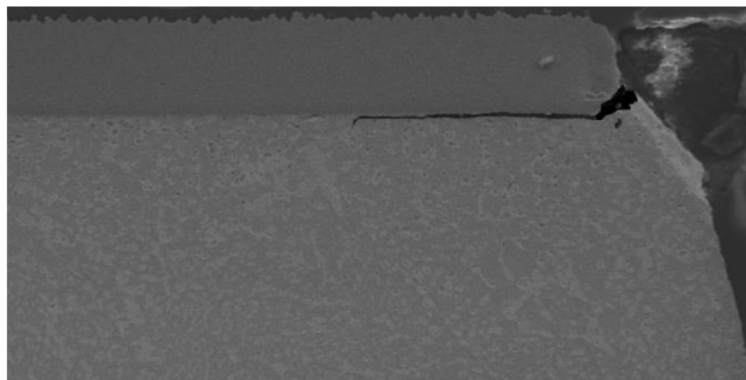

Figure 33: Cross-section of identical field extracted part subjected to thermal cycle -40ºC to 125ºC for additional.

Thus, from above values of LM and Weibull chart, the % life consumed is (N / $N_{1\%}$) = 63.7%. RUL = 1 – (N / $N_{1\%}$) = 36.3% in the anticipated new environment of -40 to 125ºC. The field

extracted part has been subjected to thermal cycling at -40 to 125ºC for additional 750 cycles. The part was cross-sectioned and the exhibited significant cracking in the solder joints. Figure 33 shows the crosssection of the solder joint with crack on the package side of the solder joint. The total prior accrued damage in the field extracted part based on experimental data in anticipated future environment is (1746 Cycles – 750 Cycles) = 1096 Cycles. The prognosticated value of 1112 Cycles correlates well with the measured value of 1096 Cycles. The prognosticated RUL in -40 to 125ºC is (1746 Cycles - 1112 Cycles) = 634 Cycles. The RUL can be any combination of thermal cycling and thermal aging. For example if 50% of the RUL is expected to be spent in thermal cycling and the remaining in thermal aging, then only 50% or (0.5*1112) Cycles = 556 Cycles of damage will be accrued in thermal cycling. The remaining 50% of the damage will be accrued in the form of reduction in fatigue life because of thermal aging. The equivalent thermal aging time can be computed from the damage equivalence relationship developed earlier in this proposal:

$N = 9.93(t)^{0.62}$

$556 = 9.93(t)^{0.62}$ (40)

$t = 660$ hrs

Thus, the 50% duty cycle in the future anticipated environment will involve storage of the part for 660 hours at 60C and 556 Cycles of -40 to 125ºC. A similar procedure can be followed for any other combination of thermal cycling and thermal aging in the operational environment.

3.10 Summary and Conclusion

A method has been developed for prognostication of accrued prior damage and remaining useful life in field-deployed electronics extracted from service after exposure to overlapping sequential environments of thermal aging and thermal cycling. The presented approach uses the Levenberg-Marquardt Algorithm in conjunction with microstructural evolution of damage based leading indicator for estimating prior accrued damage. Specific damage proxies examined include the phase-growth indicator and the intermetallic thickness. Damage equivalency relationships between thermal aging during storage life and the resulting reduction in thermo-mechanical reliability in cyclic thermal environments during field deployment has been derived and validated based on two damage proxies. Convergence of the damage mapping to a common solution from data based on the two separate leading indicators has been demonstrated.

The viability of the approach has been demonstrated for field deployed parts extracted from service without any prior knowledge of the stress histories. Percentage of the life consumed has been prognosticated. The remaining useful life has been determined in the anticipated future environment. The prognosticated values have been validated versus experimental data by two methods. The first method involved subjected pristine parts to anticipated future environment.

Weibull distribution of failures has been developed for the pristine parts. The second method, involved subjecting a subset of the field extracted parts to the anticipated future environment till failure. The prognosticated prior damage of 1112 Cycles correlates with the experimentally measured value of prior damage of 1056 Cycles from -40 to 125ºC. In addition, the prognosticated remaining useful life of 634 cycles correlates well with the measured remaining

useful life of 750 cycles. The methodology can be used for prognosticating RUL in any combination of thermal aging and cycling an example calculation of 50% duty cycle in cycling yields a value of 556 thermal cycles from -40 to 125ºC and 660 hours of thermal aging at 60C. The process can be used for any other combination of anticipated thermal cycling and thermal aging. Correlation between the prognosticated damage and the actual accrued damage demonstrates that the proposed approach can be used to assess damage accrued under overlapping thermo-mechanical stresses of thermal aging and thermal cycling. In addition, prognostics metrics have been used to quantitatively evaluate the performance of the prognostic algorithms using both the leading indicators. Results demonstrate that both damage proxies work well in estimating accrued damage and estimating residual life.

Chapter 4

Determination of Accrued Damage and Remaining Life during Field-Usage in Lead-Free Electronics Subjected to Multiple Thermo-mechanical Environments

4.1 Overview

Field deployed electronics us often subjected to a combination of thermal aging and thermal cycling. The thermal cycle magnitudes may vary over the lifetime of the product. Long-life systems may be re-deployed several times over the use life of the product. Aging has been previously shown to effect the reliability and constitutive behaviour of second-level leadfree interconnects. Often the equipment may not have any macro-indicators of damage such as cracks or delamination. The ability to identify impending failures in systems and their sub-components has great potential to mitigate the risks of unanticipated failures and reduce the support costs. The presented approach in this paper is intended to address the need for tools and techniques for prognosticating the prior accrued damage and the remaining useful life of the product prior to redeployment. Leadfree assemblies with Sn3Ag0.5Cu solder have been subjected to various duration-combinations of thermal aging at 125°C, thermal cycling from -40°C to 125°C and thermal cycling from 0°C to 100°C. The presented methodology uses leading indicators of failure based on micro-structural evolution of damage to identify accrued damage in electronic systems subjected to sequential stresses of thermal aging and thermal cycling. Leading indicators studied in this paper include the phase growth parameter and the intermetallic thickness. Damage equivalency relationships have been developed to map damage accrued in thermal aging to the

reduction in thermo-mechanical cyclic life based on damage proxies. Accrued damage between different thermal cyclic magnitudes has also been mapped for -40°C to 125°C and 0°C to 100°C thermal cycles. The presented method for interrogation of the accrued damage for the field deployed electronics, significantly prior to failure, may allow insight into the damage initiation and progression of the deployed system. The expected error with interrogation of system state and assessment of residual life has been quantified.

4.2 Test Vehicle

In this study, two different leadfree assemblies with PBGA- 676 and CABGA-256 packages have been used. The packages were full-array configuration and Sn3Ag0.5Cu solder interconnects. The ball diameter for the 676 I/O BGA is 0.63 mm. The ball diameter for the 256 I/O BGA is 0.5 mm. Package attributes are shown in Table 7. The printed circuit board was a double-sided FR4-06 material. The printed circuit board pads were solder mask defined (SMD) with immersion silver finish. Figure 34 shows the packages and their array configuration. A designed assembly is shown in Figure 35. All test vehicles were subjected to sequential environments of thermal aging at 125°C and thermal cycling from -40°C to 125°C and 0°C to 100°C for various lengths of time. The test board is a JEDEC form-factor test board with corner holes. Each test package has four daisy chain patterns corresponding to the four quadrants. Board assemblies were assembled at in-house surface mount facility of CAVE3. The reflow profile used for assembly is shown in Figure 36.

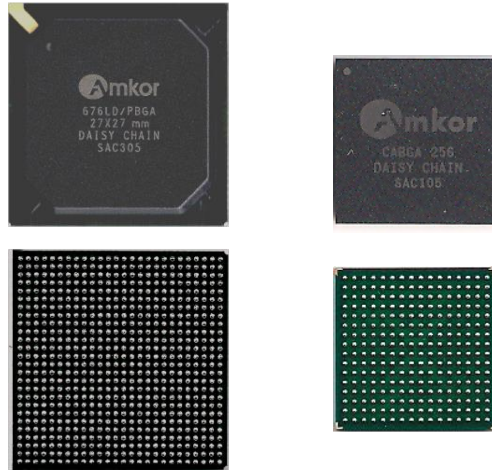

Figure 34: Top and Bottom part of PBGA 676 and PBGA 256 Packages

Table 7: Attributes of Test Vehicles

Solder	Sn3Ag0.5Cu	Sn3Ag0.5Cu
Package Type	PBGA	CABGA
Ball Matrix	27 mm	17mm
I/O Count	676	256
I/O Pitch	1 mm	1 mm
Ball Diameter	0.63mm	0.5 mm
Board Finish	ImAg	ImAg

Figure 35: Test Assembly Design

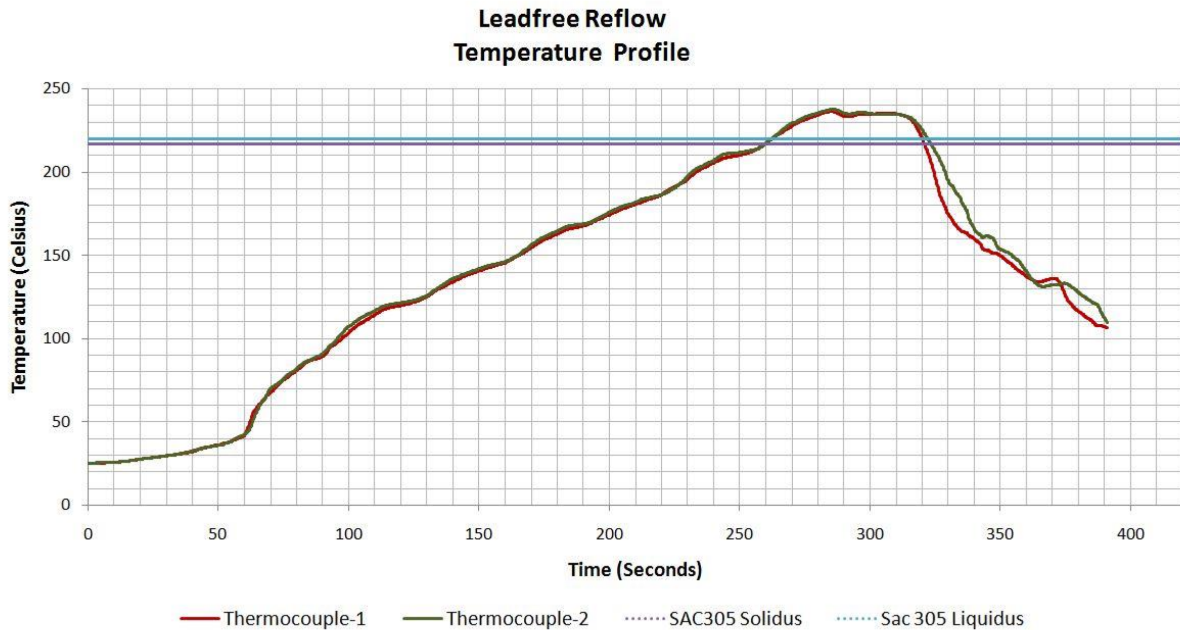

Figure 36: Reflow Profile for SAC Alloy

4.3 Approach for Prognostication of Damage from Sequential Exposure to Thermo-mechanical Stresses

The board assemblies were subjected to sequential and multiple thermal environments of thermal aging followed by thermal cycling. In order to assess damage, interrogation of system state has been done based on different leading indicators of failures. In this case phase growth parameter "S" and inter-metallic thickness (IMC) growth has been used as two leading indicators of failure for interrogation of system state and calculation of remaining useful life. Extended exposure to thermal aging may reduce thermo-mechanical reliability in cyclic environments. A framework has been developed to account for the damage incurred due to storage before the deployment to determine the operational readiness of the system and compute remaining useful life in the

intended field. In cyclic thermal environments, system-life is often measured in number of thermal cycles. However, life in thermal aging environment be measured in terms of time i.e. number of hours, days, weeks or months. Assessment of cumulative damage after exposure to multiple environments is often challenging because of the differing measurement scales and scarcity of methods for reconciling damage accrued under various environmental loads. Commonality of the damage proxies between thermal aging and thermal cycling has been used to superimpose damage in the two environments. Test assemblies were subjected to single environments of isothermal aging at 125°C (TA1). The test assemblies have been subjected to relatively harsh thermal cycle ranging from -40°C to 125°C (TC1) and a milder thermal cycle temperature from 0°C to 100°C (TC2) as shown in Figure 37. Once deployed in TC2, the operational readiness and the prior accrued damage in the assemblies has been assessed. In Figure 38, the difference in the slopes between sequential stresses thermal aging and thermal cycling indicates the differing rates of damage accrual in the environments.

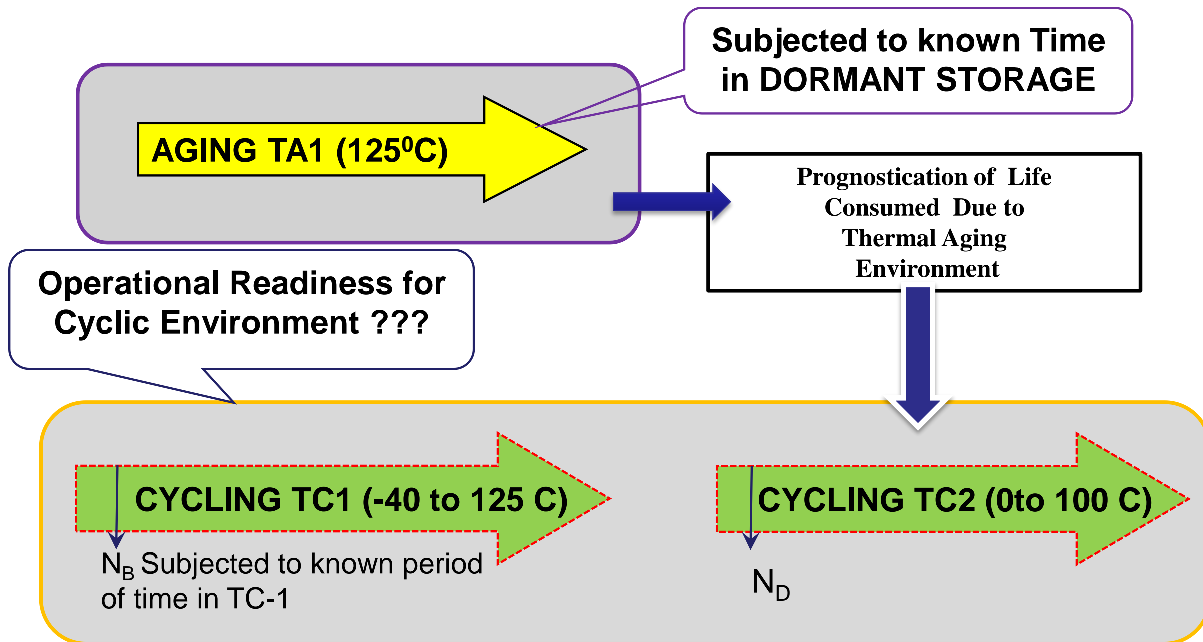

Figure 37: Exposure of Electronics Sequential Stresses of Thermal Aging and Cycling.

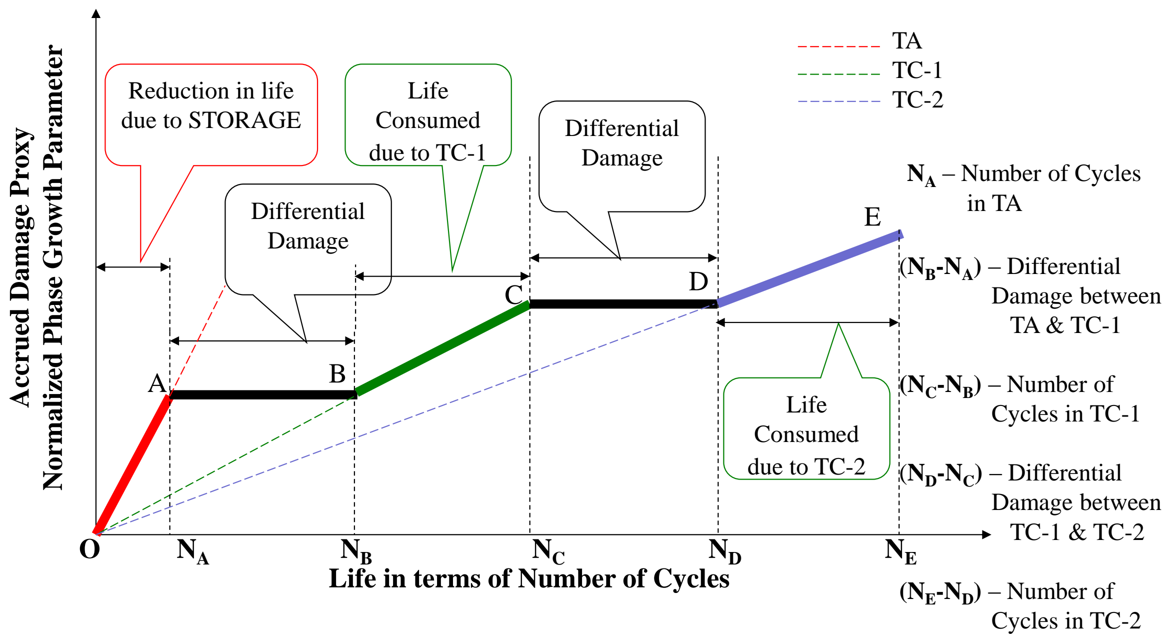

Figure 38: Life Vs Damage Curve for Multiple Thermal Environments.

4.3.1 Measurement of Leading Indicators

Damage proxies studied include the phase-growth parameter and the intermetallic thickness. Previously, it has been shown that the rate of change in phase growth parameter [d(lnS)/d(lnN)] is valid damage proxy for prognostication of thermo-mechanical damage in solder interconnects and assessment of residual life [Lall 2004a, 2005a, 2006c,d, 2007c,e, 2008c,d, 2009c,d]. The damage proxy [d(lnS)/d(lnN)] is related to the microstructural evolution of damage by the following equation:

$$S = g^4 - g_0^4 = a\,[N]b \qquad (1)$$

$$\ln S = \ln(g^4 - g_0^4) = \ln a + b \ln N \qquad (2)$$

$$\frac{d(\ln S)}{d(\ln N)} = b$$

Where, g is the average grain size at time of prognostication, g0 is the average grain size of solder after reflow, N is the number of thermal cycles, S is the phase growth parameter, parameters a and b are the coefficient and exponent respectively. The log-plot of the equation provides a straight line relationship between the phase growth parameter and the number of cycles. It is anticipated that the higher temperature cycle magnitude will result in more accrued thermo-mechanical damage and a higher slope of the phase growth parameter versus number of thermal cycle curve. Cross-sectioned/polished samples were then gold sputter coated so as to take confocal microscopic images at 1000x magnification. Most of the SnAgCu solder is comprised of Sn-phases, so that the growth rate of tin and Ag3Sn Intermetallic crystals are significant. Phase size is measured by measuring Ag3Sn particle size. The quantitative measure

of Ag3Sn particle size was established from a 100 µm x 75 µm rectangular region selected from a backscattered image of a highest strain corner solder ball. To measure the phase size, first the images were cropped to a size of 60µm x 45µm and then mapped to gray scale image to calculate the average phase size for selected region using imaging software. Figure 39 shows the mapping of actual image to gray scale using imaging software.

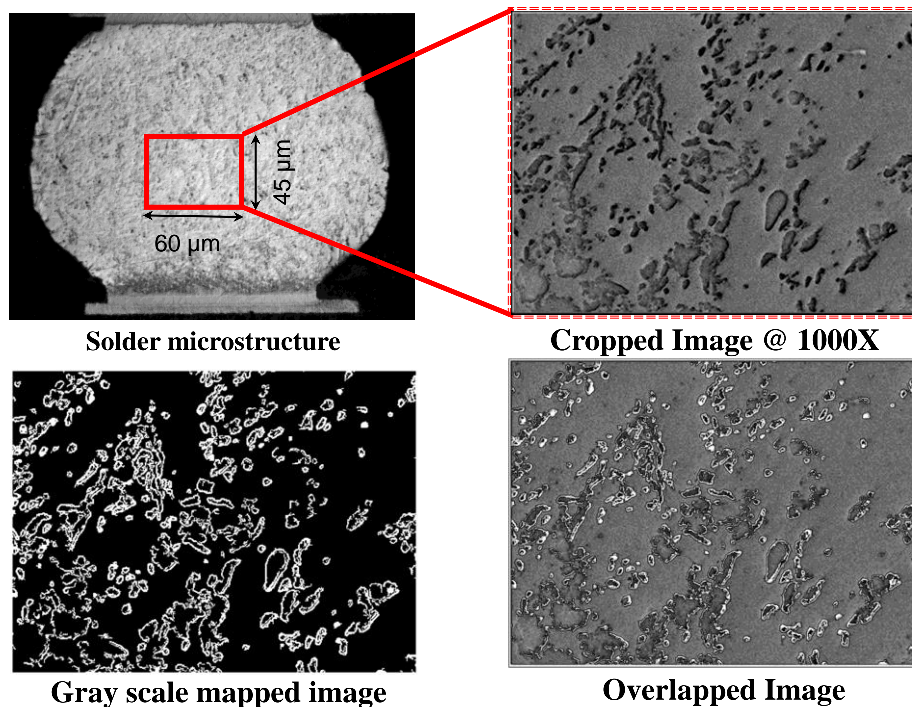

Figure 39: Micrograph and Gray scale mapping of image using image analysis software

Growth of Inter-Metallic thickness during thermal aging has been studied as another leading indicator of failure in bulk solder. From past studies it has been established that growth of Intermetallic thickness is used as a damage precursor for computation of remaining useful life [Lall 2005a, 2006c,d, 2007c,e, 2008c,d, 2009c,d]. The interfacial intermetallic layers are formed between solder and copper, and some precipitates appear near the interface of the IMCs/solder.

These intermetallic layers have been identified in SEM micrographs to consist of Cu3Sn and Cu6Sn5 phases [Lall 2005a]. In order to investigate the correlation of interfacial intermetallic thickness growth versus thermal aging and thermal cycling, components have been withdrawn and cross sectioned at various intervals of thermal aging. The aged components were cross-sectioned periodically to measure the intermetallic thickness in SEM using 1000x magnification. The mean thicknesses of intermetallic layers were measured using commercial image processing software on images, as a shown in Figure 40. Trend analysis of intermetallic thickness growth on SEM using image processing software, indicates a square root dependence of IMC thickness versus aging time,

$$y = y_0 + kt^n \quad (3)$$

where y(t) is IMC growth thickness during aging, y_0 is the initial thickness of intermetallic compounds, k is the coefficient standing for the square root of the diffusivity at aging temperature, and t is test time. The exponent value, n = ½ has been used in the above equation, which reveals a diffusion-controlled mechanism during aging.

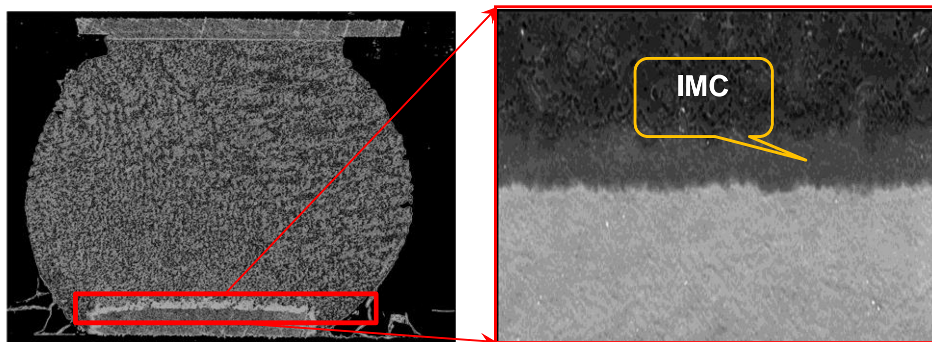

Figure 40: Back-scattered images of IMC growth (Magnification 1000x)

4.4 Levenberg-Marquardt Algorithm

The relationship between Phase growth parameter vs time relationship is highly non-linear due to the presence of terms with fourth power and also due to the fact that experimental data has been fitted using power fit. Levenberg-Marquardt (LM) algorithm is an iterative technique that computes the minimum of a non-linear function in multi-dimensional variable space [Madsen 2004, Lourakis, 2005, Nielsen 1999]. The Levenberg-Marquardt method is combination of steepest descent and the Gauss-Newton method. It is comparatively more robust because it converges to the solution even if it starts very far off the final minimum. [Mittelmann 2004].

Let *f* be a assumed functional relation between a measurement vector referred to as prior damage and the damage parameter vector, p, referred to as predictor variables. The measurement vector is the current values of the leading-indicator of failure and the parameter vector includes the prior system state, and accumulated damage and the damage evolution parameters. An initial parameter estimate p0 and a measured vector x are provided and it is desired to find the parameter vector p, that best satisfies the functional relation *f* i.e. minimizes the squared distance or squared-error, $\varepsilon^T\varepsilon$ with $\varepsilon = x - f(p)$. Assume that g(p) = ε in the squared error. The minimizer parameter vector, p, for the error function has been represented as,

$$F(p) = \frac{1}{2}\sum_{i=1}^{m}(g_i(p))^2 = \frac{1}{2}g(p)^t g(p) \qquad (15)$$

$$F`(p) = J(p)^T g(p) \qquad (16)$$

$$F''(p) = J(p)^T g(p) + \sum_{i=1}^{m} g_i(x) g_i''(x) \qquad (17)$$

where F(p) represents the objective function for the squared error term εTε , J(p) is the Jacobian, and F'(p) is the gradient, and F''(p) is the Hessian. The variation of an F-value starting at "p" and with direction "h" is expressed as a Taylor expansion, as follows:

$F(p + \alpha h) = F(p) + \alpha h^T F`(p) + O(\alpha^2)$ (18)

where α is the step-length from point "p" in the descent direction, "h". Mathematically, "h" is the descent direction of F(p) if $h^T F'(p) < 0$. If no such "h" exists, then F'(p)=0, showing that in this case the function is stationary. Since the condition for the stationary value of the objective function is that the gradient is zero, i.e. f '(p + h) = L'(h) = 0. The descent direction can be computed from the equation,

$(J^T J)h_{gn} = -J^T g$ (19)

In each step, Newton method uses α = 1 and $p = p + \alpha h_{gn}$, where subscript 'gn' indicates gauss-newton. The value of α is found by line search principle described above. Levenberg-Marquardt algorithm is a hybrid method which utilizes both steepest descent principle as well as the Gauss-Newton method. When the current solution is far from the correct one, the algorithm behaves like a steepest descent method: slow, but guaranteed to converge. When the current solution is close to the correct solution, it becomes a Gauss-Newton method. The LM method actually solves a slight variation of Equation (??), known as the augmented normal equations

$(J^T J+\mu I)\ h = -J^T g$ (20)

The term μ is called as the damping parameter, μ>0 ensures that coefficient matrix is positive definite, and this ensures that h is a descent direction. When the value of μ is very small, then the step size for LM and Gauss-Newton are identical. Algorithm has been modified to take the

equations of phase growth and inter-metallic growth under both isothermal aging and cycling loads to calculate the unknowns.

4.5 Damage Accrual Relationships

Three sets of test assemblies have been subjected to single stresses of thermal aging at 125°C, thermal cycling from - 40°C to 125°C, and thermal cycling from 0°C to 100°C. Leading indicators of damage have been measured at periodic intervals in each segment of the environment stress.

4.5.1 Thermal Aging at 125°C (TA)

Printed circuit board assemblies with 676 I/O PBGA and 256 I/O CABGA packages were subjected to thermal aging at 125°C and were withdrawn after each 168 hrs increment. The samples were cross-sectioned, polished. Phase growth and intermetallic growth was studied using microscopic images at each time intervals. The image analysis software has been used to measure the average phase size Ag3Sn and Cu6Sn5 phases. The test data for normalized phase growth has been represented by the following equation:

$$S_{Nt} = \left[\left(\frac{g_p}{g_0} \right)^4 - 1 \right] = a_{nt} (t)^{b_{nt}} \qquad (21)$$

where, g is the phase-growth, subscripts p and 0 indicate point “p” and initial time respectively, S_{Nt} is the normalized phase-growth parameter during thermal aging, ant and b_{nt} are the

normalized phase-growth coefficient and phase growth exponent for thermal aging. The data for normalized IMC thickness has been fit to an equation for the following form:

$$K_{Nt} = \left[\frac{y_p}{y_0} - 1 \right] = k_{Nt} t^{nt} \qquad (23)$$

where, y is the intermetallic thickness, subscripts p and 0 indicate point "p" and initial time respectively, k_{Nt} and nt are the normalized intermetallic growth coefficient and intermetallic growth exponent during thermal aging. The following relationship represents the evolution of intermetallic growth in thermal aging based on experimental data. The equation parameters have been derived based on experimental measurements of the intermetallic growth from cross-sections.

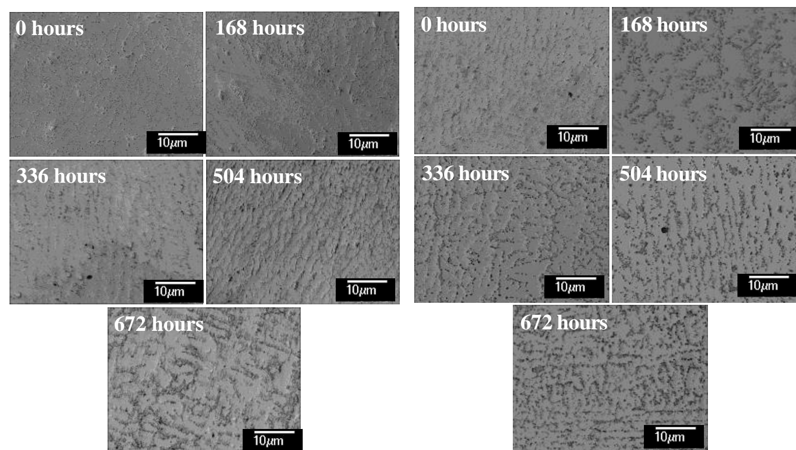

Figure 41: Backscattered image of Phase Growth versus different aging time intervals of thermal aging at 125°C (a) 676 I/O PBGA, magnification 1000x (b) 256 I/O PBGA, magnification 1000x.

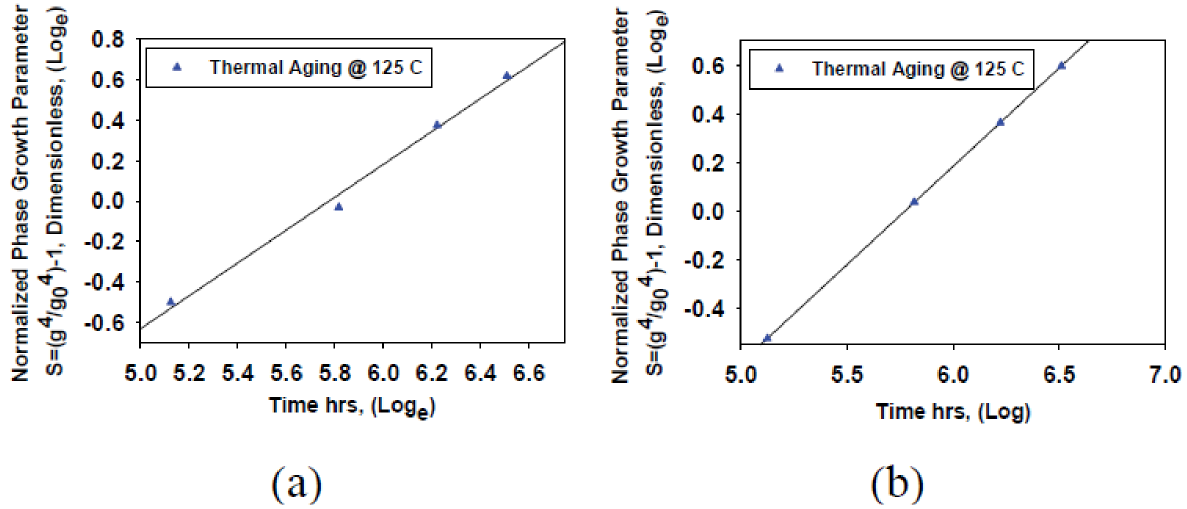

Figure 42: Phase growth parameter under thermal aging at125°C (a) 676 I/O BGA (b) 256 I/O BGA

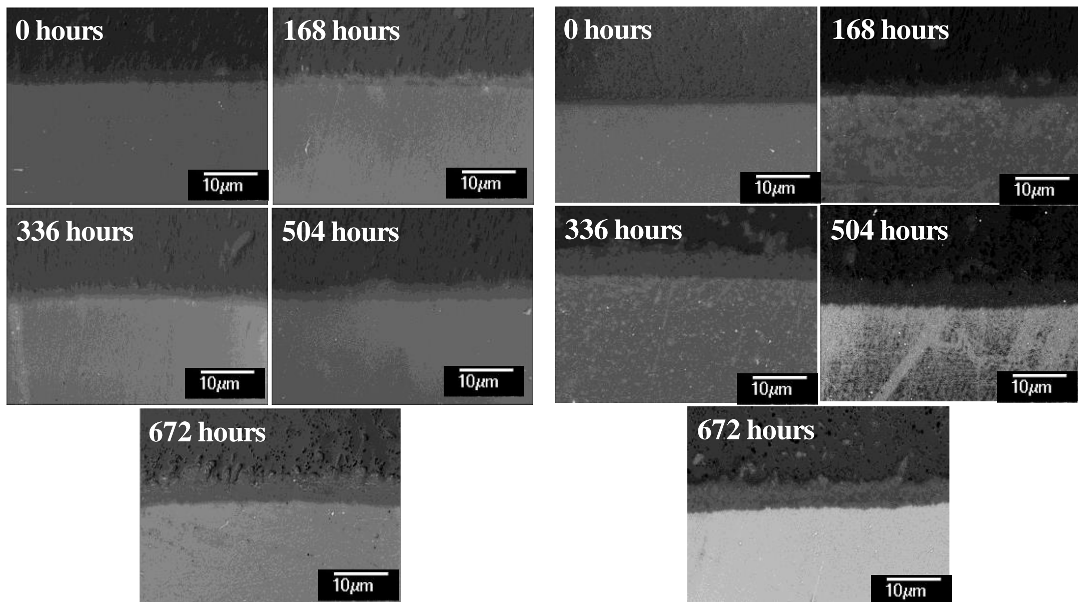

Figure 43: Backscattered image of Intermetallic thickness versus different aging time intervals of thermal aging at 125°C (a) 676 I/O PBGA, magnification 1000x (b) 256 I/O PBGA, magnification 1000x.

Figure 41a, b show the phase growth for the 676 BGA and 256 BGA respectively after various time increments under 125°C thermal aging. Figure 42a, b show the plot of the normalized phase growth parameter versus time in thermal aging for the 676 BGA and 256 BGA respectively. The data has been fit to the equation (10) and the model parameters shown in Table 8. Figure 43a, b show the IMC growth for the 676 BGA and 256 BGA respectively after various time increments under 125°C thermal aging. Figure 44a, b show the plot of the normalized IMC growth parameter versus time in thermal aging for the 676 BGA and 256 BGA respectively. The data has been fit to the equation (11) and the model parameters shown in Table 9.

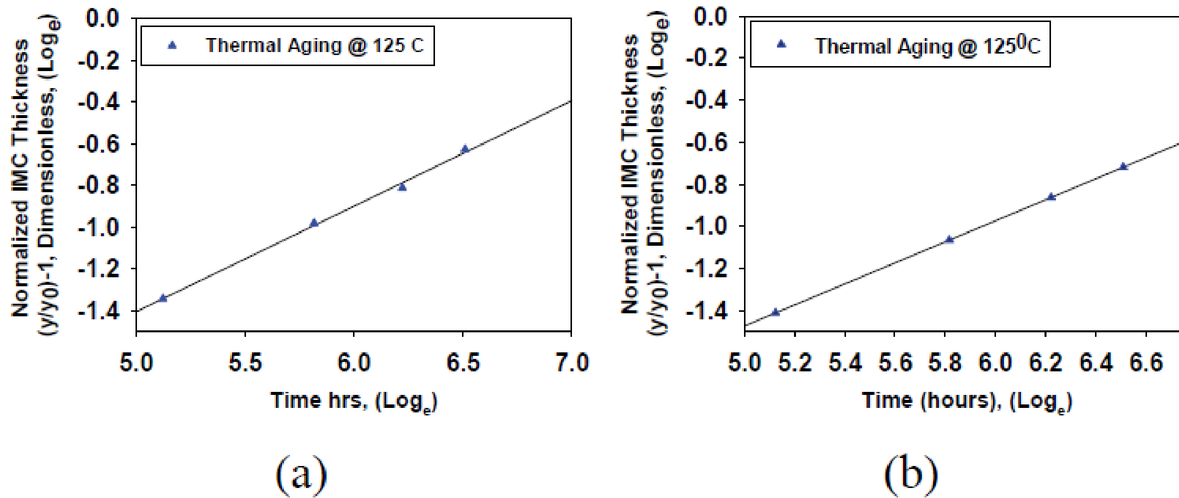

Figure 44: Normalized IMC growth under thermal aging at 125°C (a) 676 I/O BGA (b) 256 I/O BGA

Table 8: Damage accrual relationships using Phase Growth and IMC Growth as leading indicators for 676 BGA and 256 BGA.

	Thermal Aging at 125C	
	Phase Growth	IMC
676 I/O BGA	$S_N = 0.0094(t)^{0.6206}$	$K_N = 0.0195(t)^{0.5}$
256 I/O BGA	$S_N = 0.0094(t)^{0.8085}$	$K_N = 0.0188(t)^{0.5}$

4.5.2 Thermal Cycling -40 to 125C (TC1)

A different set of assemblies were subjected to thermal cycling from -40°C to 125°C and were withdrawn after each 250 cycle increments. The samples were cross-sectioned, polished. Phase growth and intermetallic growth was studied using SEM images at each cyclic intervals. The image analysis software has been used to measure the average phase size. The phase growth test data has been fit to the following equation:

$$S_{N\Delta T} = \left(\frac{g_p}{g_0}\right)^4 - 1 = a_{n\Delta T}(N)^{b_{n\Delta T}} \quad (12)$$

Where g is the phase-growth, subscripts p and 0 indicate point "p" and initial time respectively, SN□T is the normalized phase-growth parameter during thermal cycling, anΔT and bnΔT are the normalized phase-growth coefficient and phase growth exponent during thermal cycling. The IMC growth data has been fit to an equation for the following form:

$$K_{N\Delta T} = \left(\frac{y_p}{y_0} - 1\right) = k_{N\Delta T}(N)^{n\Delta T} \quad (13)$$

Where y is the intermetallic thickness, subscripts p and 0 indicate point “p” and initial time respectively, $kn\Delta T$ and $nn\Delta T$ are the normalized intermetallic growth coefficient and intermetallic growth exponent during thermal cycling. The following relationship represents the evolution of intermetallic growth in thermal cycling based on experimental data.

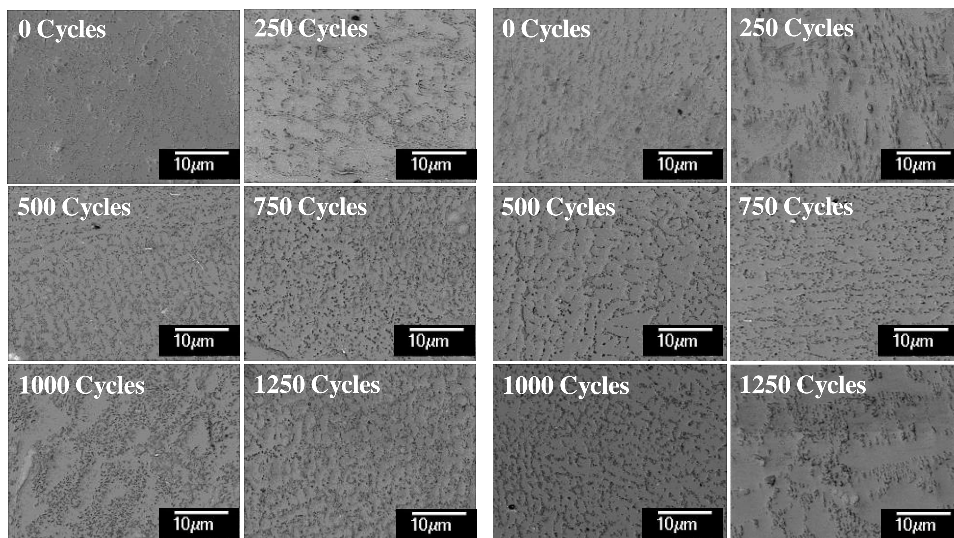

Figure 45: Backscattered image of Phase Growth versus different cycling time intervals after thermal cycling at -40°C to 125°C (a) 676 I/O PBGA, magnification 1000x (b) 256 I/O CABGA, magnification 1000x

Figure 45a, b show the phase growth for the 676 BGA and 256 BGA respectively after various cyclic increments under - 40 to 125°C thermal cycling. Figure 46a, b show the plot of the normalized phase growth parameter versus time in thermal aging for the 676 BGA and 256 BGA respectively. The data has been fit to the equation (12) and the model parameters shown in Table 3.

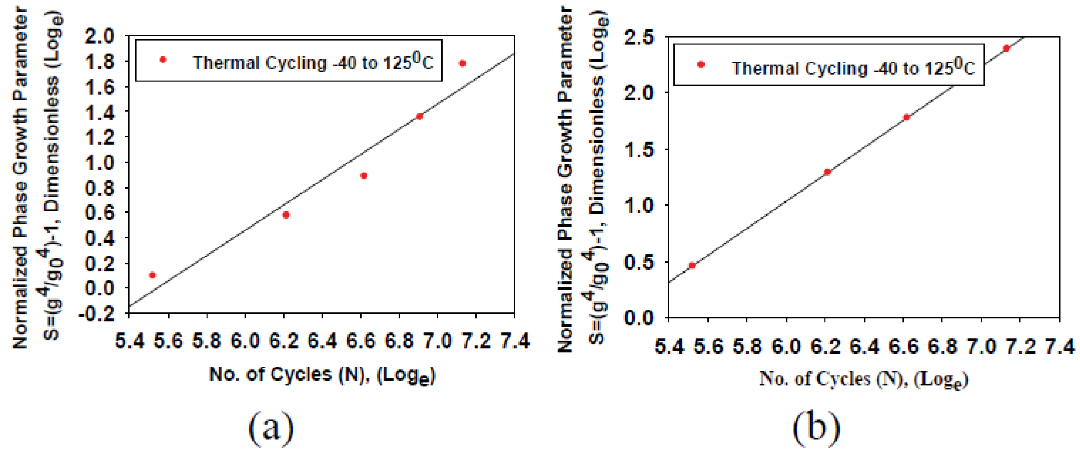

Figure 46: Phase growth parameter under thermal cycling at - 40°C to 125°C (a) 676 I/O BGA (b) 256 I/O BGA

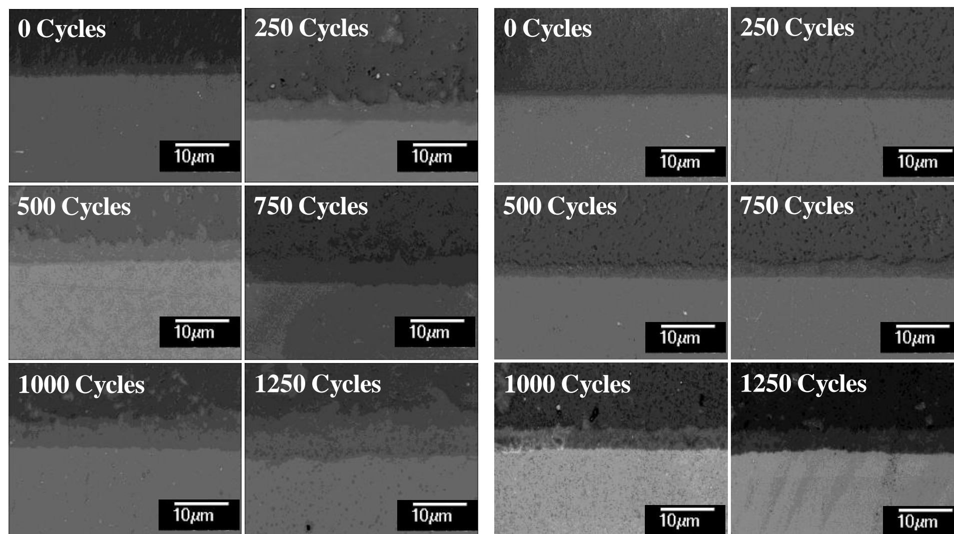

Figure 47: Backscattered image of Intermetallic thickness versus different cycling time intervals after thermal cycling at -40°C to 125°C (a) 676 I/O PBGA, magnification 1000x (b) 256 I/O CABGA, magnification 1000x

Figure 47a, b show the IMC growth for the 676 BGA and 256 BGA respectively after various cyclic increments under -40 to 125°C thermal cycling. Figure 48a, b show the plot of the normalized IMC growth parameter versus time in thermal aging for the 676 BGA and 256 BGA respectively. The data has been fit to the equation (13) and the model parameters shown in Table 9.

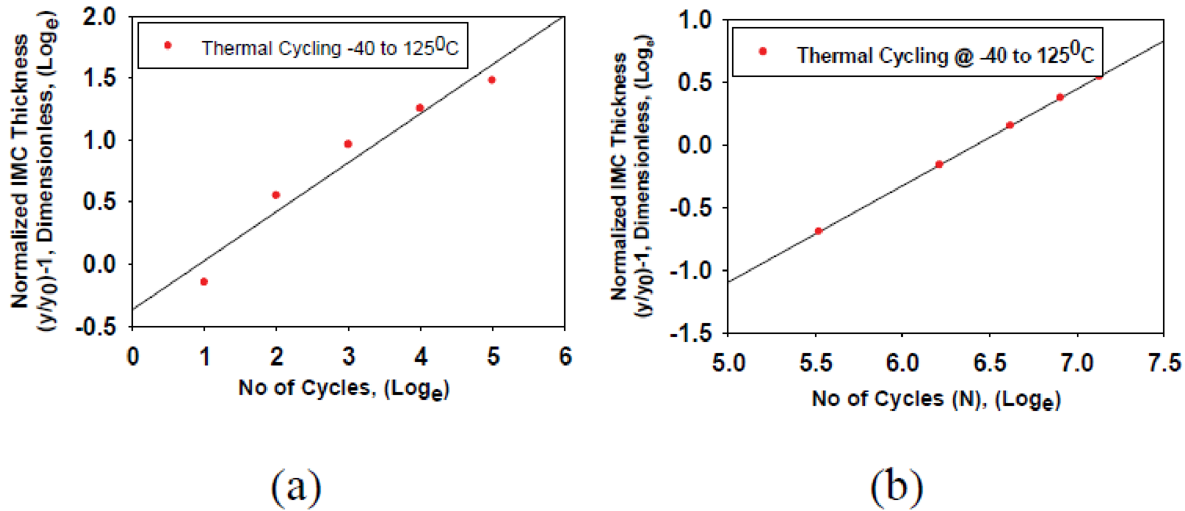

Figure 48: IMC growth under thermal cycling at -40°C to 125°C (a) 676 I/O BGA (b) 256 I/O BGA

Table 9: Damage accrual relationships using phase growth and IMC growth as leading indicators for the 676 BGA and the 256 BGA.

	Thermal Cycling -40 to 125C	
	Phase Growth	IMC
676 I/O BGA	$S_N = 0.0039(N)^{1.0027}$	$K_N = 0.0108(N)^{0.81}$
256 I/O BGA	$S_N = 0.0021(N)^{1.2}$	$K_N = 0.0071(N)^{0.77}$

4.5.3 Thermal Cycling 0 to 100C (TC2)

A different set of assemblies were subjected to thermal cycling from 0°C to 100°C and were withdrawn after each 250 cycle increments. The samples were cross-sectioned, polished. Phase growth and intermetallic growth was studied using SEM images at each cyclic intervals. The image analysis software has been used to measure the average phase size. The phase growth test data has been fit to the following equation:

$$S_{N\Delta T} = \left(\frac{g_p}{g_0} \right)^4 - 1 = a_{n\Delta T} (N)^{b_{n\Delta T}} \quad (14)$$

Where g is the phase-growth, subscripts p and 0 indicate point "p" and initial time respectively, $S_{N\Delta T}$ is the normalized phase-growth parameter during thermal cycling, $a_{n\Delta T}$ and $b_{n\Delta T}$ are the normalized phase-growth coefficient and phase growth exponent during thermal cycling. The IMC growth data has been fit to an equation for the following form:

$$K_{N\Delta T} = \left(\frac{y_p}{y_0} - 1 \right) = k_{N\Delta T} (N)^{n\Delta T} \quad (15)$$

Where y is the intermetallic thickness, subscripts p and 0 indicate point "p" and initial time respectively, knΔT and nnΔT are the normalized intermetallic growth coefficient and intermetallic growth exponent during thermal cycling. The following relationship represents the evolution of intermetallic growth in thermal cycling based on experimental data.

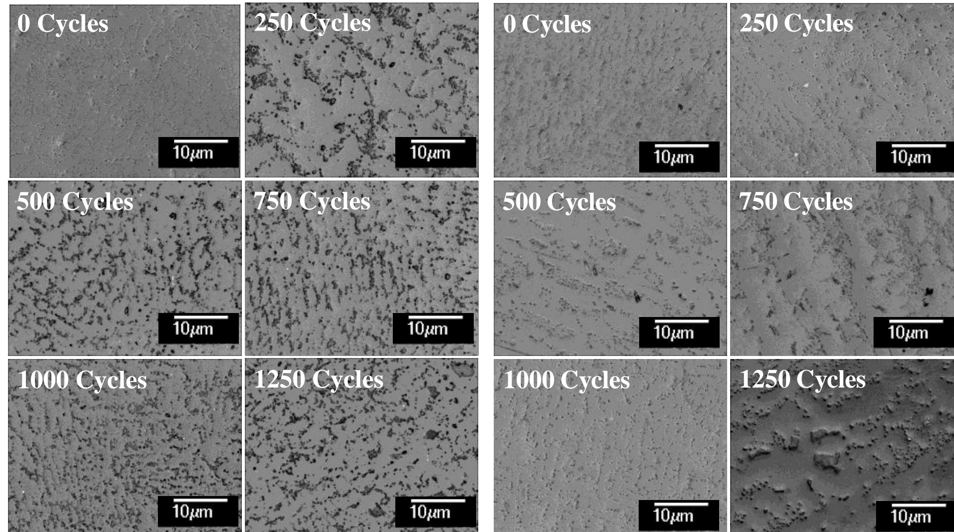

Figure 49: Backscattered image of Phase Growth versus different cycling time intervals of thermal cycling at 0°C to 100°C (a) 676 I/O PBGA, magnification 1000x (b) 256 I/O PBGA, magnification 1000x

Figure 49 a, b shows the phase growth for the 676 BGA and 256 BGA respectively after various cyclic increments under 0 to 100°C thermal cycling. Figure 50 a, b shows the plot of the normalized phase growth parameter versus time in thermal aging for the 676 BGA and 256 BGA respectively. The data has been fit to the equation (12) and the model parameters shown in Table 10.

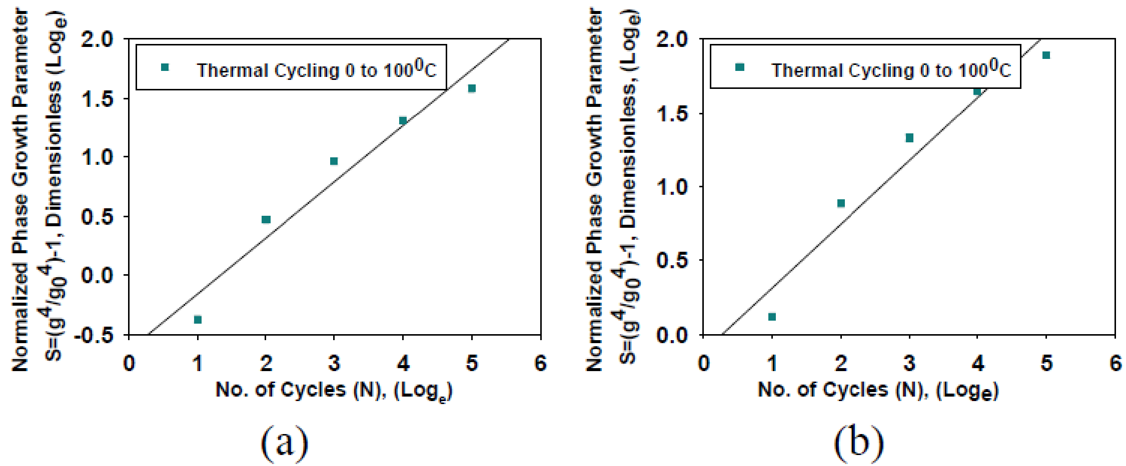

Figure 50: Phase growth parameter under thermal cycling from 0°C to 100°C (a) 676 I/O BGA (b) 256 I/O BGA

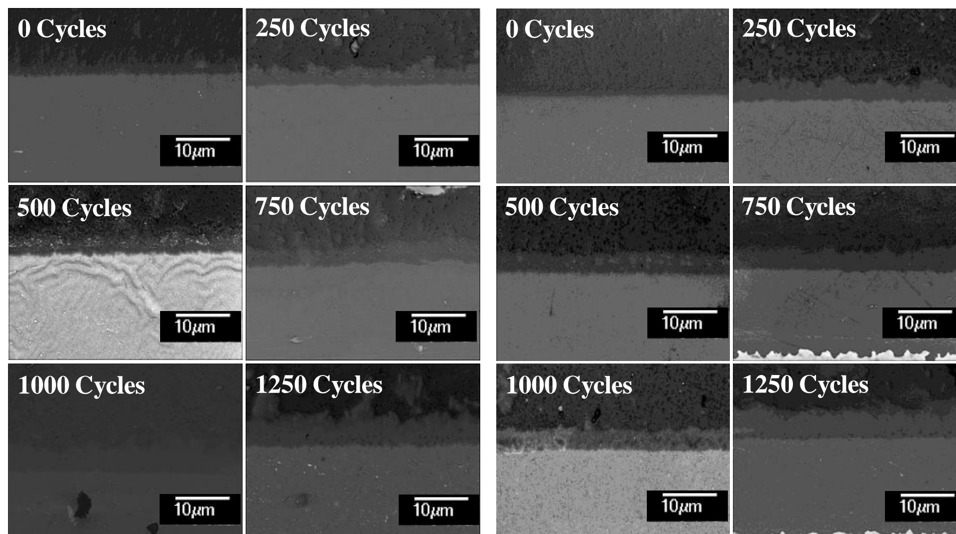

Figure 51: Backscattered image of Intermetallic thickness versus different cycling time intervals of thermal cycling at - 0°C to 100°C (a) 676 I/O PBGA, magnification 1000x (b) 256 I/O PBGA, magnification 1000x.

Figure 51a, b show the IMC growth for the 676 BGA and 256 BGA respectively after various cyclic increments under 0 to 100°C thermal cycling. Figure 52a, b show the plot of the normalized IMC growth parameter versus time in thermal aging for the 676 BGA and 256 BGA respectively. The data has been fit to the equation (13) and the model parameters shown in Table 10.

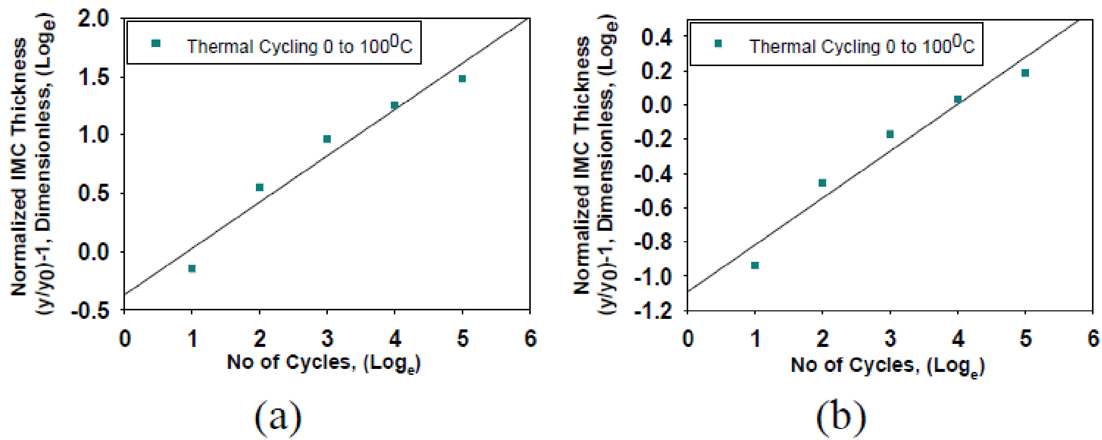

Figure 52: IMC growth under thermal cycling from 0°C to 100°C (a) 676 I/O BGA (b) 256 I/O BGA

Table 10: Damage Equivalency Relationships using Phase Growth and IMC Growth as Leading Indicators for the 676 BGA and the 256 BGA.

	TC2 (0 to 100C)	
	Phase Growth	IMC
676 I/O BGA	$S_N = 0.00085(N_{TC2})^{1.2134}$	$K_N = 0.00322(N_{TC2})^{1.0125}$
256 I/O BGA	$S_N = 0.00267(N_{TC2})^{1.12}$	$K_N = 0.0082(N_{TC2})^{0.70}$

4.6 Damage Equivalency Relationships between Thermal Aging @ 125°C and Thermal-Cycling @ -40°C to 125°C

Figure 53 shows the combined plot normalized Phase growth versus time and cycles on x-axis for PBGA-676. Damage accrued from aging and cycling environments has been equivalenced based on two damage proxies including normalized intermetallic thickness and normalized phase growth. The evolution of normalized phase growth has been plotted versus thermal cycles in -40°C to 125°C and thermal aging time at 125°C (Figure 53).

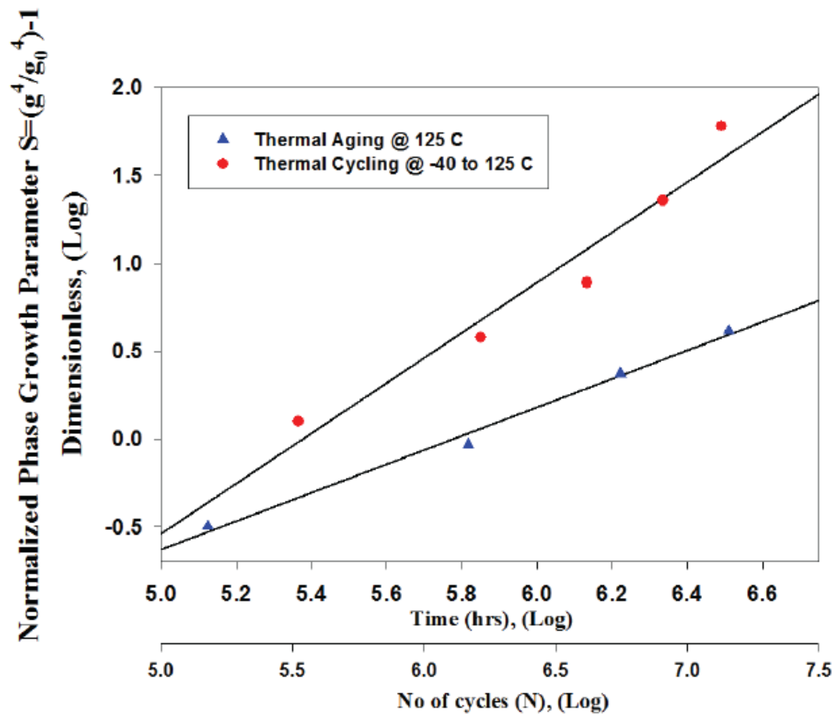

Figure 53: Combined plot Normalized Phase growth versus thermal aging time/thermal cycling for 676 PBGA.

A similar value of damage proxy can be obtained by exposure to single stresses of thermal aging and thermal cycling. The exposure length to the environmental stresses however, will be

different in each case. This combined plot is helpful for mapping of damage from thermal aging onto thermal cycling.

Intermetallic thickness can be obtained by exposure to single stresses of thermal aging and thermal cycling. The exposure length to the environmental stresses however, will be different in each case.

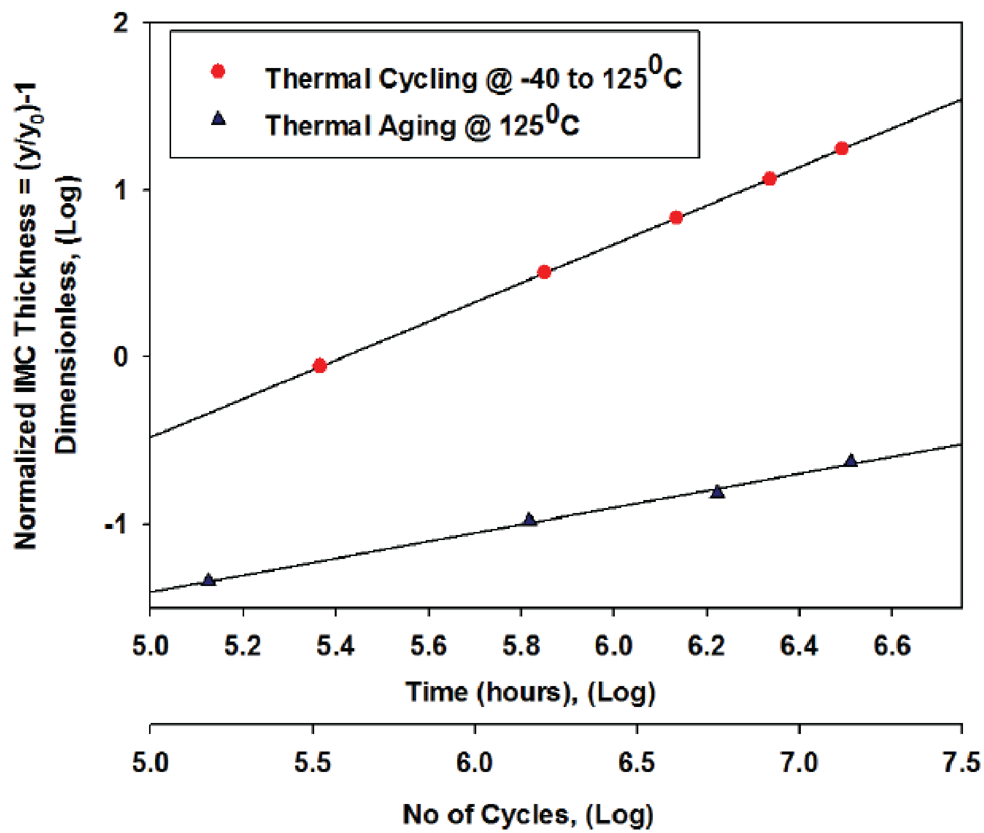

Figure 54: Combined plot for 676 PBGA of Normalized IMC thickness versus thermal aging time/thermal cycling.

Table 11: Damage equivalency between TA @ 125C and TC1 @ -40C to 125C for the 676 I/O BGA.

	Damage Equivalency	Damage Equivalency
	Phase Growth	IMC
676 I/O BGA	$0.0094(t)^{0.6206} = 0.0039(N)^{1.0027}$ $N = 2.41(t)^{0.62}$	$0.0108(N)^{0.81} = 0.0195(t)^{0.5}$ $N = 2.07(N)^{0.617}$

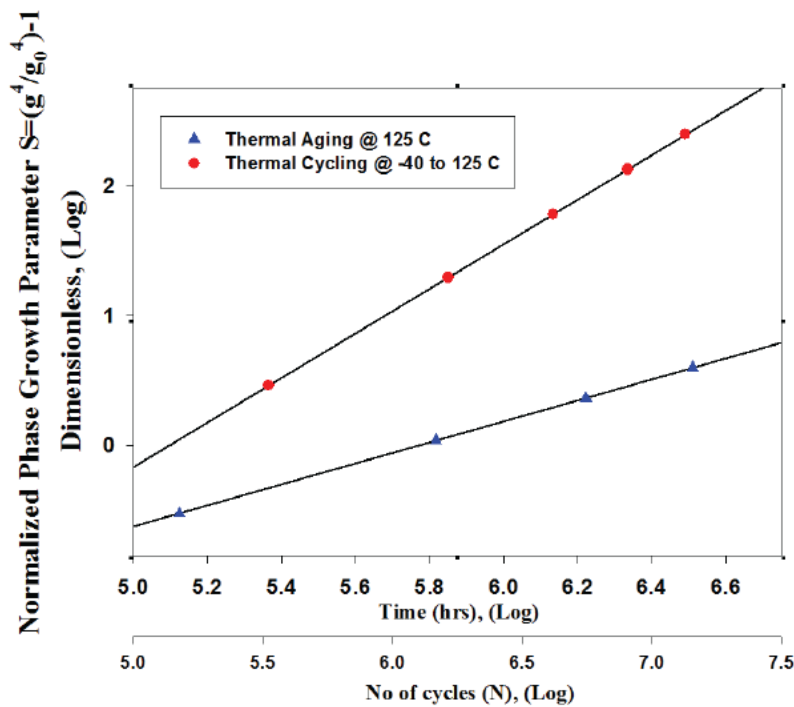

Figure 55: Combined plot Normalized Phase growth versus thermal aging time/thermal cycling for 256 CABGA.

Damage equivalency relationships between thermal aging at 125C and thermal cycling at -40C to 125C is shown in Table 11. Similar damage-mapping relationships have been obtained for both the damage proxies measured in the experiments confirming the validity of the correlation.

Figure 56 shows the combined plot of normalized phase growth versus time and cycles on x-axis for 256 CABGA. This combined plot is helpful for mapping of damage from thermal aging onto thermal cycling. The evolution of normalized intermetallic growth has been plotted versus thermal cycles in -40°C to 125°C and thermal aging time at 125°C (Figure 56).

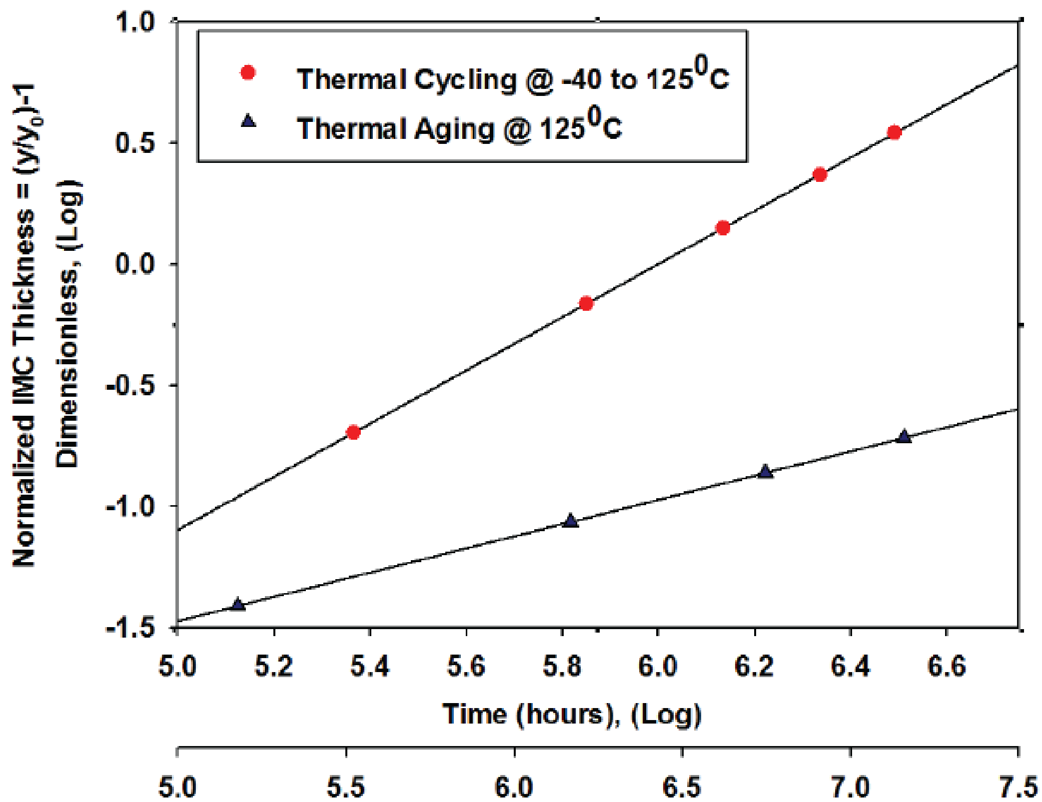

Figure 56: Combined plot for 256 CABGA of Normalized IMC thickness versus thermal aging time/thermal cycling

Table 12: Damage equivalency between TA @ 125C and TC1 @ -40C to 125C for the 676 I/O BGA.

	Damage Equivalency	Damage Equivalency
	Phase Growth	IMC
256 I/O BGA	$0.0094(t)^{0.8085} = 0.0021(N)^{1.2}$ $N = 3.48(t)^{0.673}$	$0.0071(N)^{0.77} = 0.0188(t)^{0.5}$ $N = 3.54(t)^{0.65}$

Comparison of the damage equivalency relationships for the CABGA-256 between thermal aging at 125°C and thermal cycling from -40 to 125°C, as shown Table 12, developed based on the phase-growth parameter shows that both equations have similar coefficients and exponents. The convergence of the damage equivalency parameters from two separate damage proxies shows the validity of the correlation.

Since the plastic work accrued by the 676 BGA and 256 BGA will be different, given the different size of the packages, different damage mapping relationships have been obtained for the two packages as shown in Table 11 and Table 12. Table 13 shows the effect of exposure to 168 hours of thermal aging at 125°C on the thermal cycling under -40°C to 125°C.

Table 13: Effect of exposure to 168 hours of thermal aging at 125C on the thermal cycling life under -40 to 125C.

Package Type	Aging Time hrs	Reduction in Life using Phase Growth as Damage Proxy (cycles)	Reduction in Life using IMC as Damage Proxy (cycles)
676 PBGA	168	58 cycles	49 cycles
		$N = 2.41(t)^{0.62}$	$N = 2.07(t)^{0.617}$
256 CABGA		110	99 cycles
		$N = 3.48(t)^{0.673}$	$N = 3.54(t)^{0.65}$

4.7 Damage Equivalency Relationships for Thermal-Cycling: TC1 (-40°C to 125°C) and TC2 (0°C to 100°C)

Figure 56 shows the combined plot of normalized phase growth parameter versus cycles on x-axis for PBGA-676 under -40°C to 125°C and 0°C to 100°C cycling. Damage accrued from the two different thermal cycling environments has been equivalenced based on two damage proxies including normalized intermetallic thickness and normalized phase growth. The evolution of normalized phase growth has been plotted versus thermal cycles in -40°C to 125°C and thermal cycles in 0°C to 100°C (Figure 56). A similar value of damage proxy can be obtained by exposure to single stresses of thermal aging and thermal cycling. The exposure length to the environmental stresses however, will be different in each case, which us shown by the horizontal spacing between the two plots in Figure 56. This combined plot is helpful for mapping of damage from thermal aging onto thermal cycling.

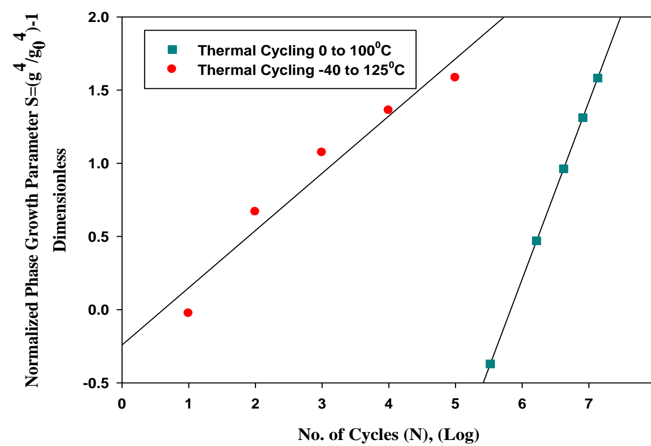

Figure 56: Combined plot Normalized Phase growth versus - 40°C to 125°C and thermal cycles in 0°C to 100°C for 676 PBGA.

Figure 57 shows the IMC growth versus the number of cycles in -40°C to 125°C and 0°C to 100°C cycling for the 676 BGA. Similar values of intermetallic thickness can be obtained by exposure to single stresses of -40°C to 125°C and 0°C to 100°C cycling. The exposure length to the environmental stresses however, will be different in each case.

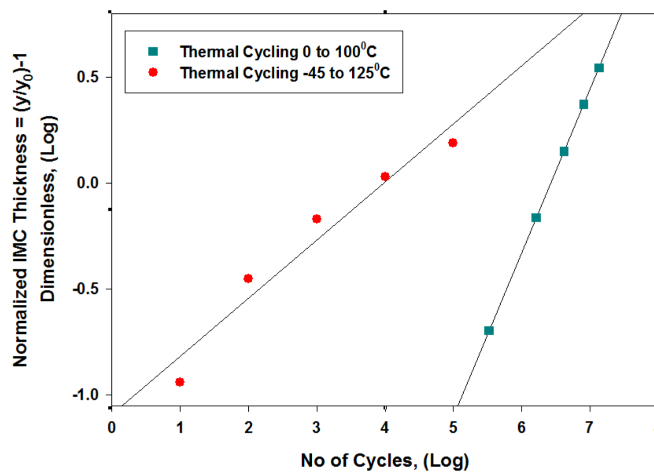

Figure 57: Combined plot for 676 PBGA of Normalized IMC thickness versus TC-1 and TC 2.

Table 14: Damage equivalency between TC1 @ -40C to 125C and TC2 @ 0C to 100C for the 676 I/O BGA.

	Damage Equivalency	Damage Equivalency
	Phase Growth	IMC
676 I/O BGA	$N_{TC2} = 3.5(N)^{0.826}$	$N_{TC2} = 3.32(N)^{0.8}$

Figure 58 shows the combined plot normalized Phase growth versus thermal cycles in -40°C to 125°C and thermal cycles in 0°C to 100°C for 256 CABGA. Figure 59 shows the IMC growth versus the number of cycles in -40°C to 125°C and 0°C to 100°C cycling for the 676 BGA. Similar values of phase growth parameter and intermetallic thickness can be obtained by

exposure to single stresses of -40°C to 125°C and 0°C to 100°C cycling. The exposure length to the environmental stresses however, will be different in each case.

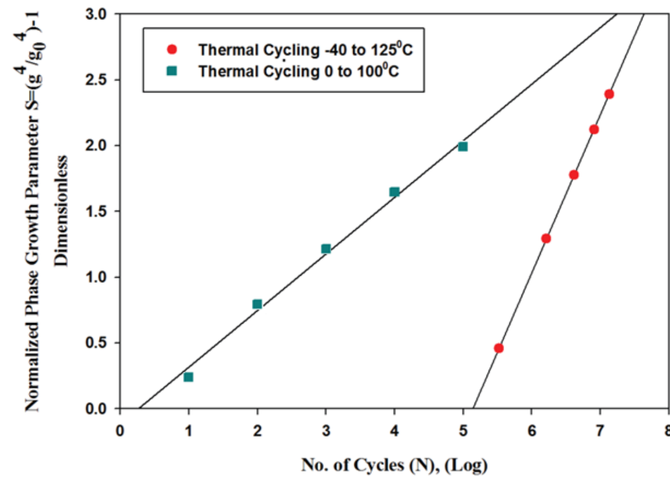

Figure 58: Combined plot Normalized Phase growth versus - 40°C to 125°C and thermal cycles in 0°C to 100°C for 256 CABGA.

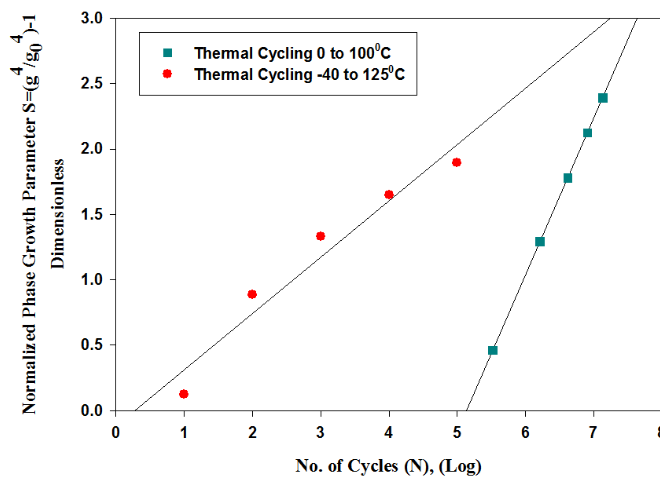

Figure 59: Combined plot for 256 CABGA of Normalized IMC thickness -40°C to 125°C and thermal cycles in 0°C to 100°C

Comparison of the damage equivalency relationships for both PBGA-676 (Table 14) and CABGA-256 (Table 14) between thermal cycling in -40°C to 125°C and thermal cycles in 0°C to 100°C, as shown in above tables, developed based on the phase-growth parameter shows that both equations have similar coefficients and exponents. The convergence of the damage equivalency parameters from two separate damage proxies shows the validity of the correlation.

Table 14: Damage equivalency between TC1 @ -40C to 125C and TC2 @ 0C to 100C for the 256 I/O BGA.

	Damage Equivalency	Damage Equivalency
	Phase Growth	IMC
256 I/O BGA	$N_{TC2} = 0.8(N)^{1.072}$	$N_{TC2} = 0.81(N)^{1.1}$

4.8 Assessment of Differential damage and Residual Life after withdrawn from TA1 + TC1 and Redeployment in TC2

Test assemblies have been previously exposed to 168 hours of aging at 125°C, followed by 250 cycles in -40°C to 125°C (TC1) and then redeployed in thermal cycling environment of 0 to 100°C (TC2). The problem statement is to find the previous consumed life and the remaining useful life in TC2. In order to prognosticate the prior accrued damage and the remaining useful life, the parts have been withdrawn at periodic intervals of 250 cycles to measure the phase growth and intermetallic growth in the TC2 deployed samples. The withdrawn samples have been cross-sectioned. The phase growth and intermetallic thickness has been studied under confocal microscope (Figure 60). The samples were prognosticated using the Levenberg-Marquardt Algorithm.

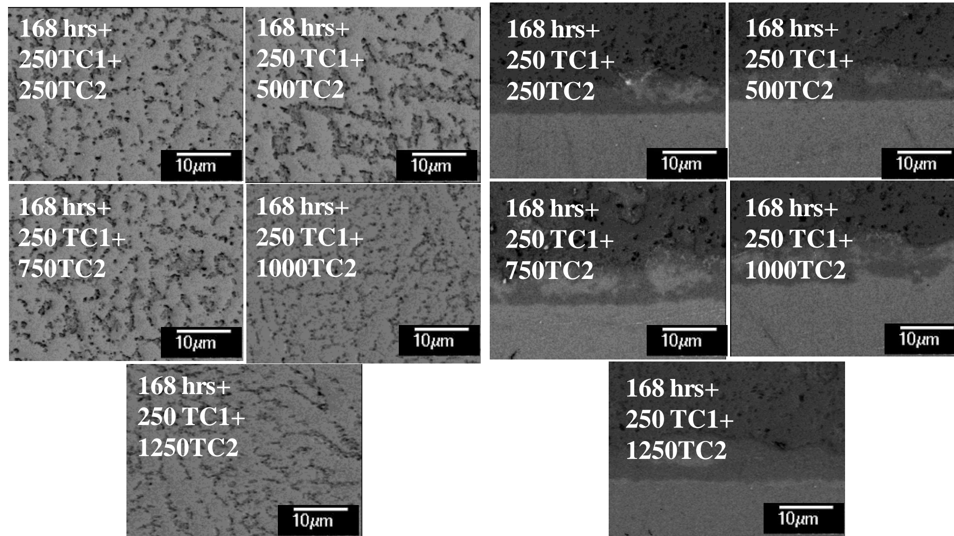

Figure 60: Back-scattered Images for samples exposed to Multiple Environments of 168 hours @ 125OC + 250 Cycles TC-1 + x-Cycles TC-2, 676 I/O PBGA, magnification 1000x (a) Phase Growth (b) IMC growth.

Figure 61 shows the prognosticated values of accrued damage in 676 BGA assemblies after they have been subjected to (a) 168 hours of thermal aging + 250 Cycles of thermal cycling in TC1 (-40°C to 125°C) + 250 cycles of thermal cycling in TC2 (0°C to 100°C) (b) 168 hours of thermal aging + 250 Cycles of thermal cycling in TC1 (-40°C to 125°C) + 500 cycles of thermal cycling in TC2 (0°C to 100°C). The accrued damage has been prognosticated using both phase growth parameter and the intermetallic growth. The prognosticated TC2 cycles for the 168h+250TC1+250TC2 case using phase growth and IMC growth are 696 cycles and 607 cycles respectively. The prognosticated TC2 cycles for the 168h+250TC1+500TC2 case using phase growth and IMC growth are 976 cycles and 835 cycles respectively.

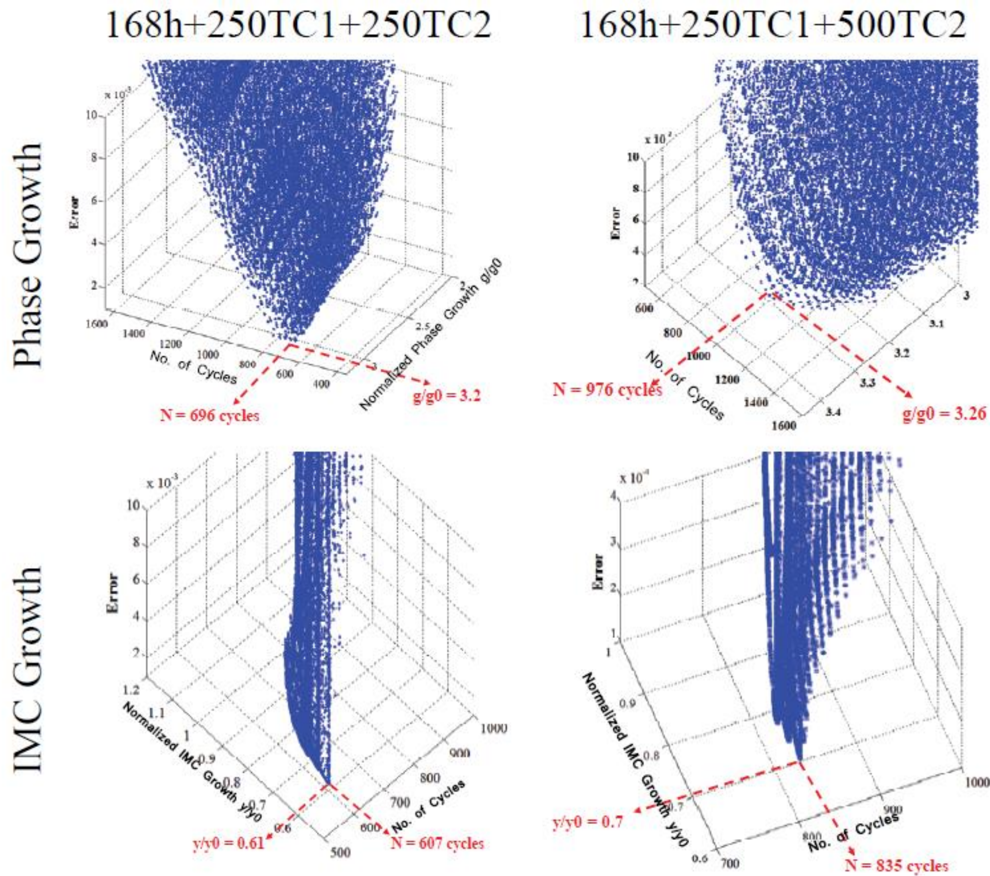

Figure 61: 3D plot of error versus Number of Cycles, Life computed from LM-algorithm for 168hrs TA + 250 cycles TC1 + 250 cycles TC2 and 168hrs TA + 250 cycles in TC1 + 500 cycles in TC2 for 676 PBGA.

A similar process is followed for the 256 BGA. The 256 BGA test assemblies have been exposed to 168 hours of aging at 125°C, followed by 250 cycles in -40°C to 125°C (TC1) and then redeployed in thermal cycling environment of 0 to 100°C (TC2). The problem statement is to find the previous consumed life and the remaining useful life in TC2. In order to prognosticate the prior accrued damage and the remaining useful life, the parts have been withdrawn at

periodic intervals of 250 cycles to measure the phase growth and intermetallic growth in the TC2 deployed samples. The withdrawn samples have been cross-sectioned. The phase growth and intermetallic thickness has been studied under confocal microscope (Figure 62). The samples were prognosticated using the Levenberg-Marquardt Algorithm.

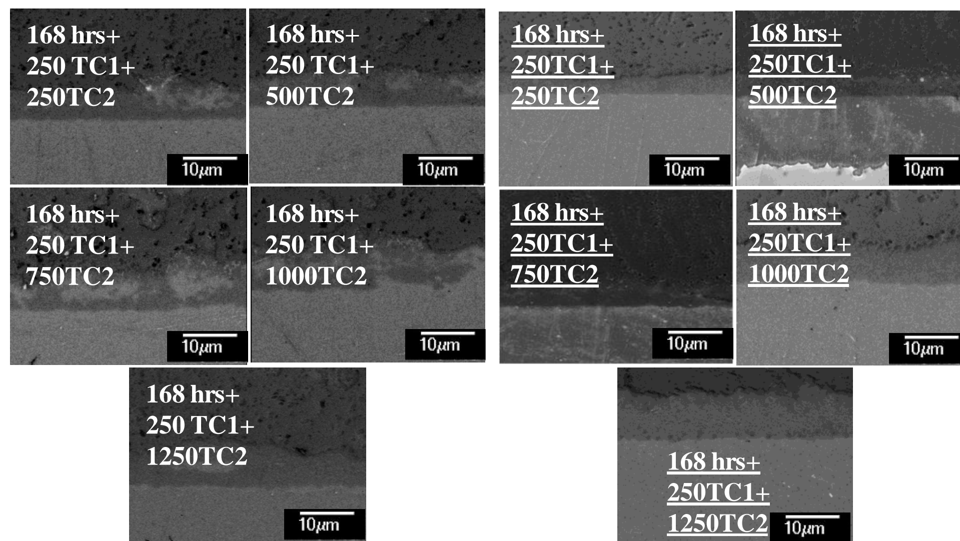

Figure 62: Back-scattered Images for samples exposed to Multiple Environments of 168 hours @ 125OC + 250 Cycles TC-1 + x-Cycles TC-2, 256 I/O PBGA, magnification 1000x (a) Phase Growth (b) IMC growth.

Figure 63 shows the prognosticated values of accrued damage in 256 BGA assemblies after they have been subjected to (a) 168 hours of thermal aging + 250 Cycles of thermal cycling in TC1 (-40°C to 125°C) + 250 cycles of thermal cycling in TC2 (0°C to 100°C) (b) 168 hours of thermal aging + 250 Cycles of thermal cycling in TC1 (-40°C to 125°C) + 500 cycles of thermal cycling in TC2 (0°C to 100°C). The accrued damage has been prognosticated using both phase growth parameter and the intermetallic growth. The prognosticated TC2 cycles for the

168h+250TC1+250TC2 case using phase growth and IMC growth are 782 cycles and 760 cycles respectively. The prognosticated TC2 cycles for the 168h+250TC1+500TC2 case using phase growth and IMC growth are 1051 cycles and 1034 cycles respectively.

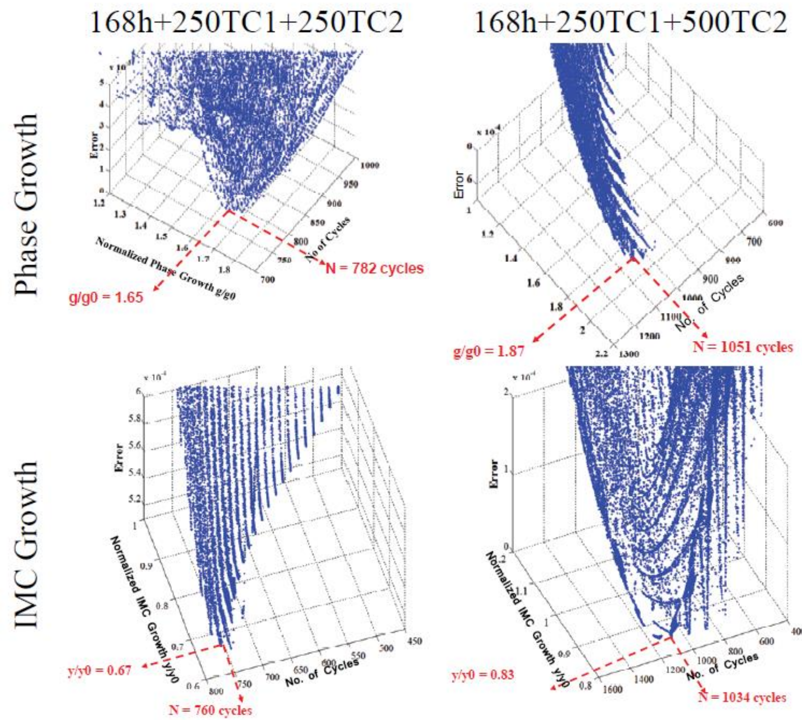

Figure 63: 3D plot of error versus Number of Cycles, Life computed from LM-algorithm for 168hrs TA + 250 cycles TC1 + 250 cycles TC2 and 168hrs TA + 250 cycles in TC1 + 500 cycles in TC2 for 256 PBGA.

4.9 Residual Life in Multiple Environments

The residual life of the assemblies subjected to multiple thermal environments has been be computed based on the following equation,

$RUL = N_{63.2\%} - N$ (16)

Where, N63.2% is the time to 63.2-percent failure of the population or the characteristic life, N is the prognosticated prior damage in the test assemblies. The N63.2% may be procured by accelerated testing of the part and correlation with the field conditions. In the present case, the test assemblies were subjected to Thermal Aging + TC-1 and TC- 2. The N63.2% value for 676-PBGA and 256-CABGA packages subjected to TC-2 (0ºC to 100ºC) was measured to be 6535 cycles (Figure 64) and 5336 cycles (Figure 65) respectively. The prior accrued damage in test assemblies subjected to 168 hours of thermal aging at 125C (TA) and 250 cycles of thermal cycling from -40C to 125C (TC1) was prognosticated to be equivalent to 348 cycles of TC1 (Table 11). The equivalent number of cycles required to accrue the same amount of damage in TC2 was calculated to be 440 cycles, using the previously developed damage mapping relationship:

$$N_{TC2} = 3.5\left[\left(N_{TC1}\right)_{eq}\right]^{0.826}$$

Test assemblies which had been subjected to 168 hours of thermal aging at 125C (TA), followed by 250 cycles of thermal cycling from -40C to 125C (TC1), followed by 250 cycles of thermal cycling from 0C to 100C (TC2) were next prognosticated for prior accrued damage.

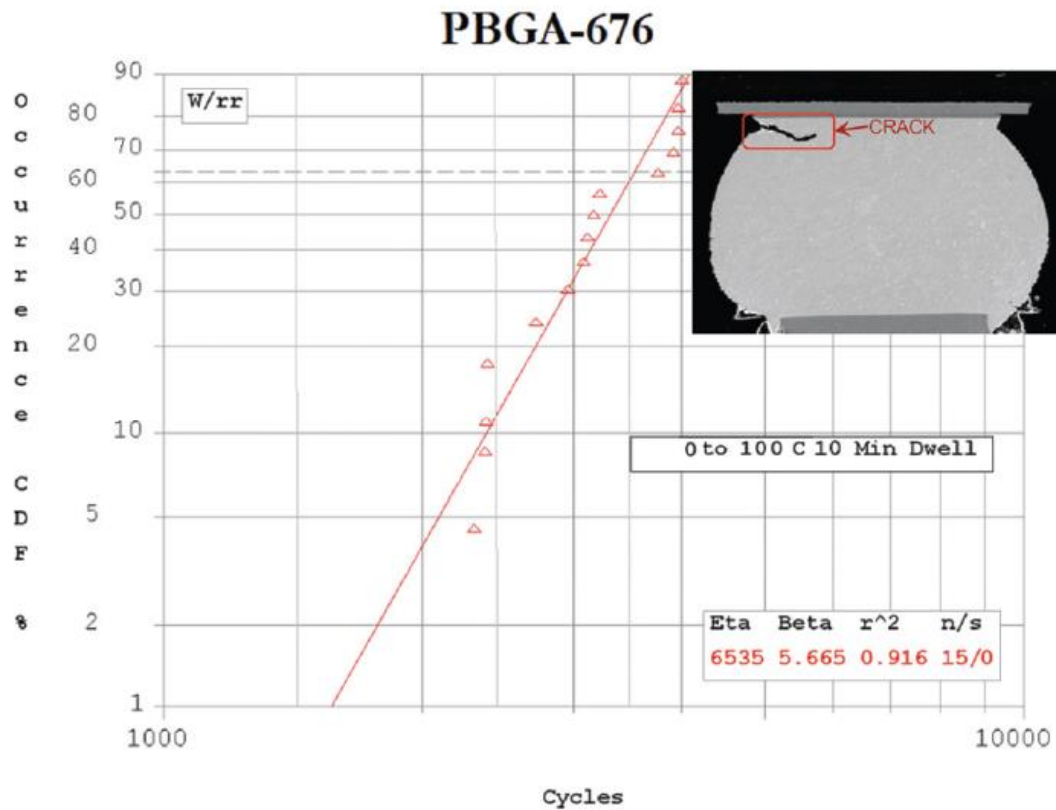

Figure 64: Weibull plot for 676-PBGA packages subjected to thermal cycle 0ºC to 100ºC.

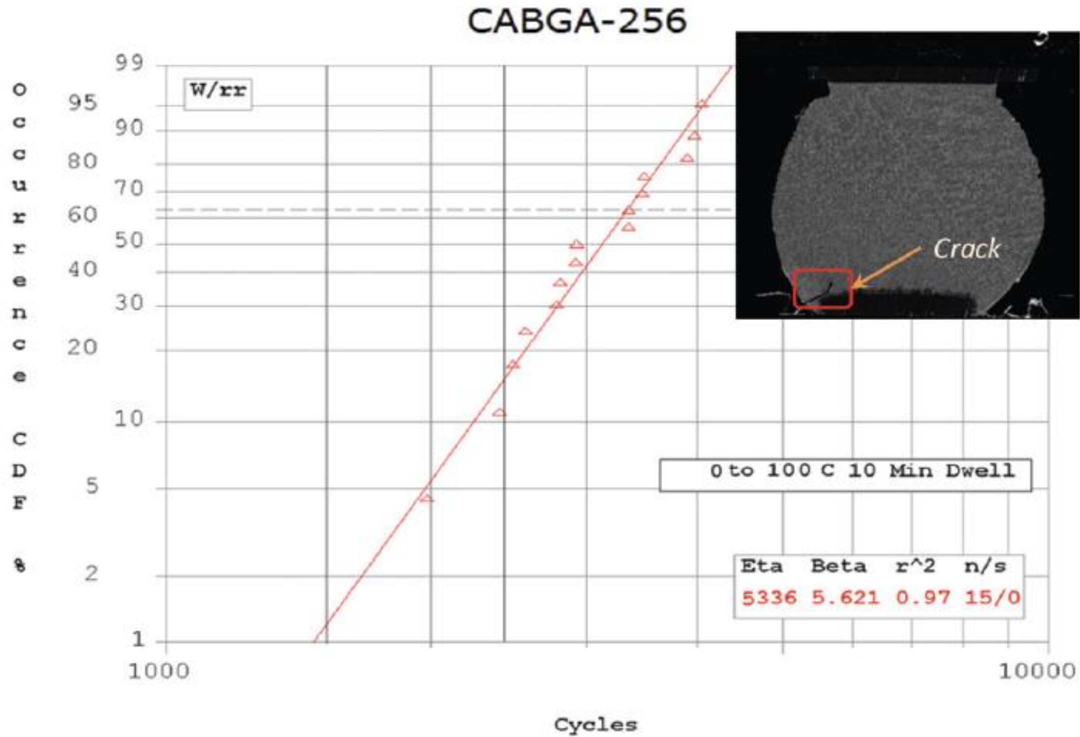

Figure 65: Weibull plot for 256-CABGA packages subjected to thermal cycle 0ºC to 100ºC

For the 676 BGA package, using phase growth parameter as the damage proxy, the prior accrued damage was calculated to be 696 TC2 cycles. It is known that the difference in the prognosticated damage between the test assemblies which have been subjected to (a) 168 hours TA + 250 Cycles TC1 and (b) 168 hours TA + 250 Cycles TC1 + 250 Cycles TC2 is 250 cycles of TC2. The actual value of 250 TC2 cycles correlates well with the prognosticated value of 256 TC2 cycles. Further, additional 676 BGA assembles have been subjected to 168 hours of thermal aging at 125C (TA), followed by 250 cycles of thermal cycling from -40C to 125C (TC1), followed by 500 cycles of thermal cycling from 0C to 100C (TC2). The prognosticated value of accrued damage in the assemblies is 976 TC2 cycles. It is known that the difference in the

prognosticated damage between the test assemblies which have been subjected to (a) 168 hours TA + 250 Cycles TC1 + 250 Cycles TC2 and (b) 168 hours TA + 250 Cycles TC1 + 500 Cycles TC2 is 250 cycles of TC2. The actual value of 250 TC2 cycles correlates well with the prognosticated value of 280 TC2 cycles. The remaining useful life can be calculated using equation (16) to be RUL = 6535-976 = 5559 cycles.

Table 15: RUL for 676 BGA after 168 hours TA + 250 Cycles TC1 + 250 Cycles TC2 using phase-growth and IMC growth as damage proxies.

	676 BGA Phase Growth	676 BGA IMC Growth
168 TA+250 TC1	348	331
(Units of TC1 Cycles), (A)		
168 TA+250 TC1 (Units of TC2 Cycles), (B) Phase: $N_{TC2} = 3.5\left[(N_{TC1})_{eq}\right]^{0.826}$ IMC: $N_{TC2} = 3.32(N)^{0.8}$	440	345
168 TA+250 TC1+250 TC2 (C)	696	607
(Prognostication of TC2 Cycles)		
(D) = (C) - (B)	256	262
(Units of TC2 Cycles)		
168 TA+250 TC1+500TC2 (E)	976	835
(Prognostication of TC2 Cycles)		
(F) = (E)-(C)	280	228
N63.2%	6535	6535
RUL=		
N63.2%-D	5559	5700

A similar process has been followed using the IMC growth damage proxy for the 676 BGA package. The prior accrued damage in test assemblies subjected to 168 hours of thermal aging at

125C (TA) and 250 cycles of thermal cycling from -40C to 125C (TC1) was prognosticated to be equivalent to 331 cycles of TC1 (Table 15). The equivalent number of cycles required to accrue the same amount of damage in TC2 was calculated to be 345 cycles, using the previously developed damage mapping relationship:

$$N_{TC2} = 3.32(N)^{0.8}$$

Test assemblies which had been subjected to 168 hours of vthermal aging at 125C (TA), followed by 250 cycles of thermal cycling from -40C to 125C (TC1), followed by 250 cycles of thermal cycling from 0C to 100C (TC2) were next prognosticated for prior accrued damage. For the 676 BGA package, using IMC growth parameter as the damage proxy,

the prior accrued damage was calculated to be 607 TC2 cycles. It is known that the difference in the prognosticated damage between the test assemblies which have been subjected to (a) 168 hours TA + 250 Cycles TC1 and (b) 168 hours TA + 250 Cycles TC1 + 250 Cycles TC2 is 250 cycles of TC2. The actual value of 250 TC2 cycles correlates well with the prognosticated value of 262 TC2 cycles. Further, additional 676 BGA assembles have been subjected to 168 hours of thermal aging at 125C (TA), followed by 250 cycles of thermal cycling from -40C to 125C (TC1), followed by 500 cycles of thermal cycling from 0C to 100C (TC2). The prognosticated value of accrued damage in the assemblies is 835 TC2 cycles. It is known that the difference in the prognosticated damage between the test assemblies which have been subjected to (a) 168 hours TA + 250 Cycles TC1 + 250 Cycles TC2 and (b) 168 hours TA + 250 Cycles TC1 + 500 Cycles TC2 is 250 cycles of TC2. The actual value of 250 TC2 cycles correlates well with the prognosticated value of 228 TC2 cycles. The remaining useful life can be calculated using

equation (16) to be RUL = 6535-835 = 5700 cycles. Further, the RUL values of 5559 cycles and 5700 cycles using the two damage proxies correlate with each other.

A similar process for the prognostication of the prior accrued damage in the 256 BGA assemblies has been followed using the damage proxies of phase growth parameter and IMC growth. The results are shown in Table 16. The remaining useful life is calculated using equation (16) to be RUL = 5336-1051 = 4285 cycles using phase growth and RUL = 5336-1034 = 4302 cycles. Further, the RUL values of 4285 cycles and 4302 cycles using the two damage proxies correlate with each other.

Table 16: RUL for the 256 BGA after 168 hours TA + 250 Cycles TC1 + 250 Cycles TC2 using Phase-Growth as Damage Proxy.

	256 BGA Phase Growth	256 BGA IMC Growth
168 TA+250 TC1	410	357
(Units of TC1 Cycles), (A)		
168 TA+250 TC1	500	521
(Units of TC2 Cycles), (B) Phase: $N_{TC2} = 0.80\left[(N_{TC1})_{eq}\right]^{1.07}$ IMC: $N_{TC2} = 0.81\left[(N_{TC1})_{eq}\right]^{1.1}$		
168 TA+250 TC1+250 TC2 (C)	782	760
(Prognostication of TC2 Cycles)		
(D) = (C) - (B)	282	239
(Units of TC2 Cycles)		
168 TA+250 TC1+500TC2 (E)	1051	1034
(Prognostication of TC2 Cycles)		
(F) = (E)-(C)	269	274
N63.2%	5336	5336
RUL=		
N63.2%-D	4285	4302

4.10 PROGNOSTICS PERFORMANCE METRICS

In this paper two separate prognostication models based on two leading indicators of failure viz. phase-growth and inter-metallic compound growth of second level solder interconnects have been proposed and implemented for the life prediction of electronics. The sole purpose of evaluating various performance metrics was to relatively compare the two models and see which leading indicator of failure accurately predicts life. For this seven different performance metrics viz. accuracy, precision, Mean Squared Error (MSE), and Mean Absolute Percentage Error (MAPE), α-λ accuracy, relative accuracy (RA) and cumulative relative accuracy (CRA) have been computed to compare the two models.

Average Bias: Average bias method averages the error in predictions made at all subsequent times after prediction starts for the lth UUT. The metric can be extended to average bias over all UUTs to establish overall bias [1].

$$B_l = \frac{\sum_{i=P}^{EOP} \left\{ \Delta^l(i) \right\}}{\left(EOP - P + 1 \right)} \qquad (43)$$

Sample Standard Deviation (S): Sample standard deviation measures the dispersion/speed of the error with respect to the sample mean of the error. This metric is restricted to the assumption of normal distribution of the error. It is, therefore, recommended to carry out a visual inspection of error plots [1, 2].

SSD $$S(i)=\sqrt{\frac{\sum_{l=1}^{n}\left(\Delta^{l}(i)-M\right)^{2}}{n-1}} \qquad (44)$$

Where M is sample mean of the error

Mean squared error (MSE): Mean squared error averages the square prediction error for multiple UUTs at the same prediction horizon. A derivative of MSE is root mean square error (RMSE) [3].

$$MSE(i)=\frac{1}{L}\sum_{i=1}^{L}\Delta^{l}(i)^{2} \qquad (45)$$

Mean absolute percentage error (MAPE): MAPE averages the absolute error in the predictions of multiple UUTs at the same prediction horizon. Instead of the mean, median can be used to compute Median absolute percentage error (MdAPE) in similar fashion [3, 4]

$$MAPE(i)=\frac{1}{L}\sum_{l=1}^{L}\left|\frac{100\Delta^{l}(i)}{r_{*}^{\,l}(i)}\right| \qquad (46)$$

α-λ accuracy: The α-λ curve has been plotted for both the models as shown in Figures 66 and 67 for 676 I/O PBGA. It is a normalized plot of Remaining Useful Life (RUL) Vs Life which is compared against the ground truth and the error bounds. In this case the ground truth is the

experimental data obtained from accelerated testing shown by blue line in the plots and ± 10% error bounds are imposed shown by dotted lines. It should be noted that the selection of error bounds is application specific and typically tighter bounds are imposed as the criticality of the system increases.

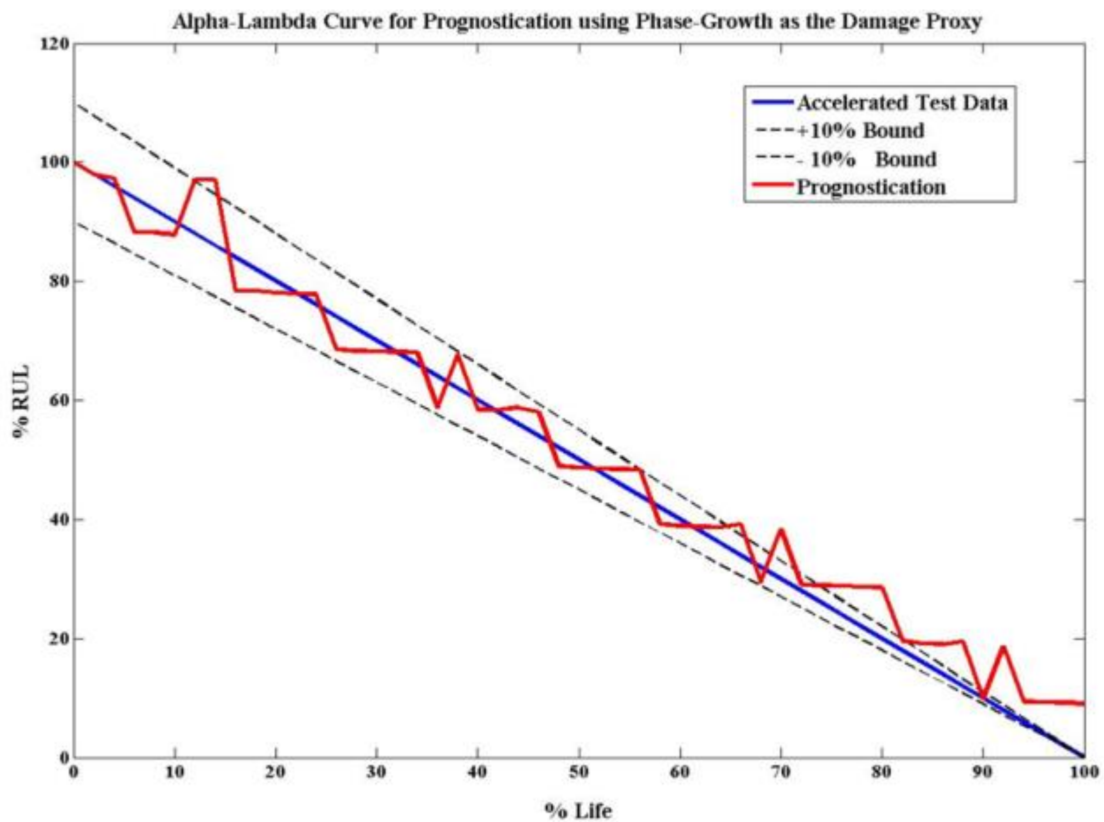

Figure 66: α-λ curve for Prognostication using phase-growth as the damage proxy

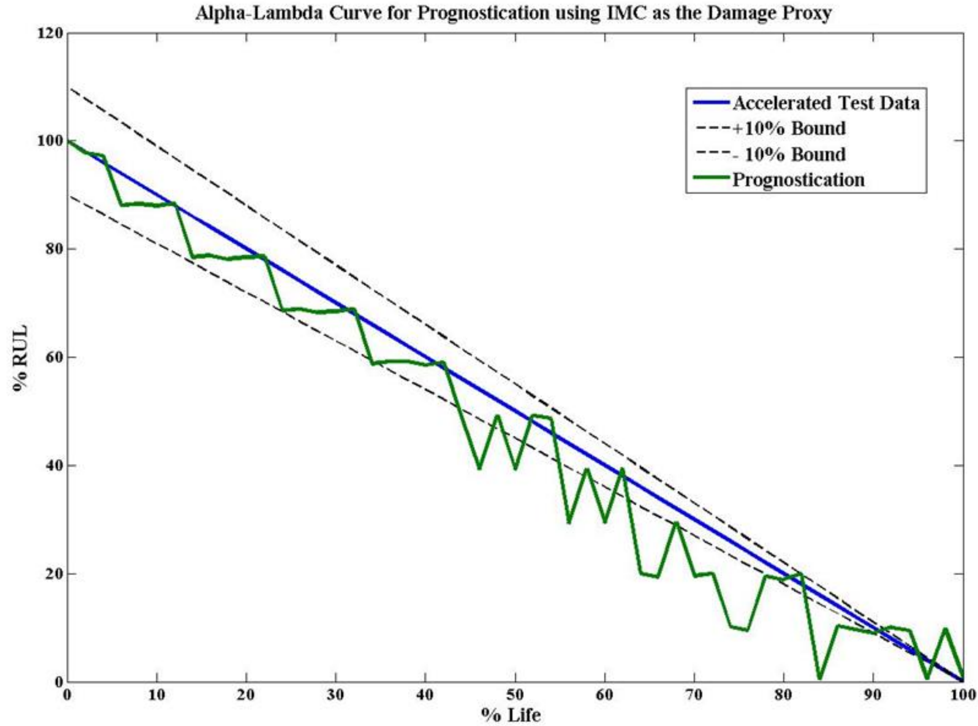

Figure 67: α-λ curve for Prognostication using IMC as the damage proxy

Relative accuracy (RA):

Relative prediction accuracy is a notion similar to α-λ *accuracy* where, instead of finding out whether the predictions fall within a given accuracy levels at a given time instant, we measure the accuracy level. The time instant is again described as a fraction of actual remaining useful life from the point when the first prediction is made. An algorithm with higher relative accuracy is desirable [5]

$$RA = 1 - \frac{\left| r_*(t_\lambda) - r^l(t_\lambda) \right|}{r_*(t_\lambda)} \qquad (47)$$

Where $t_\lambda = P + \lambda\,(EOP - P)$

CRA:

Relative accuracy can be evaluated at multiple time instances. To aggregate these accuracy levels, we define Cumulative Relative Accuracy as a normalized weighted sum of relative prediction accuracies at specific time instances [5]

$$CRA = \frac{1}{EOP - P + 1} \sum_{l=P}^{EOL} RA \qquad (48)$$

Where w is a weight factor as a function of RUL at all time indices. In most cases it is desirable to weigh the relative accuracies higher closer to the EOL.

Table 17: Comparison of Prognostics Metrics for the Two Leading Indiacators

Prognostic Metrics	LM prognostication (Phase)	LM prognostication (IMC)
Sample Standard Deviation (S)	220.6121	292.8947
MSE	54181.35	130216.3
MAPE	0.065839	0.177259
RA (λ=0.5)	0.9732	0.7836
CRA	0.007713	0.0074246

Table 12 shows relative accuracy for a point where 50% of the life of system is consumed.

The α-λ curve has been plotted for both the models as shown in Figure 68 and Figure 69 for 256 I/O CABGA.

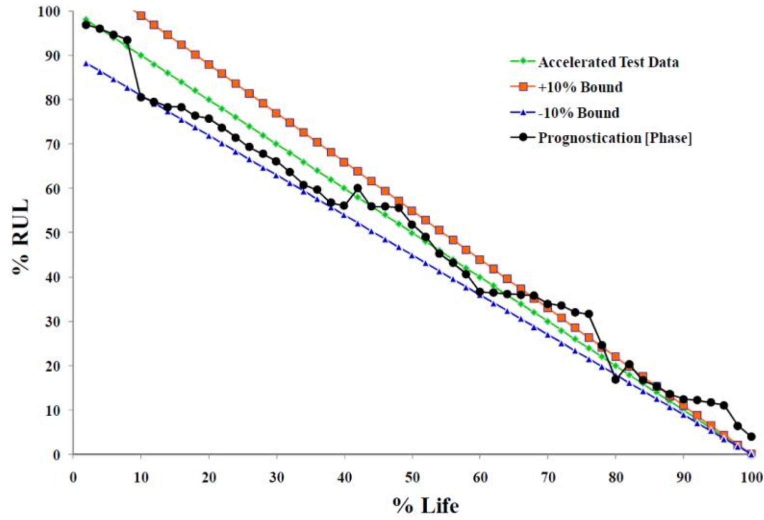

Figure 68: α-λ curve for Prognostication using phase-growth as the damage proxy

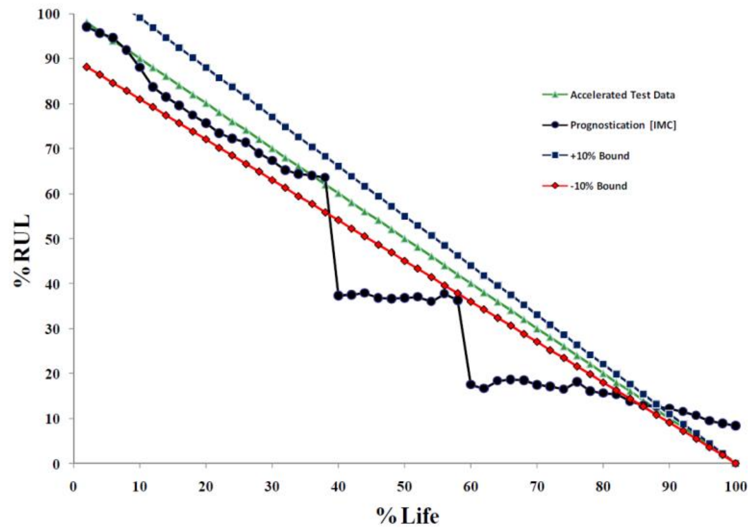

Figure 69: α-λ curve for Prognostication using IMC as the damage proxy

Table 18: Comparison of Prognostics Metrics for the Two Leading Indicators

Prognostic Metrics	LM prognostication (Phase)	LM prognostication (IMC)
Sample Standard Deviation (S)	61.7928	195.85
MSE	11225.0408	61228.84
MAPE	0.0157601	0.25
RA (λ=0.5)	0.9624	0.734
CRA	0.016282	0.0141

Table 18 shows the relative accuracy for a point where 50% of the life of system is consumed. Both leading indicator based prognostic algorithms show comparable performance.

3.11 Summary and Conclusions

A methodology has been presented to prognosticate the accrued prior damage and assess residual life in electronics subjected to multiple thermal environments. The presented approach uses the Levenberg-Marquardt Algorithm in conjunction with microstructural evolution of damage based leading indicator for estimating prior stress history. The viability of the approach has been demonstrated for test assemblies withdrawn from two different thermo-mechanical environment Thermal Aging 125C and TC1 (-40 to 125C) and redeployed in second thermo-mechanical environment TC2 (0 to 100C). The prognostication has been demonstrated at three stages of the life cycle including, prognostication of prior stress history after withdrawal from the first

environment TA + TC1, assessment of operational readiness for redeployment in environment TC2, and the assessment of prior damage and residual life after finite time of deployment of in TC2. Model predictions of total consumed life in multiple environments correlate well with the experimental data. The correlation demonstrates that the presented leading indicator based PHM technique can be used to interrogate the system state in multiple environments and thus estimate the residual life of a component. The presented approach of computing residual life can be implemented prior to appearance of any macro-indicators of damage like crack. Methodology presented using condition monitoring components to find out the residual life is promising because these components experience the same environment as actual component. In addition, prognostics metrics have been used to quantitatively evaluate the performance of the prognostic algorithms using both the leading indicators. Results demonstrate that both damage proxies work well in estimating accrued damage and estimating residual life.

Chapter 5

Damage Pre-cursor Based Assessment of Impact of High Temperature Storage on Reliability of Lead-free Electronics

5.1 Overview

Leadfree electronics in automotive, military and defense applications may be subjected to extreme high and extreme low temperature in addition to temperature cycling with intermittent prolonged period of storage. Automotive electronics may be expected to last 10-years, 100,000 miles. Military and defense electronics may be subjected to several deployments over the use-life of the system. Previous researchers have shown the detrimental effects of prolonged exposure to high temperature on the mechanical properties of lead-free alloys. Effects include the degradation in the yield strength and ultimate tensile strength of the materials. [Chou 2002, Hasegawa 2001, Zhang 2009]. The effects are most pronounced in the widely used SnAgCu based alloys including SAC105, SAC205, SAC305 and SAC405 solders. Lower silver solders such as the SAC105, often touted for their resistance to transient dynamic shock and vibration, are the most susceptible to thermal aging amongst the SAC solders. The effects have been verified in the solder alloys at both lower strain rates in the neighborhood of 10^{-4} sec-1 to 10^{-5} sec-1 typical of thermal cycling, and at 1-to-100 sec-1 typical of shock and vibration. Degradation in the neighborhood of 50% has been measured at low temperature exposures.

The property evolution of the SnAgCu solder alloys poses a challenge in the long life systems in presence of multiple redeployments over the product life. Electronics in automotive systems may perform critical functions such as collision avoidance, lane departure warning, adaptive cruise

control, and antilock braking. Aerospace electronics systems may be called on to perform a variety of function including launch, autonomous navigation, in-flight maneuvering, path correction and re-entry. Safety critical nature of the electronics systems necessitates that level-of-damage and the remaining useful life be quantified prior to any future redeployment. In electronics assemblies, the built-in-self test (BIST) circuit involving error detection and correction circuits are used to give electronic assemblies the ability to test and diagnose themselves with minimal interaction from external test equipment [Chandramouli 1996, Drees 2004, Hassan 1992, Williams 1983, Zorian 1994]. The results obtained from BIST functions can generate diagnostic information which in turn provides additional confidence in the measurement result and confirms the device availability. However, the current form of BIST gives little insight about the system level reliability or the remaining useful life of the system. Several studies conducted [Allen 2003, Drees 2004, Gao 2002, Rosenthal 1990] have shown that BIST can be prone to false alarms and can result in unnecessary costly replacement, re-qualification, delayed shipping, and loss of system availability. Fuses and Canaries may be mounted on a part to provide advance warning of failure due to specific wear out failure mechanism. Advanced warning is used to provide a maintenance-window for correction action, after an initial failure or malfunction, to prevent additional or secondary failures [Mishra 2002, Anderson 2004]. However, past efforts have provided limited insight into methods for estimation of remaining useful life.

Leadfree solder property evolution has been shown to increase in magnitude with both increase in ambient temperature and increase in time of exposure. Given the mission critical nature of the

role of electronics in such applications, there is need for tools and techniques which can be used for capturing the evolving failure threshold, and damage accrued after multiple exposures to arbitrary temperatures for unforeseen lengths of time. Capability to equivalence damage over various storage temperature and times is beyond the state of art. Previously, leading indicators of damage have been used to quantify the accrued thermomechanical damage under steady-state and cyclic temperature exposure in leadfree solders. [Lall 2004a-d, 2005a-b, 2006a-f, 2007a-e, 2008a-f, 2009a-d, 2010a-j]. In this paper, a method has been developed for calculation of equivalent damage in leadfree second level interconnects. Leadfree electronics packages have been subjected to isothermal exposure at 60°C, 75°C and 125°C for various lengths of time. Damage-state interrogation technique has been developed based on the Levenberg-Marquardt Algorithm in conjunction with the microstructural damage evolution proxies. Test cases have been presented to demonstrate the viability of the technique for assessment of prior damage, operational readiness and residual life for assemblies exposed to multiple thermomechanical environments.

5.2 Test Vehicle

In this study, CABGA 256 packages soldered to glass-epoxy laminate board assemblies were used. The CABGA256 package is 16mm x 16mm in size, with 256 I/O at 0.8mm Pitch. Package interconnects were made of Sn3Ag0.5Cu solder in both cases.

Table 19: Package Attributes

Attributes	**CABGA256**
Solder	Sn3Ag0.5Cu
Package Size (mm)	16x16

Package Type	CABGA
I/O Count	256
I/O Pitch (mm)	0.8
Ball Diameter (mm)	0.5
Mold thickness (mm)	1.5
Board Finish	INIG
PCB Thickness	1.55

The ball diameter of the solder interconnects is 0.46 mm for the CABGA36 and 0.5 mm for the CABGA256. The printed circuit board thickness was 1.55 mm in both cases. Package attributes are shown in Table 19. The printed circuit board was a double-sided FR4-06 material. The printed circuit board pads were solder mask defined (SMD) with immersion silver finish.

Figure 70: CABGA 256 Package

Figure 70 shows the CABGA 256 package and its array configuration. All test vehicles were subjected to isothermal aging at 60°C, 75°C and 125°C for various lengths of time. The test board is a JEDEC form-factor test board with corner holes. Each test package has four daisy chain patterns corresponding to the four quadrants. Packages were assembled at in-house surface mount facility of CAVE3.

5.3 Approach for Interrogation of Damage in Thermal Aging

In operational environments electronic systems may be stored after manufacture for a finite period prior to deployment. During the storage period, the systems may be exposed to a finite time-period of thermal aging at extreme low or extreme high temperatures in addition to thermal cycling. Once deployed, the systems may be exposed to further thermal aging along with intermittent thermo-mechanical cycling due to power on-off cycles or ambient temperature excursions. Extended exposure to elevated temperature aging may reduce thermo-mechanical reliability in cyclic environments. In this paper, a damage mapping method has been presented based on the underlying failure physics to relate the damage accrued under steady-state thermal aging with a particular combination of temperature and storage time. The approach has been developed in three steps.

5.3.1 Micro-structural Evolution of Damage

In this step, board assemblies have been subjected to single stresses of thermal aging. Samples have been withdrawn periodically and cross-sectioned. Damage proxies studied include the phase-growth parameter, rate of change of phase growth parameter per cycle and the intermetallic thickness. The phase-growth parameter is represented by symbol 'S' in Equation (1). Previously, it has been shown that the rate of change in phase growth parameter [d(lnS)/d(lnN)] is valid damage proxy for prognostication of thermo-mechanical damage in solder interconnects and assessment of residual life [Lall 2004a, 2005a, 2006c, 2006d, 2007c, 2007e, 2008c, 2008d, 2009c, 2009d]. The damage proxy [d(lnS)/d(lnN)] is related to the micro structural evolution of damage by the following equation:

$$S = g^4 - g_0{}^4 = at^b \exp(\frac{-E_A}{K_B T})$$

where, g is the average grain size at time of prognostication, g_0 is the average grain size of solder after reflow, t is the period of aging, S is the phase growth parameter, parameters a and b are the coefficient and exponent respectively. It is anticipated that, longer period of aging at higher temperature will result in higher accrued thermo-mechanical damage in a shorter time and result in a higher slope of the phase growth parameter versus time of aging curve. Test samples have been withdrawn and cross-sectioned at periodic intervals. Images of polished samples were taken under Optical Microscope at 1000x magnification. . Growth rate of tin and Ag3Sn phases was observed. Phase size is measured using image analysis software NI-MAQ. The quantitative measure of Ag3Sn phase size was determined from a 480μm x 360μm rectangular region selected from the optical images. Figure 71 shows the mapping of image.

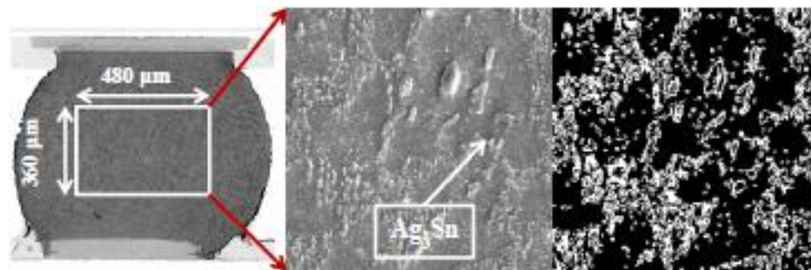

Figure 71: Micrograph and Gray scale mapping of image using image analysis software.

Growth of Inter-Metallic thickness during thermal aging has been studied as another leading indicator of failure in bulk solder. From past studies it has been established that growth of intermetallic thickness is used as a damage precursor for computation of remaining useful life [Lall 2005a, 2006c, 2006d, 2007c, 2007e, 2008c, 2008d, 2009c, 2009d]. The interfacial

intermetallic layers are formed between solder and copper, and some precipitates appear near the interface of the IMCs/solder as shown in Figure 72. These intermetallic layers have been identified to consist of Cu3Sn and Cu6Sn5 phases [Lall 2005a]. Trend analysis of intermetallic thickness growth on SEM using image processing software, indicates that IMC thickness changes with the square root of aging time,

$$y(t) = y_0 + kt^n \exp(\frac{-E_A}{K_B T})$$

where y(t) is IMC growth thickness during aging, y_0 is the initial thickness of intermetallic compounds, k is the coefficient standing for the square root of the diffusivity at aging temperature, t is aging time, E_A is the activation energy, K_B is Boltzmann's Constant (8.617x10-5 ev/K) and T_A is aging temperature in Kelvin . The exponent value, n = ½ has been used in the above equation, which reveals a diffusion-controlled mechanism during aging. A similar kind of relation can be derived for thermal cycling also.

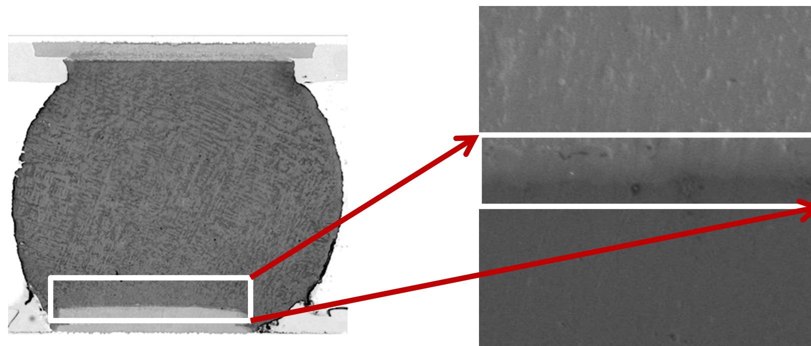

Figure 72: Image of IMC growth

5.3.2 Damage Mapping Relationships for Phase Growth

The relation between phase growth and aging time has been normalized with respect to the initial phase size, as follows,

$$S_n = (\frac{g_p}{g_0})^4 - 1 = a_0 t^{b_0} = a_1 \exp(\frac{-E_A}{K_B T}) \left[t^{b_1 \exp(\frac{-E_B}{K_B T})} \right]$$

Where Sn is the normalized phase growth parameter, 'a_1' is the coefficient for phase growth, 'b' is the phase-growth exponent, E_A is the activation energy, K_B is the Boltzmann Constant, and T is the temperature in Kelvin. The normalized phase growth expression has been rearranged as follows:

$$\ln S_n = \ln a_0 + b_0 \ln t$$

Where,

$$a_0 = a_1 \exp \frac{-E_a}{K_B T}$$

where, g is the phase-growth, subscripts p and 0 indicate point "p" and initial time respectively, S_{Nt} is the normalized phase-growth parameter during thermal aging, b_0 is the temperature dependent phase-growth exponent, E_a and E_b is the activation energy for phase-growth coefficient and exponent respectively, K is the Boltzmann constant (8.65 E-05 ev/K), T is the temperature, a_{nt} and b_{nt} are the normalized phase-growth coefficient and phase growth exponent for thermal aging.

Taking a natural logarithm of Equation, the relationship has been reduced to that of a straight line, where a'_1 is the temperature dependent phase-growth coefficient. From Equation we can write;

$Ln\ (a_0) = ln(a_1) - (E_A/K_BT)$

By using above equations the relationship between aging temperature (T) and aging time (t) for a particular level of damage state in terms of phase growth has been computed. The activation energy of the exponent term has been computed by fitting the phase growth data to the following form of the equation:

$$b_0 = b_1 \exp \frac{-E_b}{K_B T}$$

Taking a natural logarithm of Equation (6), the relationship has been reduced to that of a straight line, where 1 b is the temperature dependent phase-growth coefficient. From Equation (6) we can write;

$Ln\ (b_0) = ln(b_1) - (E_B/K_BT)$

Where b_0 is the temperature dependent phase-growth exponent, E_B is the activation energy, K_B is the Boltzmann Constant, and T is the temperature in Kelvin.

5.3.3 Damage Mapping Relationships for IMC Growth

The intermetallic thickness based proxy has been related to aging temperature and aging time using the following normalized IMC thickness equation,

$$\frac{y_p}{y_0} - 1 = Y_n = k_0 t^{0.5} = k_1 t^{0.5} \exp(\frac{-E_A}{K_B T})$$

$$Y_n = k_0 \sqrt{t} \text{ where } k_0 = k_1 \exp(\frac{-E_A}{K_B T})$$

$$\ln Y_n = \ln k_0 + \frac{1}{2} \ln t$$

Y_n is the normalized IMC growth parameter and $k_1 = k/y_0$. From the above relation we can write;

Taking a natural logarithm of Equation the relationship has been reduced to that of a straight line, where 0 k is the temperature dependent IMC-growth coefficient. We can write:

$$\ln k_0 = \ln k_1 - \frac{E_A}{K_B T}$$

By using above equations we will get a relation between aging temperature (T) and aging time (t) for a particular level of damage state in terms of IMC. Convergence between the relationships validates the damage equivalency.

5.4 Leading Indicators for Thermal Aging

A set of packages was subjected to aging at 60°C, 75°C and 125°C and were withdrawn after a periodic time-interval of 1- week or 168-hours increments. The samples were cross sectioned, polished. The same joint was examined in each cross-section. Phase growth and intermetallic growth was studied using images taken by optical microscope at each time interval.

5.4.1 Phase-Growth Damage Proxy

The image analysis software has been used to measure the average phase size. Equation represents the evolution of phase growth in thermal aging based on experimental data. The test data has been used to derive the parameters for normalized phase growth of equation. Micrographs of phase structure are shown in Figure 73 at 60°C, Figure 74 at 75°C, Figure 75 at 125°C for the CABGA 256 packages at a time-interval of 168 hours. The phase coarsening in the microstructure is clearly visible by comparison of 672 hour microstructure with 0-hour microstructure. Figure 76 show the plots of normalized phase growth at different isothermal aging temperature and at various time intervals for CABGA 256. The graphs for the higher temperature have higher normalized phase growth values. The increase in normalized phase growth parameter correlates with the underlying physics, since the higher temperatures will produce more phase growth in an identical period of time. Equation for phase growth evolution under thermal aging has been fit to experimental data. The equation parameters have been derived based statistical fit of the experimental data.

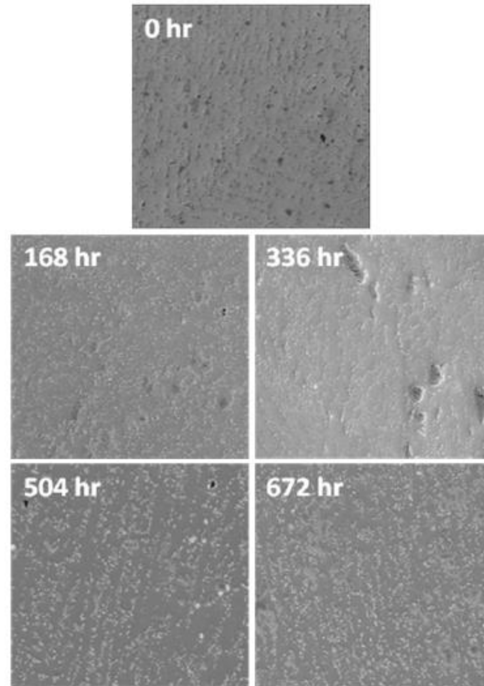

Figure 73: Optical Microscopic images of Phase Growth in CABGA256 at different time intervals at 60°C (Magnification 1000X)

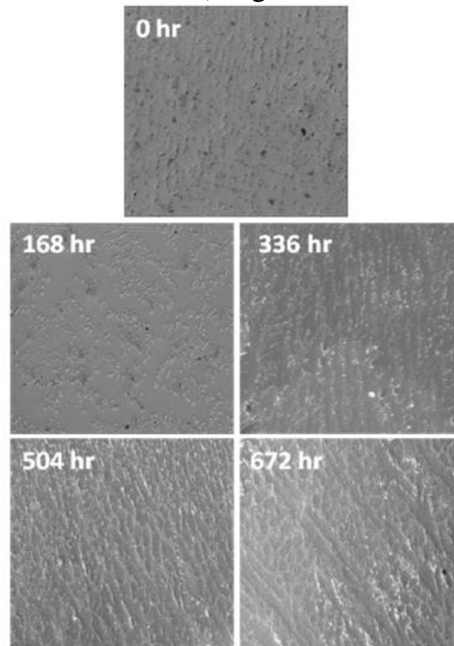

Figure 74: Optical Microscopic images of Phase Growth in CABGA256 at different time intervals at 75°C (Magnification 1000X)

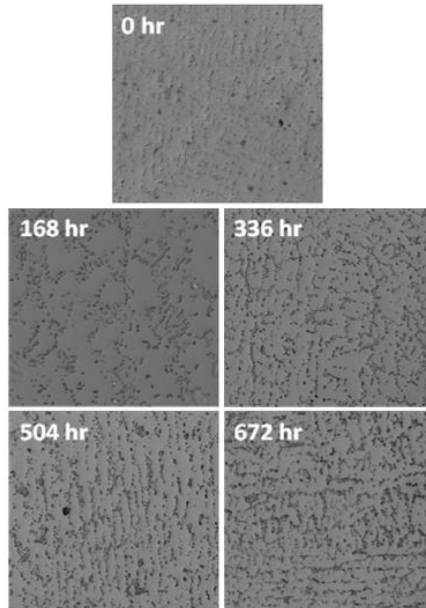

Figure 75: Optical Microscopic images of Phase Growth in CABGA256 at different time intervals at 125°C (Magnification 1000X)

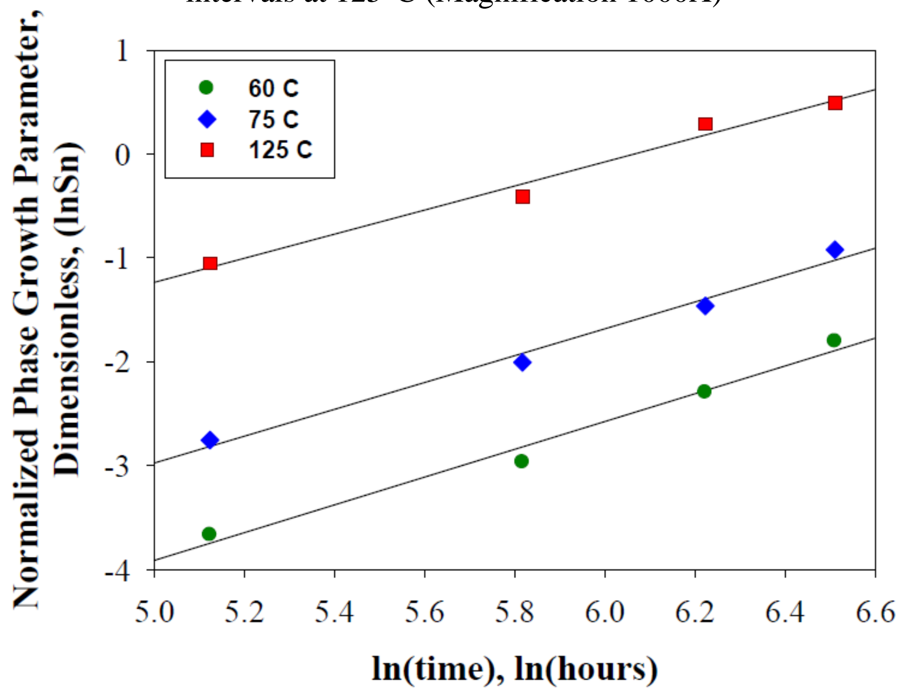

Figure 76: Relation between Normalized Phase Growth (Sn) and Aging Time (t) for CABGA

Table 20 shows the values for the phase growth coefficient and the phase growth exponent for the CABGA 256 packages. Values indicate that the aging temperature increases the value of the phase growth coefficient.

Table 20: Normalized Phase Growth Coefficients and Exponents for the CABGA 256 Package

Temperature	Equation (3) $\ln(S_n) = \ln\left[\left(\frac{g_p}{g_0}\right)^4 - 1\right] = \ln a_0 + b_0(\ln t)$	
	b_0	$\ln(a_0)$
60°C	1.338	-10.60
75°C	1.293	-9.44
125°C	1.161	-7.04

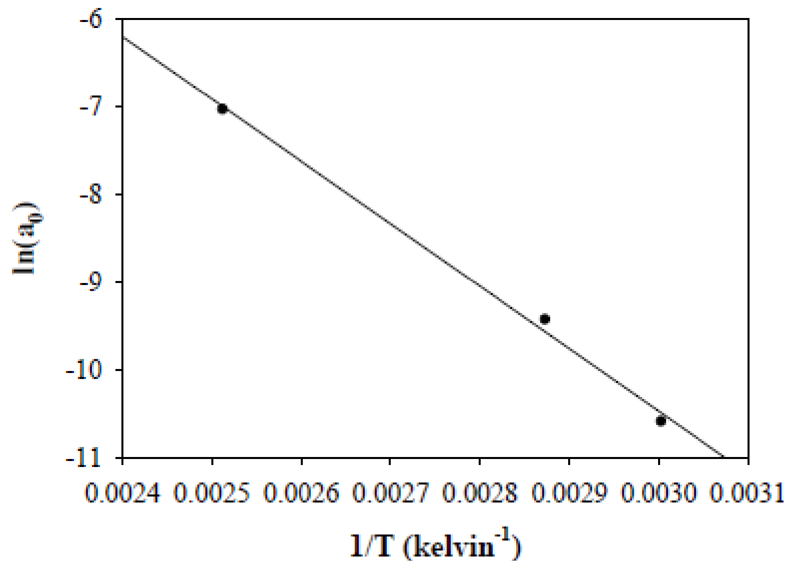

Figure 77: Plot of ln(a′) and Aging temperature for CABGA256

The coefficient term changes with temperature of exposure because of the underlying agglomeration of phases proceeds at a faster pace at a higher temperature. The activation energy

of the coefficient term has been computed by fitting the data to Equation (7). Figure 77 and Figure 78 show the relationship between ln(a0) and (1/T), where T is the absolute temperature.

Table 21: Activation Energy for Phase Growth Coefficient

	$\ln a_1$	E_A (ev)
CABGA 256	10.903	0.61

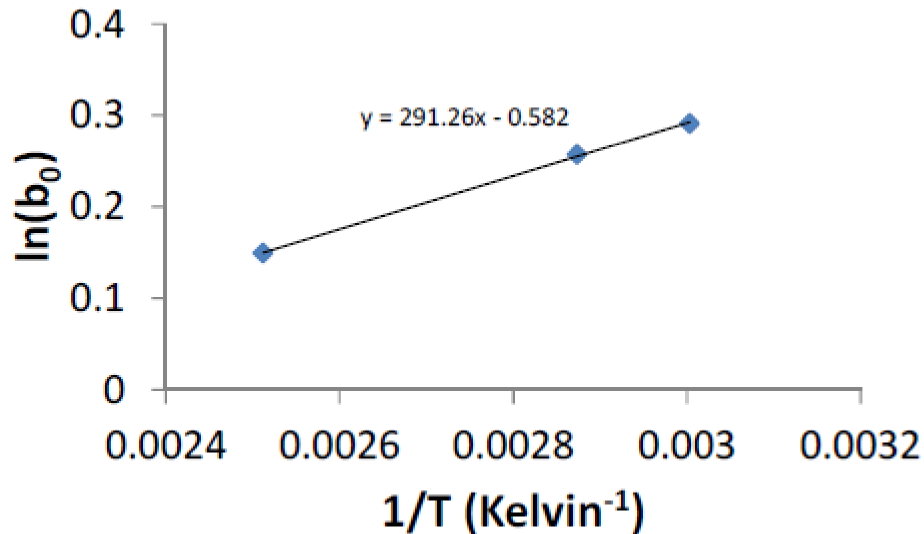

Figure 78: Plot of $\ln(b_0)$ and Aging temperature for CABGA256

Slope of the fit of ln(a1) versus (1/T) is E_A/K_B, where E_A is the activation energy; K_B is Boltzmann's Constant (8.617x10- 5 ev/K). The Activation energy of phase growth is calculated as 0.614eV for CABGA 256.

Table 22: Activation Energy for Phase Growth Exponent

	$\ln b_1$	E_B (ev)
CABGA 256	-0.582	0.025

Slope of this fit is E_B/K_B, where E_B is the activation energy; K_B is Boltzmann's Constant (8.617x10-5 ev/K). The Activation energy of phase growth is calculated as 0.025eV for CABGA 256 (Table 21 and 22).

5.4.2 Intermetallic Thickness Damage Proxy

The image analysis software has been used to measure the average intermetallic thickness. Equation represents the evolution of intermetallic growth in thermal aging based on experimental data. The equation parameters have been derived based on experimental measurements of the intermetallic growth from cross-sections. The data for normalized IMC thickness has been fit to equation. Micrographs of phase structure are shown in Figure 79 at 60°C, Figure 80 at 75°C, Figure 81 at 125°C for the CABGA 256 packages at a time-interval of 168 hours. The phase-coarsening in the microstructure is clearly visible by comparison of 672 hour microstructure with 0-hour microstructure.

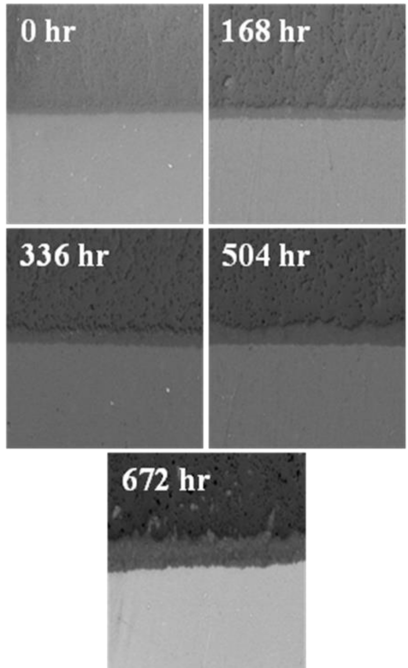

Figure 79: Optical Microscopic images of IMC Growth in CABGA256 at different time intervals at 60°C (Magnification 1000X)

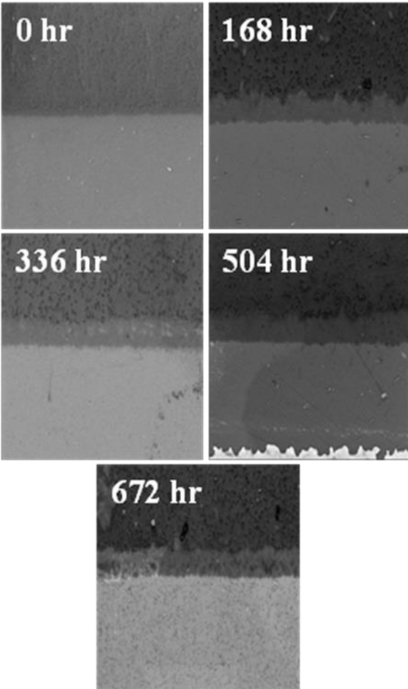

Figure 80: Optical Microscopic images of IMC Growth in CABGA256 at different time intervals at 75°C (Magnification 1000X)

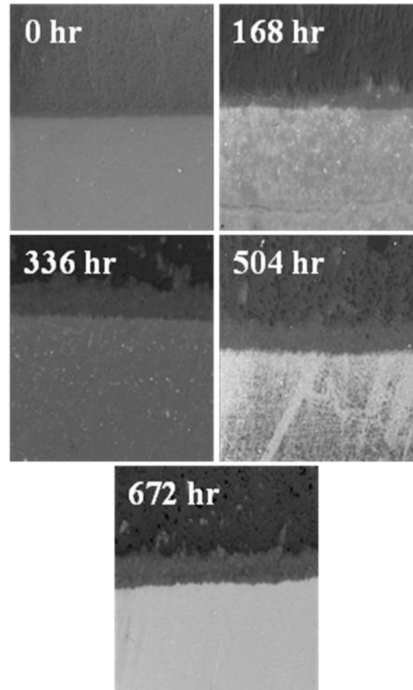

Figure 81: Optical Microscopic images of IMC Growth in CABGA256 at different time intervals at 125°C (Magnification 1000X)

Figure 82 show the plots of normalized intermetallic growth at different isothermal aging temperature and at various time intervals for CABGA 256. The graphs for the higher temperature have higher normalized intermetallic growth values. The increase in normalized intermetallic thickness parameter correlates with the underlying physics, since the higher temperatures will produce more intermetallic thickness due to higher diffusion rates in an identical period of time. Equation (11) for IMC growth under thermal aging has been fit to experimental data. The equation parameters have been derived based statistical fit of the experimental data.

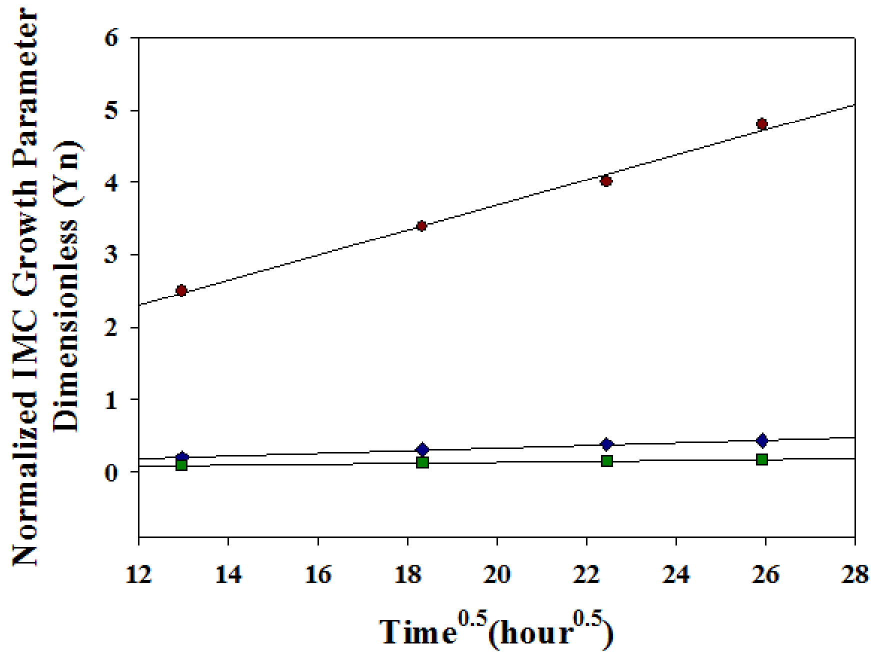

Figure 82: Relation between Normalized IMC Growth (Yn) and Aging Time (t) for CABGA 256

Table 23 shows the values for the IMC growth coefficient for the CABGA 36 and the CABGA 256 packages. Values indicate that the aging temperature increases the value of the IMC growth coefficient. The coefficient term changes with temperature of exposure because of the underlying Fickian diffusion at the interface proceeds at a faster pace at a higher temperature.

Table 23: Normalized Phase Growth Coefficients and Exponents for the CABGA 256 Package

Temperature	$Y_n = k_0 t^{0.5} = k_1 t^{0.5} \exp(\frac{-E_A}{K_B T})$
	K_0 (CABGA 256)
60°C	0.0071
75°C	0.0168
125°C	0.1833

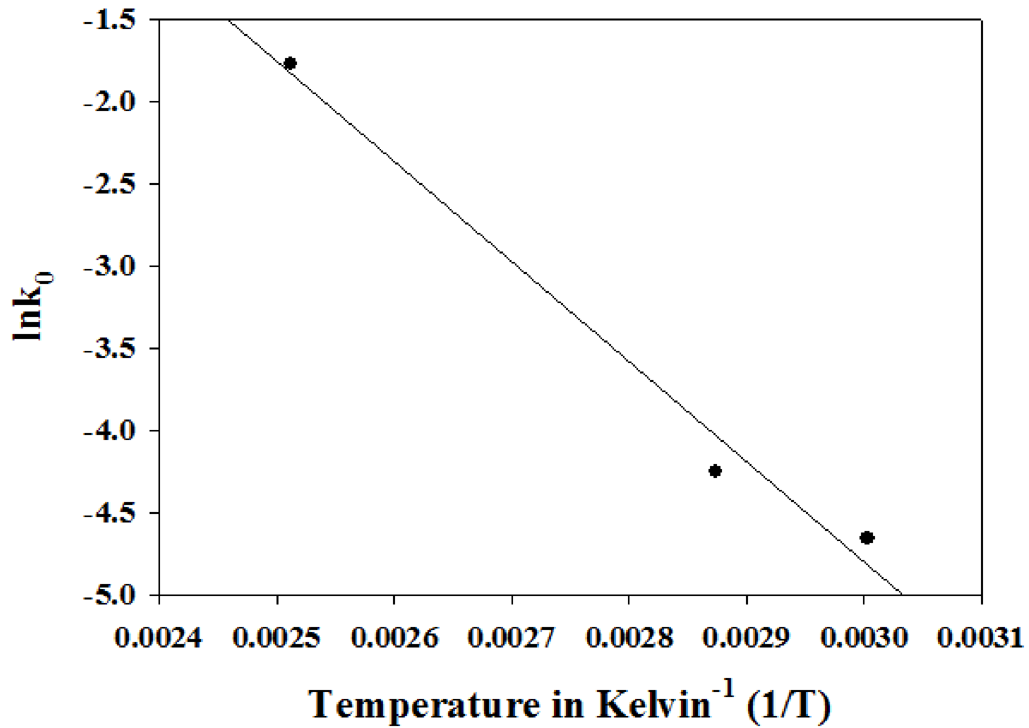

Figure 83: Plot of ln(a′) and Aging temperature for CABGA256 Activation Energy for IMC Growth Coefficient

Table 24: Activation Energy for CABGA 256

	ln k_1	E_A (ev)
CABGA 256	14.95	0.57

Slope of this fit is E_A/K_B, where E_A is the activation energy; K_B is Boltzmann's Constant (8.617x10-5 ev/K). The Activation energy of phase growth is calculated as 0.57eV for CABGA 256 as shown in Table 24.

5.5 Damage Mapping

In this section, a method for damage mapping has been developed using the data gathered on the test vehicles. Temperature and time combinations required to achieve a specified value of normalized phase growth have been calculated. The damage accrued can thus be sustained in a shorter time at a high temperature or in a longer time at a lower temperature. Re-arranging Equation (5),

$$\mathrm{lnS_n} = \ln a_0 + b_0 \ln t$$

$$\mathrm{lnS_n} = \ln\left(a_1 \exp\left(\frac{E_A}{K_B T} \right)\right) + b_1 \exp\left(\frac{E_B}{K_B T} \right) \ln t$$

Rearranging the equation

$$\mathrm{lnt} = \frac{\ln S_n - \ln a_1 + \dfrac{E_A}{K_B T}}{b_1 \exp\left(\dfrac{E_B}{K_B T} \right)}$$

Where, KB is the Boltzmann's constant, 8.617e-5 eV/K, a1 = 28796.23, Ea = 0.63 eV, b1 = 0.772, Eb = 0.019 eV. Figure 84 shows the relation between aging temperatures (1/T) in Kelvin scale and required aging time in hours for a particular value of damage state in terms of phase growth for both the CABGA 36 and CABGA 256 packages. Convergence of damage mapping has been demonstrated by comparing the damage mapping data from two identical failure mechanisms for two different parts.

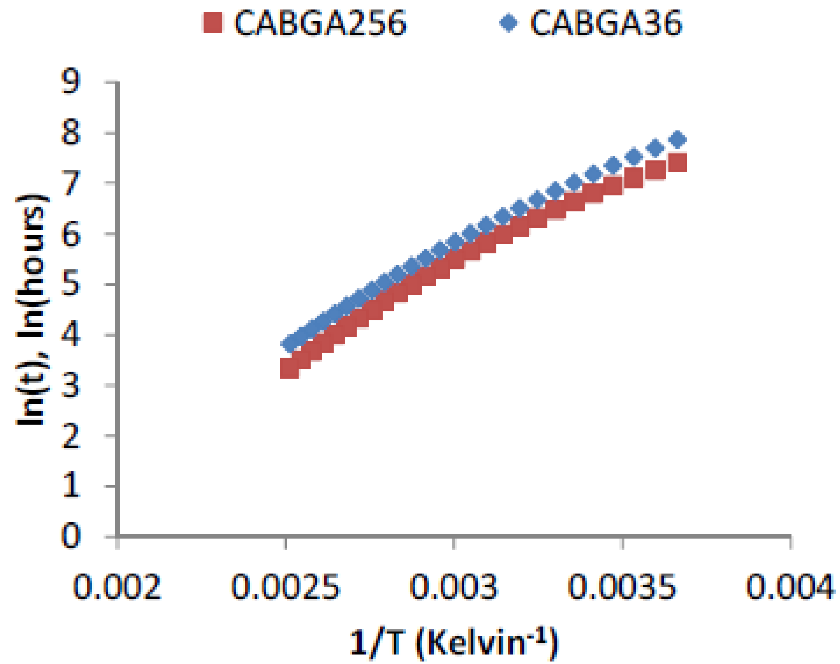

Figure 84: Iso-phase growth plots of Aging temperature (T) vs Aging time(t) for Phase Growth (CABGA 36)

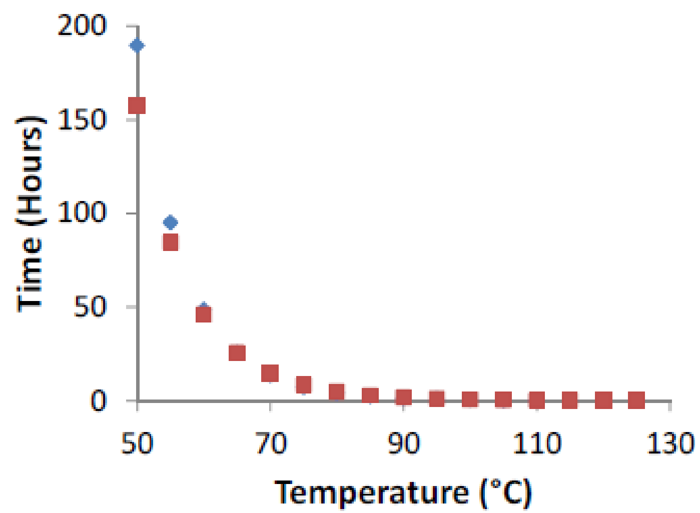

Figure 85: Iso-IMC growth plots of Aging Time, ln(T) vs Aging Temperature for CABGA 36.

Similarly, Figure 85 shows the same relations for IMC. In this section, a method for damage mapping has been developed using the data gathered on the test vehicles. Temperature and time combinations required to achieve a specified value of normalized IMC growth have been calculated. The damage accrued can thus be sustained in a shorter time at a high temperature or in a longer time at a lower temperature. Re-arranging Equation (10),

$$t = \left(\frac{Y_n}{k_1 \exp\left(\frac{-E_A}{K_B T} \right)} \right)^2$$

Where, K_B is the Boltzmann's constant, 8.617e-5 eV/K, k1 = 2.46e7. The convergence of the curves for the same failure mechanisms indicates the merit of the proposed approach.

5.5.1 Using Damage Mapping for Overlapping Thermal Environments

The 256 BGA test assemblies have been exposed to 168 hours of aging at 125°C, followed by 250 cycles in -40°C to 125°C (TC1) and then redeployed in thermal cycling environment of 0 to 100°C (TC2). The problem statement is to find the previous consumed life and the remaining useful life in TC2. In order to prognosticate the prior accrued damage and the remaining useful life, the parts have been withdrawn at periodic intervals of 250 cycles to measure the phase growth and intermetallic growth in the TC2 deployed samples. The withdrawn samples have been cross-sectioned.

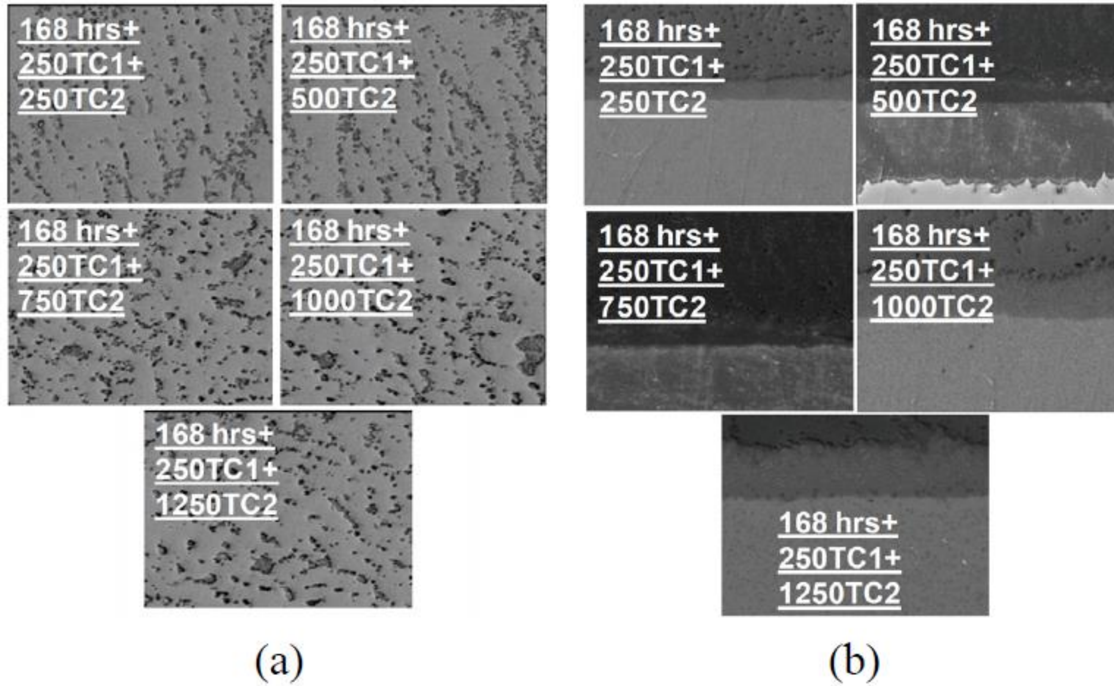

Figure 86: Back-scattered Images for samples exposed to Multiple Environments of 168 hours @ 125OC + 250 Cycles TC-1 + x-Cycles TC-2, 256 I/O PBGA, magnification 1000x (a) Phase Growth (b) IMC growth.

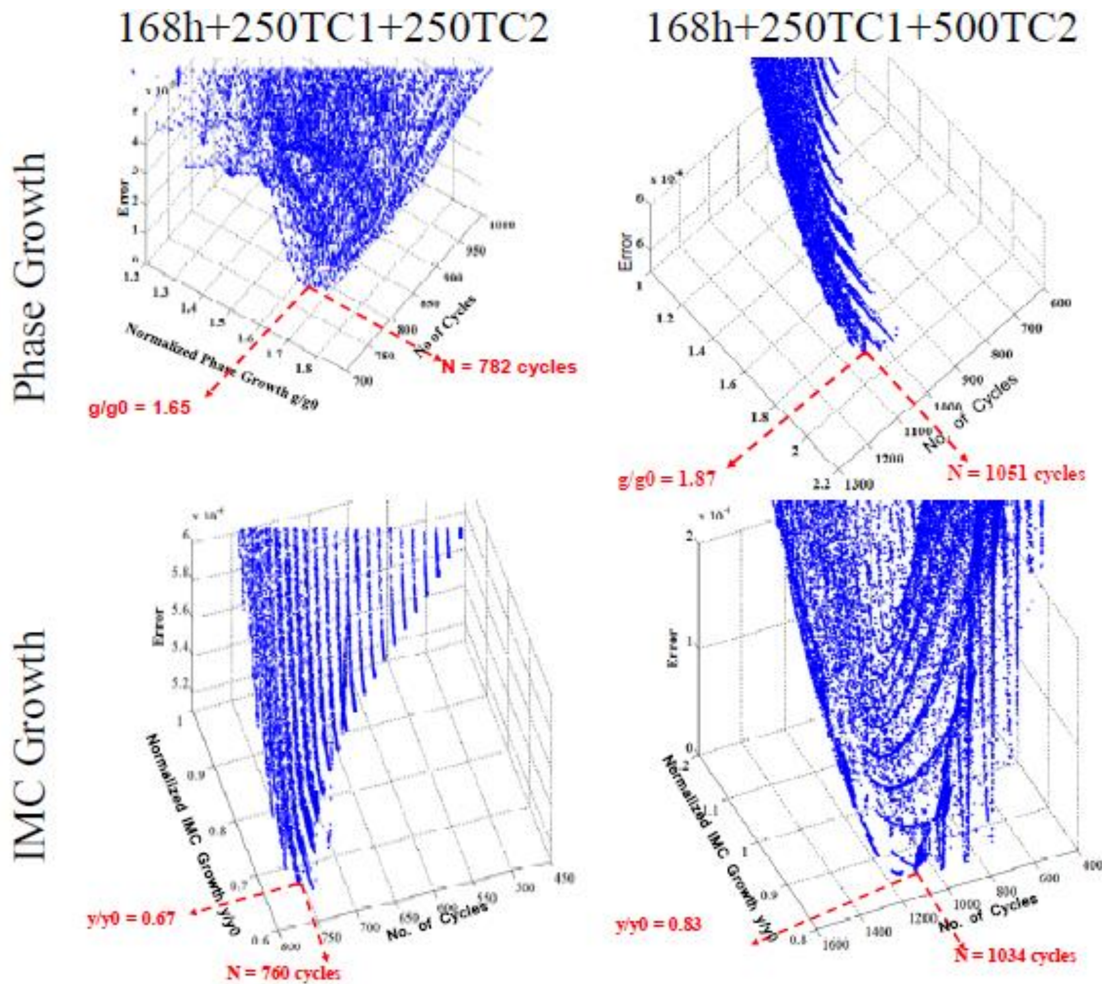

Figure 87: 3D plot of error versus Number of Cycles, Life computed from LM-algorithm for 168hrs TA + 250 cycles TC1 + 250 cycles TC2 and 168hrs TA + 250 cycles in TC1 + 500 cycles in TC2 for 256 PBGA.

The phase growth and intermetallic thickness has been studied under confocal microscope (Figure 86). The samples were prognosticated using the Levenberg-Marquardt Algorithm. Details of the LM algorithm can be found in [Madsen 2004]. Damage accrued from aging and cycling environments has been equivalenced based on two damage proxies including normalized intermetallic thickness and normalized phase growth. The measured value of damage proxy can

be obtained by exposure to single stresses of thermal aging and thermal cycling. The exposure length to the environmental stresses however, will be different in each case. This combined plot is helpful for mapping of damage from thermal aging onto thermal cycling. Intermetallic thickness can be obtained by exposure to single stresses of thermal aging and thermal cycling. The exposure length to the environmental stresses however, will be different in each case. Damage mapping relationships shown Equations (17) and (18) can be used to map damage to different storage temperature, e.g. if the test data was acquired for 168 hours at 125°C, and the intended use condition involved storage at 75°C, then an equivalent storage time to accrue identical damage could be determined. Figure 87 shows the prognosticated values of accrued damage in 256 BGA assemblies after they have been subjected to (a) 168 hours of thermal aging + 250 Cycles of thermal cycling in TC1 (-40°C to 125°C) + 250 cycles of thermal cycling in TC2 (0°C to 100°C) (b) 168 hours of thermal aging + 250 Cycles of thermal cycling in TC1 (-40°C to 125°C) + 500 cycles of thermal cycling in TC2 (0°C to 100°C). The accrued damage has been prognosticated using both phase growth parameter and the intermetallic growth. The prognosticated TC2 cycles for the 168h+250TC1+250TC2 case using phase growth and IMC growth are 782 cycles and 760 cycles respectively. The prognosticated TC2 cycles for the 168h+250TC1+500TC2 case using phase growth and IMC growth are 1051 cycles and 1034 cycles respectively.

5.6 Summary and Conclusion

A damage mapping method has been developed based on the underlying physics-based leading indicators to relate the accrued damage under accelerated steady-state thermal storage to accrued

damage under exposure to operational steady-state temperature. The method has been developed on the CABGA256 packages. Analysis results indicate convergence of damage mapping relationships for the two package architecture examined for the failure mechanisms of solder joint failure and excessive intermetallics. The usefulness of the damage equivalency relationships has been demonstrated in the presence of overlapping thermal stresses.

Chapter-6

Damage Pre-cursors Based Prognostication of Accrued Damage and Assessment of Operational Readiness of Leadfree Electronics

6.1 Overview

Electronics in high reliability applications may be stored for extended periods of time prior to deployment. Prior studies have shown the elastic modulus and ultimate tensile strength of the SAC leadfree alloys reduces under prolonged exposure to high temperatures [Zhang 2009]. The thermal cycle magnitudes may vary over the lifetime of the product. Long-life systems may be re-deployed several times over the use life of the product. Previously, the authors have identified damage pre-cursors for correlation of the damage progression with the microstructural evolution of damage in second level interconnects [Lall 2004[a-d], 2005[a-b], 2006[a-f], 2007[a-e], 2008[a-f], 2009[a-d], 2010[a-j]]. Leadfree assemblies with Sn3Ag0.5Cu solder have been subjected to variety of thermal aging conditions including 60°C, 85°C and 125°C for periods of time between 1-week and 2-months, thermal cycling from -55°C to 125°C, -40°C to 95°C and 3°C to 100°C. The presented methodology uses leading indicators of failure based on microstructural evolution of damage to identify accrued damage in electronic systems subjected to sequential stresses of thermal aging and thermal cycling. Damage equivalency relationships have been developed to map damage accrued in thermal aging to the reduction in thermo-mechanical cyclic life based on damage proxies. Accrued damage between different thermal cyclic magnitudes has also been mapped for from -55°C to 125°C, -40°C to 95°C and 3°C to 100°C thermal cycles. The presented method for interrogation of the accrued damage for the

field deployed electronics, significantly prior to failure, may allow insight into the damage initiation and progression of the deployed system. The expected error with interrogation of system state and assessment of residual life has been quantified.

6.2 Test Vehicle

For this study, leadfree assembly with PBGA-324 package was used. It was full area array configuration and Sn3Ag0.5Cu solder interconnects at 1 mm pitch. The ball diameter is 0.63 mm and the die size is 19 x 19 mm. Package attributes are shown in Table 25. The printed circuit board was a double-sided FR4-06 material. The printed circuit board pads were solder mask defined (SMD) with immersion silver finish.

Figure shows the package and its assembly. The test vehicle was subjected to variety of thermal aging conditions including 60°C, 85°C and 125°C for periods of time between 1-week to 2-months, thermal cycling from -55°C to 125°C, -40°C to 95°C and 3°C to 100°C for various lengths of time. The test board is a JEDEC form-factor test board with corner holes. Each test package has four daisy chain patterns corresponding to the four quadrants. Packages were assembled at in-house surface mount facility of CAVE[3]. The reflow profile used for soldering the SAC305 parts is shown in Figure 89.

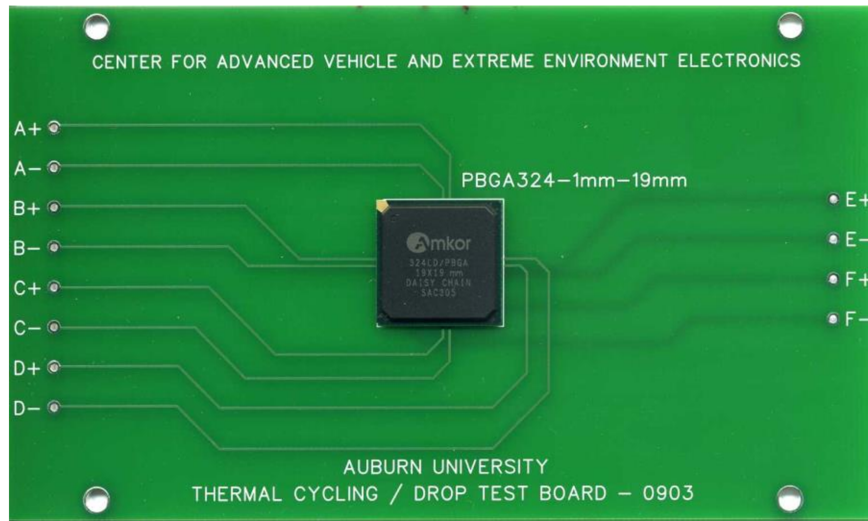

Figure 88: 324 I/O Package & Assembly

Table 25: Attributes of Test Vehicles

Solder Alloy	Sn3Ag0.5Cu
Package Size (mm)	19 mm
Package Type	Plastic BGA
I/O Count	324
I/O Pitch (mm)	1

Ball Diameter (mm)	0.5
Pad (board)	NSMD
Pad (package)	SMD
Board Surface Finish	ImAg
Daisy Chains	4
Daisy Chain Resistance	1.3 Ω ±2 Ω

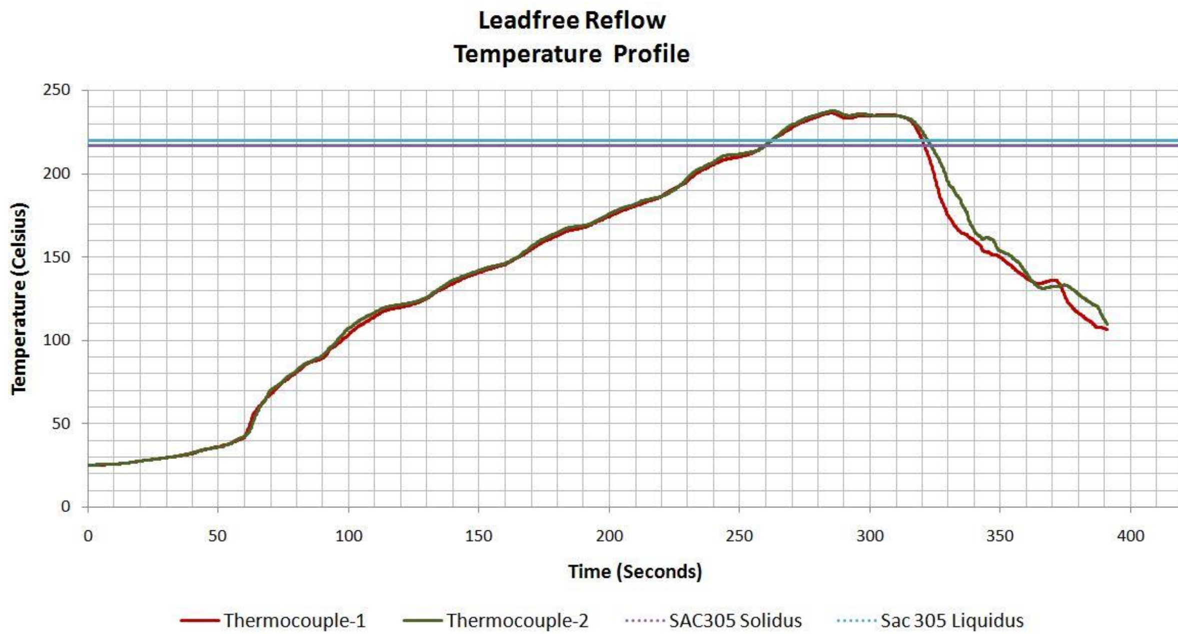

Figure 89: Reflow Profile for SAC Alloy.

6.3 Approach for Prognostication of Damage from Sequential Exposure to Thermo-mechanical Stresses

As explained in above section, in this approach packages were subjected to multiple thermal environments, first they subjected to variety of thermal aging conditions including 60°C, 85°C and 125°C for periods of time between 1-week and 2-months, thermal cycling from -55°C to 125°C, -40°C to 95°C and 3°C to 100°C. The approach has been developed in three steps as shown in Figure 90.

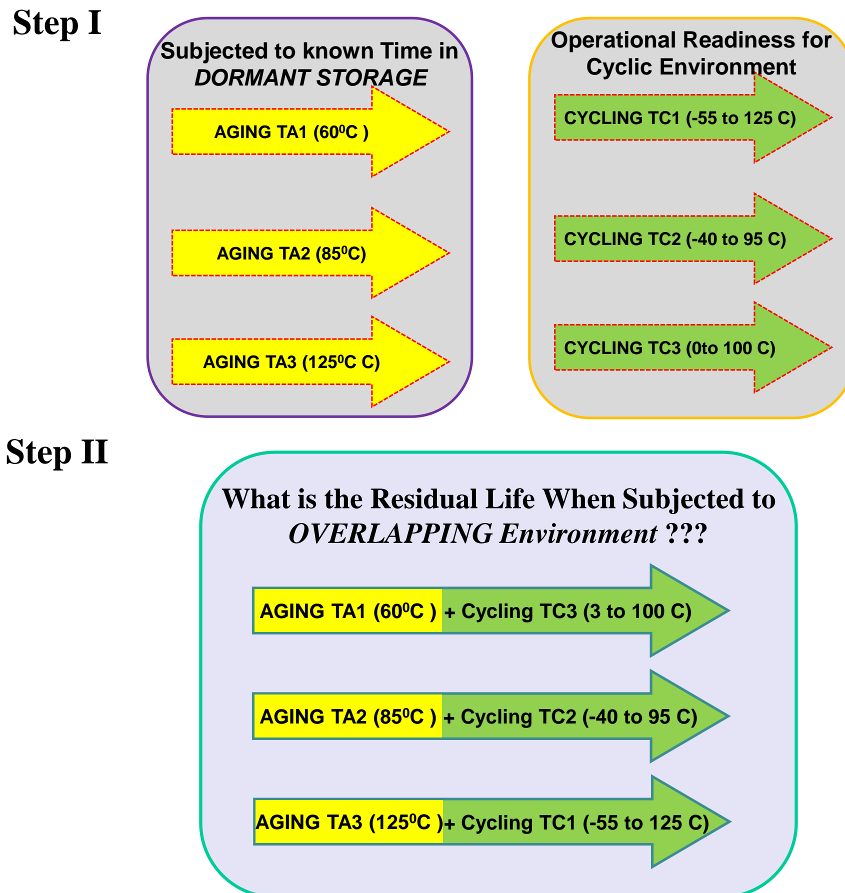

Figure 90: Exposure of Electronics Sequential Stresses of Thermal Aging and Cycling

6.3.1 Micro-structural Evolution of Damage

In this step, board assemblies have been subjected to single stresses of thermal aging and thermal cycling. Samples have been withdrawn periodically and cross- sectioned. Damage proxies studied include the phase-growth parameter and the intermetallic thickness. Previously, it has been shown that the rate of change in phase growth parameter [d(lnS)/d(lnN)] is valid damage proxy for prognostication of thermo-mechanical damage in solder interconnects and assessment of residual life [Lall 2004a-d, 2005a-b, 2006a-f, 2007a-e, 2008a-f, 2009a-d, 2010a-j, 2011]. The damage proxy [d(lnS)/d(lnN)] is related to the microstructural evolution of damage by the following equation:

$$S = g^4 - g_0{}^4 = at^b \exp\left(\frac{-E_A}{K_B T}\right)^b \qquad (1)$$

Where, g is the average grain size at time of prognostication, g0 is the average grain size of solder after reflow, N is the number of thermal cycles, S is the phase growth parameter, parameters a and b are the coefficient and exponent respectively, E_A is the activation energy, K_B is the Boltzmann Constant (8.617 x 10^{-5} ev/K), T is the temperature in Kelvin. Cross-sectioned/polished samples were then gold sputter coated so as to take confocal microscopic images at 1000x magnification. Most of the SnAgCu solder is comprised of Sn-phases, so that the growth rate of tin and Ag_3Sn Intermetallic crystals are significant. The quantitative measure of Ag3Sn particle size was established from a 100 µm x 75 µm rectangular region selected from a backscattered image of a highest strain corner solder ball. To measure the phase size, first the images were cropped to a size of 60µm x 45µm and then mapped to gray scale image to calculate

the average phase size for selected region using NI-IMAQ imaging software. Figure 91 shows the mapping of actual image to gray scale using imaging software.

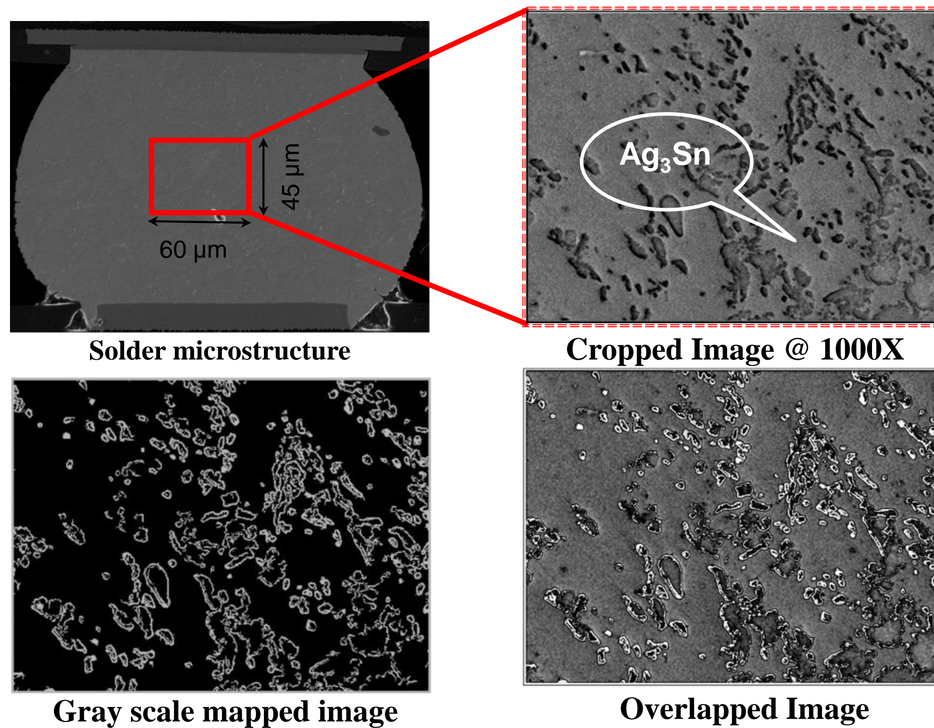

Figure 91: Micrograph and Gray scale mapping of image using image analysis software

Growth of Inter-Metallic thickness during thermal aging has been studied as another leading indicator of failure in bulk solder. From past studies it has been established that growth of Intermetallic thickness is used as a damage precursor for computation of remaining useful life [Lall 2004[a-d], 2005[a-b], 2006[a-f], 2007[a-e], 2008[a-f], 2009[a-d], 2010[a-j]]. The interfacial intermetallic layers are formed between solder and copper, and some precipitates appear near the interface of the IMCs/solder. These intermetallic layers have been identified in SEM micrographs to consist

of Cu3Sn and Cu6Sn5 phases [Lall 2005a]. In order to investigate the correlation of interfacial intermetallic thickness growth versus thermal aging and thermal cycling, components have been withdrawn and cross sectioned at various intervals of thermal aging. The aged components were cross-sectioned periodically to measure the intermetallic thickness in confocal microscope using 1000x magnification. The mean thicknesses of intermetallic layers were measured using commercial image processing software on images, as a shown in Figure 92. Trend analysis of intermetallic thickness growth on SEM using image processing software, indicates a square root dependence of IMC thickness versus aging time,

$$y(t) = y_0 + kt^n \exp(\frac{-E_A}{K_B T}) \tag{2}$$

where, $y(t)$ is IMC growth thickness during aging, y_0 is the initial thickness of intermetallic compounds, k is the coefficient standing for the square root of the diffusivity at aging temperature, and t is test time, E_A is the activation energy, K_B is Boltzmann's Constant (8.65 E-05 ev/K) and T_A is aging temperature in Kelvin. The exponent value, $n = 1/2$ has been used in the above equation, because IMC formation at interface is a diffusion-controlled mechanism during aging.

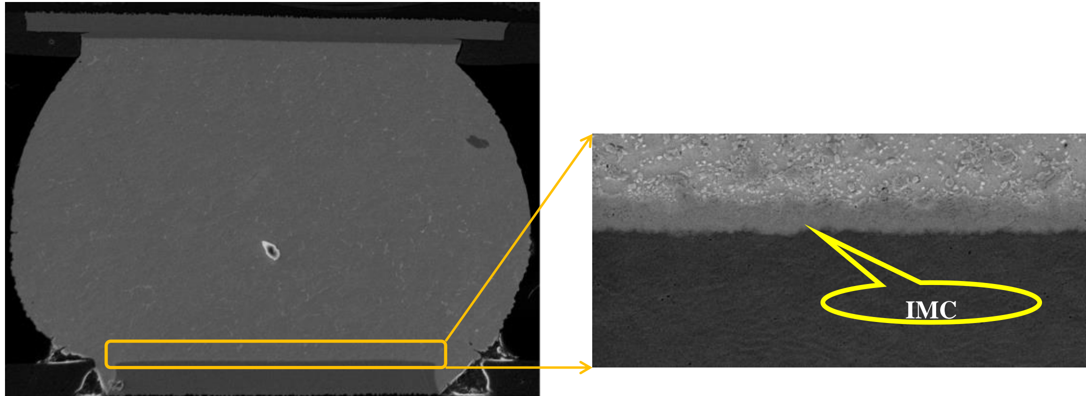

Figure 92: Back-scattered images of IMC growth (Magnification 1000x)

6.4 Damage Accrual Relationships

Three sets of test assemblies have been subjected to including 60°C, 85°C and 125°C and thermal cycling from -55°C to 125°C, -40°C to 95°C and 3°C to 100°C. Phase growth and intermetallic growth was studied using images taken by optical microscope at each time interval.

6.4.1 Thermal Aging at 60°C, 85°C and 125°C

Phase Growth as Damage Proxy

Assemblies were subjected to thermal aging at 60°C, 85°C and 125°C and withdrawn after each 168 hours increment. The samples were cross-sectioned, polished. Phase growth was studied using microscopic images at each time intervals. The image analysis software has been used to measure the average phase size Ag3Sn phases. The test data for normalized phase growth has been represented by the following equation:

$$S_{Nt} = \left[\left(\frac{g_p}{g_0}\right)^4 - 1\right] = a_0 e^{-E_a/KT} (t)^{b_0} \quad (3)$$

$$\ln S_n = \ln a_0 + b_0 \ln t \quad (4)$$

Where,

$$a_0 = a_1 \exp\frac{-E_a}{K_B T} \quad (5)$$

$$b_0 = b_1 \exp\frac{-E_b}{K_B T} \quad (6)$$

where, g is the phase-growth, subscripts p and 0 indicate point "p" and initial time respectively, S_{Nt} is the normalized phase-growth parameter during thermal aging, b_0 is the temperature dependent phase-growth exponent, E_a and E_b is the activation energy for phase-growth coefficient and exponent respectively, K is the Boltzmann constant (8.65 E-05 ev/K), T is the temperature, a_{nt} and b_{nt} are the normalized phase-growth coefficient and phase growth exponent for thermal aging.

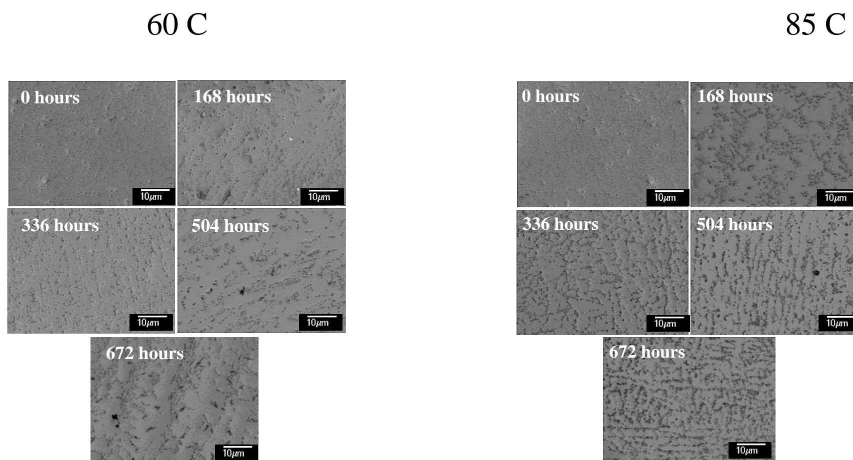

125 C

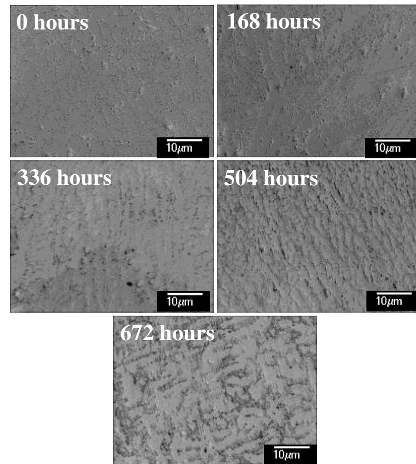

Figure 93: Backscattered image of Phase Growth versus different aging time intervals of thermal aging at (a) 60°C, (b) 85°C and (c) 125°C for 324 I/O PBGA, magnification 1000x.

Figure 94 shows the plot of normalized phase growth at different isothermal aging temperature and at various time intervals for PBGA 324. The graphs for the higher temperature have higher normalized phase growth values. The increase in normalized phase growth parameter correlates with the underlying physics, since the higher temperatures will produce more phase growth in an identical period of time. Equation (3) for phase growth evolution under thermal aging has been fit to experimental data. The equation parameters have been derived based statistical fit of the experimental data.

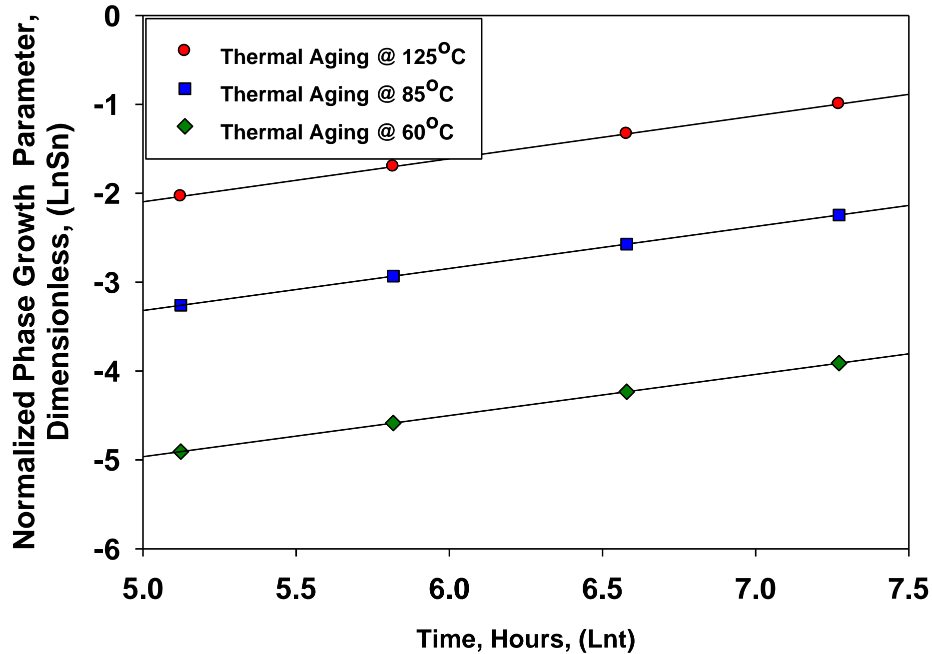

Figure 94**:** Phase growth parameter under thermal aging at 60°C, 85°C and 125°C.

Table 26 shows the values for the phase growth coefficient and the phase growth exponent for the PBGA 324. Values indicate that the aging temperature increases the value of the phase growth coefficient.

Table 26: Damage accrual relationships using phase growth as leading indicator for the 324 BGA

Thermal Aging		
60°C	**85°C**	**125°C**
S_n $=0.0007(t_{TA1})^{0.463}$	S_n $=0.0034(t_{TA1})^{0.473}$	S_n $=0.0011(t_{TA1})^{0.483}$

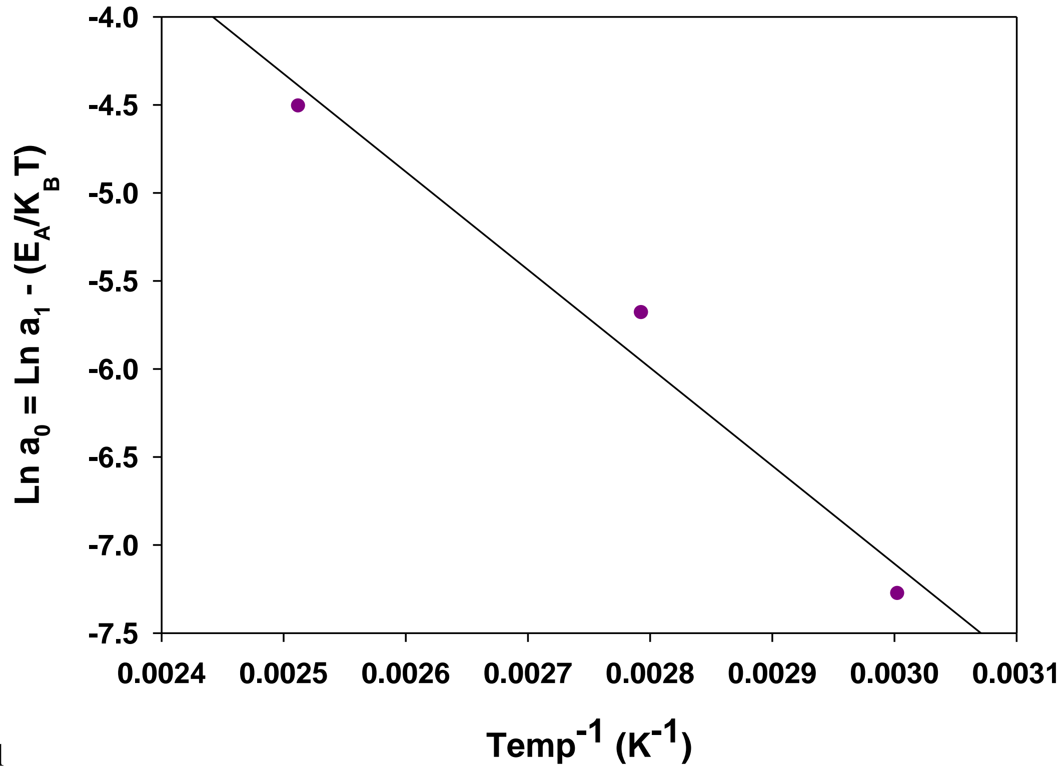

1

Figure 95: Plot between ln a_1 and Cycling temperature

Table 27: Activation energy, coefficients & exponent for all the aging temperatures

Aging Temperature (°C)	E_a	a_0	b_0
60	0.49 ev	0.00069	0.463
85		0.0034	0.473
125		0.011	0.483

Activation Energy for aging temperatures can be calculated by fitting the curve for equation (5) as shown in Figure 96. Table shows the corresponding values of activation energy, coefficients & exponent for all the aging temperatures. Slope of the fit of ln(a`) versus (1/T) is E_A/K_B, where

E_A is the activation energy; K_B is Boltzmann's Constant (8.65 E-05 ev/K). The Activation energy of phase growth is calculated as 0.49eV.

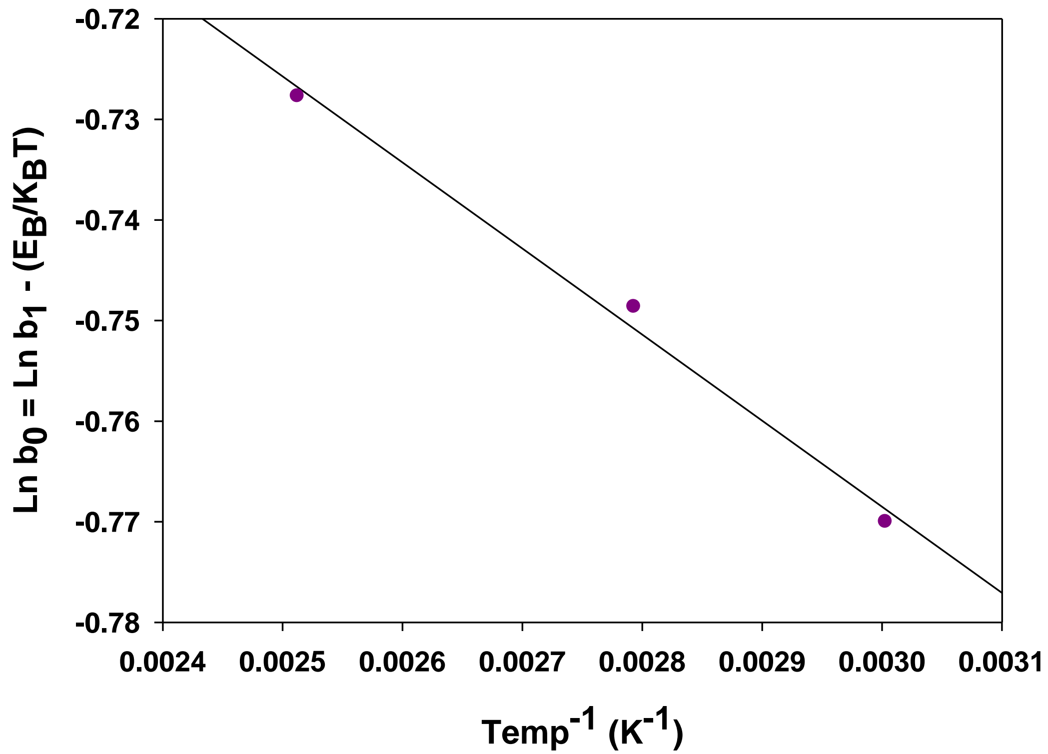

Figure 96: Plot between ln b_0 and Aging temperature

Table 28: Activation energy of Phase Growth

Package	E_b	$Ln(b_1)$
324 PBGA	0.07 ev	-2.68

Slope of this fit is E_B/K_B, where E_B is the activation energy; K_B is Boltzmann's Constant (8.65 E-05 ev/K). The Activation energy of phase growth is calculated as 0.0075eV.

Intermetallic Thickness as Damage Proxy

The intermetallic thickness based proxy has been related to aging temperature and aging time using the following normalized IMC thickness equation,

$$Y_n = \left[\frac{y_p}{y_0} - 1\right] = k_0 t^{0.5} = \left[k_1 (t)^{0.5} \exp\left(\frac{-E_{at}}{K_B T}\right)\right] \quad (7)$$

$$Y_n = k_0 \sqrt{t} \quad (8)$$

$$\ln Y_n = \ln k_0 + \frac{1}{2} \ln t \quad (9)$$

where,

$$k_0 = k_1 \exp\left(\frac{-E_{at}}{K_B T}\right) \quad (10)$$

Taking a natural logarithm of Equation (8), the relationship has been reduced to that of a straight line, where 0 k is the temperature dependent IMC-growth coefficient. From Equation (10) we can write:

$$\ln k_0 = \ln k_1 - \left(\frac{-E_A}{K_B T}\right) \quad (11)$$

By using equation (7) and (8) a relation between aging temperature (T) and aging time (t) for a particular level of damage state in terms of IMC thickness has been derived. The image analysis software has been used to measure the average intermetallic thickness. Equation (7) represents the evolution of intermetallic growth in thermal aging based on experimental data. The equation parameters have been derived based on experimental measurements of the intermetallic growth from cross-sections. The data for normalized IMC thickness has been fit to Equation (8)

Micrographs of phase structure are shown in Figure 97 for PBGA 324 at a time-interval of 168 hours. The phase-coarsening in the microstructure is clearly visible by comparison of 672 hour microstructure with 0-hour microstructure.

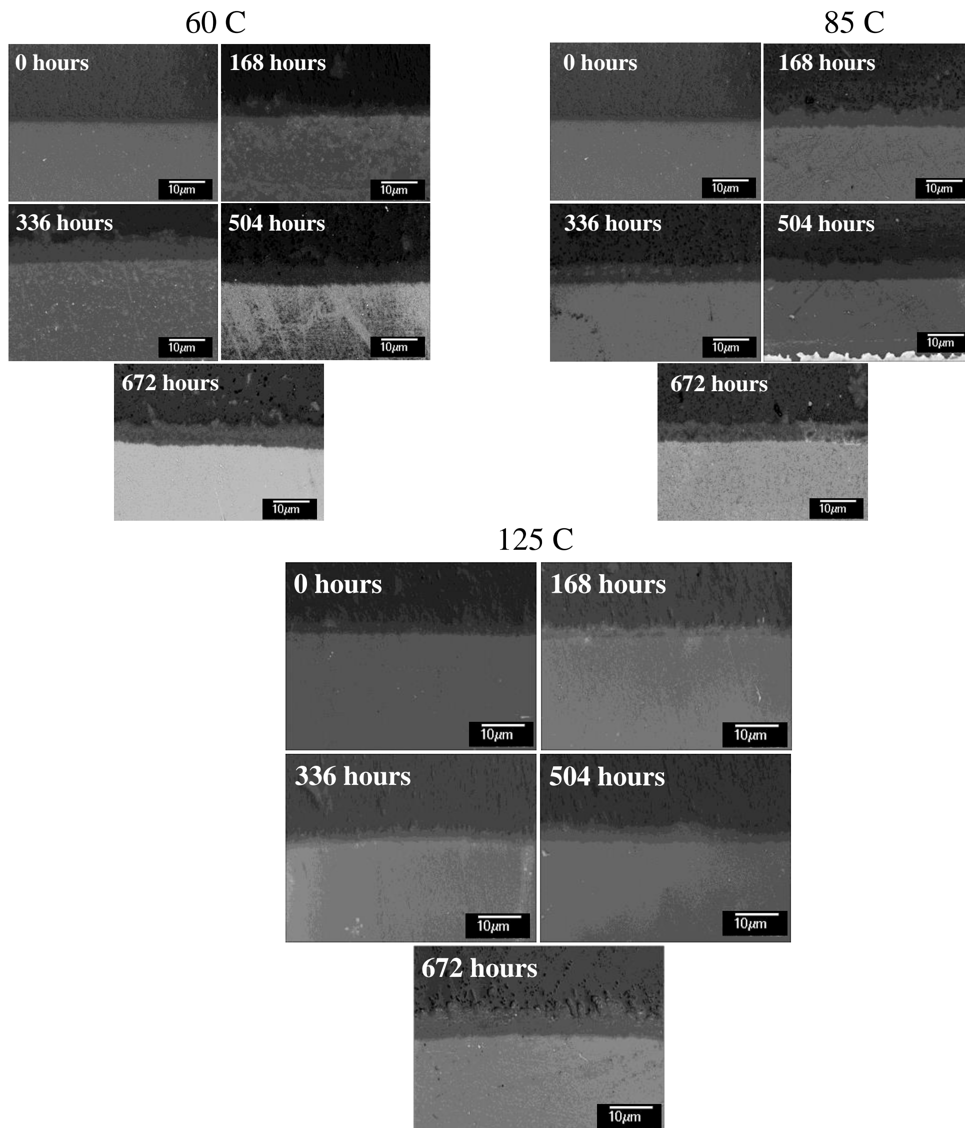

Figure 97: Backscattered image of IMC Growth versus different aging time intervals of thermal aging at (a) 60°C, (b) 85°C and (c) 125°C for 324 I/O PBGA, magnification 1000x.

Figure 98 shows the plot plots of normalized intermetallic growth at different isothermal aging temperature and at various time intervals for PBGA 324. The graphs for the higher temperature have higher normalized intermetallic growth values. The increase in normalized intermetallic thickness parameter correlates with the underlying physics, since the higher temperatures will produce more intermetallic thickness due to higher diffusion rates in an identical period of time. Equation (9) for IMC growth under thermal aging has been fit to experimental data. The equation parameters have been derived based statistical fit of the experimental data.

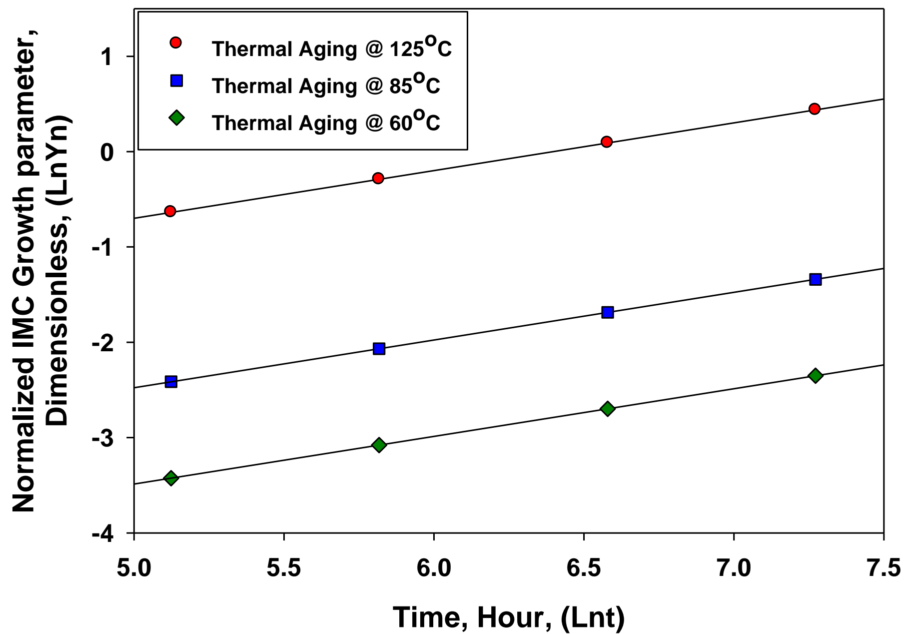

Figure 98: Relation between Normalized IMC Growth (Y_n) and Aging Time (t) for PBGA 324

Table 29 shows the values for the IMC growth coefficient for the package. Values indicate that the aging temperature increases the value of the IMC growth coefficient. The coefficient term

changes with temperature of exposure because of the underlying Fickian diffusion at the interface proceeds at a faster pace at a higher temperature.

Table 29: Values for the IMC growth coefficient

Thermal Aging		
60°C	**85°C**	**125°C**
$Y_n = 0.0025(t_{TA3})^{0.5}$	$Y_n = 0.0069(t_{TA2})^{0.5}$	$Y_n = 0.04(t_{TA1})^{0.5}$

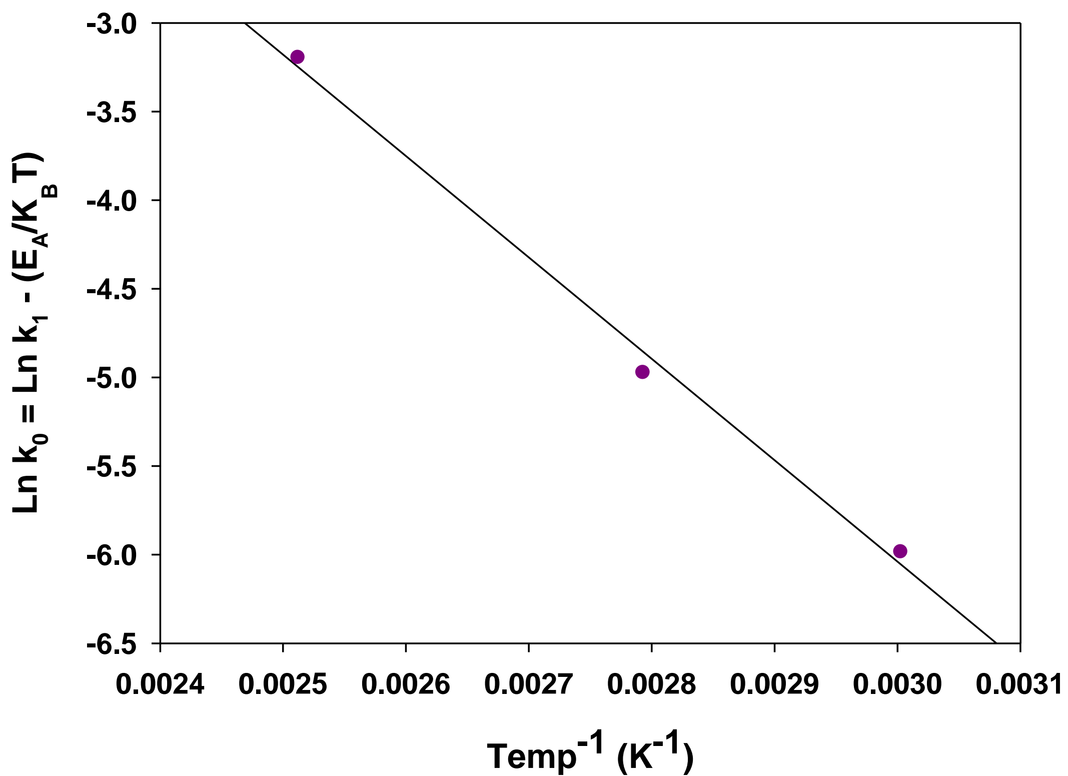

Figure 99: Plot of ln k_0 and Aging temperature Activation energy, coefficients & exponent for all the aging temperatures

Table 30: Activation Energy for IMC

Aging Temp	E_a	Lnk_1	b
60°C	0.5 ev	-5.98747	0.5
85°C		-5.28048	
125°C		-3.19907	

Slope of this fit is E_A/K_B, where E_A is the activation energy; K_B is Boltzmann's Constant (8.617 E-05 ev/K). The Activation energy of phase growth is calculated as 0.5eV.

6.4.2 Thermal Cycling at -55°C to 125°C, -40°C to 95°C and 3°C to 100°C

Phase Growth as Damage Proxy

A different set of assemblies were subjected to three different environment of thermal cycling from -55°C to 125°C, -40°C to 95°C and 3°C to 100°C and were withdrawn after each 250 cycle increments. The samples were x-sectioned, polished. Phase growth was studied using SEM images at each cyclic interval. The image analysis software has been used to measure the average phase size. The phase growth test data has been fit to the following equation:

$$S_N = \left[\left(\frac{g_p}{g_0} \right)^4 - 1 \right] = a_{N\Delta T} (\Delta T)^C e^{-E_a / K\Delta T} (N)^{b_0} \quad (12)$$

$$\ln S_N = \ln a_0 + b_0 \ln N \quad (13)$$

$$a_0 = a_{N\Delta T}(\Delta T)^C \exp\frac{-E_a}{K_B \Delta T} \tag{14}$$

Where,

$$b_0 = b_1 \exp\frac{-E_b}{K_B \Delta T} \tag{15}$$

Where g is the phase-growth, subscripts p and 0 indicate point "p" and initial time respectively, S_N is the normalized phase-growth parameter during thermal cycling, E_a is the activation energy, E_a and E_b is the activation energy for phase-growth coefficient and exponent respectively K is the Boltzmann constant (8.617 E-05 ev/K), ΔT is the temperature difference, $a_{N\Delta T}$ and $b_{N\Delta T}$ are the normalized phase-growth coefficient and phase growth exponent during thermal cycling.

-55 to 125 C

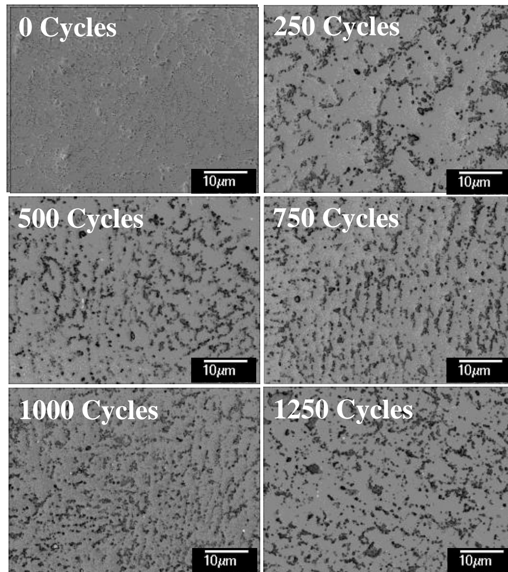

-40 to 95 C

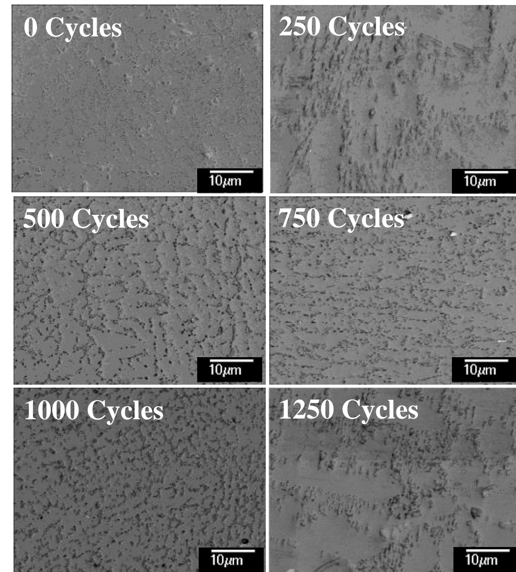

0 to 100 C

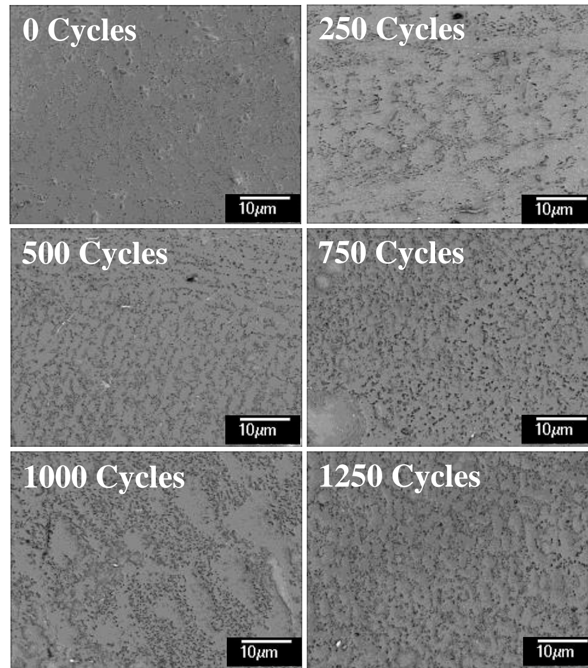

Figure 100: Backscattered image of Phase Growth versus different aging time intervals of thermal cycling at (a) -55 to 125°C, (b) -40 to 95°C and (c) 3 to 100°C for 324 I/O PBGA, magnification 1000x.

Figure 100 a, b & c shows the phase growth for the 324 BGA after various cyclic increments under -55°C to 125°C, -40°C to 95°C and 3°C to 100°C thermal cycling. Figure show the plot of the normalized phase growth parameter versus time in thermal aging.

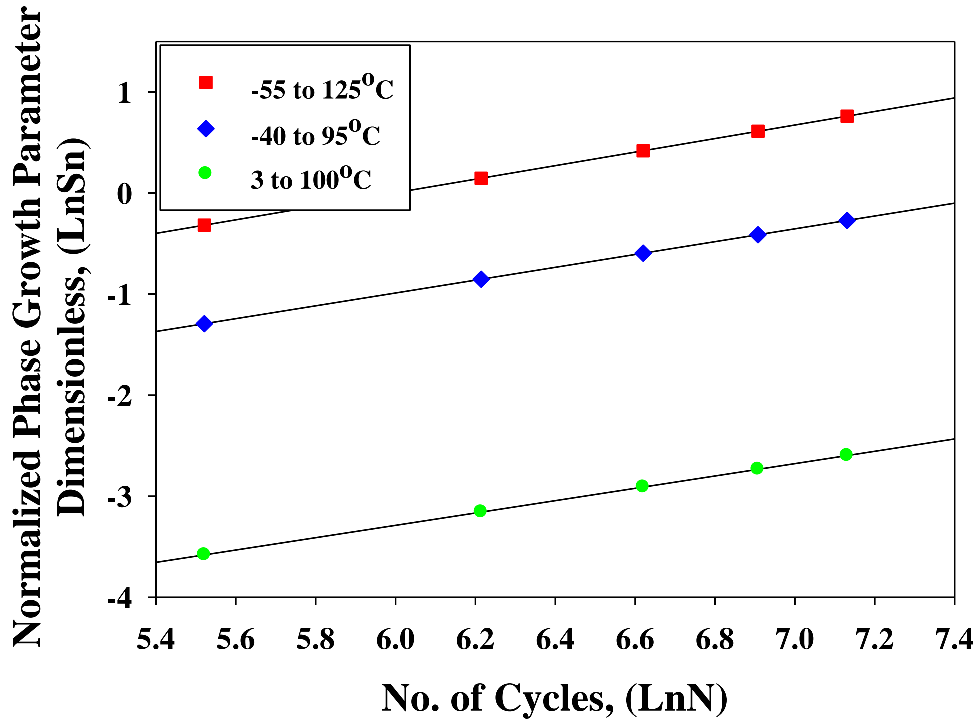

Figure 101: Plot ofPhase growth parameter vs No. of cycles under thermal cycling at -55 to 125°C, -40 to 95°C and 3 to 100°C for 324 I/O PBGA

Table 31: Damage accrual relationships using phase growth as leading indicators for the 324 BGA

Thermal Cycling		
-55 to125°C	**-40 to 95°C**	**3 to 100°C**
$S_N=$ $0.018(N_{TC1})^{0.67}$	$S_N=$ $0.00823(N_{TC2})^{0.635}$	$S_N=$ $0.00096(N_{TC3})^{0.61}$

Activation energy, coefficients and exponent can be calculated by solving the equation 13 for all the three different cyclic environments -55 to 125°C, -40 to 95°C and 3 to 100°C.

$$\ln a_0^1 = \ln a_1 + C\ln(180) - \frac{E_{aN}}{K(453)} \quad (16)$$

$$\ln a_0^2 = \ln a_2 + C\ln(135) - \frac{E_{aN}}{K(408)} \quad (17)$$

$$\ln a_0^3 = \ln a_3 + C\ln(97) - \frac{E_{aN}}{K(370)} \quad (18)$$

Solving above equations (16), (17) and (18) we get all the unknowns E_a, a, and b as shown in Table 31.

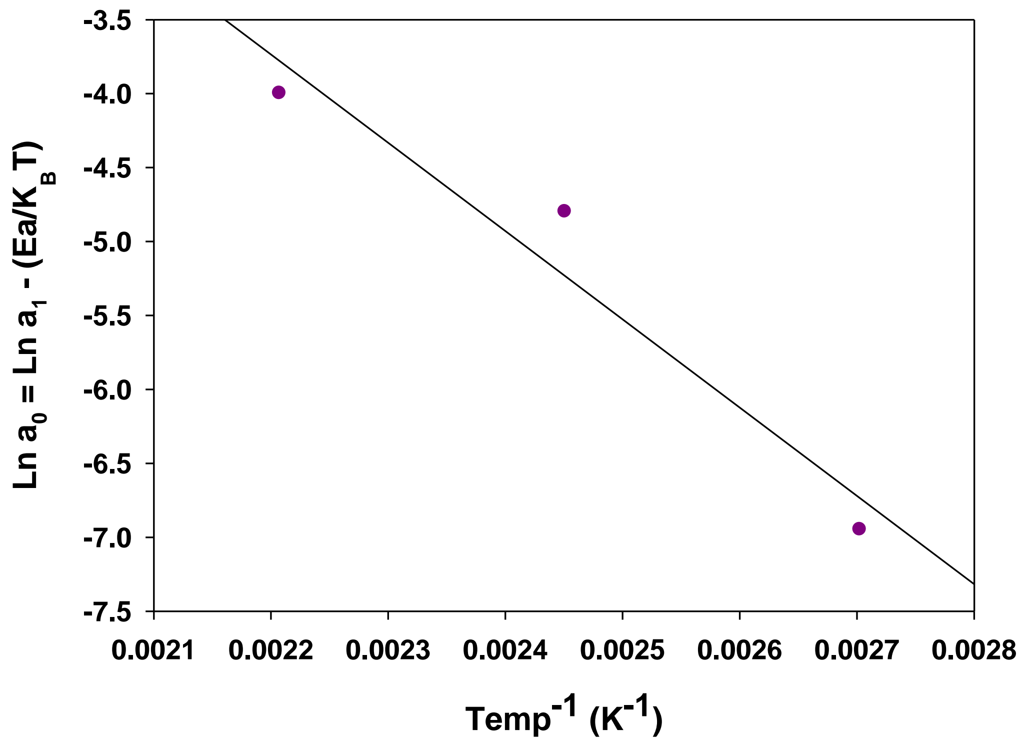

Figure 102: Plot between ln a_0 and Cycling temperature

Table 32: Activation energy, coefficients & exponent for all the cyclic temperatures

Thermal Cycling	**Ea**	**Lna`**	**b**
-55 to 125°**C**	0.52 ev	-4	0.67
-40 to 95°**C**		-4.8	0.635
3 to 100°**C**		-6.95	0.61

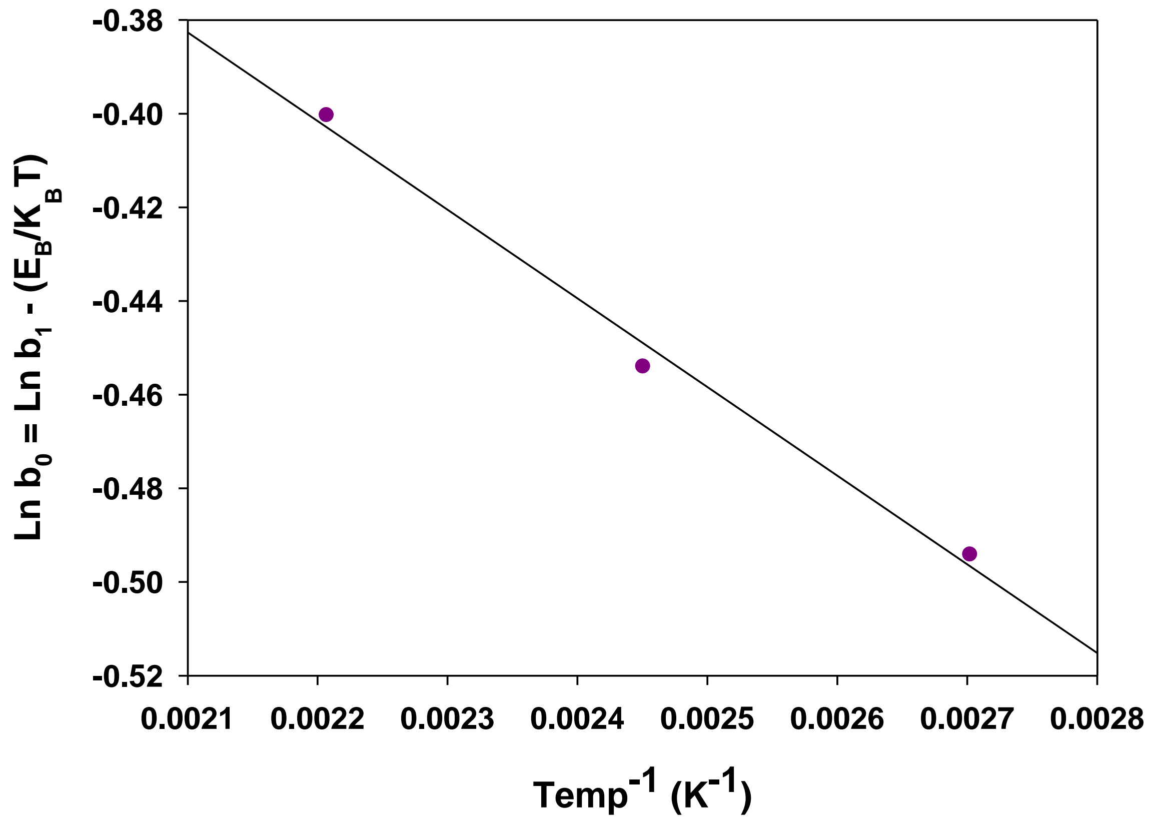

Figure 103: Plot between ln b_0 and Cycling temperature

Table 33: Activation Energy for exponent

Package	**E_b**
324 PBGA	0.016 ev

Slope of this fit is E_B/K_B, where E_B is the activation energy; K_B is Boltzmann's Constant (8.617 E-05 ev/K). The Activation energy of phase growth is calculated as 0.016eV.

Intermetallic Thickness as Damage Proxy

The intermetallic thickness based proxy has been related to cycling temperature, using the following normalized IMC thickness equation,

$$Y_N = \left[\frac{y_p}{y_0} - 1\right] = k_0 N^{b_o} = \left[k_1 (N)^{b_o} \exp\left(\frac{-E_a}{K_B \Delta T}\right)\right] \quad (19)$$

$$\ln Y_N = \ln k_0 + b_0 \ln N \quad (20)$$

where,

$$k_0 = k_1 \exp\left(\frac{-E_a}{K_B \Delta T}\right) \quad (21)$$

$$b_0 = b_1 \exp \frac{-E_b}{K_B \Delta T} \quad (22)$$

Taking a natural logarithm of Equation (19), the relationship has been reduced to that of a straight line, where 0 k is the temperature dependent IMC-growth coefficient. From Equation (21) we can write:

$$\ln k_0 = \ln k_1 - \left(\frac{-E_A}{K_B \Delta T} \right) \tag{23}$$

By using equation (10) and (14) a relation between cycling temperature (T) and cycling (N) for a particular level of damage state in terms of IMC thickness has been derived. The image analysis software has been used to measure the average intermetallic thickness. Equation (10) represents the evolution of intermetallic growth in thermal cycling based on experimental data. The equation parameters have been derived based on experimental measurements of the intermetallic growth from cross-sections. The data for normalized IMC thickness has been fit to Equation (10). Micrographs of phase structure are shown in Figure 104 for PBGA 324 at a-interval of 250 cycles.

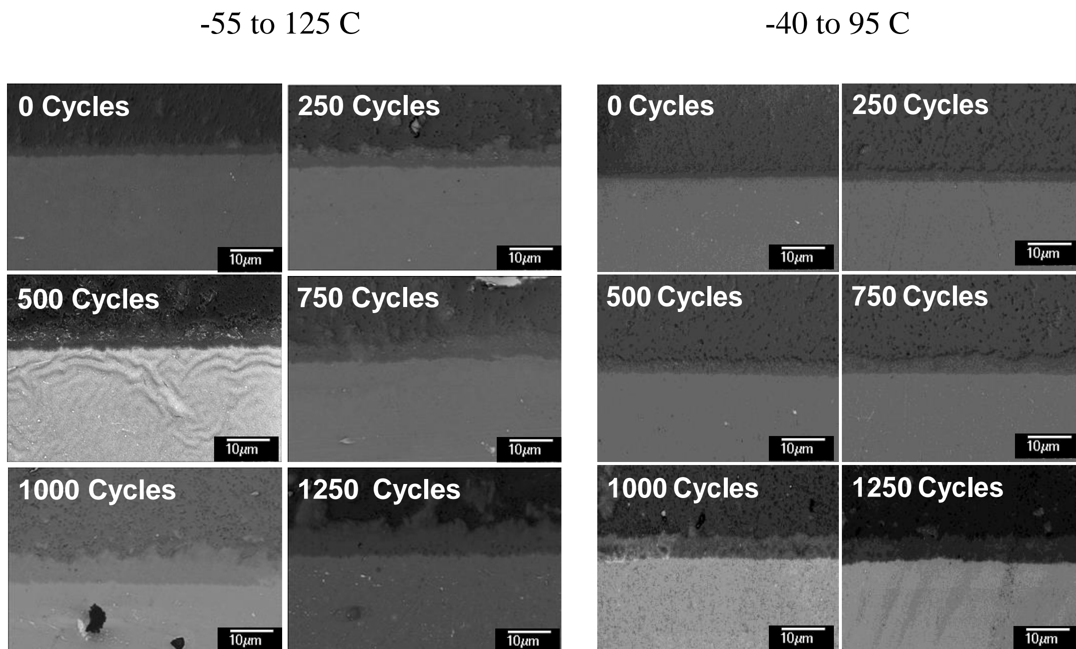

3 to 100 C

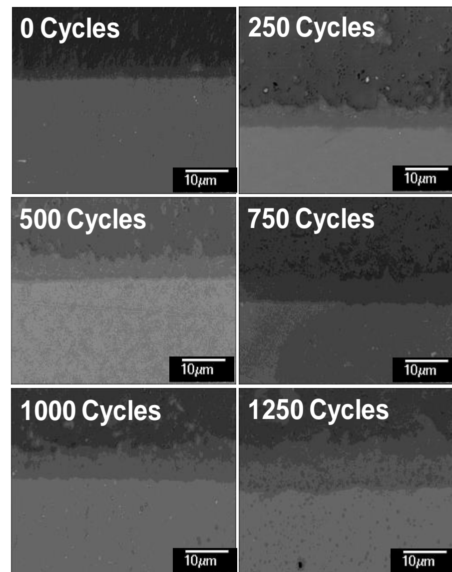

Figure 104: Backscattered image of IMC Growth versus different aging time intervals of thermal cycling at (a) -55 to 125°C, (b) -40 to 95°C and (c) 3 to 100°C for 324 I/O PBGA, magnification 1000x

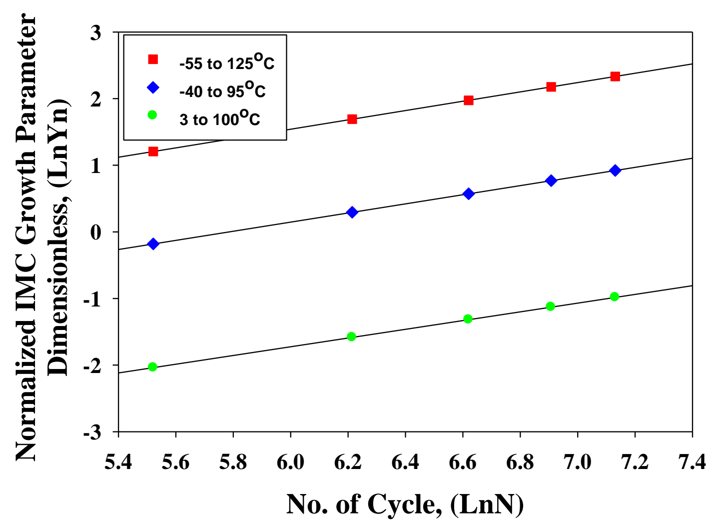

Figure 105: IMC growth parameter under thermal cycling at -55 to 125°C, -40 to 95°C and 3 to 100°C for 324 I/O PBGA

Table 34: Damage accrual relationships using IMC growth as leading indicators for the 324 BGA

	-55 to125°C	-40 to 95°C	3 to 100°C
324 BGA	$Y_N= 0.07(N)^{0.7}$	$Y_N= 0.019(N)^{0.685}$	$Y_N= 0.0035(N)^{0.655}$

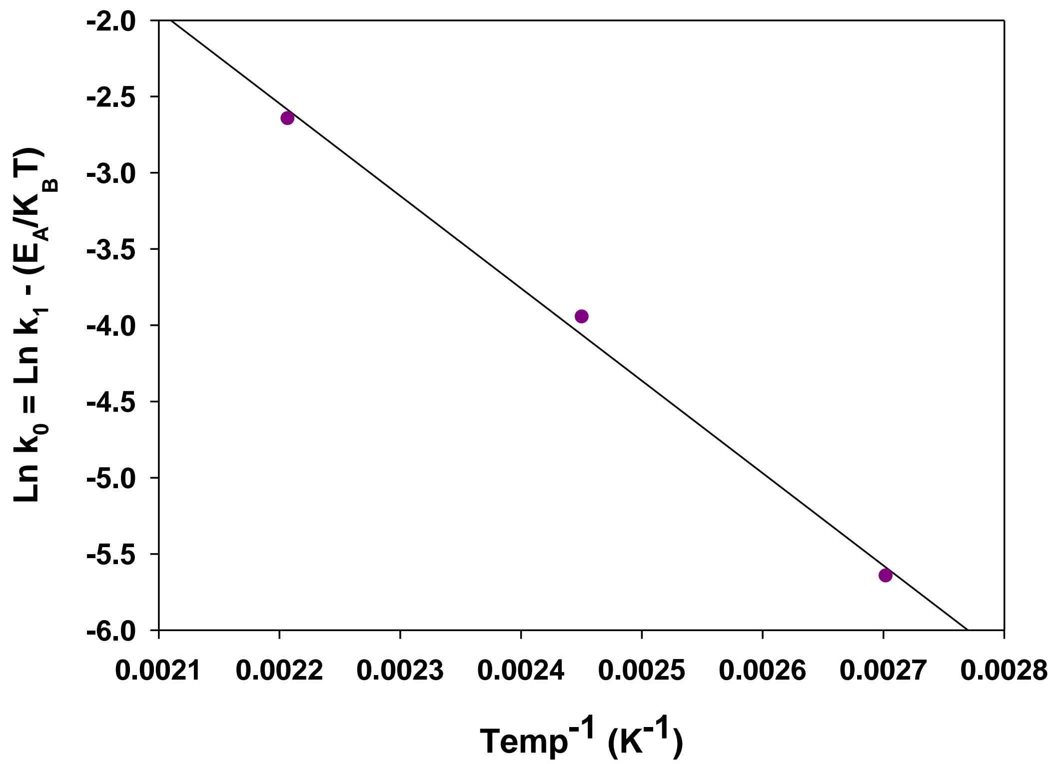

Figure 106: Plot between $\ln k_0$ and Cycling Temperature

Table 35: Activation energy, coefficients & exponent for all the cyclic temperatures

Thermal Cycling	Ea	Lnk`	b_0
-55 to 125°**C**	0.53 ev	-2.65	0.7
-40 to 95°**C**		-3.95	0.685
3 to 100°**C**		-5.65	0.655

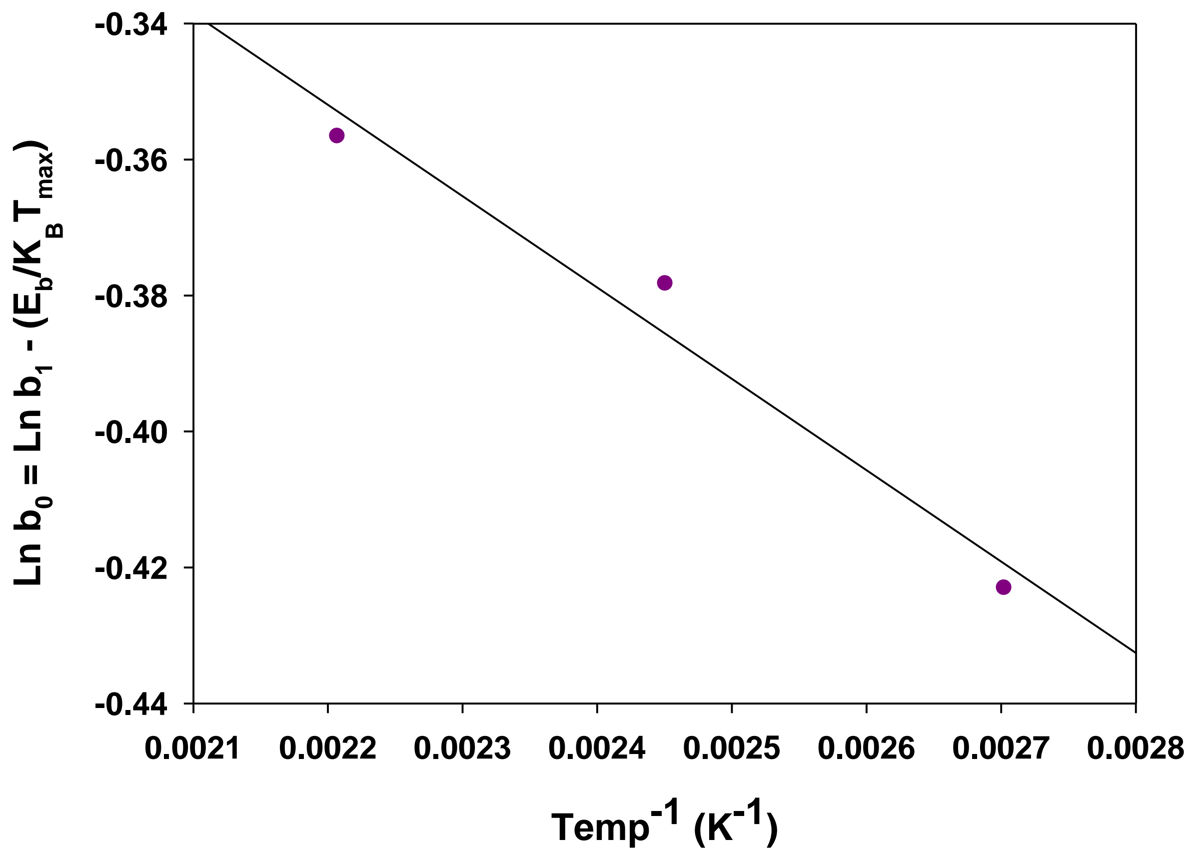

Figure 107: Plot between $\ln b_0$ and Cycling Temperature

Table 36: Value of Activation Energy

Package	E_b
324 PBGA	0.0116 ev

Slope of this fit is E_B/K_B, where E_B is the activation energy; K_B is Boltzmann's Constant (8.617 E-05 ev/K). The Activation energy of IMC growth exponent is calculated as 0.0116eV.

6.5 Damage Equivalency Relationships between Thermal Aging and Thermal-Cycling

Damage accrued from aging and cycling environments has been equivalenced based on normalized phase growth and normalized IMC growth. Damage equivalency relationships between thermal aging and thermal cycling can be obtained by equating 10 and 12.

From Phase Growth, $a_{N\Delta T}(\Delta T)^C e^{-E_a/KT_{max}}(N)^{b_{0N\Delta T}} = a_{nt} e^{-E_a/KT}(t)^{b_{0T}}$ (24)

$$N = \left[\left(\frac{a_{nt}}{a_{N\Delta T}}\right)\left(\frac{(t)^{b_{0T}}}{(\Delta T)^C}\right)\left(\frac{e^{\left(-E_{at}/K_B T\right)}}{e^{\left(-E_{aN}/K_B T_{max}\right)}}\right)\right]^{1/b_{N\Delta T}} \tag{25}$$

From IMC Growth,

$$a_t(t)^{0.5} e^{\left(-E_{at}/KT\right)} = \left[a_{N\Delta T} e^{\left(-E_{aN}/KT\right)}\right](N)^{b_{N\Delta T}} \tag{26}$$

$$N = \left[\left(\frac{a_t}{a_{N\Delta T}}\right)\left(\frac{(t)^{0.5}}{T}\right)\left(\frac{e^{\left(-E_{at}/KT\right)}}{e^{\left(-E_{aN}/KT\right)}}\right)\right]^{1/b_{N\Delta T}} \tag{27}$$

In Figure 108 the evolution of normalized phase growth normalized IMC growth has been plotted versus thermal cycles in -55°C to 125°C and thermal aging time at 125°C. This combined plot is helpful for mapping of damage from thermal aging onto thermal cycling. Intermetallic thickness can be obtained by exposure to single stresses of thermal aging and thermal cycling. The exposure length to the environmental stresses however, will be different in each case.

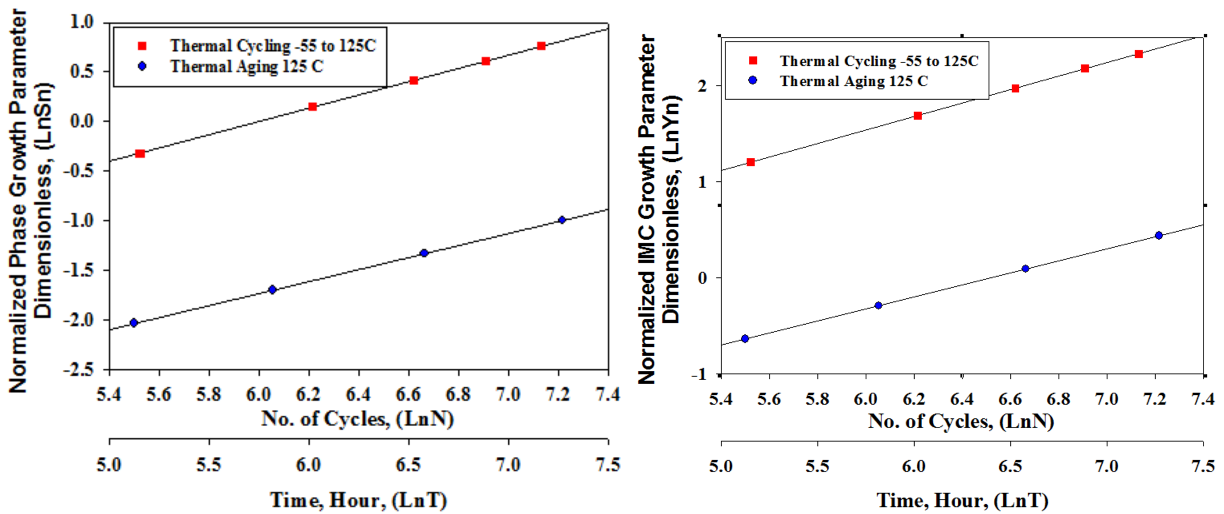

Figure 108: Combined plot Normalized Phase growth and Normalized IMC growth versus thermal aging time/thermal cycling.

Table 37**:** Damage equivalency between TA3 @ 125C and TC1 @ -55C to 125C for the 324 PBGA

Damage Equivalency	
Phase Growth	IMC
$0.011(t_{TA3})^{0.0.483} = 0.018(N_{TC1})^{0.67}$	$0.0408(t_{TA3})^{0.5} = 0.07(N_{TC1})^{0.7}$
$N_{TC1}=0.4795(t_{TA3})^{0.72}$	$N_{TC1}=0.462(t_{TA3})^{0.714}$

Similar damage-mapping relationships have been obtained for both the damage proxies measured in the experiments confirming the validity of the correlation. In Figure the evolution of

normalized phase growth normalized IMC growth has been plotted versus thermal cycles in -45°C to 95°C and thermal aging time at 85°C.

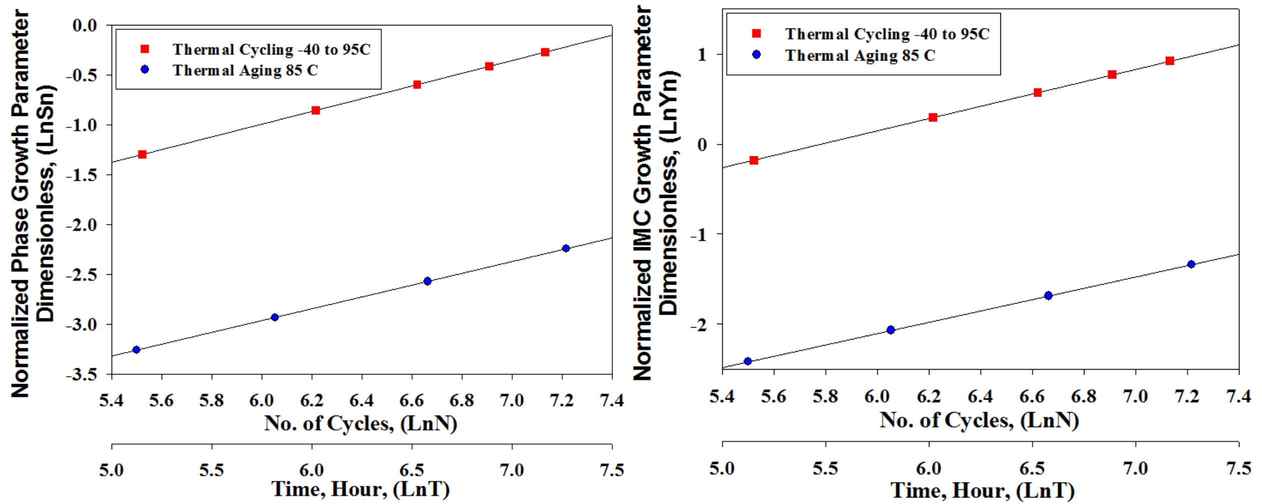

Figure 109: Combined plot Normalized Phase growth and Normalized IMC growth versus thermal aging time/thermal cycling.

Combined plot Normalized Phase growth and Normalized IMC growth versus thermal aging time/thermal cycling.

Table 38: Damage equivalency between TA2 @ 85C and TC2 @ -45C to 95C for the 324 PBGA

Damage Equivalency	
Phase Growth	IMC
$0.0034(t_{TA2})^{0.473} = 0.00823(N_{TC2})^{0.635}$	$0.0069(t_{TA2})^{0.5} = 0.019(N_{TC2})^{0.685}$
$N_{TC2}=0.25(t_{TA2})^{0.74}$	$N_{TC2}=0.23(t_{TA2})^{0.73}$

Similar damage-mapping relationships have been obtained for both the damage proxies measured in the experiments confirming the validity of the correlation. The evolution of

normalized phase growth normalized IMC growth has been plotted versus thermal cycles in 3°C to 100°C and thermal aging time at 60°C.

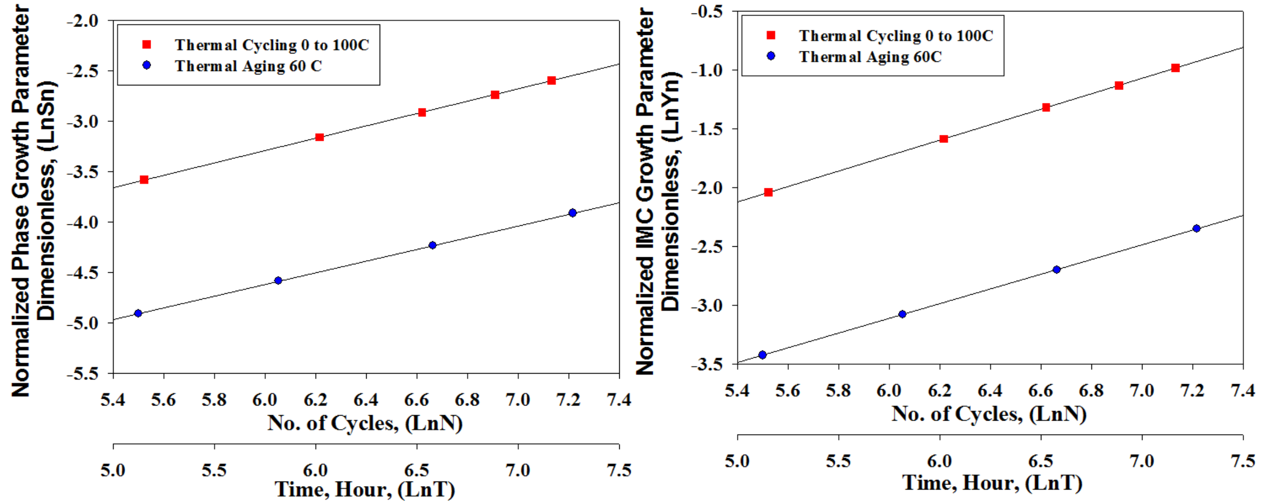

Figure 110**:** Combined plot Normalized Phase growth and Normalized IMC growth versus thermal aging time/thermal cycling.

Table 39: Damage equivalency between TA1 @ 60C and TC3 @ 0 to 100C for the 324 PBGA

Damage Equivalency	
Phase Growth	IMC
$0.00069(t_{TA1})^{0.463} = 0.00096(N_{TC3})^{0.61}$	$0.0025(t_{TA1})^{0.5} = 0.0035(N_{TC3})^{0.655}$
$N_{TC3}=0.72(t_{TA1})^{0.76}$	$N_{TC3}=0.6(t_{TA1})^{0.763}$

6.5 Prognostication of Damage under Overlapping Stresses

Test assemblies have been exposed to three different combinations of overlapping sequential stresses of thermal aging at 125°C and thermal cycling from -55 to 125°C, thermal aging at 85°C and thermal cycling from -45 to 95°C and thermal aging at 60°C and thermal cycling from 3 to 100°C. Both the steady-state exposure and cyclic-thermal exposure has been done for various lengths for multiple sets of test assemblies. The system state has been interrogated using both the damage proxies discussed in this paper including phase-growth parameter and intermetallic growth. Samples have been withdrawn at periodic intervals and x-sectioned for measurement of the damage proxies. The LM-Algorithm has been used for interrogation of system-state for accrued damage.

Case I: Overlapping sequential stresses of thermal aging at 125°C and thermal cycling from -55 to 125°C

The phase growth and intermetallic thickness has been studied under microscope (Figure 111). The samples were prognosticated using the Levenberg-Marquardt Algorithm.

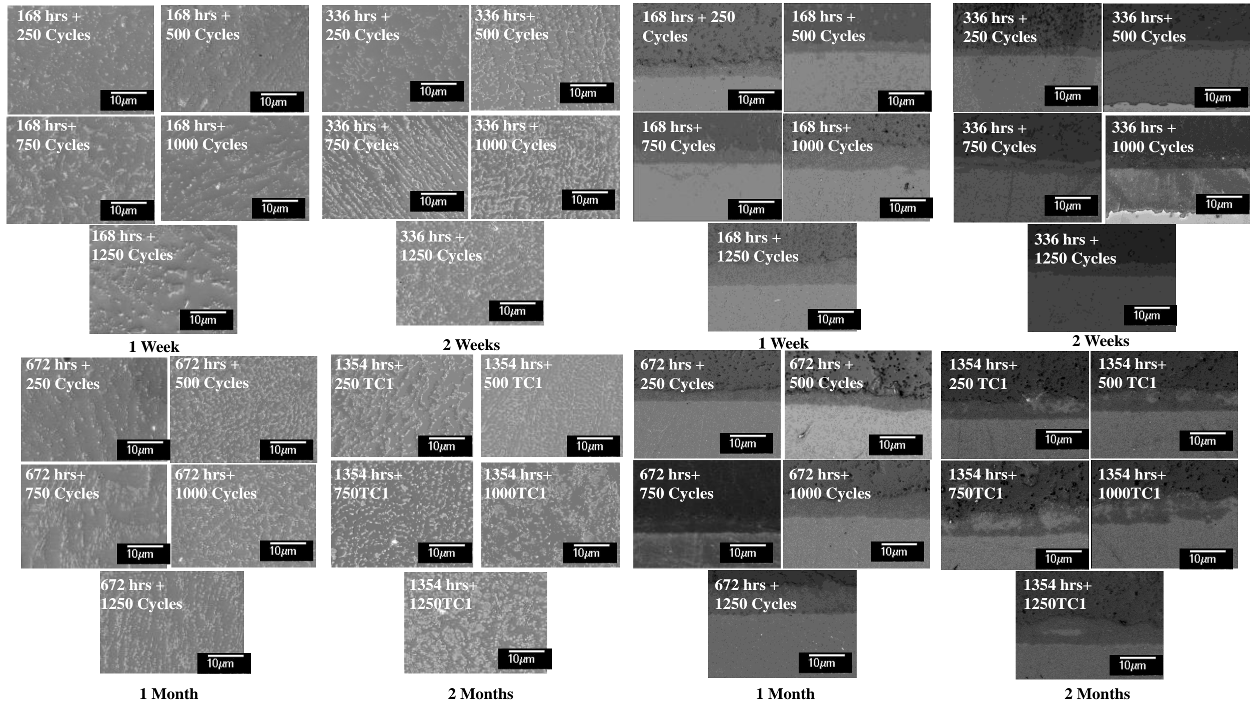

Figure 111: Back-scattered Images for samples exposed to Environments of x hours @ 125°C + y CyclesTC-1 magnification 1000x (a) Phase Growth (b) IMC, 324 I/O PBGA

Table 40 shows the effect of exposure to various hours of thermal aging at 125°C on the thermal cycling under -55°C to 125°C.

Table 40: Effect of exposure to x-hours of thermal aging at 125C on the thermal cycling life under -55 to 125C

Aging time hrs	Reduction in life using ***Phase Growth*** as Damage proxy (cycles)	Reduction in life using ***IMC*** as Damage proxy (cycles)
	$N_{TC1}=0.48(t_{TA3})^{0.72}$	$N_{TC1}=0.462(t_{TA3})^{0.714}$
168	19	18
336	32	29
672	52	48
1354	86	80

Figure 112 and Figure 113 shows the prognosticated values of accrued damage in BGA assemblies after they have been subjected to x hours of thermal aging in TC3 + 250 Cycles of thermal cycling in TC1 (-55°C to 125°C). The accrued damage has been prognosticated using both phase growth parameter and the intermetallic growth.

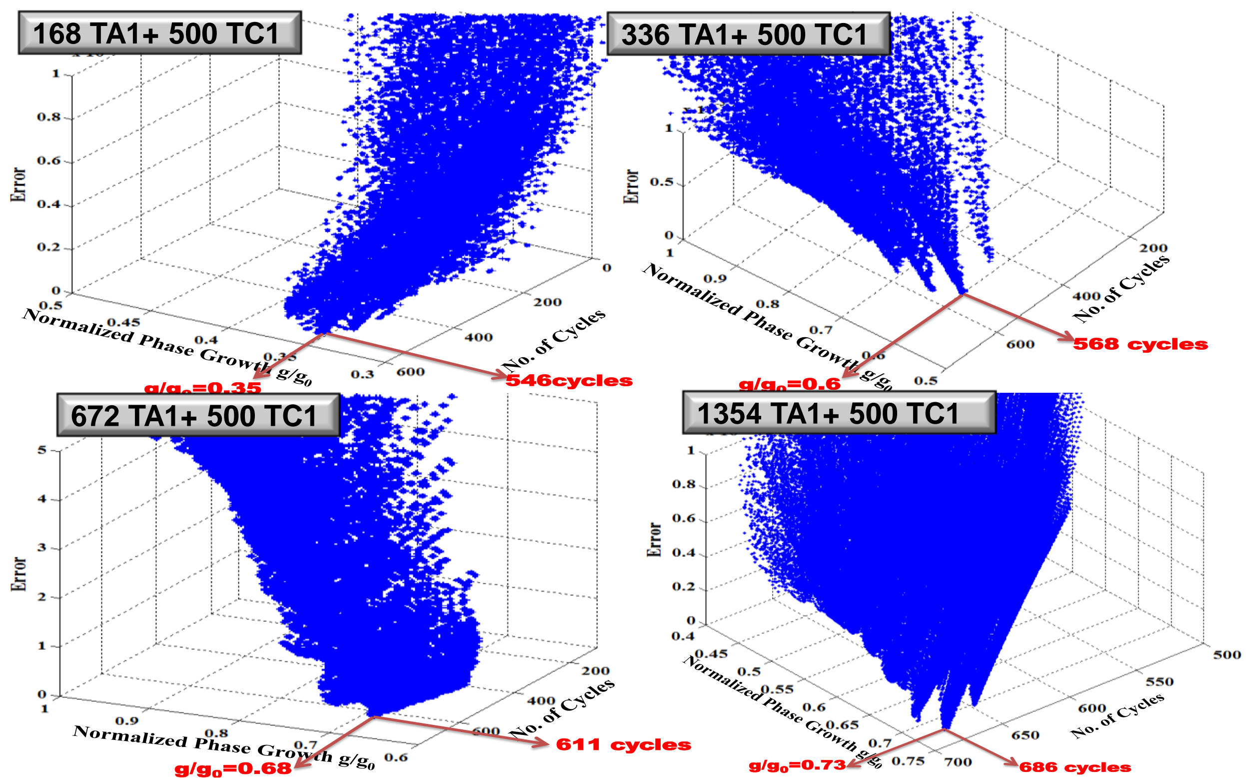

Figure 112: 3D plot of error versus Number of Cycles, Life computed from LM-algorithm for x-hrs TA3 + 250 cycles TC1 using Phase Growth as damage Proxy

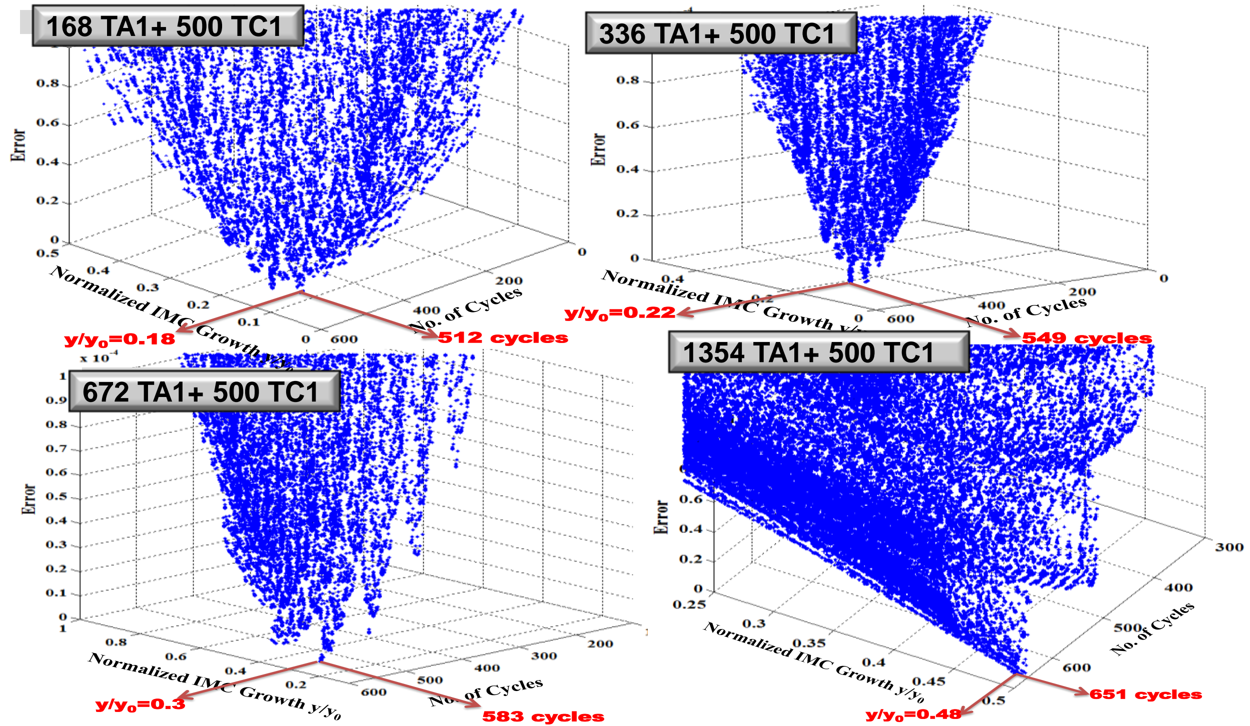

Figure 113: 3D plot of error versus Number of Cycles, Life computed from LM-algorithm for x-hrs TA3 + 250 cycles TC1 using IMC as damage Proxy

Table 41: Prognostication of Overlapping Damage

	Phase Growth	IMC Growth
168 TA1 + 250 TC1 (Units of TC1 cycles), (A)	269	268
168 TA1 + 500 TC1 (Units of TC1 cycles), (B)	523	527
(B)-(A)	254	259
336 TA1 + 250 TC1 (Units of TC1 cycles), (C)	282	279
336 TA1 + 500 TC1	542	539

(Units of TC1 cycles), (D)		
(D)-(C)	260	260
672 TA1 + 250 TC1 (Units of TC1 cycles), (E)	302	298
672 TA1 + 500 TC1 (Units of TC1 cycles), (F)	567	571
(F)-(E)	265	273
1354 TA1 + 250 TC1 (Units of TC1 cycles), (G)	336	330
1354 TA1 + 500 TC1 (Units of TC1 cycles), (H)	582	593
(H)-(G)	246	263

For the 324 BGA package, using phase growth parameter as the damage proxy, the prior accrued damage when subjected to (a) 168 hours TA3 + 250 Cycles TC1 was calculated to be 269 TC1 cycles, (b) 336 hours TA3 + 250 Cycles TC1 was calculated to be 282 TC1 cycles, (c) 672 hours TA3 + 250 Cycles TC1 was calculated to be 302 TC1 cycles and (d) 1354 hours TA3 + 250 Cycles TC1 was calculated to be 336 TC1 cycles. It is known that the difference in the prognosticated damage between the test assemblies which have been subjected to x-hours TA3 + 250 Cycles TC1 and x- hours TA3 + 500 Cycles TC1 is 250 cycles of TC1. The actual value of 250 TC1 cycles correlates well with the prognosticated values of 254, 260, 265 and 246 TC1 cycles

A similar process has been followed using the IMC growth damage proxy package, using IMC growth parameter as the damage proxy, the prior accrued damage when subjected to (a) 168 hours TA3 + 250 Cycles TC1 was calculated to be 268 TC1 cycles, (b) 336 hours TA3 + 250 Cycles TC1 was calculated to be 279 TC1 cycles, (c) 672 hours TA3 + 250 Cycles TC1 was calculated to be 298 TC1 cycles and (d) 1354 hours TA3 + 250 Cycles TC1 was calculated to be 330 TC1 cycles. It is known that the difference in the prognosticated damage between the test assemblies which have been subjected to x-hours TA3 + 250 Cycles TC1 and x- hours TA3 + 500 Cycles TC1 is 250 cycles of TC1. The actual value of 250 TC1 cycles correlates well with the prognosticated values of 259, 260, 273 and 263 TC1 cycles as shown in Table 41.

Case II: Overlapping sequential stresses of thermal aging at 85°C and thermal cycling from -45 to 95°C

The phase growth and intermetallic thickness has been studied under microscope Figure 114. The samples were prognosticated using the Levenberg-Marquardt Algorithm.

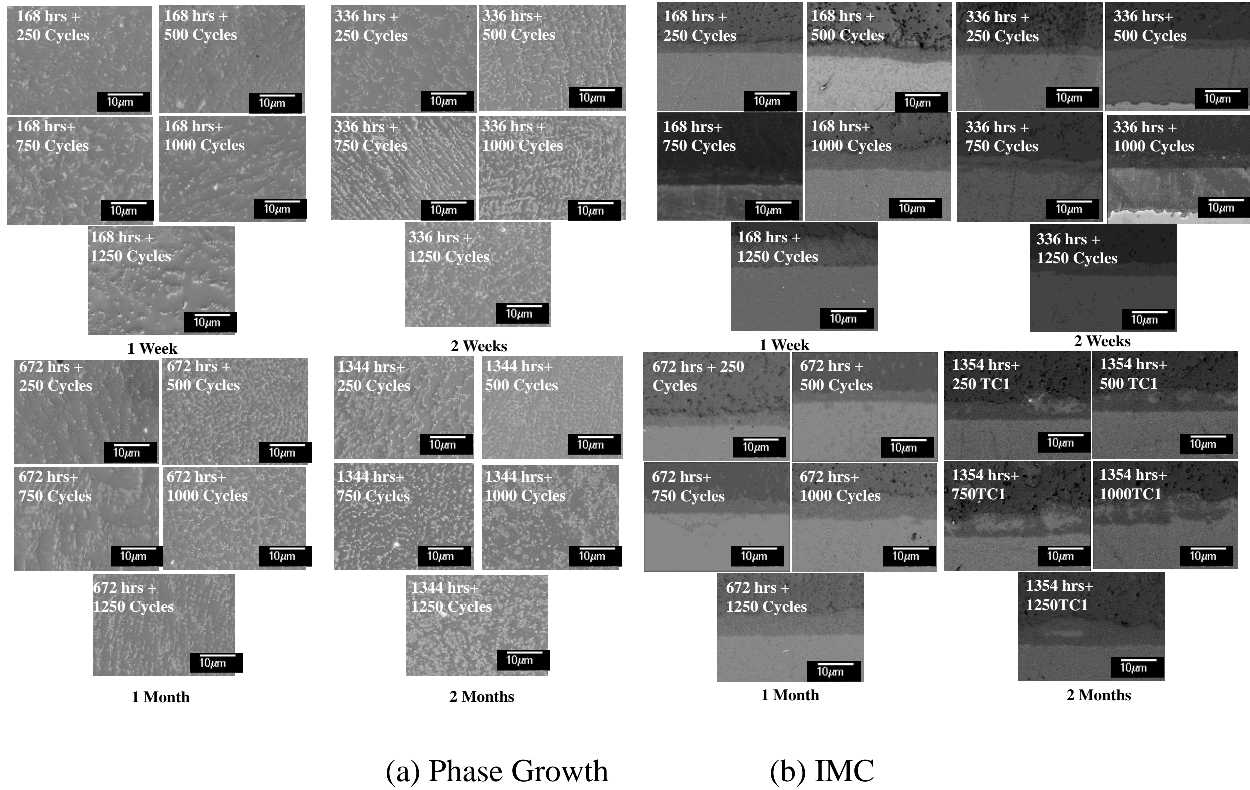

(a) Phase Growth (b) IMC

Figure 114: Back-scattered Images for samples exposed to Environments of x hours @ 85°C + y CyclesTC-2 magnification 1000x (a) Phase Growth (b) IMC, 324 I/O PBGA

Table 42 shows the effect of exposure to various hours of thermal aging at 85°C on the thermal cycling under -45°C to 95°C.

Table 42: Effect of exposure to x-hours of thermal aging at 85C on the thermal cycling life under -45 to 95C

Aging time hrs	Reduction in life using ***Phase Growth*** as Damage proxy (cycles)	Reduction in life using ***IMC*** as Damage proxy (cycles)
	$N_{TC2}=0.25(t_{TA2})^{0.744}$	$N_{TC2}=0.23(t_{TA2})^{0.73}$
168	11	10
336	19	16
672	32	27
1344	53	44

Figure 115 and Figure 116 shows the prognosticated values of accrued damage in BGA assemblies after they have been subjected to x hours of thermal aging in TA 2 (85C) + 250 Cycles of thermal cycling in TC2 (-45°C to 95°C). The accrued damage has been prognosticated using both phase growth parameter and the intermetallic growth.

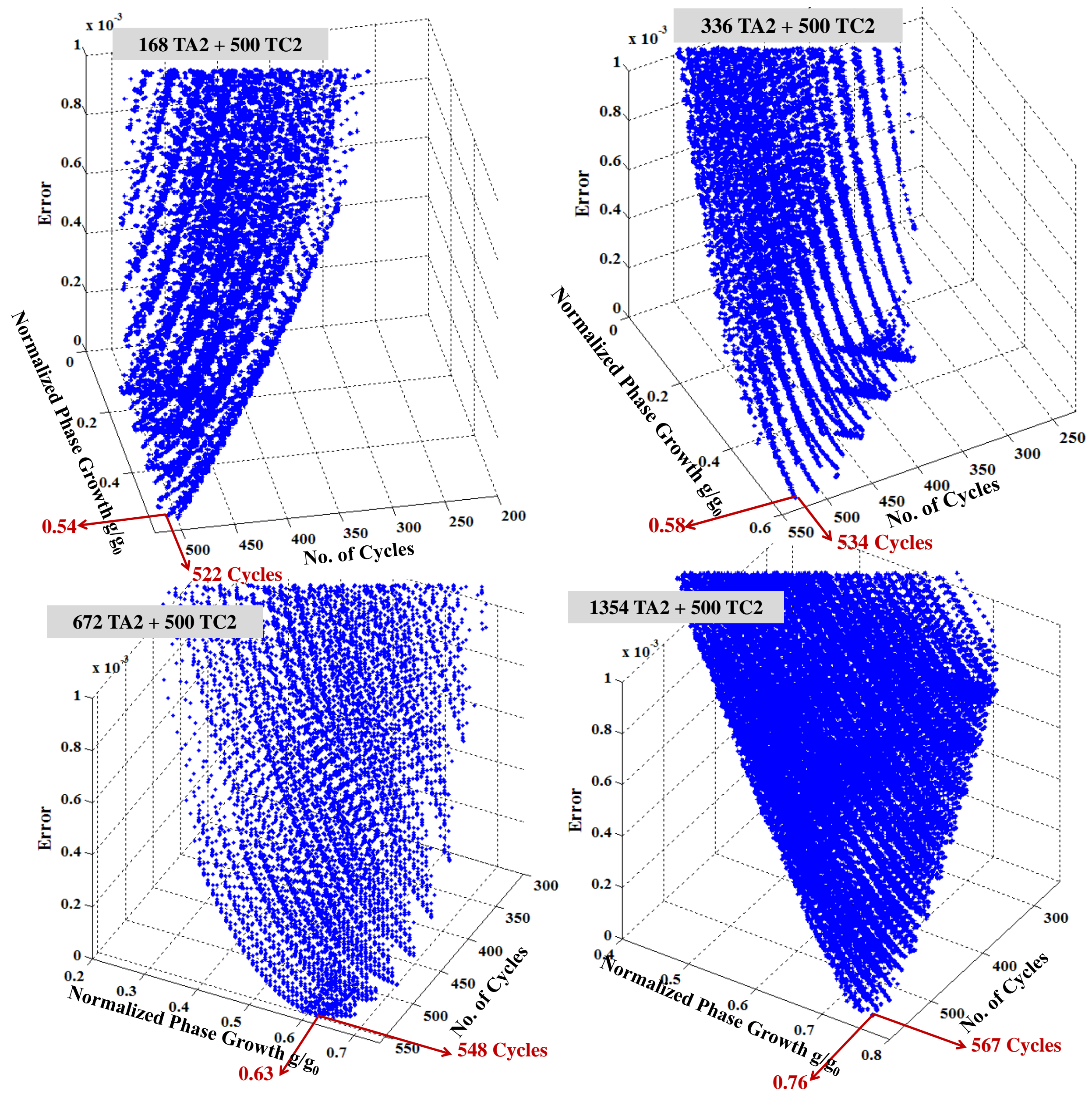

Figure 115: 3D plot of error versus Number of Cycles, Life computed from LM-algorithm for x-hrs TA2 + 250 cycles TC2 using Phase Growth as damage Proxy

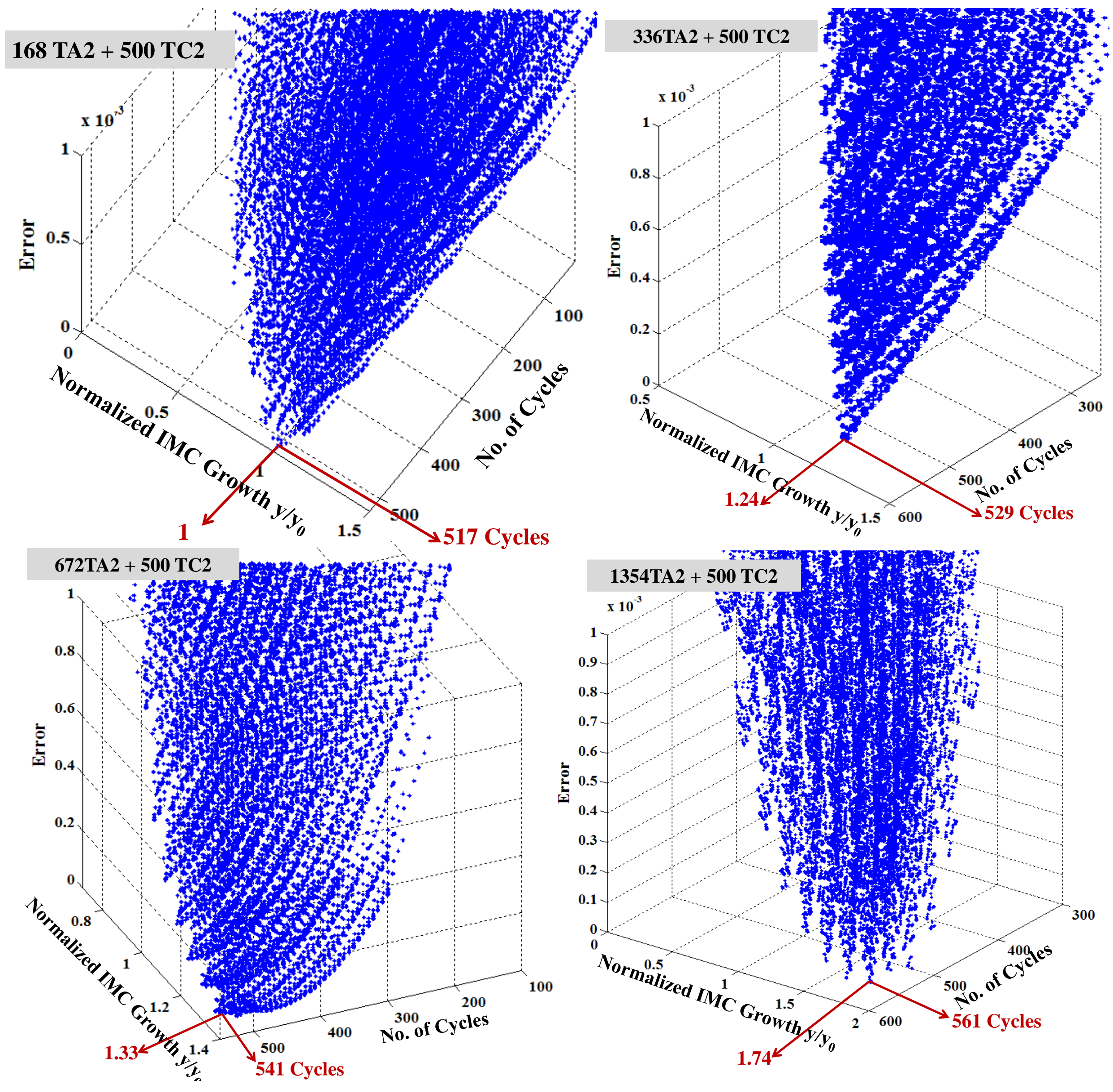

Figure 116: 3D plot of error versus Number of Cycles, Life computed from LM-algorithm for x-hrs TA2 + 250 cycles TC2 using IMC Growth as damage Proxy

Table 43: Prognostication of Overlapping Damage

	Phase Growth	IMC Growth
168 TA2 + 250 TC2 (Units of TC2 cycles), (A)	261	260
168 TA2 + 500 TC2 (Units of TC2 cycles), (B)	522	517
(B)-(A)	261	257
336 TA2 + 250 TC2 (Units of TC2 cycles), (C)	269	266
336 TA2 + 500 TC2 (Units of TC2 cycles), (D)	534	529
(D)-(C)	265	263
672 TA2 + 250 TC2 (Units of TC2 cycles), (E)	282	277
672 TA2 + 500 TC2 (Units of TC2 cycles), (F)	548	541
(F)-(E)	266	264
1354 TA2 + 250 TC2 (Units of TC2 cycles), (G)	303	294
1354 TA2 + 500 TC2 (Units of TC2 cycles), (H)	567	561
(H)-(G)	264	267

For the 324 BGA package, using phase growth parameter as the damage proxy, the prior accrued damage when subjected to (a) 168 hours TA2 + 250 Cycles TC2 was calculated to be 293 TC2

cycles, (b) 336 hours TA2 + 250 Cycles TC2 was calculated to be 323 TC2 cycles, (c) 672 hours TA2 + 250 Cycles TC2 was calculated to be 371 TC2 cycles and (d) 1354 hours TA2 + 250 Cycles TC2 was calculated to be 452 TC2 cycles. It is known that the difference in the prognosticated damage between the test assemblies which have been subjected to x-hours TA2 + 250 Cycles TC2 and x- hours TA2 + 500 Cycles TC2 is 250 cycles of TC2. The actual value of 250 TC2 cycles correlates well with the prognosticated values of 261, 265, 266 and 264 TC2 cycles.

A similar process has been followed using the IMC growth damage proxy package, using IMC growth parameter as the damage proxy, the prior accrued damage when subjected to (a) 168 hours TA2 + 250 Cycles TC2 was calculated to be 292 TC2 cycles, (b) 336 hours TA2 + 250 Cycles TC2 was calculated to be 320 TC2 cycles, (c) 672 hours TA2 + 250 Cycles TC2 was calculated to be 367 TC1 cycles and (d) 1354 hours TA2 + 250 Cycles TC2 was calculated to be 446 TC2 cycles. It is known that the difference in the prognosticated damage between the test assemblies which have been subjected to x-hours TA2 + 250 Cycles TC2 and x- hours TA2 + 500 Cycles TC2 is 250 cycles of TC2. The actual value of 250 TC2 cycles correlates well with the prognosticated values of 257, 263, 264 and 267 TC2 cycles.

Case III: Overlapping sequential stresses of thermal aging at 60°C and thermal cycling from 3 to 100°C

The phase growth and intermetallic thickness has been studied under microscope. The samples were prognosticated using the Levenberg-Marquardt Algorithm.

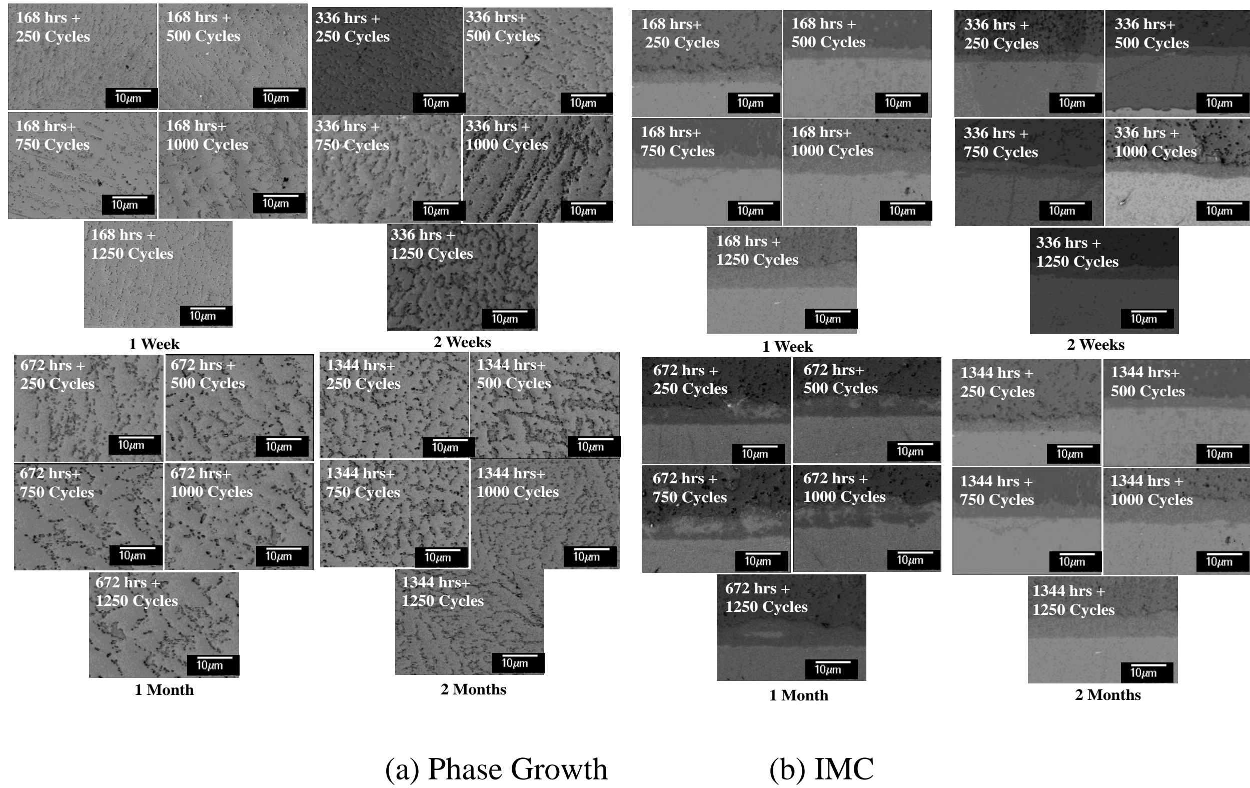

(a) Phase Growth (b) IMC

Figure 117: Back-scattered Images for samples exposed to Environments of x hours @ $60^{O}C$ + y CyclesTC-3 magnification 1000x (a) Phase Growth (b) IMC, 324 I/O PBGA

Table 44 shows the effect of exposure to various hours of thermal aging at 60°C on the thermal cycling under 3°C to 100°C.

Table 44: Effect of exposure to x-hours of thermal aging at 60C on the thermal cycling life under 3 to 100C

Aging time hrs	Reduction in life using ***Phase Growth*** as Damage proxy (cycles)	Reduction in life using ***IMC*** as Damage proxy (cycles)
	$N_{TC3}=0.72(t_{TA3})^{0.76}$	$N_{TC3}=0.6(t_{TA3})^{0.763}$
168	35	30

336	60	51
672	101	86
1344	173	147

Figure 118 and Figure 119 shows the prognosticated values of accrued damage in BGA assemblies after they have been subjected to x hours of thermal aging in TA1 (60C) + 250 Cycles of thermal cycling in TC3 (3°C to 100°C). The accrued damage has been prognosticated using both phase growth parameter and the intermetallic growth.

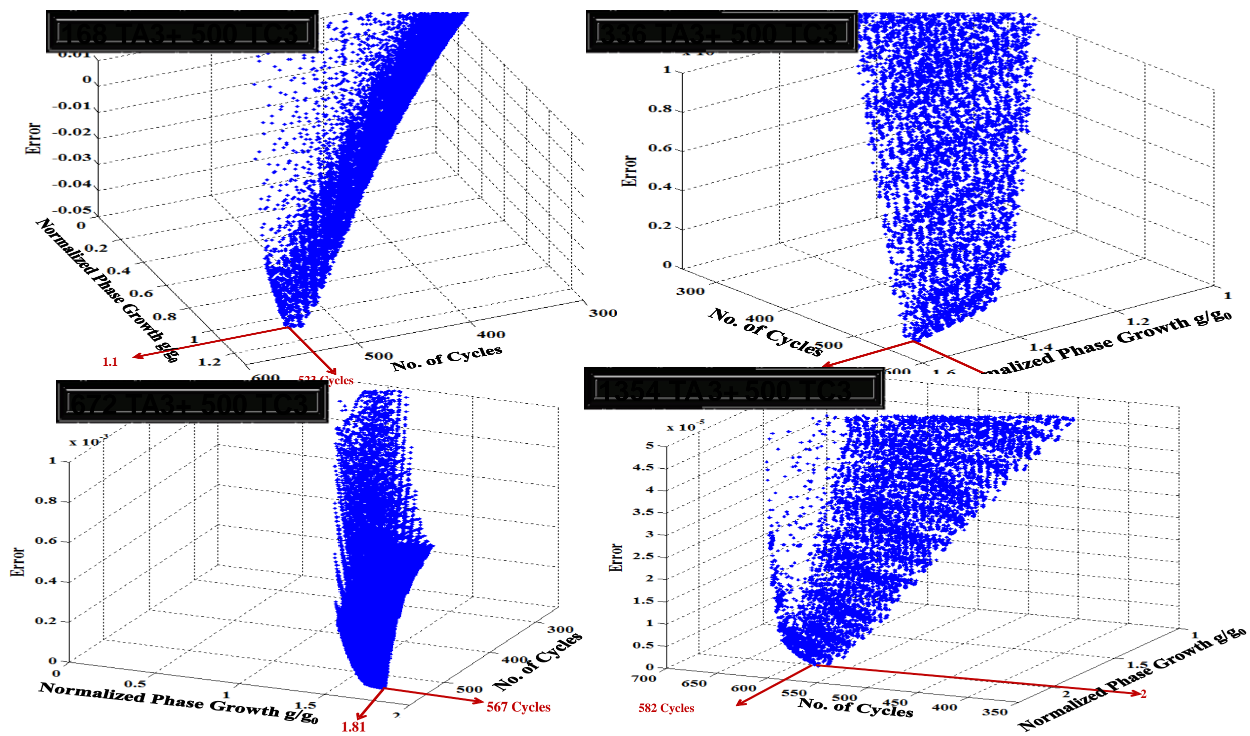

Figure 118: 3D plot of error versus Number of Cycles, Life computed from LM-algorithm for x-hrs TA1 + 250 cycles TC3 using Phase Growth as damage Proxy

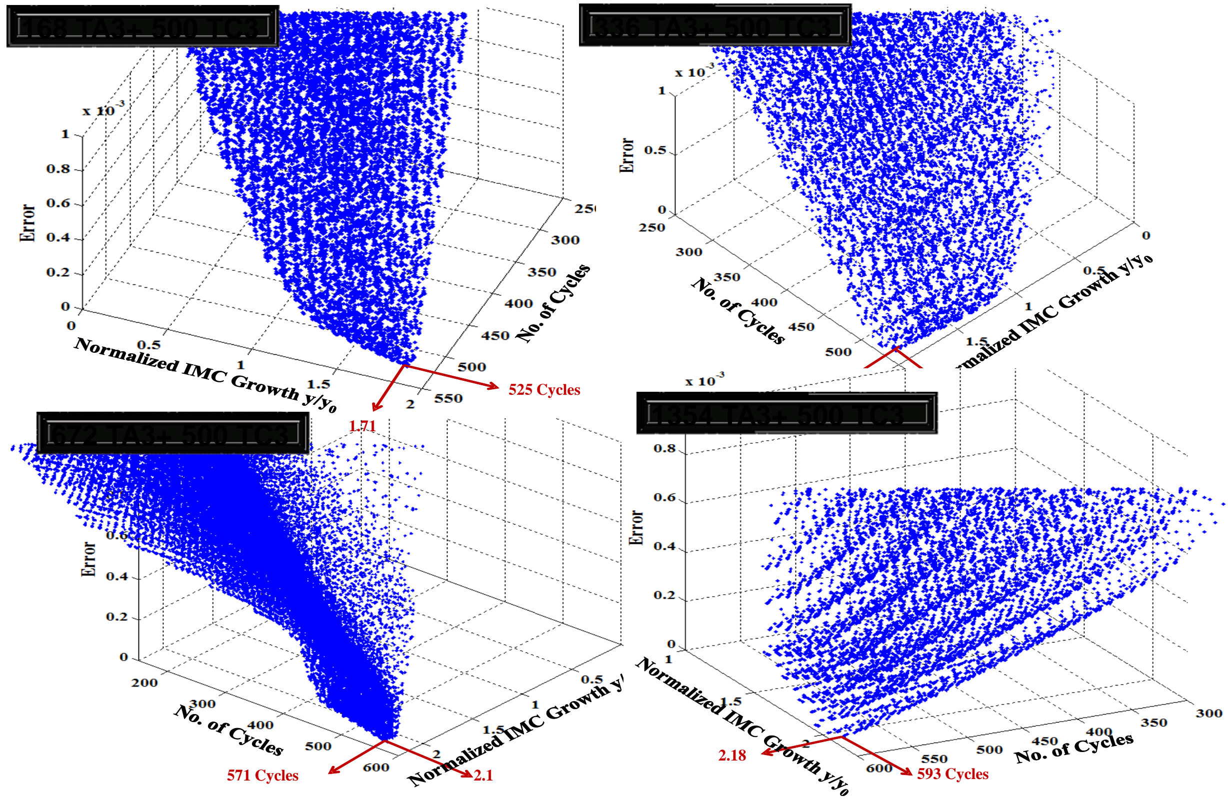

Figure 119: 3D plot of error versus Number of Cycles, Life computed from LM-algorithm for x-hrs TA1 + 250 cycles TC3 using IMC as damage Proxy

Table 45: Prognostication of Overlapping Damage

	Phase Growth	IMC Growth
168 TA3 + 250 TC3 (Units of TC3 cycles), (A)	285	269
168 TA3 + 500 TC3 (Units of TC3 cycles), (B)	546	512
(B)-(A)	261	243
336 TA3 + 250 TC3 (Units of TC3 cycles), (C)	310	301

336 TA3 + 500 TC3 (Units of TC3 cycles), (D)	568	549
(D)-(C)	258	248
672 TA3 + 250 TC3 (Units of TC3 cycles), (E)	351	336
672 TA3 + 500 TC3 (Units of TC3 cycles), (F)	611	583
(F)-(E)	260	247
1354 TA3 + 250 TC3 (Units of TC3 cycles), (G)	423	397
1354 TA3 + 500 TC3 (Units of TC3 cycles), (H)	686	651
(H)-(G)	263	254

For the 324 BGA package, using phase growth parameter as the damage proxy, the prior accrued damage when subjected to (a) 168 hours TA3 + 250 Cycles TC3 was calculated to be 269 TC3 cycles, (b) 336 hours TA3 + 250 Cycles TC3 was calculated to be 283 TC3 cycles, (c) 672 hours TA3 + 250 Cycles TC3 was calculated to be 309 TC3 cycles and (d) 1354 hours TA3 + 250 Cycles TC3 was calculated to be 353 TC3 cycles. It is known that the difference in the prognosticated damage between the test assemblies which have been subjected to x-hours TA3 + 250 Cycles TC3 and x- hours TA3 + 500 Cycles TC3 is 250 cycles of TC3. The actual value of 250 TC3 cycles correlates well with the prognosticated values of 261, 258, 260 and 263 TC3 cycles

A similar process has been followed using the IMC growth damage proxy package, using IMC growth parameter as the damage proxy, the prior accrued damage when subjected to (a) 168

hours TA3 + 250 Cycles TC3 was calculated to be 269 TC3 cycles, (b) 336 hours TA3 + 250 Cycles TC3 was calculated to be 283 TC3 cycles, (c) 672 hours TA3 + 250 Cycles TC3 was calculated to be 307 TC3 cycles and (d) 1354 hours TA3 + 250 Cycles TC3 was calculated to be 349 TC3 cycles. It is known that the difference in the prognosticated damage between the test assemblies which have been subjected to x-hours TA3 + 250 Cycles TC3 and x- hours TA3 + 500 Cycles TC3 is 250 cycles of TC3. The actual value of 250 TC3 cycles correlates well with the prognosticated values of 243, 248, 247 and 254 TC3 cycles.

6.7 Summary and Conclusions

A method has been developed for prognostication of accrued prior damage in electronics subjected to overlapping sequential environments of thermal aging and thermal cycling. The presented approach uses the Levenberg- Marquardt Algorithm in conjunction with microstructural evolution of damage based leading indicator for estimating prior stress history. Damage proxy such as phase-growth is examined. The viability of the approach has been demonstrated for leadfree test assemblies subjected to three different cases of thermal aging at 125°C, 85°C and 60°C and redeployed in cyclic thermo-mechanical environment thermal cycling from -55°C to 125°C, -40°C to 95°C and 3°C to 100°C respectively. Major factor like activation energy has been calculated. Damage equivalency relationships between thermal aging during storage life and the resulting reduction in thermo-mechanical reliability in cyclic thermal environments during field deployment have been derived. Assemblies subjected to sequential stresses have been prognosticated for accrued damage from sequential overlapping stresses of

thermal aging and thermal cycling. Correlation between the prognosticated damage and the actual accrued damage demonstrates that the proposed approach can be used to assess damage accrued under overlapping thermo-mechanical stresses of thermal aging and thermal cycling.

Chapter 7

Summary and Future Work

Electronics from a reliability perspective can be thought of as a function of three primary variables viz. materials, process, and application. There is a ton of literature available on reliability enhancement techniques specifically addressing materials and compliant processes. However even after employing all the reliability enhancement schemes it is well known that the deployed parts are observed to have erratic failure behavior and characteristics in the field even after rigorous qualification tests. Conventional life prediction models used for measuring electronics reliability are based on fear of failure whose decisions are based on pristine state and lack insight about the ongoing reliability of the system. The work presented in this thesis is an effort to address the growing need to develop techniques that can monitor in-field system state during the service life and make life predictions based on interrogation of system state. Although this technique requires condition monitoring it still eliminates the need for continuous monitoring of the system state to make life predictions which considerable saves the overhead associated with data acquisition systems. Two prognostic health management (PHM) models were presented for single and multiple thermal environments respectively.

7.1 PHM Model for Field –deployed Electronics subjected to Overlapping Thermo-Mechanical Environments

Novel prognostic health management (PHM) model was developed for electronics exposed to steady-state temperature profiles. The proposed model was implemented on commercially relevant test vehicle to demonstrate its applicability in real field deployed electronics. The PHM model allowed life estimation of electronics subjected to single isothermal aging environments. The proposed methodology enabled spot assessment of life consumed due to isothermal aging environments in the pre-failure space, without any knowledge of prior stress histories. The prognostic model was based on physics-of-failure of lead-free second level solder interconnects commonly found in today's high I/O packaging architectures. It has been shown that the physics-of-failure based damage proxy identified as inter-metallic compound (IMC) growth, formed between the second level solder interconnect and copper pad at the board side interface can be used as a leading indicator of failure. Higher learning algorithm theory like Levenberg-Marquardt algorithm was used a non-linear least square (NLLSQ) method and was employed for the first time in evaluating electronics reliability.

The prognostic model proposed in Chapter 3 has been developed for prognostication of accrued prior damage and remaining useful life in field-deployed electronics extracted from service after exposure to overlapping sequential environments of thermal aging and thermal cycling. The presented approach uses the Levenberg- Marquardt Algorithm in conjunction with microstructural evolution of damage based leading indicator for estimating prior accrued damage.

7.2 PHM Model for Sequential Thermal Environments of Thermal Aging and Thermal Cycling

In Chapter 4 a PHM model was developed for prognostication of accrued prior damage in electronics subjected to overlapping sequential environments of thermal aging and thermal cycling. Mathematical relationship between storage time and corresponding reduction in cyclic life was successfully established based on two physics-of-failure based damage proxies viz. phase-growth and inter-metallic compound (IMC) growth of second level solder interconnects. Life after storage and sequential stress application was prognosticated to show the influence of dormant storage on the cyclic life. Prognostication results were carefully studied to see if it captures the life expended during storage in thermal cyclic environment. It is clear from the prognostication results and damage equivalency relationship that the effect of dormant storage cannot be neglected as it considerably reduces the cyclic life and its effect has to be taken into account for accurate life predictions.

The viability of the proposed prognostic model was demonstrated for multiple combinations of overlapping stress environments to prove the robustness of the model. Correlation between the prognosticated damage and the actual accrued damage displays that the proposed PHM model can be used to assess damage accrued under overlapping thermo-mechanical stresses of thermal aging and thermal cycling. In addition, prognostics metrics have been used to quantitatively evaluate the performance of the prognostic algorithms using both the leading indicators. Results demonstrate that both damage proxies work well in estimating accrued damage and estimating residual life.

7.3 PHM Model for Overlapping Sequential Thermal Environments of Thermal Aging and Thermal Cycling

A method has been developed for prognostication of accrued prior damage in electronics subjected to overlapping sequential environments of thermal aging and thermal cycling. Major factor like activation energy has been calculated. Damage equivalency relationships between thermal aging during storage life and the resulting reduction in thermo-mechanical reliability in cyclic thermal environments during field deployment have been derived. Assemblies subjected to sequential stresses have been prognosticated for accrued damage from sequential overlapping stresses of thermal aging and thermal cycling with case studies involving constant temperature difference and constant maximum temperature difference.

7.4 Scope for Future Work

Prognostic model performance has been evaluated using standard prognostic metrics available in the literature. It would be interesting to relate these metrics for the model enhancement in the future. For example α-λ curve for both the leading indicator based models indicate that the models diverge at the end of life where it is critical to get tighter results. It would be worth to study various model parameters and check the sensitivity of each individual parameter with respect to the model outputs. The studied sensitivities can be incorporated in the models for accurate life predictions in the future.

Prognostic models in this thesis are based on non-linear least square (NLLSQ) method called Levenberg-Marquardt algorithm. It will also be interesting to apply other higher order learning algorithms to solve the set non-linear physic-of-failure based equations for life

computation. Various models can then be compared using prognostic metrics and ranked for specific application.

In future prognostic models can be developed for more complex environments such as multiple combinations of thermal aging and thermal cycling. Also sequential low cycle thermal fatigue and transient drop event can be studied for prognosis. It would be valuable to study the effect of thermal aging and thermal cycling on the drop reliability of electronics. Complex overlapping environment such as thermal fatigue and high strain rate drop testing can be studied to extract damage proxies which can be incorporated as leading indicators of failure in future prognostic models

BIBLIOGRAPHY

Allen, D., Probabilities Associated with a Built-in-Test System, Focus on False Alarms, Proceedings of AUTOTESTCON, IEEE Systems Readiness Technology Conference, pp. 643-645, September 22-25, 2003.

Anderson, N., and Wilcoxon, R., Framework for Prognostics of Electronic Systems, Proceedings of International Military and Aerospace Avionics COTS Conference, Seattle, WA, Aug 3-5, 2004.

Chandramouli, R., Pateras, S., Testing Systems on a Chip, IEEE Spectrum, Vol. 33, No. 11, pp. 42-47, Nov. 1996.

Drees, R., and Young, N., Role of BIT in Support System Maintenance and Availability, IEEE A&E Systems Magazine, pp. 3-7, August 2004.

Gao, R. X., Suryavanshi, A., BIT for Intelligent System Design and Condition Monitoring, IEEE Transactions on Instrumentation and Measurement, Vol. 51, Issue: 5, pp. 1061-1067, October 2002.

Hassan, A., Agarwal, V. K., Nadeau-Dostie, B., Rajski, J., BIST of PCB Interconnects Using Boundary- Scan Architecture, IEEE Transactions on Computer-Aided Design, Vol. 11, No. 10, pp. 1278-1288, October 1992.

Jarrell, D., Sisk, D., Bond, L., Prognostics and Condition Based Maintenance (CBM) A Scientific Crystal Ball, Pacific Northwest National Laboratory, Richland, WA, International Congress on Advanced Nuclear Power Plants (ICAPP), paper number 194 June 2002.

Lall, P., Islam, N., Rahim, K., Suhling, J., Gale, S., Leading Indicators-of-Failure for Prognosis of Electronic and MEMS Packaging, 54th ECTC, Las Vegas, Nevada, June 1 – 4, 2004[a].

Lall, P., Islam, N., Shete, T., Evans, J., Suhling, J., Gale, S., Damage Mechanics of Electronics on Metal-Backed Substrates in Harsh Environments, 54th ECTC, Las Vegas, Nevada, June 1 - 4, 2004[b].

Lall, P., N. Islam, J. C. Suhling, and R. Darveaux, Model for BGA and CSP Reliability in Automotive Underhood Applications, IEEE Transactions on Components and Packaging Technologies, Vol 27, No. 3, pp. 585-593, 2004[c].

Lall, P., D. Panchagade, Y. Liu, R. W. Johnson, and J. C. Suhling, Models for Reliability Prediction of Fine-Pitch BGAs and CSPs in Shock and Drop-Impact, 54th ECTC, pp. 1296-1303, Las Vegas, NV, June 1-4, 2004[d].

Lall, P., Islam, N., Choudhary, P., Suhling, J., Prognostication and Health Monitoring of Leaded and Lead Free Electronic and MEMS Packages in Harsh Environments, 55th ECTC, pp. 1-9, Orlando, FL, June 1-3, 2005[a].

Lall, P., Panchagade, D., Choudhary, P., Suhling, J., Gupte, S., Failure-Envelope Approach to Modeling Shock and Vibration Survivability of Electronic and MEMS Packaging, 55th ECTC, Orlando, FL, pp. 480 – 490, June 1 – 3, 2005[b].

Lall, P., Gupte, S., Choudhary, P., Suhling, J., Solder-Joint Reliability in Electronics Under Shock and Vibration using Explicit Finite Element Sub-modeling, 56th ECTC, San Diego, California, pp.428-435, May 30-June 2, 2006[a].

Lall, P., Choudhary, P., Gupte, S., Suhling, J., Health Monitoring for Damage Initiation & Progression during Mechanical Shock in Electronic Assemblies, 56th ECTC, San Diego, California, pp.85-94, May 30-June 2, 2006[b].

Lall, P., Hande, M., Singh, N., Suhling, J., Lee, J., Feature Extraction and Damage Data for Prognostication of Leaded and Leadfree Electronics, 56th ECTC, San Diego, California, pp.718-727, May 30-June 2, 2006[c].

Lall, P., Islam, N., Rahim, K., Suhling, J., Gale, S., Prognostics and Health Management of Electronic Packaging, IEEE Transactions on Components and Packaging Technologies, Vol. 29, No. 3, pp. 666-677, September 2006[d].

Lall, P., Islam, N., Shete, T., Evans, J., Suhling, J., Gale, S., Damage Mechanics of Electronics on Metal-Backed Substrates in Harsh Environments, IEEE Transactions on Components and Packaging Technologies, Vol. 29, No. 1, pp. 204-212, March 2006[e].

Lall, P., D. Panchagade, Y. Liu, R. W. Johnson, and J. C. Suhling, Models for Reliability Prediction of Fine-Pitch BGAs and CSPs in Shock and Drop-Impact, IEEE Transactions on Components and Packaging Technologies, Vol. 29, No. 3, pp. 464-474, September 2006[f].

Lall, P., Choudhary, P., Gupte, S., Suhling, J., Hofmeister, J., Statistical Pattern Recognition and Built-In Reliability Test for Feature Extraction and Health Monitoring of Electronics under Shock Loads, 57th ECTC, Reno, Nevada, pp. 1161-1178, May 30-June 1, 2007[a].

Lall, P., Gupte, S., Choudhary, P., Suhling, J., Solder-Joint Reliability in Electronics Under Shock and Vibration using Explicit Finite Element Sub-modeling, IEEE Transactions on Electronic Packaging Manufacturing, Vol. 30, No. 1, pp. 74-83, January 2007[b].

Lall, P., M. Hande, C. Bhat, J. Suhling, Jay Lee, Prognostics Health Monitoring (PHM) for Prior-Damage Assessment in Electronics Equipment under Thermo-Mechanical Loads, 57th ECTC, Reno, Nevada, pp. 1097-1111, May 29 – June 1, 2007[c].

Lall, P. Panchagade, D., Liu, Y., Johnson, W., Suhling, J., Smeared Property Models for Shock-Impact Reliability of Area-Array Packages, ASME Journal of Electronic Packaging, Volume 129, pp. 373-381, December 2007[d].

Lall, P., Hande, M., Bhat, C., Islam, N., Suhling, J., Lee, J., Feature Extraction and Damage-Precursors for Prognostication of Lead-Free Electronics, Microelectronics Reliability, Vol. 47, pp. 1907–1920, December 2007[e].

Lall, P., Choudhary, P., Gupte, S., Suhling, J., Health Monitoring for Damage Initiation and Progression during Mechanical Shock in Electronic Assemblies, IEEE Transactions on Components and Packaging Technologies, Vol. 31, No. 1, pp. 173-183, March 2008[a].

Lall, P., Panchagade, D., Choudhary, P., Gupte, S., Suhling, J., Failure-Envelope Approach to Modeling Shock and Vibration Survivability of Electronic and MEMS Packaging, IEEE Transactions on Components and Packaging Technologies, Vol. 31, No. 1, pp. 104-113, March 2008[b].

Lall, P., Hande, M., Bhat, C., More, V., Vaidya, R., Suhling, J., Algorithms for Prognostication of Prior Damage and Residual Life in Lead-Free Electronics Subjected to Thermo-Mechanical Loads, Proceedings of the 10th ITherm, Orlando, Florida, pp. 638-651, May 28-31, 2008[c].

Lall, P., Bhat, C., Hande, M., More, V., Vaidya, R, Pandher, R., Suhling, J., Goebel, K., Interrogation of System State for Damage Assessment in Lead-free Electronics Subjected to Thermo-Mechanical Loads, 58th ECTC, Orlando, Florida, pp. 918-929, May 27-30, 2008[d].

Lall, P., Iyengar, D., Shantaram, S., S., Gupta, P., Panchagade, D., Suhling, J., KEYNOTE PRESENTATION: Feature Extraction and Health Monitoring using Image Correlation for Survivability of Leadfree Packaging under Shock and Vibration, EuroSIME, Freiburg, Germany, pp. 594-608, April 16-18, 2008[e].

Lall, P., Iyengar, D., Shantaram, S., Pandher, R., Panchagade, D., Suhling, J., Design Envelopes and Optical Feature Extraction Techniques for Survivability of SnAg Leadfree Packaging Architectures under Shock and Vibration, 58th ECTC, Orlando, Florida, pp. 1036-1047, May 27-30, 2008[f].

Lall, P., Shantaran, S., Angral, A., Kulkarni, M., Explicit Submodeling and Digital Image Correlation Based Life-Prediction of Leadfree Electronics under Shock-Impact, 59th ECTC, pp. 542-555, San Diego, California USA, May 25-29, 2009[a].

Lall, P., Gupta, P., Panchagade, D., Angral, A., Fault-Mode Classification for Health Monitoring of Electronics Subjected to Drop and Shock, 59th ECTC, pp. 668-681, San Diego, California USA, May 25-29, 2009[b].

Lall. P., More, V., Vaidya, R., Goebel, K., Prognostication of Latent Damage and Residual Life in Leadfree Electronics Subjected to Multiple Thermal-Environments, 59th ECTC, pp. 1381-1392, San Diego, California USA, May 25-29, 2009[c].

Lall. P., Lowe, R., Goebel, K., Resistance Spectroscopy-based Condition Monitoring for Prognostication of High Reliability Electronics Under Shock-Impact, Proceedings of 59th ECTC, pp. 1245-1255, San Diego, California USA, May 25-29, 2009d.

Lall. P., Lowe, R., Goebel, K., Prognostics Using Kalman-Filter Models and Metrics for Risk Assessment in BGAs Under Shock and Vibration Loads, Proceedings of 60th ECTC, pp. 889-901, Las Vegas, Nevada, USA, June 2-5, 2010d.

Lall. P., More, V., Vaidya, R., Goebel, K., Assessment of Residual Damage in Lead-free Electronics Subjected to Multiple Thermal Environments of Thermal Aging and Thermal Cycling, Proceedings of 60th ECTC, pp. 206-218, Las Vegas, Nevada, USA, June 2-5, 2010d.

Lall, P., Gupta, P., Panchagade, D., Self-Organized Mapping of Failure Modes in Portable Electronics Subjected to Drop and Shock, Proceedings of 60th ECTC, pp. 1195-1208, Las Vegas, Nevada, USA, June 2-5, 2010d.

Lall. P., Lowe, R., Goebel, K., Use of Prognostics in Risk-Based Decision Making For BGAs Under Shock And Vibration Loads, Proceedings of ITHERM 2010, Las Vegas, NV, June 2-5, 2010.

Lall. P., More, V., Vaidya, R., Goebel, K., PHM-Based Residual Life Computation of Electronics Subjected to a Combination of Multiple Cyclic-Thermal Environments, Proceedings of ITHERM 2010, Las Vegas, NV, June 2-5, 2010.

Lall, P., Gupta, P., Panchagade, D., Angral, A., Fault-Isolation in Portable Electronics Subjected to Drop And Shock, Proceedings of ITHERM 2010, Las Vegas, NV, June 2-5, 2010.

Lall P., Hinshaw R., Pandher R., Harsha M., Suhling J., Thermo-Mechanical Reliability of SAC Lead-free Alloys Proceedings of ITHERM 2010, Las Vegas, NV, June 2-5, 2010.

Lall P., Angral A., Suhling J., Board Trace Fatigue Models and Design Guidelines for Electronics Under Shock-Impact , Proceedings of ITHERM 2010, Las Vegas, NV, June 2-5, 2010.

Lall P., Kulkarni M., Angral A., Panchagade D., Suhling J.,Digital-Image Correlation and XFEM Based Shock-Reliability Models for Leadfree and Advanced Interconnects Electronic Components and Technology Conference, 2010. ECTC 2010. 60th, 91-105, 2010

Lall P., Shantaram S., Panchagade D.,Peridynamic-Models Using Finite Elements for Shock and Vibration Reliability of Lead-free Electronics Proceedings of ITHERM 2010, Las Vegas, NV, June 2-5, 2010.

Lourakis, M., I., A., A brief Description of the Levenberg-Marquardt algorithm implemented by Levmar, Foundation of Research and Technology – Hellas (Forth), Greece, pp. 1- 6, Feb 11, 2005.

Madsen, K., Nielsen, H., B., Tingleff, O., Methods for Non-Linear Least Squares Problems, Technical University of Denmark, Lecture notes, available at http://www.imm.dtu.dk/courses/02611/nllsq.pdf, 2nd Edition, pp. 1-30, 2004.

Marko, K.A., J.V. James, T.M. Feldkamp, C.V. Puskorius, J.A. Feldkamp, and D. Roller, Applications of Neural Networks to the Construction of "Virtual" Sensors and Model-Based Diagnostics, Proceedings of ISATA 29th International Symposium on Automotive Technology and Automation, pp.133-138, June 3-6, 1996.

McCann, R. S., L. Spirkovska, Human Factors of Integrated Systems Health Management on Next-Generation Spacecraft, First International Forum on Integrated System Health Engineering and Management in Aerospace, Napa, CA, pp. 1-18, November 7-10, 2005.

Mishra, S., Pecht, M., In-situ Sensors for Product Reliability Monitoring, Proceedings of SPIE, vol. 4755, pp. 10-19, 2002.

Nielsen, H., B, Damping Parameter in Marquardt's Method, Technical Report, IMM-REP-1999-05, Technical University of Denmark, Available at http://www.imm.dtu.dk/~hbn, pp. 1-16, 1999.

Rosenthal, D., and Wadell, B., Predicting and Eliminating Built-in Test False Alarms, IEEE Transactions on Reliability, Vol. 39, No 4, pp. 500-505, October 1990.

Saxena, A., J. Celaya, B. Saha, S. Saha, and K. Goebel, Evaluating Algorithm Performance Metrics Tailored for Prognostics, IEEE Aerospace Conference, Big Sky, MT, pp. 1-11, March 2008[a].

Saxena, A., J. Celaya, E. Balaban, K. Goebel, B. Saha, S Saha, and M. Schwabacher, Metrics for Evaluating Performance of Prognostic Techniques, Intl. Conf. on Prognostics and Health Management, Denver, Colorado, pp. 1-17, October 2008[b].

Schauz, J. R., Wavelet Neural Networks for EEG Modeling and Classification, PhD Thesis, Georgia Institute of Technology, 1996.

Shiroishi, J., Y. Li, S. Liang, T. Kurfess, and S. Danyluk, Bearing Condition Diagnostics via Vibration and Acoustic Emission Measurements, Mechanical Systems and Signal Processing, Vol.11, No.5, pp.693-705, Sept. 1997.

Williams, T. W., Parker, K. P., Design for Testability- Survey, Proceedings of the IEEE, Vol. 71, No. 1, pp. 98-112, January 1983.

Zhang, Y., Cai, Z., Suhling, J., Lall, P., Bozack M., The Effects of SAC Alloy Composition on Aging Resistance and Reliability, 59th Electronic Component and Technology Conference, San Diego, CA, pp. 370 – 389, May 26-29, 2009.

Zorian, Y., A Structured Testability Approach for Multi Chip Boards Based on BIST and Boundary Scan, IEEE Transactions on Components, Packaging, and Manufacturing Technology-Part B, Vo l. 17, No. 3, pp. 283-290, August 1994.

Appendix

Polishing Procedure

Step I – Potting or Mounting

1. Clean specimen properly.
2. Use Smaplklip if necessary to align specimen.
3. Carefully mix 5 part of Epokwick resin with 1 part of Epokwick hardener. Mixing Instructions are available in detail near polishing table.
4. Apply release agent to the inner part of mounting cups. If necessary give two coats at interval of 5 minutes.
5. Place specimen inside mounting cup properly (ideally at center) and pour mixture of resin and hardener, exactly on top of specimen, slowly and carefully so that bubbles will not form.
6. It will be cured in 90 minutes. On safer side, grinding and polishing can be started after 180 minutes.

Step – II Grinding

Goal of grinding is to remove damage resulting from sectioning, establish a planer surface and reach a specific plane near to area of interest. Speed of wheel at the time of grinding should be not more than 350rpm. High speed removes material at high rate, but also causes excessive and deep scratching, which can damage part permanently. Pressure applied on specimen while grinding should be optimum, so that it will not get excessively stressed. Also after each step, rinse sample with water, remove debris and make it dry using compressed air.

1. Start with 240 Grit paper. Make sure to apply proper force to avoid major damage to part.
2. Use 360 Grit paper to remove scratches formed by 240 grit paper.
3. Use 400 grit paper. This is final rough grinding paper which can remove material effectively. At the end of this stpe, there will be scratches on surface, but they will be small in size, and shallow in depth. If not, redo step 1, 2, and 3.
4. Use 600 grit paper to reach desired plane.
5. Use 800 grit paper, which removes major scratches effectively, and at this stage, we start getting clear image, with minor scratches.

Grinding papers can be reused. If the paper is good, but you are done with it, please keep it in shelf. There is one whole shelf dedicated for this. If the paper is worn out, tear it and throw it in to dustbin.

Step III – Polishing

For polishing, wheel speed should be around 300rpm to avoid smearing of soft material.

1. Use 1200 grit paper. This will remove remaining scratches, and surface will be cleaner.
2. Use 4000P paper.

After this step, rinse sample with solution of 50ml water and few drops of general dish washing soap. Make sure that all debris is removed. Use compressed air to make specimen dry.

Step IV – Final Polishing

After use of each polishing cloth rinse thoroughly with water, clean it properly, and keep at proper place. These cloths can be used for several times. Grinding wheel speed should not be more than 200 rpm.

1. Use MetaDi Supreme polycrystalline diamond suspension (3µm crystal size) on Micro cloth or Polycloth (from Buehler). Before use, rice cloth with DI water, and then mount on grinding wheel.
2. Use MetaDi Supreme polycrystalline diamond suspension (1µm crystal size) on Micro cloth or Polycloth (from Buehler). Before use, rice cloth with DI water, and then mount on grinding wheel. Do not use same cloth for 3µm and 1µm suspension.

Step V – Cleaning

Clean polished surface with solution of 50ml water and few drops of general dish washing soap. Use propanol to displace water. Make surface dry using compressed nitrogen.